

EFFECT OF INTERSTITIAL SOLUTES ON THE STRENGTH AND DUCTILITY OF TITANIUM

*Hans Conrad**

Metallurgical Engineering and Materials Science Department, and
Institute for Mining and Minerals Research, University of Kentucky,
Lexington, KY 40506, U.S.A.

CONTENTS

1. INTRODUCTION	129
2. SOME PERTINENT CHEMICAL AND PHYSICAL PROPERTIES	131
2.1 Phase Equilibria	131
2.2 Crystallography Relating to Interstitial Solutes	131
2.3 Elastic Moduli	134
2.4 Diffusion Coefficients and Bond Energies	138
2.5 Deformation Modes and Dislocation Properties	143
2.6 Fracture Modes	146

*Presently with Materials Engineering Department, North Carolina State University,
Raleigh, N.C. 27650.

3. THEORETICAL CONSIDERATIONS	148
3.1 Dislocation - Interstitial Solute Interactions	148
3.1.1 Elastic Interactions	148
Size Misfit Interaction	148
Modulus Interaction	150
Combined Size Misfit and Modulus Interactions	151
Sessile Splitting of Screw Dislocations	155
3.1.2 Chemical Interactions	158
Short Range Order or Clustering	158
Stacking Fault Considerations	158
Dislocation Core Structure	159
Breaking of Chemical Bonds	159
3.1.3 Electrical Interactions	160
3.2 Solid Solution Strengthening Models	160
3.3 Dislocation Kinetics	165
3.3.1 Low Temperatures: Moving Dislocations and Stationary Interstitial Solutes	166
Single Set of Discrete Obstacles	166
Spectrum of Obstacles	171
Additional Comments	173
3.3.2 Intermediate Temperatures: Moving Dislocation and Mobile Interstitial Solutes	174
Collection of the Atmosphere	175
Breaking Away From the Atmosphere	175
Dislocation Multiplication	175
Disappearance of Dynamic Strain Aging	176
Sweeping of Solute Atoms	176
3.3.3 High Temperatures: Moving Dislocations and Rapidly Moving Interstitial Solutes	177
4. EXPERIMENTAL RESULTS	179
4.1 Single Crystals	179

EFFECT OF INTERSTITIAL SOLUTES ON TITANIUM	125
4.1.1 {10\bar{1}0} <11\bar{2}0> Prism Glide	179
Stress-Strain Behavior	179
Slip Line Appearance, Occurrence of Twinning and Schmid's Critical Shear Stress Law	183
Dislocation Structure	183
Effects of Temperature, Strain Rate and Interstitial Content on the Critical Resolved Shear Stress	185
Dislocation Velocity	194
Deformation Kinetics	194
4.1.2 (0001) <11\bar{2}0> Basal Glide	196
Stress-Strain Behavior	196
Slip Line Appearance and Dislocation Structure	197
Effects of Temperature, Strain Rate and Interstitial Content on the Critical Resolved Shear Stress	198
Deformation Kinetics	199
4.1.3 {10\bar{1}1} <11\bar{2}0> Pyramidal Glide and $\vec{c} + \vec{a}$ Dislocations	200
4.1.4 Twinning	202
4.1.5 Influence of Substitutional Solutes	206
4.2 Polycrystals	208
4.2.1 Characterization of Materials	208
Chemistry	208
Texture	211
Grain Structure	211
4.2.2 General Deformation Behavior	212
Stress-Strain Curves	212
Effects of Temperature and Strain Rate on the Flow Stress	213
Creep and Stress Relaxation	216
Twinning	218
Dislocation Structure	220
Summary	224
4.2.3 Very Low Temperatures ($T \sim 0.002T_m$)	225

4.2.4 Low Temperatures ($0.002 < T/T_m < 0.3$)	226
Effects of Grain Size, Interstitial Content, Temperature and Strain Rate on the Flow Stress and Hardness	226
Strain Hardening	247
Internal Stress	252
Deformation Kinetics	260
Fracture and Ductility	265
4.2.5 Intermediate Temperatures ($0.3 < T_m < 0.4$)	274
Static Strain Aging	274
Dynamic Strain Aging	276
Deformation Kinetics	281
Fracture	283
4.2.6 High Temperatures ($T/T_m > 0.4$)	284
General	284
Deformation Kinetics	284
4.2.7 Summary of Deformation Kinetics	287
5. MODELS AND MECHANISMS	289
5.1 Low Temperatures ($T < 0.3 T_m$)	289
5.1.1 Serrations in Stress-Strain Curves at 4.2K.	289
Criterion for Plastic Instability	289
Magnitude of Stress Drops	290
5.1.2 Prism Glide - Solution Strengthening by Interstitials	294
Nature of Interstitial Solute Obstacles	294
Concentration Dependence of the Strengthening	296
Concentration Dependence of the Activation Volume	299
Sob, Kratochvil and Kroupa Model	301
Solution Strengthening Model	304
Stress Equivalence of Solution Strengthening	305
Force-Activation Distance Curve	307
Dislocation Kinetics	310

EFFECT OF INTERSTITIAL SOLUTES ON TITANIUM	127
Temperature Dependence of the Flow Stress	325
Strengthening Due to Two or More Interstitial Solutes	328
Mott-Labusch Statistics	329
Summary	329
5.1.3 Prism Glide - Strain Hardening	331
5.1.4 Basal Glide and Relative Ease of Basal and Prism Glide	333
5.1.5 $\langle \bar{c} + \bar{a} \rangle$ Glide and Twinning	338
5.1.6 Plastic Deformation of Polycrystals	342
Active Deformation Modes	342
Dislocation Multiplication and Structure	343
Yield Point	357
Strain Hardening	358
Grain Size Hardening	364
Internal Stress	366
5.1.7 Fracture of Polycrystals	367
5.2 Intermediate Temperatures ($0.3 < T/T_m < 0.4$)	369
5.2.1 Prism and Basal Glide in Single Crystals	369
5.2.2 Plastic Deformation and Fracture of Polycrystals	370
Static Strain Aging	370
Dynamic Strain Aging	371
Fracture	371
5.3 High Temperatures ($T > 0.4 T_m$)	373
5.3.1 Prism and Basal Glide in Single Crystals	373
5.3.2 Plastic Deformation and Fracture of Polycrystals	374
Plastic Deformation	374
Stress Rupture	377
5.4 Deformation and Fracture Maps	377
5.5 Tensile Instability	380
ACKNOWLEDGEMENTS	392
REFERENCES	393

1. INTRODUCTION

It is now well established that the mechanical properties of titanium and its alloys are sensitively dependent on the presence of the interstitial solutes oxygen, nitrogen, carbon and hydrogen. A review of the status of this subject at the time was prepared by Jaffee in 1958 (Ref. 1). Progress made during the subsequent 15 years was reviewed by Conrad and coworkers in 1973 (Ref. 2). In more recent times additional work has been performed which focuses more sharply on the dislocation-solute interactions responsible for the effect of the interstitial solutes on the flow stress of titanium and its alloys; see, for example, Refs. 3 and 4. The subject has reached a stage where a comprehensive review of the effect of interstitial solutes on the strength and ductility of titanium seems desirable, and is therefore undertaken here.

The present review will concern itself mainly with the effects of very dilute solid solutions of oxygen, nitrogen, carbon and hydrogen in the CPH crystal structure of unalloyed titanium, i.e. with concentrations less than the solubility limit of each interstitial solute, or less than about 1 at. % if the solubility is higher. Any effects which might be due to clustering, precipitation or ordering of the solutes are thus minimized. Furthermore, this is the composition regime for these interstitial solutes in most commercial titanium alloys. Although consideration is given to all four interstitial solutes, most of the discussion will deal with oxygen, nitrogen and carbon, since only meager data are available for the effects of hydrogen in solid solution. Although the present paper will be mainly concerned with interstitial solutes in titanium containing only small amounts of substitutional solutes, relevant results on more concentrated substitutional alloys will also be discussed.

The effects of the interstitial solutes on the following phenomena will be considered: deformation kinetics (effects of temperature and strain rate on the flow stress), strain hardening, grain size hardening, ductility and fracture. The behavior of both single crystals and polycrystals will be reviewed. Further, behavior in each of three temperature regions will be discussed: (a) low temperatures, $T/T_m < 0.3$, where T_m is the melting temperature in °K, (b) intermediate temperatures $0.3 < T/T_m < 0.4$ and (c) high temperatures, $T/T_m > 0.4$. The reasons for the choice of these particular temperature regimes will become evident during the course of the paper. Since most of the definitive work on the effects of interstitial solutes on the deformation of titanium has been at low temperatures, this temperature regime is given most attention. Further, since the plastic deformation of titanium polycrystals at low and intermediate temperatures appears to be governed to a large extent by the interaction of dislocations gliding on the first order prism planes with interstitial solute atom obstacles, a good amount of attention is given to this particular interaction.

The approach to be followed in the paper will be to first list in Chapter 2 some of the pertinent chemical and physical properties important to the subsequent analyses. This is followed in Chapter 3 by a consideration of some of the theoretical aspects of the subject, namely (a) the interaction energies and forces

between dislocations gliding on the first order prism planes and the interstitial solute atom obstacles, (b) solid solution strengthening models and (c) the effects of temperature and strain rate on the flow stress (deformation kinetics). The pertinent experimental data are then reviewed in Chapter 4, which is followed in Chapter 5 by a discussion of the deformation modes and dislocation mechanisms responsible for the observed macroscopic mechanical behavior.

2. SOME PERTINENT CHEMICAL AND PHYSICAL PROPERTIES

2.1 Phase Equilibria

The melting temperature of pure titanium is 1941K and a phase change from BCC (β) to CPH (α) crystal structure occurs at 1156K (Ref. 5). The Debye temperature for the α phase is reported to be 365 to 428K (Refs. 6-8), yielding a Debye frequency ν_0 of approximately $9 \times 10^{12} \text{ s}^{-1}$. The Debye temperature for the β phase is 295-299K (Refs. 7,8).

Existing phase diagrams (Refs. 1,9,10) for the Ti-O, Ti-N, Ti-C and Ti-H systems indicate that hydrogen stabilizes the β phase, whereas oxygen, nitrogen and carbon stabilize the α -phase. The maximum solubility of oxygen in the α -phase is of the order of 30 at. %, that of nitrogen 19 at. %, carbon 2 at. % and hydrogen 8 at. %. A large solubility of oxygen persists at room temperature; however, ordering of the oxygen atoms occurs at concentrations as low as 5 at. % (Ref. 11). The work of Jaffee, Ogden and Maykuth (Ref. 12) indicates that at least 2.5 at. % of nitrogen is soluble at room temperature following an anneal at 1123K, whereas only about 1 at. % of carbon is soluble for the same annealing treatment. According to Lenning, Craighead and Jaffee (Ref. 13) and Beck (Ref. 14) only about 0.1 at. % of hydrogen is soluble in titanium at room temperature, which amount does not appear to be altered significantly by the presence of oxygen or nitrogen.

2.2 Crystallography Relating to Interstitial Solutes

The lattice structure of α -titanium and the location of the octahedral and tetrahedral interstitial sites are shown in Fig. 2.1. The octahedral sites have coordinates $\frac{1}{3}, \frac{2}{3}, \frac{1}{4}$, $\frac{1}{3}, \frac{2}{3}, \frac{3}{4}$ which is equivalent to a vector $\frac{1}{12}[04\bar{4}3]$ of magnitude $a/\sqrt{2}$ from the origin. The four tetrahedral sites per unit cell are located at coordinates $\frac{2}{3}, \frac{1}{3}, \frac{1}{8}$, $\frac{2}{3}, \frac{1}{8}, \frac{7}{8}$, $00\frac{3}{8}$, $00\frac{5}{8}$. There are thus one octahedral and two tetrahedral sites per titanium atom. If the titanium atoms are assumed to be rigid spheres of radius r in contact along close-packed directions, the maximum radius of sphere which can be accommodated in an octahedral or tetrahedral site is $0.41r$ and $0.22r$ respectively.

It is now fairly well established that the interstitial solutes in α -titanium occupy the octahedral hole positions (Refs. 15-17) and produce a tetragonal distortion of the lattice (Refs. 18-23). Moreover, thermodynamic data (Refs. 24,25) indicate that for the very dilute concentrations considered here (less than ~1 at. %) the interstitial solutes are randomly distributed as single atoms.

The octahedral and tetrahedral interstitial hole sizes in the CPH crystal structure and the tetrahedral interstitial hole size in the BCC crystal structure of titanium are given in Table 2.1; the radii of the neutral atoms of oxygen, nitrogen, carbon and hydrogen are listed in Table 2.2. To be noted is that the octahedral

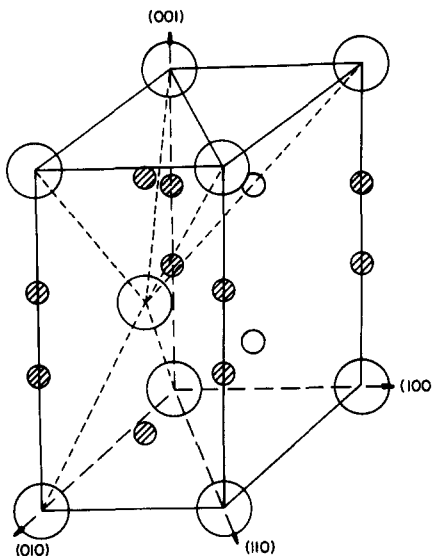


Fig. 2.1. The lattice structure of α -titanium.
The open small circles are the octahedral sites;
the shaded circles are the tetrahedral sites.

TABLE 2.1. Interstitial Hole Sizes in Alpha and Beta Titanium

	Octahedral Radius Å	Tetrahedral Radius Å
α -Ti	0.61	0.33
β -Ti		0.44

TABLE 2.2. Neutral Atomic Radius, Volume Expansion of the Lattice and Maximum Solubility in the α Phase of Interstitial Solutes in Titanium

	Neutral Atomic Radius Å	Volume Expansion † Å ³ per at. %	Maximum Alpha Solubility † At. %
Oxygen	0.60	0.13	30
Nitrogen	0.71	0.18	19
Carbon	0.77	0.49	2
Hydrogen	0.46	Nil	8

† From R. I. Jaffee, Prog. Met. Phys. 7, 65 (1968).

hole size in the CPH structure is larger than the tetrahedral hole size in both the α and β phases. Moreover, the sizes of the neutral atoms are either less than, or only slightly larger than, the octahedral hole size. Hence, one might expect the interstitial solutes to reside in the octahedral sites of the CPH structure and to be α -phase stabilizers, which is observed except for the case of hydrogen. The small size of the hydrogen atom suggests that it could fit as well into the tetrahedral site of the BCC structure and this could then explain why hydrogen is a β -stabilizer, since the entropy of the BCC phase is higher than that of the CPH phase (Ref. 26).

The effects of oxygen, nitrogen and carbon on the lattice parameters of α -titanium are illustrated in Fig. 2.2. The interstitials produce an increase in both a_0 and c_0 , the effect being greater for c_0 , so that an increase in the c/a ratio occurs. No data are available for the effect of hydrogen on the lattice parameters of titanium; however, in view of its small size it is not expected to have a marked effect (Ref. 1).

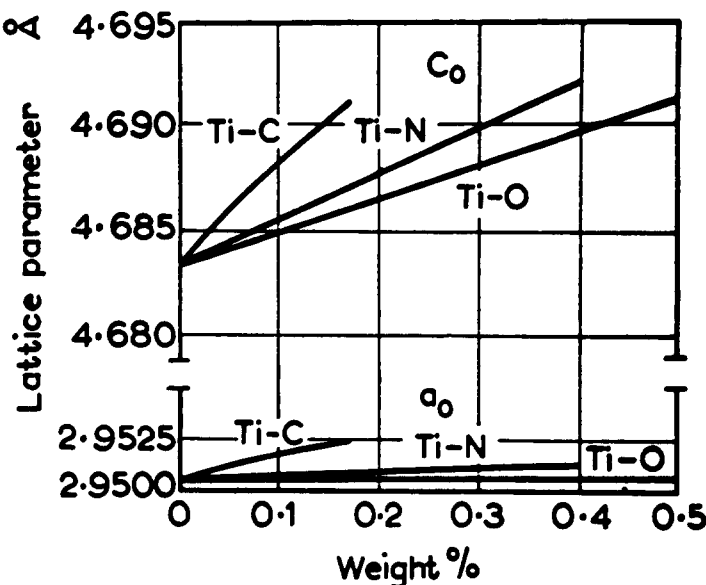


Fig. 2.2. Effects of oxygen, nitrogen and carbon on the lattice parameters of Ti. From Jaffee (Ref. 1) based on the data of Clark (Ref. 18).

A compilation of significant data available regarding the effects of oxygen, nitrogen and carbon on the lattice parameters of α -titanium is given in Table 2.3; also included are the values of the lattice strain parameters $\epsilon_a = (\Delta a/a_0)_{C_i=0.5}$ and $\epsilon_c = (\Delta c/c_0)_{C_i=0.5}$ where C_i is the interstitial solute concentration and 0.5 reflects the ratio of octahedral interstitial sites to titanium atom sites in the CPH structure. It is seen that both strain parameters increase in the order oxygen, nitrogen, carbon. This is also the order for the volume expansion of the unit cell of α -titanium and the maximum solubility in the α -phase, Table 2.2, suggesting that the size factor plays a significant role in the solubility limits of these interstitials. The anomalously low solubility of hydrogen indicates that other factors are also important in this case.

TABLE 2.3. Effect of the Interstitial Solutes O, N and C on the Lattice Parameters of Alpha-Titanium

Solute	c_0	c_1	a_0	a_1	ϵ_c	ϵ_a	Ref. [†]
Oxygen	4.68	1.04	2.95	0.000	0.111	0.000	(a)
		0.387		0.074	0.041	0.013	(b)
		0.48		0.000	0.051	0.000	(c)
		0.57		0.000	<u>0.061</u>	<u>0.000</u>	(d)
			Avg.	0.066	0.003		
Nitrogen	4.68	0.675	2.95	0.045	0.072	0.008	(c)
		0.89		0.110	0.095	0.019	(e)
		0.82		0.055	<u>0.088</u>	<u>0.009</u>	(d)
			Avg.	0.085	0.012		
Carbon	4.68	1.27	2.95	0.286	0.136	0.049	(f)
		1.25		0.255	<u>0.133</u>	<u>0.038</u>	(d)
			Avg.	0.135	0.044		

Notes: $c = c_0 + c_1 C_i (\text{\AA})$ $\epsilon_c = \left(\frac{\Delta c}{c_0} \right) C_i = 0.5$

$a = a_0 + a_1 C_i (\text{\AA})$ $\epsilon_a = \left(\frac{\Delta a}{a_0} \right) C_i = 0.5$

C_i = atomic concentration of interstitials

[†]References

- a. D. Gupta and S. Weinig, Trans. AIME 215, 209, 1959.
- b. S. Anderson, B. Collen, U. Kuylenstierna and A. Magneli, Acta. Chem. Scand. 11, 1641, 1957.
- c. H. T. Clark, Jr., Trans. AIME 185, 588, 1949.
- d. W. L. Finley and J. A. Snyder, Trans. AIME 188, 277, 1950.
- e. B. Holmberg, Acta. Chem. Scand. 16, 1255, 1962.
- f. I. Cadoff and J. P. Nielsen, Trans. AIME 197, 248, 1953.

2.3 Elastic Moduli

Pertinent elastic constants of pure titanium are given in Fig. 2.3, where it is seen that they exhibit a fairly strong temperature dependence. Here E and μ are the Youngs modulus and shear modulus respectively for polycrystals and K_{edge} and K_{screw} are the energy factors for prism plane edge and screw dislocations respectively of Burgers vector \vec{a} (Ref. 29); the other coefficients have their usual meaning. The relative temperature dependence of the various moduli is depicted in Fig. 2.4. Considerations by Fisher and Alfred (Ref. 30) and Tang, Kratochvil and Conrad (Ref. 31) indicate that the elastic behavior of titanium is nearly isotropic. In general, both interstitial and substitutional α -stabilizing solutes tend to

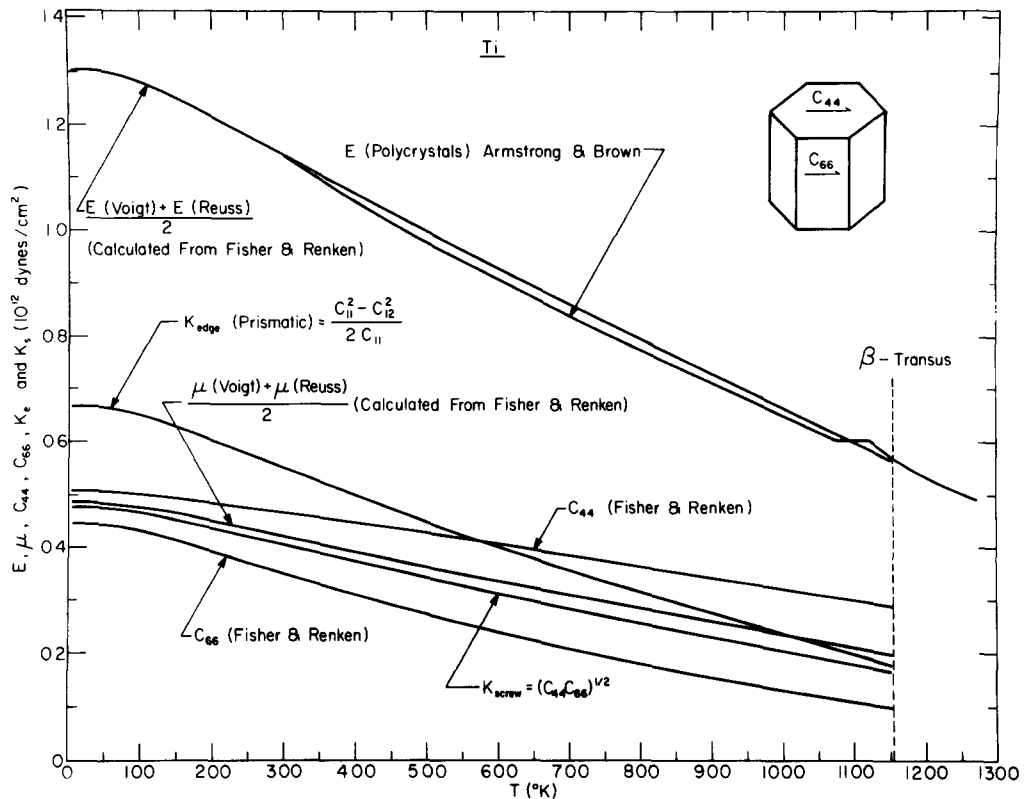


Fig. 2.3. Effect of temperature on the various elastic constants of Ti. Data from Refs. 27 and 28.

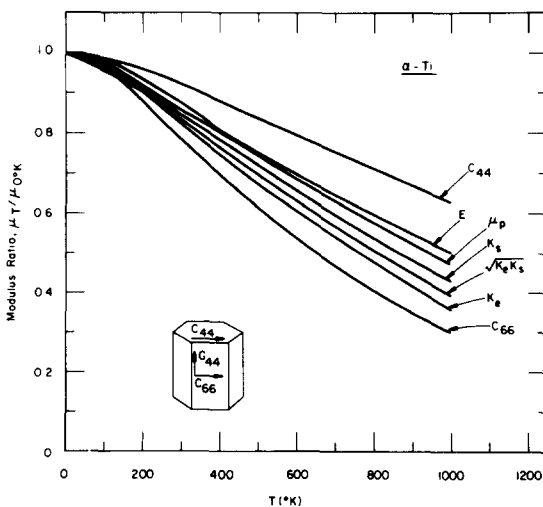


Fig. 2.4. Ratio of the modulus at temperature T to that at 0°K versus the temperature for various moduli of Ti.

increase the elastic moduli (Refs. 8,32,33); their effect on the temperature dependence is not clear, but they do not appear to alter it significantly. The addition of β -stabilizing solutes generally leads to a decrease in modulus (Ref. 8).

Available data on the effects of oxygen, nitrogen and carbon in solid solution on Youngs modulus E of α -titanium are presented in Figs. 2.5 and 2.6; the values of the modulus parameter $\eta = \frac{1}{E} \frac{dE}{dC_i}$ derived from these figures are listed in Table 2.4.

Only for oxygen are there sufficient data to place any confidence in the value of

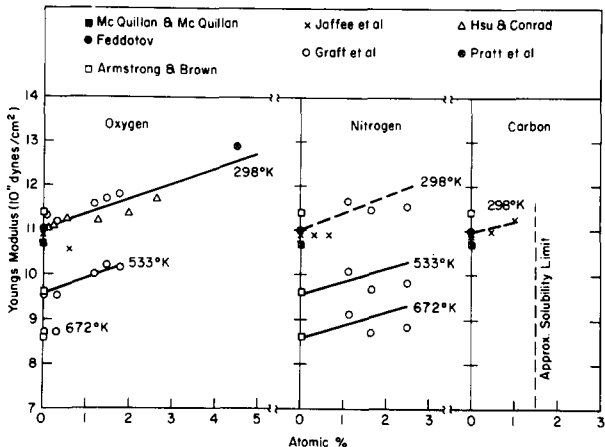


Fig. 2.5. Effect of oxygen, nitrogen and carbon on Youngs modulus of Ti at several temperatures. Data from Refs. 9,12,27,33-36.

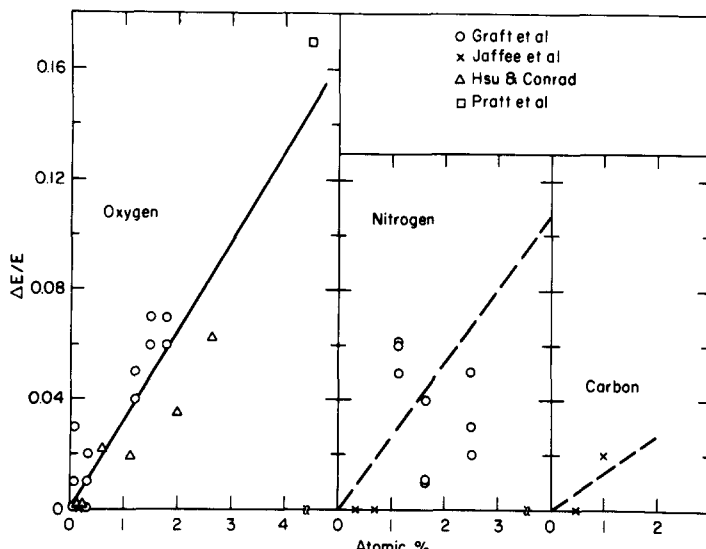


Fig. 2.6. The fractional change in Youngs modulus with interstitial content. Data from Refs. 12,33,34,36.

η ; the values for nitrogen and carbon are only rough estimates and must await further work for their final definition. For example, values of η appreciably different from those listed in Table 2.4 were derived for nitrogen and carbon by de Meester (Ref. 37) and used in Ref. 3.

TABLE 2.4. Effect of Oxygen, Nitrogen and Carbon on Youngs Modulus of α -titanium.

Solute	$\eta = \frac{1}{E} \frac{dE}{dC_i}^+$
Oxygen	3.288
Nitrogen	2.950
Carbon	1.330

[†]Derived from Figs. 2.5 and 2.6; E = Youngs modulus;
 C_i = interstitial solute concentration

TABLE 2.5. Self Diffusion and Substitutional Solute Diffusion in Titanium

Atom Species	D_{01} cm ² /sec	Q_1 Kcal/mole	D_{02} cm ² /sec	Q_2 Kcal/mole
α -Ti				
Self	-	58 [†]	-	-
	-	71.3 ^{††}	-	-
	1.0	57.8 ^{†††}		
β -Ti ^{††††}				
Self	1.1	60	3.6×10^{-4}	31.2
Substitutional Solutes	0.2-20	51-73	$3 \times 10^{-4} - 80 \times 10^{-4}$	29-43

Note: Two values of D_0 and Q are given for β -Ti because of curvature in the Arrhenius plots. The subscript 1 refers to the high temperature results, the subscript 2 to low temperature data.

[†] Energy for the formation of vacancies plus that for migration determined from the recovery of electrical resistivity after plastic deformation: private communication K. Okazaki (1972).

^{††} Twice the energy to form vacancies determined from heat capacity measurements: V. O. Shestopol, Soviet Phys. Solid State 7, 232, 1966.

^{†††} Derived from high temperature flow stress measurements: M. Doner and H. Conrad, Met. Trans. 4, 2809, 1975.

^{††††} Data for β -Ti: H. Conrad, B. de Meester, M. Doner and K. Okazaki, Titanium Science and Technology, Plenum Press, 969, 1973.

2.4 Diffusion Coefficients and Bond Energies

Values of the diffusion coefficient D_0 and the activation energy Q for self and substitutional solute diffusion in α and β titanium gleaned from the literature are listed in Table 2.5; those for the diffusion of the interstitial solutes are given in Table 2.6. The activation energy for the diffusion of the interstitial solutes tends to increase in the order: hydrogen, carbon, oxygen, nitrogen, with the values for oxygen and nitrogen approaching those for self diffusion.

The relatively high values of the activation energy for diffusion of the interstitial solutes in titanium and, other evidence (Ref. 38), suggest that these solutes may be chemically bonded to the surrounding titanium atoms. Some measure of this bonding can be obtained from thermodynamic and surface energy measurements for the compounds TiO , TiN , TiC and TiH , which all have the FCC sodium chloride structure (Refs. 9,10). In this structure each "interstitial" atom is surrounded by six titanium atoms, so that the energy per titanium-interstitial atom bond may be considered to be one-sixth the bond energy of the compound.

A common approach for obtaining the bond energy of a compound is from the enthalpy required to disassociate the compound into its separate gaseous atoms. For example, consider the case of solid, crystalline TiO ; the total bond energy ΔH^θ is given by the enthalpy of the reaction



This reaction can be taken to consist of the following steps



so that

$$\Delta H_1^\theta = \Delta H_f + \Delta H_s + \Delta H_d = 296 \text{ Kcal/mole}$$

The energy e per titanium-oxygen bond in the crystalline solid is then

$$e = (1/6) \Delta H_1^\theta = 49.3 \text{ Kcal/mole} = 2.14 \text{ ev/bond}$$

Similar considerations yield 2.22 and 2.38 ev per bond for nitrogen and carbon respectively; see Table 2.7.

An alternative approach for arriving at the bond energy for the reaction of Eq. 2.1 is through the following steps and employing spectroscopic data



so that

$$\Delta H_2^\theta = \Delta H'_f + \Delta H_s = 293 \text{ Kcal/mole}$$

and

$$e = \frac{1}{6} \Delta H_2^\theta = 48.8 \text{ Kcal/mole} = 2.12 \text{ ev/bond}$$

The corresponding values of e for nitrogen and carbon obtained in this manner are 2.22 ev and 1.97 ev respectively, Table 2.7.

TABLE 2.6. Interstitial Solute Diffusion in α -titanium

Atom Species	Activation Energy, Q (Kcal/mole)	Frequency Factor, D_0 (cm ² /s)		Ref.
O	48.0	-	Ti-3 at.% O-Internal Friction	a
	33.5	5.1×10^{-3}	Concentration Gradient	b
	45.0 ± 5.0	1	Ti-0.2 at.% O-0.1 at.% (V,Zr,Al, Nb) Internal Friction	c
	58.5 ± 2.5		Ti	
	58.5 ± 2.5		Ti + 0.3 at.% O	Internal Friction
	57.0 ± 2.5		Ti + 0.6 at.% O	
	52.5	8.9	Low-pressure oxidation	e
	48.6	7.8×10^{-1}	Oxidation	f
	52.0	1.6×10^1	Oxidation	g
	48.6 ± 5.0		Internal Friction	h
N	45.25	1.2×10^{-2}		i
	57.50 ± 2.50		Internal Friction	j
	57.00	0.2	X-ray and Microhardness	k
	68.00	6.75	Metallography and Microhardness	l
C	48.5		Internal Friction	m
	43.5	5.06	Diffusion Couples	n
H	12.38 ± 0.68	1.8×10^{-2}	Iodide Ti	i
	14.70 ± 0.65	3.0×10^{-1}		n
	11.0	1.15×10^{-2}		o
	12.75	1.45×10^{-2}	Iodide Ti	p
	12.40	8.60×10^{-1}	Commercial Purity Ti	p

References:

- a. J. N. Pratt, W. J. Bratina and B. Chalmers, Acta Met. 2, 203, 1954.
- b. N. P. Roe, H. R. Palmer and W. R. Opie, Trans. ASM 52, 191, 1960.
- c. D. Gupta and S. Weinig, Acta Met. 10, 292, 1962.
- d. D. R. Miller, Trans. TMS-AIME 224, 275, 1962.
- e. P. Kofstad, J. Less-common Metals, 12, 449, 1967.
- f. C. S. Rosa, Met. Trans. 1, 2517, 1970
- g. L. F. Sokirianskii, D. V. Ignatov and A. Ya. Shinvaev, Diffusion Data 4, 220, 1970.

- h. K. M. Browne, Acta. Met. 20, 507, 1972.
 i. R. J. Wasilewski and G. L. Kehl, Metallurgia 50, 225, 1954.
 j. V. S. Eremeev, Yu. M. Ivanov and A. S. Panov, Diffusion Data 4, 66, 1970.
 k. Yu. V. Levinskii, et al, Diffusion Data 3, 295, 1969.
 l. D. R. Miller and K. M. Browne, The Science, Technology and Application of Titanium, Pergamon Press, 401, 1970.
 m. F. C. Wagner, E. J. Bucur and M. A. Steinberg, Trans. ASM 48, 742, 1956.
 n. T. P. Papazoglu and M. T. Hepworth, Trans. TMS-AIME 242, 698, 1968.
 o. B. A. Kolachev, D. P. Nasimov and L. M. Zhuravlev, Diffusion Data 4, 219, 1970.
 p. W. M. Albrecht and M. W. Mallet, Trans. TMS-AIME 212, 204, 1958.

TABLE 2.7. Heats of Formation ΔH and Bond Energy e for TiO, TiN and TiC Compounds

Reaction	ΔH Kcal/mole	ΔH_1^θ Kcal/mole	ΔH_2^θ Kcal/mole	e_1 eV	e_2 eV
1. $TiO(s) \rightarrow Ti(s) + 1/2 O_2(g)$	124(a)+++++				
2. $TiN(s) \rightarrow Ti(s) + 1/2 N_2(g)$	81(a)				
3. $TiC(s) \rightarrow Ti(s) + C(g)$	44(a)				
4. $Ti(s) + Ti(g)$	113(b)				
5. $C(s) \rightarrow C(g)$	172(b)				
6. $1/2 O(g) \rightarrow O(g)$	59(c)				
7. $1/2 N(g) \rightarrow N(g)$					
8. $TiO(g) \rightarrow Ti(g) + O(g)$	158(d)				
9. $TiN(g) \rightarrow Ti(g) + N(g)$	111(e)				
10. $TiC(g) \rightarrow Ti(g) + C(g)$	128(f)				
11. $TiO(s) \rightarrow TiO(g)$	135(g)				
12. $TiN(s) \rightarrow TiN(g)$	196(h)				
13. $TiC(s) \rightarrow TiC(g)$	144(i)				
14. $TiO(s) \rightarrow Ti(g) + O(g)$		296	293	2.14	2.12
15. $TiN(s) \rightarrow Ti(g) + N(g)$		307	307	2.22	2.22
16. $TiC(s) \rightarrow Ti(g) + C(g)$		329	272	2.38	1.97

Notes: $^\dagger \Delta H_1^\theta = \Sigma \Delta H$ (Reactions 1,4,6) or $\Sigma \Delta H$ (Reactions 2,4,7) or $\Sigma \Delta H$ (Reactions 3,4,5)

$^{\ddagger \ddagger} \Delta H_2^\theta = \Sigma \Delta H$ (Reactions 8,11) or $\Sigma \Delta H$ (Reactions 9,12) or $\Sigma \Delta H$ Reactions 10,13

$$^{\dagger \dagger \dagger} e_1 = \frac{1}{6} \Delta H_1^\theta ; \quad ^{\dagger \dagger \dagger \dagger} e_2 = \frac{1}{6} \Delta H_2^\theta$$

+++++References

- (a) H. L. Schick, Thermodynamics of Certain Refractory Compounds, Academic Press, 1966.
 (b) L. Brewer, High Strength Materials, Wiley, 12, 1965.
 (c) L. Pauling, The Nature of the Chemical Bond, Cornell Univ. Press, 86, 1960.
 (d) L. Brewer and G. M. Rosenblatt, High Temp. Sci. 2, 1, 1969.
 (e) C. A. Stearns and F. J. Kohl, High Temp. Sci. 2, 146, 1970.

- (f) A. G. Gaydon, Dissociation Energy and Spectra of Diatomic Molecules, 3rd, Ed., Chapman Hall, 285, 1968.
 - (g) I. S. Kulikov, Thermal Dissociation of Chemical Compounds, Israel Program for Scientific Translations, 149, 1967.
 - (h) C. A. Stearns and F. J. Kohl, NASA-TN-D-5027, NASA-Lewis Res. Center, 1969.
 - (i) S. Fujishiro and N. A. Goken, J. Phys. Chem. 65, 161, 1961.
-

Estimates of the bond energy may also be obtained from the sublimation energy and the surface energy of the compounds (Ref. 39). In the case of the sublimation energy, the bond energy may be taken as the heat of sublimation ΔH_s divided by the total number of bonds in a crystal containing N_0 atoms (or molecules)

$$e = \Delta H_s / (\frac{1}{2} Z_b N_0) \quad (2.2)$$

where Z_b is the number of bonds per atom (or molecule). The factor of 1/2 enters because each bond is counted twice. When ΔH_s is the sublimation energy per gram atom (or per mole), N_0 is Avogadro's number. For the titanium compounds considered here the number of bonds is 5 for each titanium atom and 5 for each "interstitial" atom making a total of 10 titanium-interstitial atom bonds per molecule so that Eq. 2.2 becomes

$$e = \Delta H_s / 5N_0 \quad (2.2a)$$

Employing Eq. 2.2a and taking the values of ΔH_s for the compounds given in Table 2.7, one obtains 1.17, 1.70 and 1.25 ev respectively for the bonding energy of oxygen, nitrogen and carbon to titanium.

In the case of the surface energy, the bond energy is given by

$$e = 2\gamma_s / N_b \quad (2.3)$$

where γ_s is the surface energy and N_b is the number of atomic bonds broken per unit area within the crystal to form the two new surfaces. The factor 2 accounts for the fact that two new surfaces are formed. Considering the (100) planes of the compounds (which possess the FCC rock salt crystal structure of lattice parameter a_0), one finds two titanium atoms and two "interstitial" atoms per cube face of the unit cell. Hence, there exists four titanium-interstitial bonds per a_0^2 across this face and Eq. 2.3 becomes

$$e = 2\gamma_s a_0^2 / 4 = \gamma_s a_0^2 / 2 \quad (2.3a)$$

Only a few measurements have been made of the surface energy of the compounds under consideration; these are listed in Table 2.8. Estimates can, however, be made from the heat of sublimation and from Young's modulus (Ref. 39). Substituting Eq. 2.2a for e into Eq. 2.3a, one obtains for the compounds

$$\gamma_s = \frac{2}{5} \left(\frac{\Delta H_s}{N_0} \right) \frac{1}{a_0^2} \quad (2.4)$$

Moreover, it can be shown (Ref. 39) from an analysis of the work required to fracture a solid that

$$\gamma_s = \left(\frac{E}{4\pi^2}\right) \frac{a_0}{2} \quad (2.5)$$

where E is Youngs modulus. Values for γ_s calculated using Eqs. 2.4 and 2.5 are listed in Table 2.8; they are in reasonable accord with those measured directly. Also included in Table 2.8 are the bond energies derived using the average of the various values for the surface energy.

TABLE 2.8. Surface Energies γ_s and Bond Energies e Derived Therefrom for TiO, TiN and TiC

Cmpd.	a_0 (Å)	E^\dagger (10^{10} dynes/cm 2)	γ_s (ergs/cm 2)			e ⁺⁺⁺⁺ eV
			Measured	Calculated	Avg.	
TiO	4.170(a)	----	----	----	2158 ⁺⁺⁺	2158
TiN	4.243(a)	35.2(b) ⁺⁺⁺⁺⁺	2660(c)	1892 ⁺⁺	3027 ⁺⁺⁺	2526
TiC	4.327(a)	45.8(d)	1190(h)	2484 ⁺⁺	2136 ⁺⁺⁺	1928
		38.0(e)	1900(i)			
		49.4(f)				
		<u>47.8(g)</u>				
	Avg.	45.3				

Notes:

[†] E = Youngs modulus; a_0 = lattice constant; ⁺⁺⁺ $\gamma_s = \frac{4}{5} \frac{\Delta H_s}{N_0}$
 ΔH_s = heat of sublimation; N_0 = Avogadros number.

⁺⁺ $\gamma_s = \left(\frac{E}{4\pi^2}\right) \frac{a_0}{2}$ ⁺⁺⁺⁺ $e = \frac{\gamma_s a_0^2}{2}$

+++++ References

- a. A. D. McQuillan and M. K. McQuillan, Titanium, Academic Press, 1956.
- b. J. E. Gordon, Proc. Roy. Soc. A282, 16, 1964.
- c. C. A. Stearns and F. J. Kohl, NASA Tech Note, NASA-TD-D-5027, NASA-Lewis Res. Center, 1969.
- d. J. J. Gilman and B. W. Roberts, J. Appl. Phys. 32, 1405, 1961.
- e. J. Deklerk, Rev. Sci. Inst. 36, 1540, 1965.
- f. W. S. Williams and R. G. Lye, Prog. Rept. No. 2, AD449-222 (WPAFB), 1963.
- g. R. Chang and L. J. Graham, J. Appl. Phys. 37, 2778, 1966.
- h. D. T. Livey and P. Murray, J. Amer. Cer. Soc. 39, 363, 1963.
- i. B. D. Powell and D. Tabor, J. Phys. & Appl. Phys. 3, 783, 1970.

A summary of the average values of the bond energies obtained by the various methods is given in Table 2.9. It is seen that the values obtained from the heats of sublimation and the surface energy are similar in magnitude, but definitely lower than those obtained from the heats of formation. This is not surprising, for one might expect some recovery of bond energy upon going from a condition of complete dissociation of the compound into individual atoms (heat of formation) to

TABLE 2.9. Summary of Bond Energies, e , for TiO , TiN and TiC Compounds Determined by Various Methods and the Activation Energy for Diffusion, Q_D , for Dilute Solutions of the Interstitial Solutes in α -Ti.

System	Bond Energy e (eV) Derived From [†]	Activation Energy for Diffusion Q_D (eV)		
		ΔH^θ	ΔH_s	γ_s
Ti-O	2.13	1.17	1.17	2.18
Ti-N	2.22	1.70	1.42	2.50
Ti-C	2.18	1.25	1.13	2.00

Notes:

[†] ΔH^θ = heat of formation; ΔH_s = heat of sublimation; γ_s = surface energy.

that of the dissociation into individual molecules (heat of sublimation) to that of the creation of a surface (surface energy). Also included in Table 2.9 is the activation energy Q_D for diffusion of the interstitials in dilute solution in α -titanium. Of interest is that Q_D is approximately twice the bond energy derived from the surface energy, suggesting that the diffusion process is equivalent to the breaking of two bonds.

2.5 Deformation Modes and Dislocation Properties

A review of the crystallography, deformation modes and dislocations in CPH metals has been presented by Partridge (Ref. 40). Only some of the more pertinent aspects of these subjects will be considered here. The slip and twinning modes observed for α -titanium are listed in Table 2.10. It is now well established that the most common slip modes in CPH α -titanium are, in order of ease of operation, the $\{10\bar{1}0\}$, $\{10\bar{1}1\}$ and (0001) planes with the \hat{a} direction, $<11\bar{2}0>$, as the slip direction; see Fig. 2.7. This order seems to prevail over the entire temperature range of the CPH structure; however, slip on the $\{10\bar{1}1\}$ and the (0001) planes tends to become more favorable compared to the $\{10\bar{1}0\}$ planes as the interstitial content or the temperature is increased. The three listed glide planes with the slip vector in the basal plane constitute a total of four independent slip systems. Equi-Schmid factor lines for glide on these planes have been calculated by Shechtman and Brandon (Ref. 42). A hard sphere model of the three slip planes showing the positions of the octahedral interstitial sites is illustrated in Fig. 2.8. As pointed out by Churchman (Ref. 43), the titanium atoms in the basal layers are all coplanar,

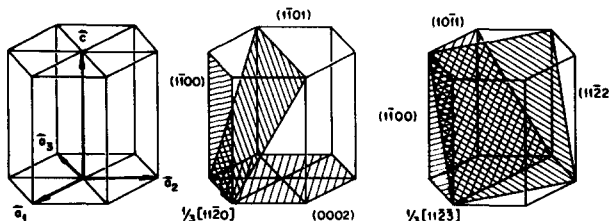


Fig. 2.7. Slip systems in α -titanium. From Yoo (Ref. 41)

TABLE 2.10. Slip and Twinning Modes in α -titanium[†]

Slip Modes		Twinning Modes ^{††} (a-c, g-n)					
Vector	Mode	K ₁	K ₂	η_1	η_2	Twin Shear Calc.	Twin Shear Obs.
$\vec{a}(a-c)$	{0001} <1120>	1011	1013	1012	3032	0.104(h)	0.11(h)
	{1010} <1120>	1012	1012	1011	1011	0.174(k)	0.12-0.17(m)
	{1011} <1120>	1121	0001	1126	1120	0.63 (k) 0.63 (o)	0.67(m)
		1122	1122	1123	1123	0.958(k)	----
$\vec{c}/2(d)$	{ ? } <0001>	1122	1124	1123	2243	0.22 (j,k) 0.218(o)	0.21(h)
		1123	0001	1122	1120	0.914(k)	----
		1124	----	2243	----	0.22 (k) 0.218(o)	----
$\vec{c} + \vec{a}(d-g)$	{1011} <1123>						
	{1122} <1123>						

Notes: [†]Letters a-n refer to references given below.

^{††} K₁ = twin plane η_1 = twin shear direction

K₂ = second undistorted plane η_2 = intersection of K₂ with plane of shear

References:

- a. F. D. Rosi, C. A. Dube and B. H. Alexander, Trans. AIME 197, 257, 1953.
- b. E. A. Anderson, D. C. Jillson and S. R. Dunbar, Trans. AIME 197, 1191, 1953.
- c. A. T. Churchman, Proc. Roy. Soc. A226, 216, 1954.
- d. N. E. Paton, J. C. Williams and G. P. Rauscher, Titanium Science and Technology 2, 1049, 1973.
- e. J. C. Williams and M. J. Blackburn, Phys. Stat. Sol. 25, K1, 1968.
- f. T. R. Cass, The Science Technology and Application of Titanium, Pergamon Press, 459, 1970.
- g. F. D. Rosi, F. C. Perkins and L. L. Seigle, Trans. AIME 206, 115, 1956.
- h. N. E. Paton and W. A. Backofen, Met. Trans. I, 2839, 1970.
- i. T. S. Liu and M. A. Steinberg, Trans. AIME 200, 697, 1954.
- j. P. G. Partridge, Met. Reviews 118, 169, 1968.
- k. A. G. Crocker and M. Bevis, The Science Technology and Application of Titanium, Pergamon Press, 453, 1970.
- l. A. Akhtar, Met. Trans. 6A, 1105, 1975.
- m. S. Fujishiro and J. W. Edington, "Mechanical Twinning of Titanium Single Crystals", Tech. Rept. AFML-TR-70-176, 1970.
- n. F. H. Beck, "Effect of Hydrogen on the Mechanical Properties of Titanium and Its Alloys", NASA Grant No. NGL-36-008-051, Ohio State Univ., 1975.
- o. H. Khio, J. Phys. Soc. Japan, 13 269 (1959).

whereas the {1010} and the {1011} planes have corrugated repeat layers. Further, none of the interstitial sites are coplanar with the (0001) and {1010} layers. However, one-half of the sites are coplanar with each of the {1011} planes.

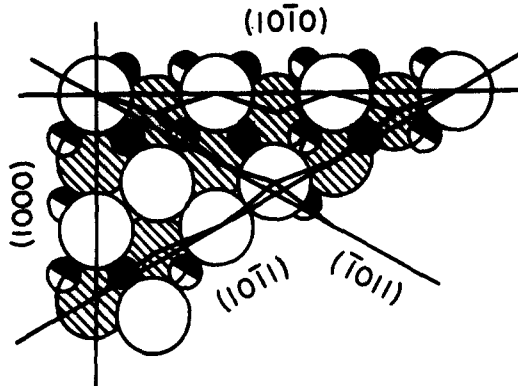


Fig. 2.8. A section in the $\{11\bar{2}0\}$ plane through a ball model of the CPH crystal structure. The bounding surfaces are the repeat layers of the (0001) , $(10\bar{1}0)$ and $(10\bar{1}1)$ planes. The small filled circles are the octahedral interstitial sites. From Churchman (Ref. 43).

Evidence for glide with a $\vec{c} + \vec{a}$ vector has been obtained by slip trace analysis and by transmission electron microscopy (Refs. 42,44-47). The slip planes associated with this glide have been deduced to be $\{11\bar{2}2\}$ and $\{10\bar{1}1\}$. This slip vector was especially prevalent in compression tests along the c-axis and its amount increased with temperature (Ref. 46). A third slip vector which has been reported for titanium is $\vec{c}/2$. Limited occurrence of slip with this vector was found for the deformation of polycrystalline commercial purity titanium at 475°K (Ref. 47).

Although the slip systems operative in unalloyed single crystals of BCC β -titanium have not been established, it is expected that they are the same as those for other metals of the BCC structure, namely $\{110\}$, $\{112\}$ and $\{123\}$ slip planes with $<111>$ as the slip direction. For stable BCC alloys of titanium with vanadium (20 to 50 at. % V) and with molybdenum (15 at. % Mo) the slip direction was reported to be $<111>$ with $\{110\}$, $\{112\}$ and $\{123\}$ as possible slip planes (Refs. 48-50).

The magnitudes of the shears associated with various twinning systems are given in Table 2.10. Worthy of note is that the $\{10\bar{1}2\}$, $\{11\bar{2}1\}$ and $\{11\bar{2}3\}$ twinning modes give an extension along the c-axis, whereas the $\{11\bar{2}2\}$, $\{11\bar{2}4\}$ and $\{10\bar{1}1\}$ modes cause a reduction along this axis. In general, the tendency for twinning in titanium decreases with increase in temperature and in interstitial content. However, Paton and Backofen (Ref. 46) found that the stress for the $\{10\bar{1}1\}$ twinning mode decreased with increase in temperature above about 700K.

The properties of dislocations in titanium have been considered by a number of investigators (Refs. 40,51-56). Fisher and Alfred (Ref. 52) conclude that the energy factor $K(\alpha)$ for mixed dislocations with Burgers vector \vec{a} in titanium is given with reasonable accuracy for $\alpha < 60$ deg by the relation

$$K(\alpha) = \left(\frac{K_e + K_s}{2} \right) - \left(\frac{K_e - K_s}{2} \right) \cos^2 \alpha \quad (2.6)$$

where K_e and K_s are the energy factors for edge ($\alpha = 90$ deg) and screw ($\alpha = 0$ deg) dislocations respectively (Fig. 2.3). Further, they find that as the temperature increases the core radius of a screw dislocation with $b = \vec{a}$ becomes significantly elongated in the $[0001]$ direction and shorter within the basal planes. Edge

dislocations with this Burgers vector also increase in width within the prism plane as the temperature increases.

A technique for revealing dislocations by etch pitting is described by Cass (Ref. 57). Methods for preparing thin foils for transmission electron microscopy are presented by Blackburn and Williams (Refs. 58,59) and by Rice, Hinesley and Conrad (Ref. 60). The identification of Burgers vectors of dislocations in α -titanium is discussed by Rice and DeAngelis (Ref. 61).

2.6 Fracture Modes

For interstitial solute contents below about 1.5 at. %, fracture in titanium single crystals tested in tension occurs by ductile shearing at temperatures as low as 78K (Refs. 62,63). However, large grained polycrystals (3 to 6 grains/mm²) containing about 1 at. % interstitials fractured in a brittle manner at temperatures below about 116K (Refs. 63,64). The brittle fracture resulted from the nucleation and growth of microcracks which developed at stresses just beyond the yield stress. The microcracks were almost always associated with {1122} twinning, but were found only at points of second order twinning within the original twins at the following three locations (see Fig. 2.9): (a) Primary twin-matrix boundary, (b) Primary twin-second order twin boundary and (c) Second order twin-matrix boundary. The microcracks which propagated to fracture were generally those which occurred along the boundary between the second order twin and the matrix. Upon

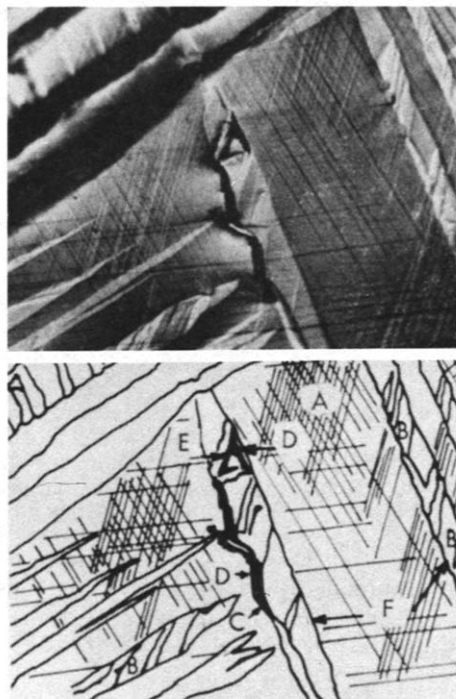


Fig. 2.9. Microcracks associated with second order twins in large grain size Ti with ~1 at. % interstitial solutes tested in tension at 97K. A, slip lines; B, second order twins; C, primary twin-matrix crack; D, second order twin-matrix crack; E, primary twin-second order twin boundary cracks; F, primary twins. Orig. magnification 250x. From Amateau, Burrier and Ebert (Ref. 64).

straining, such cracks extended along the entire length of the twin, eventually separating the primary twin from the matrix. For the same material, ductile behavior occurred as low as 78K when the grain size was reduced to 2000 grains/mm².

Titanium polycrystals with an oxygen content of 1 at. % have been found to fracture by cleavage under certain specific chemical environments and testing conditions (Refs. 65,66).

3. THEORETICAL CONSIDERATIONS

3.1 Dislocation-Interstitial Solute Interactions

In principle, the interaction energy between a dislocation and an interstitial solute could be calculated from a knowledge of the electronic rearrangements which occur in a crystal when a solute atom is taken from some far-removed position in the lattice to one close to the dislocation. However, since the present state of our understanding does not yet permit such a sophisticated analysis, the approach generally used is to consider the interaction in terms of one or more measurable macroscopic properties. The potential energy so derived is the Helmholtz free energy F^* . Using this approach the interaction of dislocations with solute atoms is generally considered to be of three principal types: elastic, chemical and electrical. Each of these interactions will now be considered for the case of interstitial solutes and $\{10\bar{1}0\} 1/3 <11\bar{2}0>$ dislocations in titanium.

3.1.1 Elastic Interactions

An elastic interaction between a solute atom and a dislocation results from the change in elastic strain energy stored in the crystal as the two approach each other and consists of two parts: (a) that due to the distortion of the lattice produced by the size difference between the solute atom and the lattice site in which it resides and (b) that due to the difference in elastic moduli of the solute atom and the host matrix. Let us now consider each of these interactions for interstitial solutes in titanium.

Size Misfit Interaction:

As mentioned above, the interstitial solutes reside in the octahedral sites of the CPH lattice of α -titanium and produce a tetragonal distortion oriented along the c-axis. A point defect with tetragonality will interact not only with the hydrostatic part of the stress field of a dislocation, but also with its shear stress field. Defects producing tetragonal distortions will therefore in general have a large interaction with both screw and edge dislocations.

The general method for finding the size misfit interaction energy for a solute producing a tetragonal distortion was first described by Cochardt, Schoeck and Wiedersich (Ref. 67) and successfully applied to the case of carbon in BCC iron. Their method has also been applied to determine the energies of interaction for various defects in FCC crystals (Ref. 68). In the derivation, the displacements caused by the defect are considered to work against the stress field of the dislocation. For the point defect to be forced into a unit cell of the lattice, each face of the cell must be strained by an amount ϵ_{ij}^{cell} against the stress field of the dislocation; this then gives for the interaction energy

$$E_e = V_{cell} \sum_{ij} \sigma_{ij}^{dis} \epsilon_{ij}^{cell} \quad (3.1)$$

where V_{cell} is the volume of the undeformed cell. To evaluate Eq. 3.1 it is necessary to establish the strain along each edge of the unit cell produced by the presence of the solute and the component of the dislocation stress field in the direction of that strain, the latter being determined by the crystallographic orientation of the dislocation with respect to the cell containing the defect. The rate of change of the lattice parameter with point defect concentration is used as a measure of the strain and therefore the volume of the cell replaces the actual volume of the point defect in the expression for the interaction energy.

The calculation of the size misfit interaction energy between a tetragonal distortion oriented along the c-axis of the CPH structure and $1/3<11\bar{2}0>$ dislocations gliding on the first-order prism planes has been performed by Tyson (Refs. 69,70). Using isotropic elasticity he obtained for an edge dislocation

$$\frac{E^e}{\epsilon} = \frac{\mu b}{\pi(1-v)} \frac{\sin\theta}{r} (\epsilon_b + v\epsilon_c) V_{\text{cell}} \quad (3.2)$$

where θ is the angle between the Burgers vector b and the radius vector r , the distance from the solute atom to the dislocation, and v is Poisson's ratio. ϵ_b and ϵ_c are the strains in the a and c directions of the CPH structure produced by the interstitial solute. They can be obtained from the rate of change in the lattice parameters with interstitial concentration (Refs. 71,72), and for interstitial solutes in titanium are given by extrapolating lattice parameter measurements to an atomic concentration $C_i = 0.5$, i.e. $\epsilon_b = \left(\frac{\Delta a}{a_0}\right) C_i = 0.5$ and $\epsilon_c = \left(\frac{\Delta c}{c_0}\right) C_i = 0.5$. It is clear from an examination of Eq. 3.2 that the maximum interaction energy occurs when the solute atom lies either in the extra half plane of the dislocation or directly below it. Here, a positive interaction energy represents a repulsive interaction between the solute and the dislocation and a negative interaction energy an attraction. When $(\epsilon_b + v\epsilon_c)$ is positive, a repulsive interaction occurs for solute atoms above the slip plane and an attractive interaction for atoms below the slip plane.

In the case of a screw dislocation, Tyson (Refs. 69,70) found that no interaction occurred between the octahedral solutes and $\{10\bar{1}0\} 1/3<11\bar{2}0>$ screw dislocations so that

$$\frac{E^s}{\epsilon} = 0 \quad (3.3)$$

Thus, even though there might be a very strong tetragonal distortion of the cell, there is no interaction between a screw dislocation on the first-order prism plane and interstitial solutes in titanium. Detailed calculations by Sthele and Seeger (Ref. 73) show, however, that there exists a volume expansion about a screw dislocation, which is given by $\frac{\Delta V}{V} = \frac{Kb^2}{4\pi^2 r^2}$, where K is a constant having a value between 0.1 and 1.0 for most metals. This expansion can be imagined to result from the sliding of close-packed layers of atoms over one another, and if atoms are considered as rigid spheres, the planes must separate from their close packed configuration as the shear occurs. Fleischer (Ref. 74) and Saxl (Ref. 75) have extended Cottrell and Bilby's (Ref. 76) original treatment for the case of the interaction of a dislocation with a spherical distortion and calculated the hydrostatic stress P from the volume expansion of the screw to be

$$P = \frac{\Delta V}{V} \frac{2\mu(1+v)}{3(1-2v)} = \frac{Kb^2 \mu(1+v)}{6(1-2v)\pi^2 r^2} \quad (3.4)$$

where $\frac{2(1+v)\mu}{3(1-2v)}$ is the bulk modulus. In the case of tetragonal distortions, Cottrell and Bilby's original treatment can be further extended in the method of Cochardt, Schoeck and Wildersich (Ref. 67) by adding the hydrostatic stress tensor to the deviatoric stress tensor of the screw dislocation as calculated from linear elasticity theory. This then gives

$$\begin{aligned} E_{\epsilon}^S &= -P(2\epsilon_b + \epsilon_c) V_{cell} \\ &= -\frac{K\mu b^2(1+v)}{6(1-2v)\pi^2} \frac{(2\epsilon_b + \epsilon_c)}{r^2} V_{cell} \end{aligned} \quad (3.5)$$

Thus, for positive values of $(2\epsilon_b + \epsilon_c)$ there occurs an attraction between a screw dislocation and interstitial solutes residing both below and above the prism slip plane.

Modulus Interaction:

An elastic interaction in addition to that resulting from the distortion of the lattice will arise whenever the matrix and the defect possess different moduli, since the defect acts as an elastic inhomogeneity in the stress field of the dislocation. This modulus interaction can be understood from the following physical considerations. Assume that the point defect behaves as an elastic sphere in an elastic continuum. If the defect has a lower modulus than the matrix, the energy of the dislocation strain field is reduced by distorting the defect as compared to the matrix, which in turn results in an attraction between the solute and the dislocation.

A complete theory of the modulus interaction between a dislocation and a point defect is not yet clearly established for the most general conditions. It has been solved only for the case when the size interaction is zero and the solute atom is considered as a sphere (Refs. 74,75,77). This gives for a screw dislocation

$$E_{\mu}^S = \frac{\mu b^2}{8\pi^2} \frac{1}{r^2} n' V_{cell} \quad (3.6)$$

where $n' = \frac{n}{1+|n/2|}$ with $n = \frac{1}{\mu} \frac{d\mu}{dC_i}$. As in the case of the size interaction energy, it is not necessary to state the actual volume of the inhomogeneity, nor the magnitude of the elastic modulus in the inhomogeneity, since they have been combined to form a constant determined from macroscopic properties of the material.

In the case of an edge dislocation, Fleischer (Refs. 74,78,79) considered that a good approximation would be obtained by multiplying Eq. 3.6 for a screw by $1/(1-v)$. A more refined calculation by Saxl (Ref. 75) suggests that the multiplying factor should be $(1-v)^2$, so that a more correct expression appears to be (Ref. 80)

$$E_{\mu}^e = \frac{\mu b^2}{8\pi^2(1-v)^2} \frac{1}{r^2} n' V_{cell} \quad (3.7)$$

The modulus interaction energy with an edge dislocation does not change sign according to the side of the slip plane under consideration. This is in contrast to what happens for the size interaction energy and has been pointed out by several

authors (Refs. 79-83).

Combined Size Misfit and Modulus Interactions:

Eshelby (Ref. 84) has shown that according to the theory of linear elasticity one may add the various elastic interactions between dislocations and defects. This will be done here for the size misfit and modulus mismatch interactions and their sum is given in Table 3.1. As mentioned above, this total interaction energy is the Helmholtz free energy F^* , which is often designated as G or G_b in the literature. It should be emphasized, however, that it is not the Gibbs free energy, except at zero stress. The derivative of F^* with respect to the position of the dislocation at constant temperature and pressure gives the internal resisting force f_i^* on the dislocation. The equations for this "back-force" are presented in Table 3.2.

TABLE 3.1. Interaction Energies of Interstitial Solutes with Dislocations Gliding on the First-Order Prism Planes in α -Ti.

	Edge dislocation	Screw dislocation
Size	$\pm \frac{\mu b}{\pi(1-v)} \frac{y}{r^2} \epsilon_e V_{cell}$	$-\frac{\mu b^2 K(1+v)}{6\pi^2(1-2v)} \frac{1}{r^2} \epsilon_s V_{cell}$
Modulus	$\frac{\mu^2}{8\pi^2(1-v)^2} \frac{1}{r^2} n' V_{cell}$	$\frac{\mu b^2}{8\pi^2} \frac{1}{r^2} n' V_{cell}$
Total	$F_e^* = E_e (n' \pm \alpha_e \epsilon_e)$	$F_s^* = E_s (n' - \alpha_s \epsilon_s)$
	$E_e = \frac{\mu b^2}{8\pi^2(1-v)^2} \frac{1}{r^2} V_{cell}$	$E_s = \frac{\mu b^2}{8\pi^2} \frac{1}{r^2} V_{cell}$
	$\alpha_e = 8\pi(1-v) \frac{y}{b}$	$\alpha_s = \frac{4K(1+v)}{3(1-2v)}$
	$\epsilon_e = \epsilon_b + v\epsilon_c$	$\epsilon_s = 2\epsilon_b + \epsilon_c$

Notes: x = distance of the dislocation from the interstitial measured along the slip plane

y = distance of the interstitial above or below the slip plane

$$r^2 = x^2 + y^2$$

$$\epsilon_b = \left(\frac{\Delta a}{a_0}\right) C_i = 0.5; \quad \epsilon_c = \left(\frac{\Delta c}{c_0}\right) C_i = 0.5; \quad n' = \frac{n}{1+|n/2|}; \quad n = \frac{1}{\mu} \frac{du}{dc_i}$$

K = constant having a value between 0.1 and 1.0

Positive interaction energies are repulsive; negative interaction energies are attractive.

TABLE 3.2. Forces of Interaction Between Interstitial Solutes and Dislocations Gliding on the First-Order Prism Planes in α -Ti.

	Edge dislocation	Screw dislocation
Size	$\pm \frac{2\mu b}{\pi(1-\nu)} \frac{xy}{r^4} \epsilon_e V_{cell}$	$-\frac{\mu b^2 K(1+\nu)}{3(1-2\nu)\pi^2} \frac{x}{r^4} \epsilon_s V_{cell}$
Modulus	$\frac{\mu b^2}{4\pi^2(1-\nu)^2} \frac{x}{r^4} n' V_{cell}$	$\frac{\mu b^2}{4\pi^2} \frac{x}{r^4} n' V_{cell}$
Total	$f_i^* = f_0^e(n' \pm \alpha_e \epsilon_e)$	$f_i^* = f_0^s(n' - \alpha_s \epsilon_s)$
	$f_0^e = \frac{\mu b^2}{4\pi^2(1-\nu)^2} \frac{x}{r^4} V_{cell}$	$f_0^s = \frac{\mu b^2}{4\pi^2} \frac{x}{r^4} V_{cell}$

Notes: Positive force of interaction is repulsive; negative force of interaction is attractive.

Definition of the various terms and parameters are given in Table 3.1.

The forms of the F^* versus x curve and the f_i^* versus x curve (where x is the distance between the dislocation and the interstitial solute along the slip plane) for edge dislocations are illustrated in Fig. 3.1. The curves for screw dislocations are similar, except the values of F_e^* and f_e^* are smaller by the factor $(1-\nu)^2 \approx 4/9$. To be noted from Fig. 3.1 is that the larger part of the interaction occurs for x less than $\sim 1b$, i.e. well within the core region of the dislocation, where linear elasticity no longer applies.

It should be mentioned at this point that the equations for the interaction energies and forces given in Tables 3.1 and 3.2 were derived using isotropic elasticity. However, since titanium is nearly isotropic (Refs. 30,31), it is expected that they represent a reasonable approximation for this metal. In accord with this conclusion, Tyson (Ref. 85) found that the size misfit interaction for interstitials in titanium using anisotropic elasticity did not differ appreciably from that based on isotropic elasticity.

The maximum of the interaction energy F_0^* occurs for $x=0$, where x is the distance of the dislocation from the interstitial measured along the slip plane. This gives for the Gibbs free energy of activation at zero stress ΔG_0 , for edge dislocations

$$\Delta G_0^e = \frac{\mu b^2}{8\pi^2(1-\nu)^2} \left(\frac{1}{y^2}\right) V_{cell} I_e \quad (3.8)$$

and for screw dislocations

$$\Delta G_0^s = \frac{\mu b^2}{8\pi^2} \frac{1}{y^2} V_{cell} I_s \quad (3.9)$$

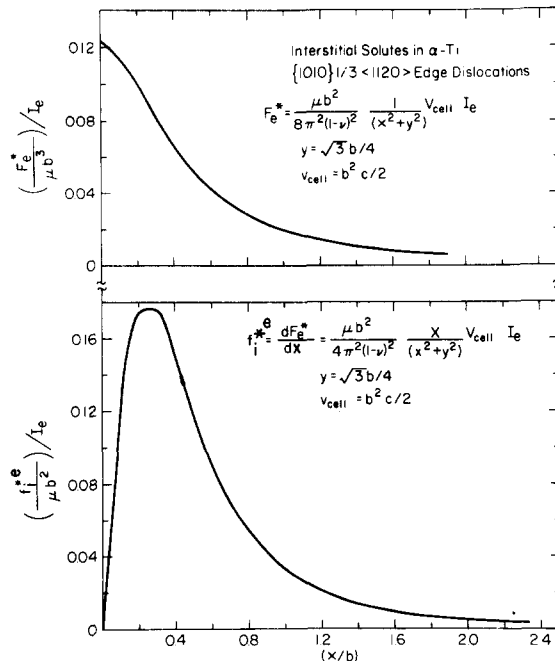


Fig. 3.1. Normalized interaction energy and interaction force versus distance for $\{10\bar{1}0\} 1/3 < 1\bar{1}20 >$ edge dislocations in Ti considering both the size misfit and the modulus mismatch effects due to interstitial solutes.

where I_e and I_s are the interaction parameters pertaining to edge and screw dislocations respectively.

$$I_e = n' \pm \alpha_e \varepsilon_e \quad (3.10)$$

and

$$I_s = n' - \alpha_s \varepsilon_s \quad (3.11)$$

where $\alpha_e = 8\pi(1-\nu)y/b$, $\varepsilon_e = (\varepsilon_b + \nu\varepsilon_c)$, $\alpha_s = \frac{4K(1+\nu)}{3(1-2\nu)}$ and $\varepsilon_s = (2\varepsilon_b + \varepsilon_c)$.

The maximum forces of interaction $f_{i,0}^{*e}$ are obtained by setting the derivatives of the interaction forces with respect to the distance x equal to zero. The maximum occurs for $x = y/\sqrt{3}$ and at this value of x , $\frac{x}{r_0^4} = \frac{x}{(x_0^2 + y^2)^2} = \frac{3\sqrt{3}}{16y^3}$. This then gives for the maximum force associated with the edge dislocation interaction

$$f_{i,0}^{*e} = \frac{\mu b^2}{4\pi^2(1-\nu)^2} \left(\frac{3\sqrt{3}}{16y^3}\right) V_{cell} I_e \quad (3.12)$$

and for the screw dislocation interaction

$$f_{i,0}^{*s} = \frac{\mu b^2}{4\pi^2} \left(\frac{3\sqrt{3}}{16y^3} \right) V_{cell} I_s \quad (3.13)$$

Having derived the general equations for the interaction energies and forces between $\{10\bar{1}0\} 1/3 <1\bar{1}\bar{2}0>$ dislocations and interstitial solute atoms in α -titanium, it is now desired to obtain quantitative values for the energies and forces. For this one needs to know the values of the parameters V_{cell} , y , ϵ_b , ϵ_c , η and K . In keeping with Tyson (Ref. 69) we will take $V_{cell} = b^2 c/2$, since there are two octahedral sites per cell. The assignment of a value to y , the distance the interstitials lie above or below the glide plane is more difficult, because the first-order prism planes consist of two corrugated layers of atoms; see Fig. 3.2. From purely geometrical considerations based on a hard sphere model, the distance from the center line of the more distant row of atoms gives $y = b\sqrt{3}/4$, whereas the nearer row of atoms gives $y = b\sqrt{3}/6$. Since the interaction energies vary as $1/y^2$, the magnitude of the derived energy can thus vary by a factor of two or three depending on the value used for y .

As indicated previously, the size misfit parameters $\epsilon_e (= \epsilon_b + v\epsilon_c)$ and $\epsilon_s (= 2\epsilon_b + \epsilon_c)$ can be evaluated from the rate of change of the lattice constants $b (= a)$ and c with interstitial content. The values of ϵ_e and ϵ_s calculated from the average values of ϵ_a and ϵ_c of Table 2.3 are given in Table 3.3. They are found to increase in the same order as the size of the neutral atom; see Table 2.2.

TABLE 3.3. Combined Size Misfit and Modulus Mismatch Parameters for Interstitials in α -titanium.

Solute	ϵ_e	ϵ_s	η'	I_e		I_s	
				$ y + \alpha_e \epsilon_e $	$\sqrt{2\{(y')^2 + (\alpha_e \epsilon_e)^2\}}^{1/2}$	$y = b\sqrt{3}/6$	$y = b\sqrt{3}/4$
O	0.025	0.072	1.24	1.36	1.42	1.76	1.77
N	0.047	0.106	1.19	1.42	1.53	1.70	1.73
C	0.083	0.222	0.80	1.20	1.40	1.27	1.45

Notes:

$$\epsilon_e = \epsilon_b + v\epsilon_c \quad \epsilon_s = 2\epsilon_b + \epsilon_c \quad \eta' = \frac{\eta}{1+\eta/2}$$

$$\alpha_e = 8\pi(1-v)y/b \quad \alpha_s = \frac{4K(1+v)}{3(1-2v)} \quad n = \frac{1}{\mu} \frac{d\mu}{dC_i}$$

$$= 4.837(y = b\sqrt{3}/6) \quad = \frac{16}{9} \quad (K = 1/3)$$

$$= 7.255(y = b\sqrt{3}/4)$$

The modulus mismatch interaction parameter $n' = n/(1+|\eta'/2|)$ can be evaluated from the rate of change of the shear modulus with interstitial content. Except for the addition of 4.5 at. % oxygen to titanium (Ref. 34), no such data could be found.

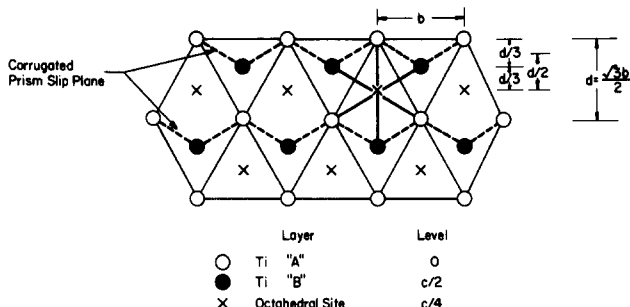


Fig. 3.2. Position of atoms and distances in the CPH structure looking down on the basal plane.

However, there exist some data on Youngs modulus (Figs. 2.3 and 2.4 and Table 2.4) and these were therefore employed. Since titanium is nearly isotropic (Refs. 30, 31) it is expected that η' derived on the basis of Youngs modulus should not differ appreciably from that based on the shear modulus.

Combined Interaction:

The size misfit and the modulus mismatch parameters are combined in Table 3.3 to give the total interaction parameter. For screw dislocations the size interaction parameter $\alpha_s \epsilon_s$ is negative, whereas the modulus interaction parameter η' is positive. Hence the controlling interaction is given by the algebraic sum of the two. For edge dislocations the value of the quantity $\alpha_e \epsilon_e$ may be positive or negative depending on whether the solute atom lies above or below the glide plane. Labusch (Ref. 86) has proposed that the average interaction force in this case is given by $(f_a^2 + f_b^2)^{1/2}$ where $f_a = K_1 (\eta' - \alpha_e \epsilon_e)$ and $f_b = K_1 (\eta' + \alpha_e \epsilon_e)$. This yields $\sqrt{2}((\eta')^2 + (\alpha_e \epsilon_e)^2)^{1/2}$ as the average interaction parameter for edge dislocations. The values of ΔG_0 and f_0^* derived using Eqs. 3.8 and 3.9 and 3.12 and 3.13 respectively and taking I_e and I_s from Table 3.3 are given in Table 3.4. They are essentially in the same order as the bond and diffusion energies given in Table 2.9. Moreover, the values of ΔG_0 for edge dislocations with $y = b\sqrt{3}/4$ and screw dislocations with $y = b\sqrt{3}/6$ are similar in magnitude to the bond and diffusion energies.

Sessile Splitting of Screw Dislocations:

In the above discussion of elastic interactions we have assumed that the dislocations are total or perfect $[10\bar{1}0] 1/3 <11\bar{2}0>$ dislocations gliding on the first-order prism planes. However, Söb (Ref. 87) and Söb, Kratochvil and Kroupa (Ref. 88) have recently proposed that the screw dislocations in the CPH metals of Group IVB (Ti, Zr, Hf) may be dissociated into three partials D_1 , D_2 , and D_3 simultaneously on the prism and basal planes (Fig. 3.3a) according to the reactions.

$$b \rightarrow b/3 + (b/6 + H) + (b/2 - H) \quad (3.14)$$

$$b \rightarrow b/3 + (b/2 + H') + (b/6 - H') \quad (3.15)$$

or on the prism and first-order pyramidal planes (Fig. 3.3b) according to

$$b \rightarrow b/3 + (b/2 + H'') + (b/6 - H'') \quad (3.16)$$

where $b = 1/3 <11\bar{2}0>$ is the Burgers vector of a perfect screw dislocation and H , H'

TABLE 3.4. Calculated Values of ΔG_0 and $f_{i,0}^*$ for Elastic Interactions of
Interstitial Solutes with Edge and Screw Dislocations in $\alpha\text{-Ti}$.

System	y	$\Delta G_0/\mu b^3$		$f_{i,0}^*/\mu b^2$		screw	
		edge	screw	edge	screw		
Ti-0	$b\sqrt{3}/4$	$I_e = \sqrt{2}\{(n')^2 + (\alpha_e \epsilon_e)^2\}^{1/2}$	$I_s = n' - \alpha_s \epsilon_s$	$I_e = \sqrt{2}\{(n')^2 + (\alpha_e \epsilon_e)^2\}^{1/2}$	$I_s = n' + \alpha_s \epsilon_s$	$I_s = n' - \alpha_s \epsilon_s$	
	$b\sqrt{3}/6$	0.21 0.48	0.17 0.37	0.06 0.13	0.32 1.08		
Ti-N	$b\sqrt{3}/4$	0.21 0.46	0.19 0.38	0.05 0.12	0.31 1.03	0.08 0.27	
	$b\sqrt{3}/6$	0.18 0.34	0.17 0.32	0.02 0.05	0.26 0.78		
Ti-C	$b\sqrt{3}/4$	0.18 0.34	0.17 0.32	0.02 0.05	0.25 0.74	0.03 0.11	
	$b\sqrt{3}/6$	0.11	0.11	0.05	0.74		
Notes:	$b = 2.95\text{\AA}$ $\mu_0^e = K_0^e = 6.78 \times 10^{11}$ dynes/cm ² $\mu_0^s = K_0^s = 4.84 \times 10^{11}$ dynes/cm ²						
	$\mu_0 b^3 \text{ (edge)} = 10.87 \text{ eV}$ $\mu_0 b^3 \text{ (screw)} = 7.75 \text{ eV}$						

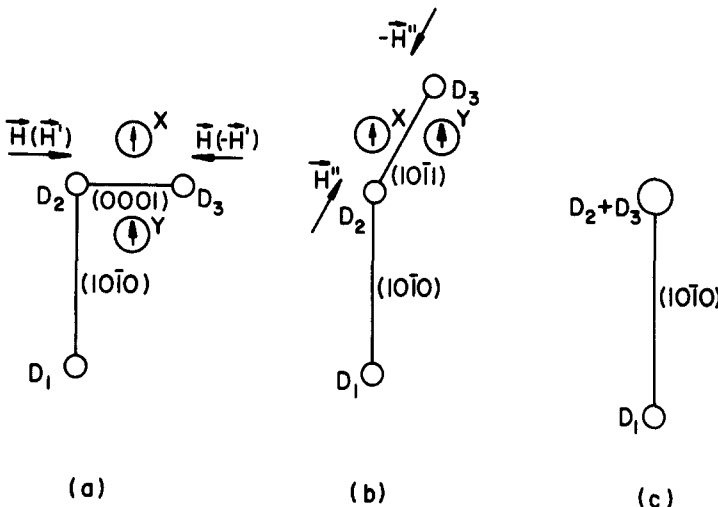


Fig. 3.3. Splitting of screw dislocations in CPH metals: (a) sessile splitting on the prism and basal planes, (b) sessile splitting on the prism and first-order pyramidal planes and (c) glissile splitting on the prism plane. The position of the interstitial atoms impeding the sessile-glissile transformation are denoted as X and Y. From Šob, Kratochvil and Kroupa (Ref. 88).

and H'' denote the Burgers vectors of the edge components of the partial D_2 in the dissociation of Eqs. 3.14, 3.15 and 3.16 respectively. H and H' lie in the basal plane, H'' in the first-order pyramidal plane. H was determined to have the value $1/6 <1\bar{1}00> = 0.29b$; $H' \approx 0.18b$ and $H'' \approx 0.06b$.

Šob, Kratochvil and Kroupa (Ref. 88) deduced that the important dissociation in the plastic flow of titanium was the splitting into the first-order pyramidal plane (Fig. 3.3b). They further suggested that the deformation of titanium at low temperatures is governed by the recombination of this sessile configuration into a higher energy glissile configuration on the prism plane (Fig. 3.3c) according to the reaction $b + b/3 + 2b/3$ originally proposed by Regnier and Dupouy (Ref. 89). The strengthening effect of the interstitial solutes was attributed to their influence on the sessile-glissile transformation of the screw dislocation according to the theory of elastic interactions discussed above. (They, however, only considered the size misfit interaction, neglecting the stronger modulus mismatch interaction). This interpretation of the deformation of CPH metals at low temperatures is similar to that which has been proposed for BCC metals (Refs. 90-94).

According to the model of Šob, Kratochvil and Kroupa, the total energy of a dissociated dislocation of length L is given by

$$F_0^* = L(e_d + e_\gamma + e_{\tau^*}) + \sum E_i \quad (3.17)$$

where e_d is the interaction energy of the partials D_1 , D_2 , and D_3 , e_γ the energy of the stacking faults, e_{τ^*} the contribution of the applied stress field and $\sum E_i$ the sum over all interstitials affecting the sessile-glissile transformation of the dissociated configuration of length L . Since the interaction energy between the dislocation D_3 and the interstitials decreases rapidly with distance it was assumed

that only interstitial solute atoms in the slip planes and in neighboring atomic planes influence the sessile-glissile transformation.

Sób, Kratochvil and Kroupa (Ref. 88) derived values for the various energy terms in Eq. 3.17 to yield F_0^* for the case in which the sessile-glissile transformation is influenced by individual interstitial atoms due to the tetragonal distortion produced by them. It was found that this model was not capable of explaining the observed strengthening of titanium by interstitials because of the weakness of the interaction (~0.06 ev) between the edge component of D_3 and one interstitial atom. They therefore proposed that the activation length L may not be determined by the spacing between interstitials, but rather is given by the relation developed for pure BCC metals (Ref. 93)

$$L = 0.2\mu b [\ln 0.0265\mu b/\gamma_2]^{2/3}/\tau^* \quad (3.18)$$

where γ_2 is the stacking fault energy on the first-order pyramidal plane. As a result, during the sessile-glissile transformation the segment of the dislocation D_3 must overcome a number of interstitial atoms simultaneously. This collective effect increases significantly the influence of the interstitials on the transformation.

3.1.2 Chemical Interactions

The free energy of an atom in a crystal is determined by the type and geometrical arrangement of the atoms which surround it. Therefore a "chemical" interaction between a dislocation and an interstitial atom will occur if the presence of the dislocation changes the environment surrounding the solute. The various types of chemical interactions include those related to short-range order, clustering of solutes, stacking faults between the partials of dissociated dislocations, the structure of the dislocation core and the breaking of directed atomic bonds.

Short-Range Order or Clustering:

For the dilute concentrations considered here (<-lat.%), one does not expect short-range order to be a factor in the strengthening of titanium by interstitial solutes. Moreover, thermodynamic data (Ref. 24,25) suggest that the oxygen atoms in titanium are randomly distributed, so we can neglect clustering as well. However, it should be mentioned that Ruano and Elssner (Ref. 95) observed bright spots in electron microscope weak-beam images of zirconium-oxygen alloys, which they attributed to clusters of interstitially dissolved oxygen atoms in the α -zirconium lattice. Furthermore, there occurred pronounced changes in the slope of the flow stress versus temperature curves and peaks in the activation volume versus temperature curves for these alloys at ~300°K, which they attributed to a change in rate-controlling mechanism from the overcoming of individual interstitial oxygen atoms at lower temperatures to overcoming of clusters at higher temperatures. Whether or not clusters exist in titanium-interstitial alloys has not been unambiguously determined.

Stacking Fault Considerations:

Suzuki (Ref. 96) was the first to point out that there could exist an interaction energy between solute atoms and the faulted region between split partial dislocations due to the difference in crystal structure in the fault compared to the matrix. His original considerations applied to the case when the stacking fault extends over several atomic distances, i.e. in material of low stacking fault energy. Since the stacking fault energy in titanium is considered to be relatively high (Refs. 40,97), this interaction is not considered to be important in titanium-interstitial alloys.

Dislocation Core Structure:

The core region of a dislocation has a structure which is different from that of the matrix; hence the free energy of a solute atom will change as it enters the core. As pointed out by Tyson (Ref. 4), the interaction energy resulting from this can be considered as an extension of the Suzuki stacking fault concept to narrow dislocations. Since the core region of $\{10\bar{1}0\} 1/3 <1\bar{1}\bar{2}0>$ dislocations in the CPH lattice can be considered to have a BCC structure (Ref. 89), an interaction energy would result from any difference in free energy of the interstitial atom in the BCC phase as compared to the CPH phase. Since the interstitials oxygen, nitrogen and carbon are α -stabilizers, it is expected that their energy will be higher in the BCC structure of the dislocation core than in the matrix, leading to a short-range repulsive interaction; similarly an attraction might occur for hydrogen. At present there exist insufficient thermodynamic data to evaluate these effects quantitatively for titanium; however, a rough estimate by Tyson and Conrad (Ref. 98) for oxygen in hafnium yielded a reasonable value for the interaction energy due to this cause.

Breaking of Chemical Bonds:

If strong directional bonds exist between a solute atom and the surrounding matrix atoms, then the passage of a dislocation can lead to the breaking of such bonds. This is illustrated in Fig. 3.4 for the case of prism plane dislocations and interstitial solutes in titanium. It is here seen that one of six titanium-interstitial bonds can be considered to be broken when the interstitial atom finds itself in the core region of the dislocation. Tyson (Ref. 69) first proposed that the large energy of interaction between interstitial solutes and dislocations in titanium might be due to the breaking of directed atomic bonds between the solute and its neighbors as the coordination number is changed. Later, Sargent and Conrad (Ref. 38) presented some evidence supporting the idea that oxygen was covalently bonded to titanium in solid solution and that the energy of a Ti-O bond should be approximately 1/6 of the heat of formation of the compound TiO^+ . Estimates of the bond energies between the interstitial solute atoms and the surrounding titanium atoms are given in Table 2.9. They are similar in magnitude to the elastic interaction energies derived above and listed in Table 3.4.

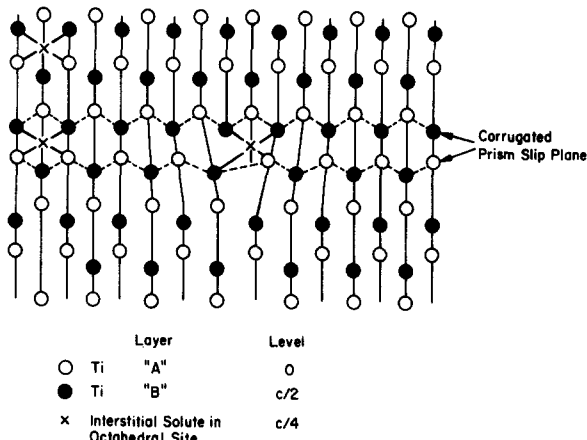


Fig. 3.4. Edge dislocation on prism plane in CPH structure looking down on the basal plane. Note that the passage of the edge dislocation can be considered to break one of the six Ti-interstitial bonds.

[†]In Ref. 38 the compound is wrongly given as Ti_2O rather than TiO .

3.1.3 Electrical Interactions

As mentioned above, all interactions between dislocations and solute atoms in crystals can be considered to be electrical in nature, since they result from alterations in the energies of the electrons. For example, the overlap of atom core electrons produces the lattice expansion which leads to the size effect, and alterations in the density of conduction electrons leads to changes in the elastic moduli. However, we have not yet reached the state of sophistication in our understanding of electronic behavior in solids that we can describe these complex changes in a quantitative manner. There is, however, one electrical interaction in metals which has been evaluated in some detail (Ref. 99). This interaction can be understood from the concept that the electrons of the conduction band have the characteristics of a gas. Since the gas tends to resist compression, the electrons rearrange their distribution by going from the compressed side of an edge dislocation to the dilated side, thereby creating a dipole. The electrons of solute atoms near a dislocation undergo a similar rearrangement. Thus, in a monovalent matrix crystal the extra conduction electrons introduced by a polyvalent solute atom will tend to redistribute themselves according to the hydrostatic pressure they experience in the vicinity of a dislocation.

Cottrell, Hunter and Nabarro (Ref. 99) calculated the interaction energy between the dipoles formed around a dislocation and a solute in copper and found that the effect was negligible. Friedel (Ref. 77) also points out that the electrical interaction is expected to be very small, i.e. less than one-hundredth of an electron-volt. Fleischer (Ref. 74) has noted that, since the hardening due to solute atoms in FCC copper can be explained in terms of the elastic interactions only, there is no place left for an electrical interaction, unless it is related to these. This has also been confirmed recently for CPH magnesium (Ref. 83), for which it was found that the valency term obtained from an empirical correlation is equivalent to the modulus interaction. Although no detailed analysis has been made for interstitial solutes in metals, one expects on the basis of the above considerations that the electrical interaction (dipole interaction) is also small for interstitial solutes in titanium.

3.2 Solid Solution Strengthening Models

It is now recognized (Refs. 100,101) that the strengthening due to a random array of solutes in the immediate vicinity of a slip plane can be considered to be of two types: (a) the obstacles to the dislocations are individual solute atoms (Fig. 3.5a) and (b) the obstacles reflect the collective action of groups of solute atoms (Fig. 3.5b). The former represents the solid solution strengthening model originally proposed by Friedel (Refs. 77,102-103) and Fleischer (Ref. 74), while the latter is similar to that originally proposed by Mott and Nabarro (Refs. 104-106) and reviewed by Cottrell (Ref. 107). The theoretical base for each of these two models will now be briefly reviewed. The approach taken here is along the lines of Kocks, Argon and Ashby (Ref. 101). Similar results were obtained by Labusch (Refs. 86,100) employing a somewhat more sophisticated statistical analysis.

Referring to Fig. 3.5a, the obstacle (solute atom) exerts on the dislocation a force f_i^* whose effective range of interaction is w , which distance is small compared to the effective spacing between obstacles λ^* . Upon application of an effective resolved shear stress τ^* , equilibrium is achieved when the force f^* due to the applied stress just balances that due to the obstacle f_i^* , i.e.

$$\tau^* b \lambda^* = f^* = f_i^* \quad (3.19)$$

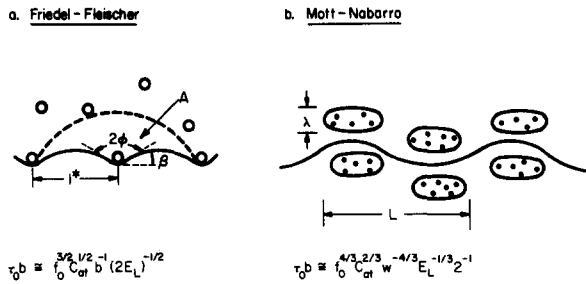


Fig. 3.5. Solid solution strengthening models.

τ^* is the difference between the applied stress τ and the long-range internal stress τ_μ existing in the region of the obstacle under consideration:

$$\tau^* = \tau - \tau_\mu \quad (3.20)$$

Under the action of the applied stress the dislocation will bow between the obstacles, the radius of curvature R being given by

$$R = \frac{E_L}{\tau^* b} = \frac{\ell^*}{2 \sin \beta} = \frac{\ell^*}{2 \cos \phi} \quad (3.21)$$

where E_L is the dislocation line tension, β the bow-out angle and ϕ one-half the cusp angle. Substituting for $\tau^* b \ell^*$ from Eq. 3.21 into Eq. 3.19, we obtain

$$f_i^* = 2E_L \cos \phi = 2E_L \sin \beta \quad (3.22)$$

which relates the interaction force to the amount of dislocation bow-out. Rearranging Eq. 3.22 one obtains

$$\kappa^* = \cos \phi = f_i^*/2E_L \quad (3.23)$$

where κ^* now gives the interaction force normalized with respect to the dislocation line tension. Further, Eqs. 3.19, 3.22 and 3.23 give for the stress required to overcome the obstacle at 0°K

$$\tau_0^* = \frac{2E_L (\cos \phi)_0}{b \ell^*} = \frac{f_{i,0}^*}{b \ell^*} = \frac{2E_L \kappa_0^*}{b \ell^*} \quad (3.24)$$

To evaluate τ_0^* for glide over an appreciable area of the slip plane we need to express ℓ^* , the effective obstacle spacing, in terms of the average spacing ℓ of the obstacles on the slip plane. A simple approach to this problem was first proposed by Friedel (Ref. 77) and is based on the steady-state propagation of quasi-straight dislocation lines. He assumed that when a dislocation overcomes one obstacle it comes into contact on the average with exactly one more.[†] Therefore, the

[†]This assumption was also later made by Fleischer (Ref. 74) and Fleischer and Hibbard (Ref. 108) in their treatment of solid solution strengthening.

area A of the slip plane swept-out following the release must on the average be equal to the average area per obstacle, ℓ^2 . Geometrical considerations then give

$$A = \ell^2 = 1/2 \frac{(\ell^*)^3}{R} \quad (3.25)$$

Substituting for R from Eq. 3.21 yields

$$\ell^* = s\ell^{2/3} \left(\frac{2E_L}{\tau_0^* b} \right)^{1/3} \quad (3.26)$$

where s' is a factor of the order of one. Upon substituting Eq. 3.26 into Eq. 3.19 gives

$$\tau_0^* = sf_{i,0}^{*3/2} / b\ell(2E_L)^{1/2} = s\kappa_0^{*3/2} (2E_L)/b\ell \quad (3.27)$$

which is the stress required for large-scale glide at absolute zero.

The average spacing of obstacles on the slip plane is related to the atomic concentration C of solutes by

$$\ell = 1/\sqrt{N} = \alpha b/\sqrt{C} \quad (3.28)$$

where N is the number of obstacles per unit area and α is a geometric constant equal to $\sqrt{0.8}$ for the {1010} plane in titanium. Substituting for ℓ into Eq. 3.27 gives

$$\tau_0^* = \frac{sf_{i,0}^{*3/2} C^{1/2}}{\alpha b^2 (2E_L)^{1/2}} = \frac{s2E_L}{\alpha b^2} \kappa_0^{*3/2} C^{1/2} \quad (3.29)$$

i.e. a square root dependence of the flow stress on composition.

τ_0^* given by Eq. 3.27 is in good accord with the results from the more detailed statistical theories of Kocks (Refs. 109-112) and Argon (Ref. 113) and the computer experiments of Foreman and Makin (Ref. 114) for obstacle strengths represented by θ values greater than $\sim\pi/4$ (κ_0^* values up to ~ 0.5). For $\theta < \pi/4$ the Friedel statistics no longer apply and $\kappa_0^{*3/2}$ of Eq. 3.27 must be replaced by another function of κ_0^* (Refs. 109-114). Brown and Ham (Ref. 115) propose that a good description of the flow stress is then

$$\tau_0^* = 0.8\kappa_0^{*3/2} (2E_L)/b\ell \quad (3.30)$$

In the above derivation it is assumed that the obstacles are point-like and only interact with a dislocation on contact. In reality, obstacles have a finite interaction range w and the dislocation will be attracted or repelled by all obstacles whose centers are inside a strip of width w around it. At zero stress the dislocation would react to these attractions and repulsions and take on a zig-zag shape rather than remaining straight. The interactions are expected to influence the analysis given above when the bow-out arc between two adjacent obstacles in the strip has an excursion of about $w/2$, giving

$$\sin\beta = \cos\phi = \frac{f_{i,0}^*}{2E_L} \geq w/\ell_1 \quad (3.31)$$

where ℓ_1 is the average distance of the obstacles along the dislocation, which is given by

$$\ell_1 = \ell^2/w \quad (3.32)$$

Substituting for ℓ_1 from Eq. 3.32 into 3.31 and considering Eq. 3.23, we obtain

$$\left(\frac{f_{i,0}^* \ell^2}{2E_L} \right)^{1/2} = \left(\frac{f_{i,0}^* (\alpha b)^2}{2E_L C} \right)^{1/2} = \left(\frac{\kappa_0^* (\alpha b)^2}{C} \right)^{1/2} > w \quad (3.33)$$

as the condition required for the Friedel statistics to apply. It is expected that w is similar in magnitude for most solutes ($w \approx 2b$) and therefore according to Eq. 3.33 the Friedel-Fleischer (F-F) solid solution strengthening model is favored by strong interaction forces and dilute concentrations. Upon employing Eq. 3.33 one finds that for the stress range of usual interest (10^{-4} to $10^{-2}\mu$) the Friedel statistics apply over a rather wide range of conditions, the exception being fairly high concentrations of relatively weak obstacles such as substitutional solutes. In contrast, Labusch (Ref. 100) employing a slightly different approach obtains a limiting condition in which left hand side of Eq. 3.33 is 1/6 that given above, making the F-F model somewhat more restrictive. However, results quite similar in magnitude to Eq. 3.33 (by a factor of $1/\sqrt{2}$) were obtained by him upon using a more sophisticated statistical theory.

For conditions in which the left side of Eq. 3.33 is less than w , the initial zig-zagging of the dislocation must be taken into account and the Friedel statistics no longer apply. The statistics which are then generally employed are those originally considered by Mott and Nabarro (Refs. 104-106) and subsequently by Cottrell (Ref. 107), Friedel (Refs. 77,102,103), Riddhagni and Asimow (Ref. 116) and more recently by Labusch (Refs. 86,100) and by Kocks, Argon and Ashby (Ref. 101). All of the approaches by these various authors yield the same result to within a numerical constant, if the various detailed assumptions are made comparable (Refs. 100,117). The assumptions of Labusch and Kocks, Argon and Ashby give

$$\tau_0^* = \frac{Af_{i,0}^{*4/3} w^{1/3}}{(2E_L)^{1/3} b \ell^{4/3}} = \frac{Af_{i,0}^{*4/3} w^{1/3} C^{2/3}}{(2E_L)^{1/3} b^{7/3} \alpha^{4/3}} = \frac{A(2E_L)}{\alpha^{4/3} b^2} \left(\frac{w}{b} \right)^{1/3} \kappa_0^{*4/3} C^{2/3} \quad (3.34)$$

Where $A = 1/(3 \cdot 2^{1/3})$ in Labusch's analysis (Ref. 86) and 1/2 in that by Kocks, Argon and Ashby (Ref. 101). Eq. 3.34 yields a $C^{2/3}$ concentration dependence of the flow stress, compared to a $C^{1/2}$ dependence in Eq. 3.29. Employing somewhat different assumptions, Mott and Nabarro, Cottrell and Friedel obtain for the case when the size-effect is predominant

$$\tau_0^* = \alpha \mu \epsilon^n C \quad (3.35)$$

where ϵ is the size misfit parameter and α and n are constants. Depending on the

details of the model, α varies between 0.25 and 2.5 and n between 1 and 2. A linear dependence of the flow stress on concentration was also obtained by Hirth and Loethe (Ref. 118) for concentrated random solid solutions.

In the case of relatively dilute solid solutions, Kocks, Labusch and Schwarz (Refs. 119,120) obtained the following expression for the finite range of interaction between the solute atom obstacles and a dislocation

$$\tau_0^* = \frac{s^2 E_L}{\alpha b^2} (\kappa_0^*)^{3/2} C^{1/2} [1 + \beta C^{1/2}/\kappa_0^*]^{1/2} \quad (3.36)$$

which is an expansion about the Friedel-Fleischer limit.

To account for the fact that the solute atom dislocation interaction has a finite range, Friedel (Refs. 77,102,103) considered the solute atoms to have two distinct actions on a dislocation: (1) The atoms near to a dislocation line exert on it an average internal stress of wavelength $\lambda (=b/C^{1/3})$, the average spacing of the solute atoms in the volume and (2) the few atoms actually on the dislocation line interact much more strongly with it. The flow stress is then given by the sum of the two interactions

$$\tau_0 = \tau_\lambda + \tau_0^* \quad (3.37)$$

where τ_λ is a long-range athermal interaction and τ^* is a short-range interaction, which can be overcome with the aid of thermal fluctuations. When the size-effect predominates, Friedel calculated

$$\tau_0^* = F_0^* C / 2b^3 = \frac{1}{4} \mu e C \quad (3.38)$$

and

$$\tau_\lambda = \frac{1}{4} \frac{\tau_i}{b} \left| \frac{F_0^*}{\mu} \right|^{1/3} C^{1/3} = \frac{1}{4} \mu (e C)^{1/3} \quad (3.39)$$

where $F_0^* (=1/2 \mu b^3 e)$ is the maximum interaction energy and $\tau_i (= \mu e C)$ is the average long-range stress on the slip plane due to the solute atoms. Since τ^* decreases rapidly with temperature, only the relatively temperature independent component τ_λ will be observed at higher temperatures and therefrom the contribution of each component at lower temperatures can then be determined. Combining the two components given by Eqs. 3.38 and 3.39 one obtains

$$\tau_0 = \frac{1}{4} \mu e C [1 + (e C)^{1/3}] \quad (3.40)$$

In the above considerations the obstacles are all taken to be of the same strength (f_i^*). In a real alloy we can expect a variation in obstacle strengths, and in such cases the effect of two (or more) obstacles will depend on their relative strengths. Two general cases of interest which can be readily treated for point obstacles are: (a) $f_i^*(1) \ll f_i^*(2)$ and (b) $f_i^*(1) = f_i^*(2)$ where (1) and (2) refer to two obstacles. For the former case it can be shown (Refs. 101,111,112) that if $N_2 \gg N_1$ (N = area density of obstacles) then

$$\tau^* b \ell_2 = f_i^*(2) + n f_i^*(1) \quad (3.41)$$

where $n (= \ell_2^*/\ell_1^*)$ is the number of obstacles with strength $f_i^*(1)$ and spacing $\ell_1^* (= 1/N_1)$ along the dislocation strongly pinned by the obstacles of strength $f_i^*(2)$ and spacing $\ell_2^* (= 1/N_2)$. Substituting for n in Eq. 3.41 and dividing through by $b\ell_2^*$ gives

$$\tau^* = \frac{f_i^*(1)}{b\ell_1^*} + \frac{f_i^*(2)}{b\ell_2^*} \quad (3.42)$$

or

$$\tau^* = \tau_1^* + \tau_2^* \quad (3.43)$$

for the case of many weak obstacles and a few strong ones. When $N_2 \approx N_1$ (i.e. $\ell_2^* \approx \ell_1^*$), then since $f_i^*(1) \ll f_i^*(2)$, Eq. 3.42 reduces to

$$\tau^* \approx \tau_2^* \quad (3.44)$$

For the case when $f_i^*(1) \approx f_i^*(2)$, we obtain from Eqs. 3.27 and 3.28

$$\tau^* \approx \frac{f_i^{*3/2} N^{1/2}}{b^2 (2E_L)^{1/2}} \quad (3.45)$$

where $N = N_1 + N_2$. Squaring both sides of Eq. 3.45 gives

$$\tau^{*2} \approx \frac{f_i^{*3} N_1}{b^4 (2E_L)} + \frac{f_i^{*3} N_2}{b^4 (2E_L)} \quad (3.46)$$

yielding

$$\tau^{*2} = \tau_1^{*2} + \tau_2^{*2} \quad (3.47)$$

which is the relation originally proposed by Koppenaal and Kuhlman-Wilsdorf (Ref. 121). Computer experiments by Foreman and Maken (Ref. 114) have confirmed the relations of Eqs. 3.43, 3.44 and 3.47 and the ranges in between.

3.3 Dislocation Kinetics

The previous section dealt with the nature of the interaction between dislocations and interstitial solutes in α -titanium and the applied stress required to overcome this interaction at 0K. In the present section we will be concerned with the effects of temperature and dislocation velocity (strain rate) on this stress, which subject is termed dislocation kinetics. Three temperature regimes are considered: (a) low temperatures where moving dislocations interact with stationary solutes, (b) intermediate temperatures where moving dislocations interact with slowly moving solutes and (c) high temperatures where the solutes can move rapidly.

3.3.1 Low Temperatures: Moving Dislocations and Stationary Interstitial Solutes

An excellent review of the thermodynamics and kinetics of dislocation motion in crystalline solids at low temperatures has recently been prepared by Kocks, Argon and Ashby (Ref. 101). Those aspects of the subject which apply specifically to the interaction of dislocations with stationary discrete obstacles will now be considered. The discussion will follow along the lines developed by the author and his co-workers (Ref. 122).

Single Set of Discrete Obstacles:

The interaction of a dislocation with an interstitial solute atom in titanium is considered to occur as depicted in Fig. 3.6. The force f_i exerted by the obstacle on the dislocation may then vary with distance x as indicated in the upper part of Fig. 3.7. For isothermal and reversible conditions, and neglecting any small changes in volume which may occur, the Helmholtz free energy F , the Gibbs free energy G and the Gibbs free energy of activation ΔG associated with an externally applied force f are given by:

$$F = U - TS = \int f_i dx \quad (3.48)$$

$$G = H - TS = F - f_i x \quad (3.49)$$

$$\Delta G = \Delta H - T\Delta S = \int_1^2 (f_i - f) dx \quad (3.50)$$

$$\Delta F = \Delta G(f=0) \quad (3.51)$$

where U is the internal energy, S the entropy and T the temperature. These quantities and their relationship to the f_i - x curve are depicted in the lower part of Fig. 3.7.

Statistical mechanics (Ref. 123) and chemical rate theory (Refs. 124,125) indicate that for an applied force less than the maximum resisting force due to the obstacle the probability p of cooperative thermal motion of atoms leading to a successful overcoming of the solute atom obstacle is given by

$$p = v^* \exp - \left[\frac{\Delta G(f, T)}{kT} \right] \quad (3.52)$$

where v^* is the frequency of vibration (attack frequency) of the dislocation segment length $2\ell^*$, ΔG is the Gibbs free energy of activation associated with the obstacle given by Eq. 3.50, and k is Boltzmann's constant. ΔG is a decreasing function of the applied force f and may also be a function of the temperature T . Granato, Lücke, Schlipf and Teutonico (Ref. 123) and Kocks, Argon and Ashby (Ref. 101) come to the conclusion that v^* is independent of ℓ^* and has a value of the order of $10^{-2} v_D$ or $10^{11} s^{-1}$, where v_D is the Debye frequency. This is in contrast to the early consideration by Friedel (Ref. 77) which gave $v^* \approx v_D b / 2\ell^*$. Frank and Grydman (Ref. 126) have recently reconsidered the problem in terms of non-equilibrium transition-state theory and come to the conclusion that v^* must lie in the range between $v_D b / 2\ell^*$ and $v_D \sqrt{b / 2\ell^*}$.

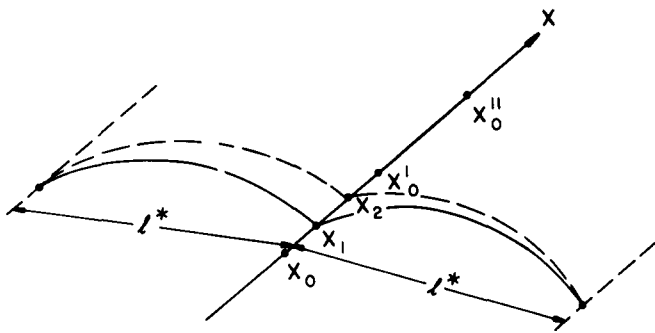


Fig. 3.6. Illustration of a dislocation segment length held up at an obstacle on the x -axis. Positions x_0 , x'_0 and x''_0 are equilibrium positions for zero applied force acting on the dislocation segment. Positions x_1 and x_2 are equilibrium positions for force f acting on the dislocation segment.

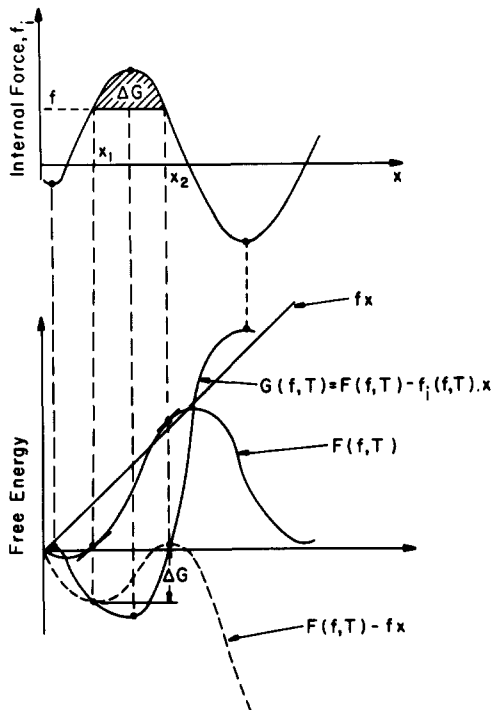


Fig. 3.7. Illustrations of the internal resisting force f_i versus distance curve for overcoming point obstacles and the related thermodynamic functions.

Dislocation theory gives for the shear strain rate

$$\dot{\gamma} = \rho_m b \frac{\dot{x}}{x} \quad (3.53)$$

where ρ_m is the density of mobile dislocations whose average velocity is \dot{x} and b is the Burgers vector. Assuming that the motion of dislocations over a large area is governed by many individual events of the type depicted in Fig. 3.2, one can write

$$\dot{x} = \left[\frac{A}{\ell^*} \right] p \quad (3.54)$$

where A is the average area of the slip plane swept out following each successful thermal fluctuation. Combining Eqs. 3.52 to 3.54 and taking $f = \tau b \ell^*$ gives for the plastic strain rate

$$\dot{\gamma} = \left[\frac{\rho_m}{\ell^*} \right] A b v^* \exp - \left[\frac{\Delta G(\tau, T)}{kT} \right] \quad (3.55)$$

$$= \dot{\gamma}_0 \exp - \left[\frac{\Delta G(\tau, T)}{kT} \right] \quad (3.56)$$

Taking the logarithm of both sides and rearranging yields

$$\Delta G(\tau, T) = kT \ln(\dot{\gamma}_0 / \dot{\gamma}) \quad (3.57)$$

For tensile tests on polycrystals it is generally assumed that $\tau = \sigma / \bar{M}$ and $\gamma = \bar{M}\epsilon$, where \bar{M} is the average orientation factor (the so-called Taylor factor) relating the tensile stress σ and the tensile strain ϵ to the resolved shear stress and shear strain respectively (Ref. 127).

In a real crystal there will exist two general types of obstacles to dislocation motion. One type consists of those whose interaction energy with the dislocation is so high for the temperature under consideration that thermal energy is insufficient to help the dislocation overcome them (i.e., p is extremely small). The stress field of such obstacles generally extends over large distances (greater than about 10 atomic distances) and hence they are called "long-range" or "athermal" obstacles. Two common athermal obstacles are dislocations and precipitate particles. The second type of obstacles are those whose interaction energy is sufficiently small that they can be overcome with the aid of thermal fluctuations. These generally extend only over the order of several atomic distances and are therefore called "short-range" or "thermal" obstacles. Point defects including solute atoms are a common type of thermal obstacles.

When the force field of an athermal obstacle extends over an appreciable distance (as, for example, that associated with dislocations) it will add algebraically to that of the thermal obstacle, so that (see Fig. 3.8)

$$f_i = f_i^* + f_i^H \quad (3.58)$$

where f_i is the total internal resisting force, f_i^* is that due to the short-range obstacle and f_i^H that due to the long-range obstacle, which is expected to be proportional to the shear modulus μ . Under equilibrium conditions the applied force on a dislocation will be just balanced by the total internal resisting force f_i and

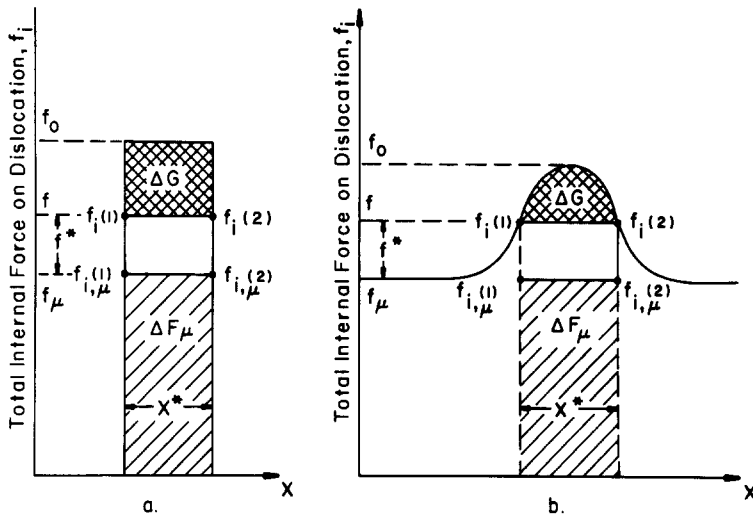


Fig. 3.8. The thermal and athermal thermodynamic model subsystems for (a) x^* is constant and (b) x^* is a function of the total applied force f . ΔF_μ is given by the single-hatched area.

one can consider the externally applied force f to consist of two components, i.e.

$$f = f^* + f_\mu \quad (3.59)$$

It then follows from Eq. 3.19 that the applied stress consists of a thermal and an athermal component, so that

$$\tau = \tau^* + \tau_\mu \quad (3.60)$$

Furthermore, it can be shown (Ref. 122) that the thermodynamic parameters ΔU , ΔH and ΔS , which contain terms related to the total work during the thermal activation process, can be divided into two parts, one associated with the short-range obstacle, the other with the long-range obstacle, so that

$$\Delta U = \Delta U^* + \Delta U_\mu \quad (3.61)$$

$$\Delta H = \Delta H^* + \Delta H_\mu \quad (3.62)$$

$$\Delta S = \Delta S^* + \Delta S_\mu \quad (3.63)$$

$$\Delta F = \Delta F^* + \Delta F_\mu \quad (3.64)$$

ΔG has an exceptional position for it represents the excess work required to bring the system into the activated state and therefore does not contain any term related to the work during the activation process. Consequently, the value of ΔG is unaffected by the inclusion of a long-range obstacle into the thermodynamic system of the short-range obstacle; see Fig. 3.8.

An important parameter in the above considerations is the dislocation segment length between obstacles ℓ^* , which needs to be expressed in terms of the average spacing $\ell (=1/N)$ between solutes in a random array. For the obstacle strengths and concentrations considered here a good expression for ℓ^* is that given by Eq. 3.26.

Taking the above into consideration and assuming that the force of interaction at each position is independent of the applied stress, one can obtain directly the value of ΔH^* for the short-range obstacle from experimental measurements of the interrelationship between the flow stress, temperature and strain rate. It can be shown (Ref. 122) that if $\dot{\gamma}_0$ is independent of stress and temperature we obtain for discrete obstacles

$$\Delta H^* = Q - \alpha_1 v \tau + (3/2) \alpha \tau^* \quad (3.65)$$

where

$$Q = -k \left(\frac{\partial \ln \dot{\gamma}}{\partial 1/T} \right)_\tau = -T v \left(\frac{\partial \tau}{\partial T} \right)_\gamma \quad (\text{Structure} = \text{Const.}) \quad (3.66)$$

$$\alpha_1 = -\frac{T}{\mu} \frac{d\mu}{dT} \quad (3.67)$$

and

$$v = - \left(\frac{\partial \Delta G}{\partial \tau} \right)_T = kT \left(\frac{\partial \ln \dot{\gamma}}{\partial \tau} \right)_T = ab \quad (\text{Structure} = \text{Const.}) \quad (3.68)$$

Q is the activation enthalpy at constant stress, ΔH_τ , and is often called an apparent activation energy; v is often called an apparent activation volume, since it has the dimension of a volume. a is the so-called apparent activation area. For a random array of discrete obstacles, the (true) activation volume v^* is related to v by (Refs. 111,122).

$$v^* = b \ell^* x^* = (3/2) v \quad (3.69)$$

where $x^*(=x_2 - x_1)$ is the activation distance. Similarly the (true) activation area a^* is given by

$$a^* = \ell^* x^* = (3/2) a \quad (3.70)$$

To obtain the value of ΔG one needs to know its temperature dependence in addition to the values of the parameters of Eqs. 3.66-3.68. Two assumptions are generally made in this regard: (a) ΔG is independent of temperature, i.e. $\left. \frac{\partial f_i^*}{\partial T} \right|_{f,x} = 0$;

and (b) ΔG is proportional to the shear modulus μ , i.e. $\left. \frac{\partial f_i^*}{\partial T} \right|_{f,x} = \frac{\alpha f_i^*}{T}$, where f_i^* is proportional to the shear modulus. In the former case, $\Delta S^* = 0$ and

$$\Delta G^0 = \Delta H^* \quad (3.71)$$

In the latter, an entropy factor results from the temperature dependence of the modulus and (Refs. 122,128)

$$\Delta G^\mu = \frac{Q - \alpha_1 v \tau}{1 + \alpha_1} \quad (3.72)$$

Worthy of mention at this point is that ΔH^* and ΔG can be obtained directly from tensile tests on single or polycrystals without a knowledge of the orientation factor M , since a cancellation of M occurs in the product $v\tau$ and $v\tau^*$. Also, it is seen from Eq. 3.72 that when ΔG is proportional to the modulus there is no need to separate the flow stress into a thermal and athermal component to obtain the Gibbs free energy of activation. Moreover, for this case Eq. 3.72 still gives ΔG^H even though γ_0 varies with τ and T , providing γ_0 is only a function of τ/μ (Ref. 129).

A force-activation distance curve for the dislocation-solute atom interaction can also be derived from the experimental data. The force f_i^* is given by Eq. 3.19 and the activation distance $x^*(=x_2 - x_1)$ is obtained from the apparent activation volume v through Eq. 3.69. The total work done by the applied stress during the thermally activated overcoming of the obstacle is

$$W = f^* x^* = \tau b \ell x^* = \frac{3}{2} \tau v \quad (3.73)$$

The work done by the effective stress is

$$W^* = f^* x^* = \tau^* b \ell x^* = \frac{3}{2} \tau^* v \quad (3.74)$$

Since according to Eq. 3.57 ΔG is constant for a constant strain rate and temperature, we see from Fig. 3.8 that W and W^* are also constant. Eqs. 3.73 and 3.74 thus give τ and τ^* proportional to $1/v$ for a constant strain rate and temperature.

Spectrum of Obstacles:

The thermally activated motion of dislocations in the presence of a spectrum of obstacles of differing strengths has been treated theoretically by Frank (Refs. 130, 131). All of the parameters in the general equations derived by him have to be determined theoretically, or by other means, and then introduced into the equations to compare the actual behavior of the material with what is theoretically predicted. The interesting conclusion which nevertheless comes out of his analysis is that an Arrhenius-type rate equation is still followed. One merely needs to replace ΔG for a single set of obstacles with an appropriate average ΔG for the spectrum.

Kocks, Argon and Ashby (Ref. 101) have considered the case where the flow stress is given by the sum of two separate obstacles, i.e.

$$\tau = \tau_1 + \tau_2 \quad (3.43a)$$

Taking the derivative of Eq. 3.43a with respect to ΔG at a fixed obstacle spacing gives

$$\left. \frac{\partial \tau}{\partial \Delta G} \right|_{\ell, T} = \left. \frac{\partial \tau_1}{\partial \Delta G} \right|_{\ell, T} + \left. \frac{\partial \tau_2}{\partial \Delta G} \right|_{\ell, T} \quad (3.75)$$

which upon considering Eq. 3.68 leads to

$$\frac{1}{v} = \frac{1}{v_1} + \frac{1}{v_2} \quad (3.76)$$

By changing the concentration of one obstacle we obtain

$$\tau_1 = \tau(\ell_1) - \tau_2 \quad (3.77)$$

and substituting this relation along with Eq. 3.73 into Eq. 3.75 gives

$$\frac{1}{v(\ell_1)} = \frac{1}{v_2} + \frac{3}{2} \left\{ \frac{[\tau(\ell_1) - \tau_2]}{W_1(T, \dot{\gamma})} \right\} \quad (3.78)$$

If τ_2 is a long-range internal stress, then $1/v_2 = 0$ and a plot of $1/v(\ell_1)$ versus $\tau(\ell_1)$ will yield a straight line of slope $3/(2W_1)$, and intercept on the stress axis proportional to the shear modulus μ (Fig. 3.9a). When τ_2 is proportional to τ_1 , the straight line passes through the origin. This occurs when dislocations are both the short-range and the long-range obstacles and leads to the Cottrell-Stokes Law. When τ_2 has a stronger temperature dependence than the modulus, i.e. when it represents a short-range obstacle (e.g. a lattice friction stress) a plot of $1/v(\ell_1)$ versus $\tau(\ell_1)$ yields straight lines whose intercepts show a stronger temperature dependence than μ . Also, the intercepts no longer represent τ_2 (see Fig. 3.9b).

When both v_1 and v_2 represent discrete obstacles, the contributions from each set to the flow stress and the activation volume can be determined by varying the concentration of each separately. Eq. 3.78 applies to the first set and a similar equation can be written for the second set, namely

$$\frac{1}{v(\ell_2)} = \frac{1}{v_1} + \frac{\tau(\ell_2) - \tau_1}{2/3W_2} \quad (3.79)$$

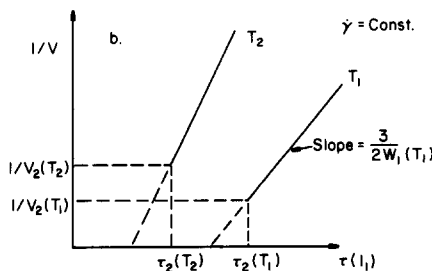
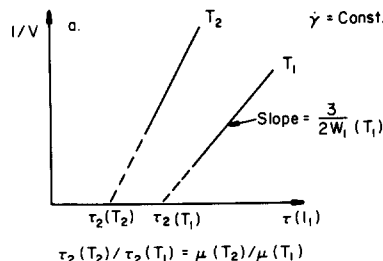


Fig. 3.9. Schematic of $1/v$ versus applied stress τ for discrete obstacles plus: (a) long-range internal stress (b) lattice friction stress.

Plots of Eqs. 3.78 and 3.79 as applied to two sets of discrete obstacles are depicted in Fig. 3.10. It follows that the stress at the intersection of the two straight lines is equal to $\tau_1 + \tau_2$ and that $\tau_1/\tau_2 = Y_2/|Y_1|$ and $V_1/V_2 = X_1/|X_2|$. As pointed out by Kocks, Argon and Ashby (Ref. 101), a particularly useful application of this technique is for separating the relative effects of forest dislocations from other obstacles. When a variation in strain (and presumably thereby the forest dislocation spacing) gives a straight line which does not go through the origin, then there must be other obstacles. When the intercept on the stress axis is negative, these are more subject to thermal activation than the forest dislocations; when it is positive, they are less sensitive.

Additional Comments:

The treatment presented above is for the thermally activated overcoming of randomly dispersed discrete obstacles in contact with a dislocation. Along similar lines, Friedel (Ref. 77) has analyzed the case in which ΔG represents the gain in free energy as a dislocation segment leaves one solute atom to move to the next and during the process straightens from the zig-zag configuration imposed upon it by the pinning solute atoms. Labusch, Grange, Ahearn and Haasen (Ref. 132) have treated the more complicated case when fluctuations in solute atom distribution lead to multiple solute atom ("effective") obstacles. Their treatment yields a plateau in the yield stress versus temperature curve at higher temperatures and gives a $C^{2/3}$ dependence at all temperatures.

The macroscopic plastic deformation parameters generally used to determine the atomic thermal activation parameters are the three deformation partials $(\partial \ln \dot{\gamma} / \partial T)_T$, $(\partial \ln \dot{\gamma} / \partial \tau)_T$ and $(\partial \tau / \partial T)_\gamma$ obtained at a constant microstructure (crystal defect structure). These partials are related through

$$\left. \frac{\partial \ln \dot{\gamma}}{\partial \tau} \right|_T \cdot \left. \frac{\partial \tau}{\partial T} \right|_\gamma \cdot \left. \frac{\partial T}{\partial \ln \dot{\gamma}} \right|_\tau = -1 \quad (3.80)$$

The equations which yield the relevant thermal activation parameters from the deformation partials depend on the details of the thermally activated event under consideration. If these details are not known, then all we can obtain are "apparent" parameters, such as $\Delta H_t(Q)$, v , ΔG^U (given by Eqs. 3.66, 3.68 and 3.72 respectively)

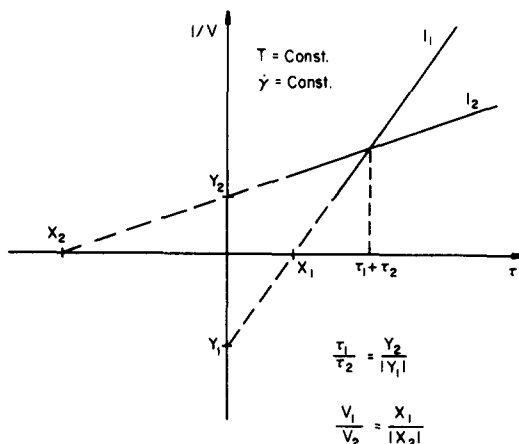


Fig. 3.10. Schematic of $1/V$ versus applied stress τ for two sets of discrete obstacles.

and $\Delta H_{\tau^*} = Q - \alpha_1 v \tau_{\mu}$. ΔG^H is unique in that it will represent the "true" Gibbs free energy if the obstacle strength is proportional to the modulus.

3.3.2 Intermediate Temperatures: Moving Dislocations and Mobile Interstitial Solutes

The mean atomic jump time for interstitial solutes in titanium is given by

$$t_j \approx b^2/D = b^2/D_0 \exp - Q_D/kT \quad (3.81)$$

where D is the diffusion coefficient. From Table 2.6 we obtain $Q_D \approx 26T_m$ (cal/mole) for carbon, nitrogen and oxygen in titanium, where T_m is the melting temperature in °K. Taking this value for Q_D and taking $D_0 = 10^{-1} \text{ cm}^2 \text{s}^{-1}$, we obtain $T_s = 0.4T_m$ (775K) for the temperature at which the mean jump time is one second, i.e. the temperature where the migration of these interstitial solutes first occurs at a significant rate. Since Q_D for hydrogen is about one-quarter that for the other interstitial solutes, T_s for this solute occurs at about $0.1T_m$. In the vicinity of these temperatures, the respective interstitial solutes will be sufficiently mobile that they can no longer be considered as stationary obstacles and plastic deformation will reflect the interaction between moving dislocations and mobile interstitial solute atoms, resulting in the behavior known as dynamic strain aging. Some of the phenomena associated with dynamic strain aging include (Ref. 133): (a) serrations in the stress-strain curves, (b) an increased rate of strain hardening, (c) a low positive, or even negative, strain rate sensitivity and (d) a decrease in the uniform and total elongations. The fact that the obstacles to dislocation motion are themselves mobile adds additional complexity to the problem of deriving the flow stress.

Dynamic strain aging is generally explained in the following manner:

1. During the time a dislocation is held up at some obstacle it collects by the process of diffusion an atmosphere or cloud of solute atoms around it.
2. The atmosphere exerts a strong resisting (pinning) force on the dislocation opposing its continued motion. The resisting force depends on the strength of the interaction per solute atom and the degree of saturation of the atmosphere.
3. Having attained a critical saturation, to continue its motion the dislocation must either break away from the atmosphere or the atmosphere must diffuse along with the dislocation. If neither occurs sufficiently rapid, new dislocations must be generated from other sources for plastic flow to continue. A drop in stress will occur following either the break-away or the generation of new dislocations due to the sudden higher density of mobile dislocations which results.
4. Repeated pinning and break-away (or multiplication) produce serrations in the stress-strain curve, which disappear at higher temperatures when the mobility of solute atoms becomes sufficiently high that they can easily move along with the dislocation at the velocity needed to meet the imposed strain rate, or when they evaporate from the dislocation.
5. An increase in strain hardening results from the additional dislocations generated during the multiplication process.

6. The decrease in uniform elongation and total elongation are related to the inhomogeneous nature of the break-away or multiplication processes, and to the low strain rate sensitivity of the flow stress. Existing theoretical treatments of some of these features will now be considered.

Collection of the Atmosphere:

If we assume that a critical concentration C_1 of solute atoms is required to pin a dislocation, then the time t_a required for an atmosphere with this concentration to form about a dislocation is (Ref. 77)

$$t_a = \frac{kTb^2}{n(n+2)DF_0^*} \left(\frac{C_1}{C_0} \right)^{\frac{n+2}{2}} \quad (3.81)$$

where C_0 is the concentration of solute atoms far away from the dislocation, D the diffusion coefficient of the solute, F_0^* the maximum interaction free energy (attractive) and n a constant, where n = 1 for size effects and n = 2 for differences in elastic constants. Pinning of mobile dislocations is then expected to occur when the waiting time t_w of a dislocation at some obstacle is equal to, or greater than, t_a . The waiting time is related to the velocity \dot{x} of the dislocation through

$$\dot{x} = A/\lambda^* t_w \quad (3.82)$$

where A is the area of the slip plane swept out per successful thermal fluctuation and λ^* is the average spacing of solute atoms along the dislocation. Since the strain rate is related to the average dislocation velocity through Eq. 3.53, the strain rate at which dynamic strain aging is expected to occur is then

$$\dot{\gamma} \leq \left(\frac{A}{\lambda^*} \right) \frac{n(n+2)DF_0^*}{kTb^2} \left(\frac{C_0}{C_1} \right)^{\frac{n+2}{2}} \quad (3.83)$$

Breaking Away From the Atmosphere:

Friedel (Ref. 77) has shown that the escape of a dislocation from a non-saturated atmosphere is given by

$$\dot{\gamma} = \frac{\rho b A v^*}{\lambda^*} \exp - \left[\frac{F_0^* - \sigma b^2 \lambda^*}{kT} \right] \quad (3.84)$$

where A is the area of the slip plane swept out before stopping and λ^* is the distance between pinning points along the dislocation:

$$\lambda^* = \frac{b}{C_0} \exp - \left[\frac{F_0^*}{kT} \right] \quad (3.85)$$

Dislocation Multiplication:

Detailed expressions for the density of mobile and immobile dislocations which result from the repetitive pinning and breaking-away (or multiplication from other sources) and the effects these have on the flow stress have not yet been developed. However, Bergstrom and Roberts (Refs. 134,135) have analyzed dynamic strain aging

in mild steel in terms of the parameters of the equation for the total dislocation density ρ produced during straining

$$\rho = \frac{B-A}{\phi} (1-e^{-\phi\epsilon}) + \rho_0 e^{-\phi\epsilon} \quad (3.86)$$

where B is the rate at which mobile dislocations are immobilized, A the rate at which they are annihilated, ϕ the probability for the remobilization or annihilation of immobile dislocations and ϵ is the true strain. The flow stress is then obtained from the commonly observed relation

$$\tau = \tau_f + \alpha \mu b \rho^{1/2} \quad (3.87)$$

where τ_f includes the contribution of all obstacles to dislocation motion other than dislocations themselves and α is a constant of the order of 0.1 - 0.5.

Disappearance of Dynamic Strain Aging:

Dynamic strain aging will disappear if either the solute atom atmosphere evaporates and no longer saturates the dislocations, or if it diffuses sufficiently fast that it no longer stops the dislocations. The temperature for the former condition is (Ref. 77)

$$T_c \geq \frac{F_0^*}{k \ln(C_0/C_1)} \approx \frac{F_0^*}{k \ln C_0} \quad (3.88)$$

while for the latter (Ref. 77) it is obtained from

$$\dot{\gamma} \leq \frac{2\rho b D}{\ell^*} \sinh \left[\frac{\tau b^2 \ell^*}{kT} \right] \quad (3.89)$$

Eq. 3.89 is based on the model depicted for position 1 in Fig. 3.11 where with the help of the applied stress a solute atom jumps forward a distance b from B into B' . The hyperbolic sine results from taking into account both forward and backward jumps. Again ℓ^* is the spacing between the solute atoms along the dislocation and is given by Eq. 3.85. For small stresses Eq. 3.89 reduces to

$$\dot{\gamma} \leq \frac{2\rho D b^3 \tau}{kT} \quad (3.90)$$

giving a strain rate proportional to the stress and independent of the concentration of the solute forming the atmosphere.

Sweeping of Solute Atoms:

The considerations of Sec. 3.1 indicate that the interaction energy between interstitial solutes and dislocations in titanium could be positive and hence that the solute atoms are repelled from the dislocations rather than being attracted. If this is actually the case, then the collection of solute atoms by the dislocations must occur by some means other than by the diffusion of the solutes to them under the driving force of a negative interaction energy. One possibility for this is that if the waiting time t_w is larger than the mean jump time t_j , then the solute under the applied force will jump into a site ahead of the dislocation (Fig. 3.11, position 1). If this is repeated a sufficient number of times, the dislocation will sweep up solute atoms along its length as it moves across the slip plane, thereby decreasing the spacing ℓ^* between the solute atoms along the dislocation

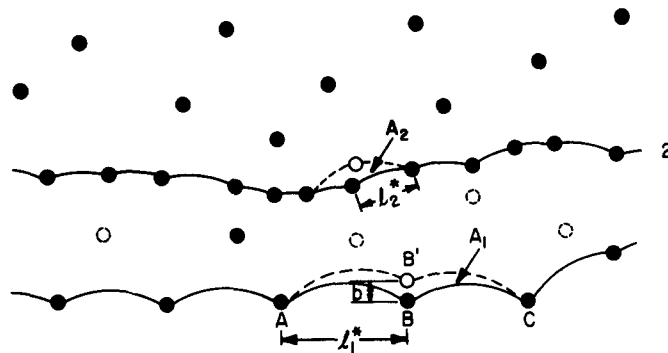


Fig. 3.11. Dislocation motion at temperatures where the solute atoms are mobile. Position 1, forward motion of the dislocation controlled by jump of solute atom from position B to B'. Position 2, dislocation has collected an atmosphere by sweeping solute atoms from the area of the slip plane between positions 1 and 2.

and in turn the area swept out each time a solute jump occurs (e.g. position 2, Fig. 3.11). Both factors lead to a decrease in the dislocation velocity for a given applied stress. The dislocation will then gradually slow down until either break-away or the generation of additional dislocations takes place to maintain the strain rate, similar to the situation discussed above for attractive interactions. Likewise, strain aging will disappear when the rate of diffusion is sufficiently high that the solutes can keep pace with the dislocation velocity required for the imposed strain rate at the existing mobile dislocation density. It is expected that an equation similar to Eq. 3.89 will describe this dislocation "pushing" behavior except that λ will be determined by the area of the slip plane over which the dislocation has moved and will soon have a magnitude approaching b . Moreover, each trailing dislocation will encounter a much lower density of obstacles and hence will pile-up behind the lead dislocation, causing a stress concentration which will help the lead dislocation to break away from its "atmosphere".

3.3.3 High Temperatures: Moving Dislocations and Rapidly Moving Interstitial Solutes

Bird, Mukherjee and Dorn (Ref. 136) have shown that the deformation of metals at high temperatures can generally be represented by the dimensionless equation

$$\frac{\dot{\gamma}kT}{D\mu b} = A \left(\frac{\tau}{\mu} \right)^n \quad (3.91)$$

where D is the appropriate diffusivity coefficient and A and n are constants depending upon the particular controlling mechanism. Values of A and n derived for various high temperature deformation mechanisms are listed in Table 3.5.

TABLE 3.5. Diffusion Controlled Deformation Mechanisms Applicable to Titanium

Mechanism	A	n	Ref
Glide and Climb	3×10^5	4.5	a
Subgrain Climb (Blum)	1.4×10^4	4	b
Subgrain Climb (Ivanov & Yanuskevich)	1.4×10^{-4}	3	c
Subgrain Nabarro-Herring	1.2×10^{-2}	3	d
Subgrain Creep for Pile-up	2.1×10^2	3	d
Nabarro	2.2×10^{-1}	3	a
Nabarro-Bardeen-Herring	$\{12\pi\ln(\frac{8}{\pi}\frac{\mu}{\sigma})\}^{-1}$	3	e
Viscous Glide	5×10^{-1}	3	f
Jogged Screw	$2\ell_j/b$	3	g

Notes: μ = shear modulus; σ = tensile stress; ℓ_j = mean jog separation;
b = Burgers vector

References:

- a. J. Weertman, Trans. ASM 61, 681, 1968.
- b. W. Blum, Phys. Stat. Sol. (b) 45, 561, 1971.
- c. L. T. Ivanov and V. A. Yanushkevich, Phys. Met. Metallog. 17, 102, 1964.
- d. J. Weertman, Rate Processes in Plastic Deformation of Materials, ASM, Cleveland, 315, 1975.
- e. F. R. N. Nabarro, Phil. Mag. 16, 231, 1967.
- f. J. E. Bird, A. K. Mukherjee and J. E. Dorn, Quantitative Relation Between Properties and Microstructure, Israel Univ. Press, 255, 1969.
- g. G. B. Gibbs, Mat. Sci. Eng. 4, 313, 1969.

4. EXPERIMENTAL RESULTS

4.1 Single Crystals

4.1.1 {10\bar{1}0} <11\bar{2}0> Prism Glide

Most of the studies on the deformation of titanium single crystals have been on this slip system, as it is the one which occurs easiest.

Stress-Strain Behavior:

The effect of temperature in the range of 78 to 723K on the resolved shear stress τ - resolved shear strain γ curves for prism slip in zone-refined titanium crystals is shown in Fig. 4.1. The three stages generally observed for the plastic deformation of metal single crystals are evident, namely an initial, approximately linear stage of small slope (Stage I), which is followed by a region of appreciably more rapid strain hardening (Stage II), leading to a region of decreasing hardening with further strain (Stage III). The strain hardening coefficient $\theta = d\tau/d\gamma$ for

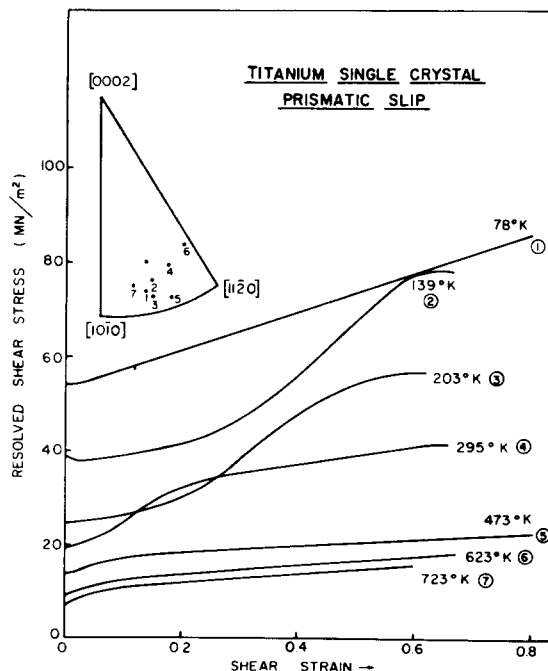


Fig. 4.1. Resolved shear stress versus resolved shear strain curves for prism slip in zone-refined Ti single crystals deformed at an initial unresolved strain rate of $1.66 \times 10^{-4} \text{ s}^{-1}$. From Akhtar and Tehtsoonian (Ref. 137).

Stages I and II and the strain at which Stage II begins reported by Aktar and Tehtsoonian (Ref. 137) are listed in Table 4.1. It is noted that θ_I/μ (where $\mu = \sqrt{K_e K_s}$) increases with increase in temperature, whereas θ_{II} is relatively independent of temperature. Further, the strain at which the transition from Stage I to Stage II occurs, $\gamma_{I \rightarrow II}$, decreases with increase in temperature. In another investigation (Ref. 138), the titanium crystals were oriented to give maximum shear stress on the prism plane and the effect of temperature on θ was determined on one crystal by employing temperature-cycle tests. For these conditions, θ_I is of similar magnitude as that by Aktar and Tehtsoonian (Ref. 137), but relatively independent of temperature; see Fig. 4.2. Also included in Fig. 4.2 is the value of θ_I at 300K determined by Brehm and Lehr (Ref. 139). The θ_I values by Tanaka and Conrad (Ref. 138) and Brehm and Lehr (Ref. 139) given in Fig. 4.2 are the minimum values they reported. Other crystals exhibited θ_I values up to five times larger. No significant effect of interstitial content on θ_I was found (Refs. 14,139).

Although Tanaka and Conrad (Ref. 138) found θ_I to be relatively independent of temperature between 78 and 650K (Fig. 4.2), other tests by them starting at 4.2K gave θ_I significantly higher at this temperature compared to 78K; i.e. θ_I increased markedly below 78K.

The stress for the onset of Stage III decreases with increase in temperature (Fig. 4.1) and with decrease in strain rate, Fig. 4.3. It was found (see Fig. 4.4

TABLE 4.1. Strain Hardening Parameters for $\{10\bar{1}0\} <11\bar{2}0>$ Glide
in Titanium. From Aktar and Tehtsoonian (Ref. 137).

Temp. °K	θ_I/μ^+	$\gamma_{I \rightarrow II}^{++}$	θ_{II}/μ^+
78	3.75×10^{-4}	>1.1	----
139	4.18×10^{-4}	0.29	21.3×10^{-4}
~200	4.31×10^{-4}	0.21	25.5×10^{-4}
295	7.34×10^{-4}	0.06	19.2×10^{-4}
423	8.78×10^{-4}	0.03	19.3×10^{-4}

Notes: $\mu = \sqrt{K_e K_s}$

$\gamma_{I \rightarrow II}^{++}$ = extent of easy glide

[†]Since the detailed mechanism of strain hardening is not known, the geometric average of the modulus coefficients K_e (edge) and K_s (screw) for prism slip is here employed. In titanium this geometric average has nearly the same value as the arithmetic average, $(K_e + K_s)/2$.

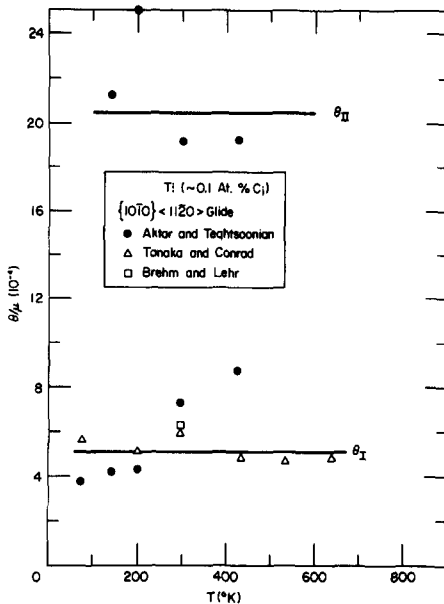


Fig. 4.2. Effect of temperature on the strain hardening coefficients θ_I and θ_{II} for Stages I and II of prism slip in zone-refined Ti. $\mu = \sqrt{K_e K_s}$. Data from Refs. 137-139.

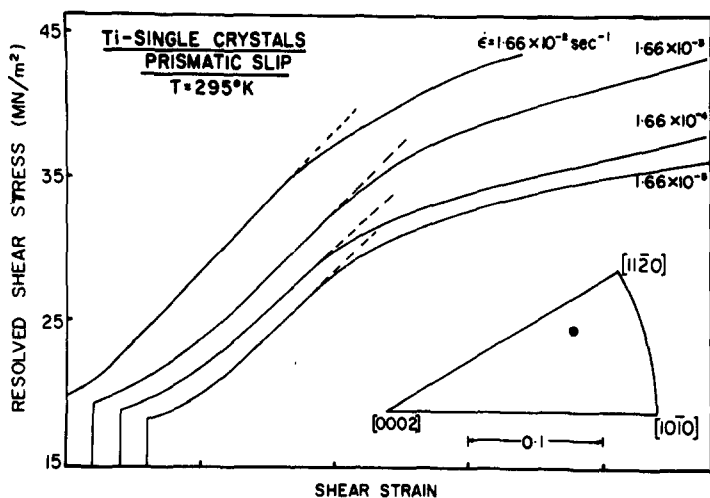


Fig. 4.3. Effect of strain rate on the stress τ_{III} at which Stage III first occurs during prism slip in Ti. From Akhtar and Techtsoonian (Ref. 137).

and 4.5) that τ_{III} is well described by the equation for thermally activated cross-slip (Refs. 140,141), namely

$$\ln \tau_{III}(T, \dot{\gamma}) = \ln \tau_{III}(0) - \frac{kT}{A} \ln (\dot{\gamma}_0 / \dot{\gamma}) \quad (4.1)$$

where $\tau_{III}(0)$ is the value of τ_{III} at 0K and $\dot{\gamma}_0$ and A are material constants.

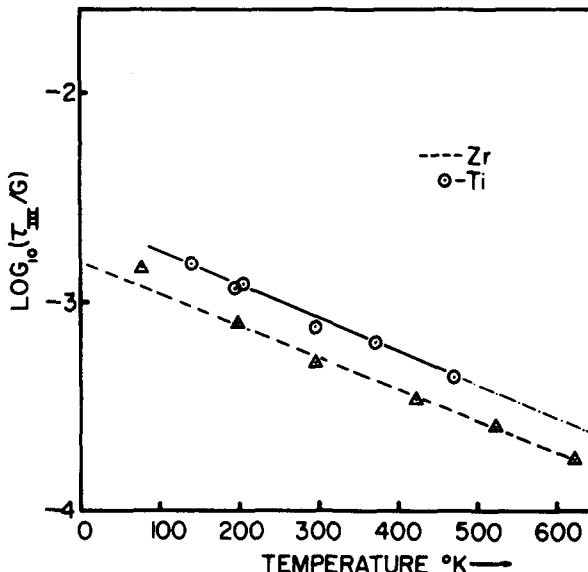


Fig. 4.4. Effect of temperature on τ_{III} for prism slip in Ti and Zr. $G = \sqrt{C_{44} \cdot C_{66}}$. From Akhtar and Teightsoonian (Ref. 137).

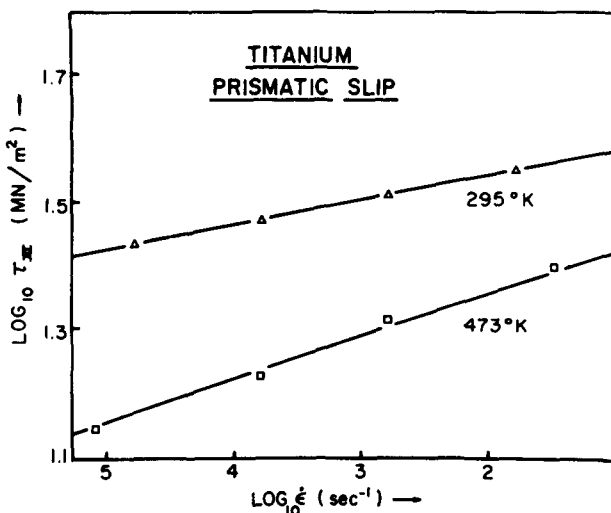


Fig. 4.5. Effect of strain rate on τ_{III} for prism slip in Ti at 295 and 473K. From Akhtar and Teightsoonian (Ref. 137).

Slip Line Appearance, Occurrence of Twinning and Schmid's Critical Resolved Shear Stress Law:

The appearance of the slip lines in Stage I deformation of titanium (Fig. 4.6) is typical of that for easy glide. With increasing strain the spacing between the slip bands decreased. In Stage II, fine slip lines corresponding to the next most highly stressed {1010} plane become evident as well as the primary slip lines, see for example Fig. 4.7. Stage III deformation is characterized by wavy slip lines, Fig. 4.8.

For specimens deformed in tension at 78K and above, no twins were observed in any of the specimens whose orientations were such that prism slip might easily occur (Refs. 137,138). However, even for specimens favorably oriented for prism slip twinning was considered to have occurred for certain orientations at 4.2K (Ref. 138).

Sakai and Fine (Ref. 142) noted for compression tests that Schmid's critical resolved shear stress law did not hold for prism slip in a dilute Ti-Al (0.87 at.%Al) alloy when the compression axis was less than 55 deg. from the c-axis. Further, Akhtar (Ref. 143) showed that twinning and basal slip occur in high purity Ti crystals tested in tension when the c-axis makes an angle of 43 deg. or less with the tensile axis. Hence, a critical resolved shear stress law for prism glide in uniaxial loading is restricted to orientations where the basal plane makes an angle less than 45 deg. with the testing direction, i.e. to orientations with Schmid factors favoring slip on a single prism plane.

Dislocation Structure:

Only limited studies have been made of the dislocation structure in deformed titanium single crystals. The structures observed by transmission electron microscopy (TEM) in sections perpendicular to, and parallel to, an active prism glide plane in a commercially pure titanium specimen deformed in tension at 298K are

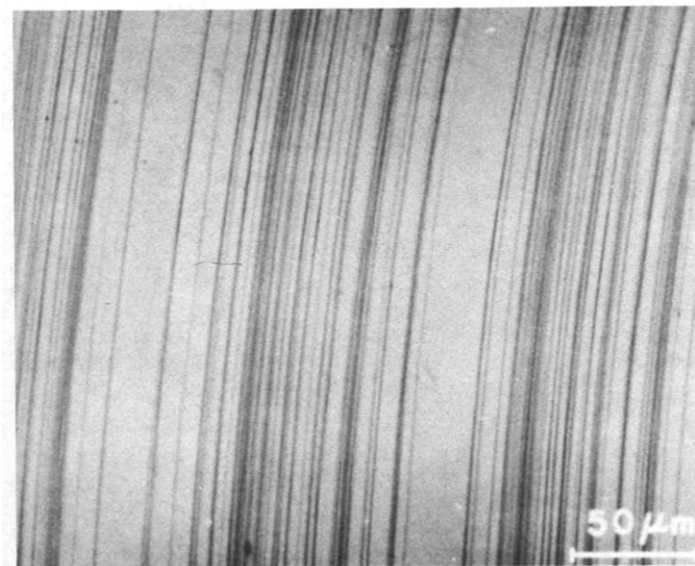


Fig. 4.6. Prism slip lines on the surface of a Ti crystal deformed to a shear strain of 0.015 at 295K. From Akhtar and Teightsoonian (Ref. 137).

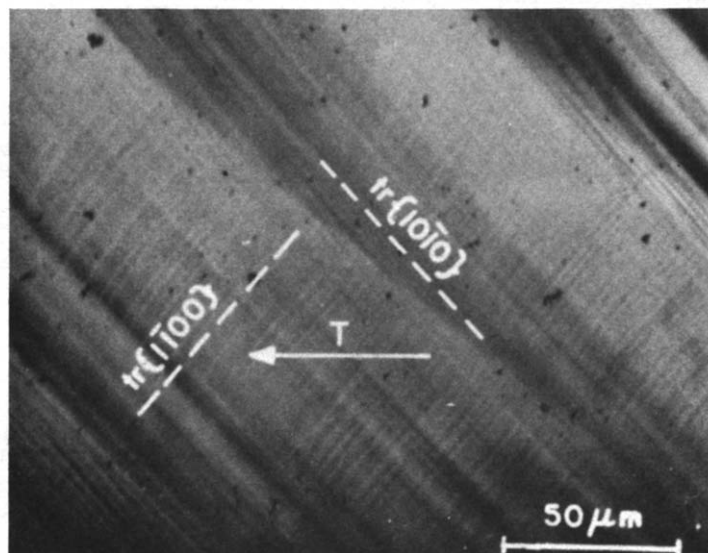


Fig. 4.7. Prism slip markings on a Ti crystal deformed to a shear strain of 0.5 (Stage II) at 133K. Evident are long primary and shorter secondary slip lines. From Akhtar and Teghtsoonian (Ref. 137).

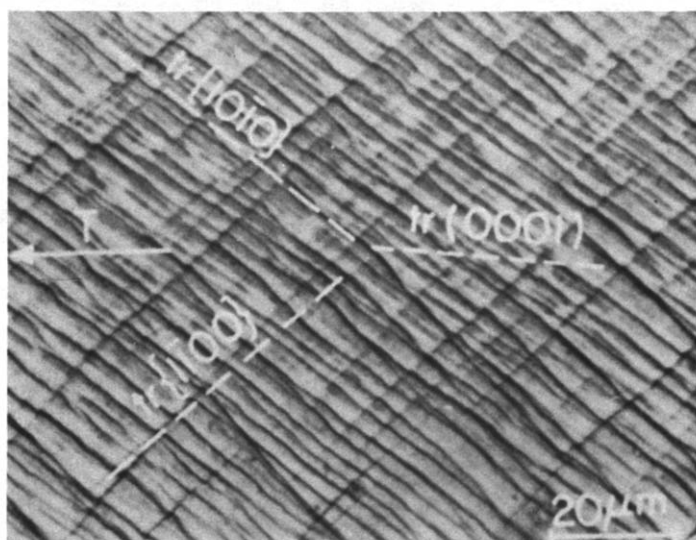


Fig. 4.8. Wavy slip lines on a Ti crystal deformed to a shear strain of 0.65 (Stage III) in prism slip at 295K. From Akhtar and Teghtsoonian (Ref. 137).

shown in Figs. 4.9 and 4.10 respectively. The dislocations are elongated along the <1120> directions; i.e. they are predominantly of screw orientation. These screw dislocations trail a great number of resolvable and presumably unresolvable dipoles. The dislocations were distributed uniformly over the observable area of the foil, their density being of the order of 4×10^8 to $3 \times 10^9 \text{ cm}^{-2}$ for a shear strain of ~0.06 (Refs. 45,144).

The dislocation structure observed in single crystals of dilute Ti-Al (<2 at. % Al) alloys with approximately 0.15 at. % interstitial solutes deformed in prism slip at 298K (Ref. 147) was similar to that described above for commercial titanium, i.e. the dislocations were predominantly of screw orientation with a large number of loops and dipoles. Deformation at lower temperatures resulted in essentially the same structure as at 298K; however, very long dislocation dipoles ~2 μm in length were often seen in crystals deformed at 155K. Deformation at higher temperatures (500K) produced large elongated tangles lying perpendicular to the slip direction and containing a number of dislocation dipoles and elongated loops. Increasing the interstitial content to approximately 0.3 at. % resulted in a dislocation structure which was mainly edge in character and there was less tendency for the dislocations to align along a certain orientation.

Effects of Temperature, Strain Rate and Interstitial Content on the Resolved Shear Stress:

Elssner, Krohn and Ruano (Ref. 145) investigated the effects of interstitial content and temperature on the yield stress (0.1 strain or the lower yield stress) of 1 mm dia. titanium wire specimens with a bamboo structure consisting of single crystals 1-3 mm in length. The Schmid orientation factor for prism slip in the crystals ranged between 0.4 and 0.5. Although they did not establish the operative slip system, it is expected that the primary deformation mode in their specimens

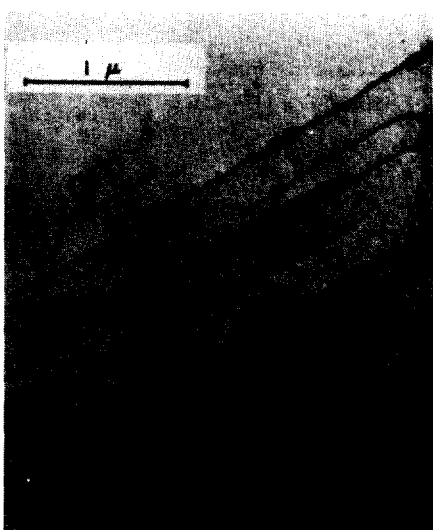


Fig. 4.9. Dislocation structure in a section perpendicular to a prism glide band of a commercially pure Ti crystal deformed 6% at 298K. From Cass (Ref. 45).

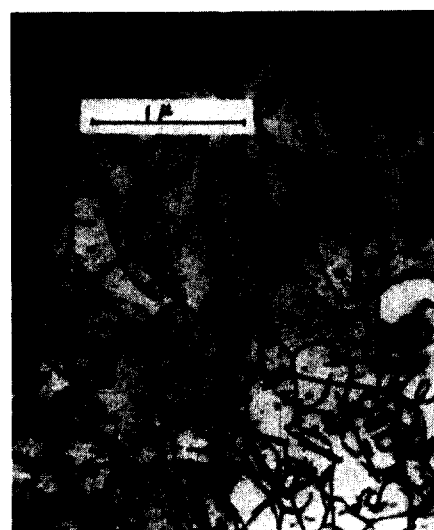


Fig. 4.10. Dislocation structure in a section parallel to a prism glide band of commercially pure Ti crystal deformed 6% at 298K. From Cass (Ref. 45).

was $\{10\bar{1}0\} \langle 11\bar{2}0 \rangle$ glide. A plot of the yield stress versus temperature as a function of oxygen content representing data taken from Elssner, Krohn and Ruano (Ref. 145) is presented in Fig. 4.11. It is here seen that the yield stress increases markedly with interstitial content, the effect becoming larger as the temperature is decreased. Further, a rather sharp change in slope (a kink) occurs in the curves for the two higher oxygen contents at ~250K. Such kinks in the stress versus temperature curves also occurred for zirconium and hafnium specimens with a bamboo structure (Refs. 95,145), the temperature of the kink increasing in the order: Ti, Zr, Hf.

A summary of data in the literature on the effects of temperature and purity on the critical resolved shear stress, τ_{CRSS} , for prism slip in titanium is given in Fig. 4.12. The interstitial contents reported for the materials considered and the τ_{CRSS} at several temperatures are listed in Table 4.2. The curve in Fig. 4.12 representing the highest purity materials has a form similar to that often observed for crystalline solids, namely a plateau in an intermediate temperature region (~600 - 800K for titanium), the stress increasing significantly at lower temperatures and decreasing at higher temperatures, with possibly a second plateau occurring at the highest temperatures. Following Seeger (Ref. 146), one can therefore consider τ_{CRSS} for prism slip below 800K to consist of two components, namely a thermal component τ^* which is sensitively dependent on temperature T and strain rate $\dot{\gamma}$ and an athermal component τ_μ which varies with temperature only as the modulus μ so that

$$\tau_{CRSS} = \tau^*(T, \dot{\gamma}) + \tau_\mu(\mu) \quad T < T_c \quad (C_f = \text{const.}) \quad (4.2)$$

$$\tau_{CRSS} = \tau_\mu \quad T \geq T_c \quad (T_c \approx 600\text{K for Ti}) \quad (4.3)$$

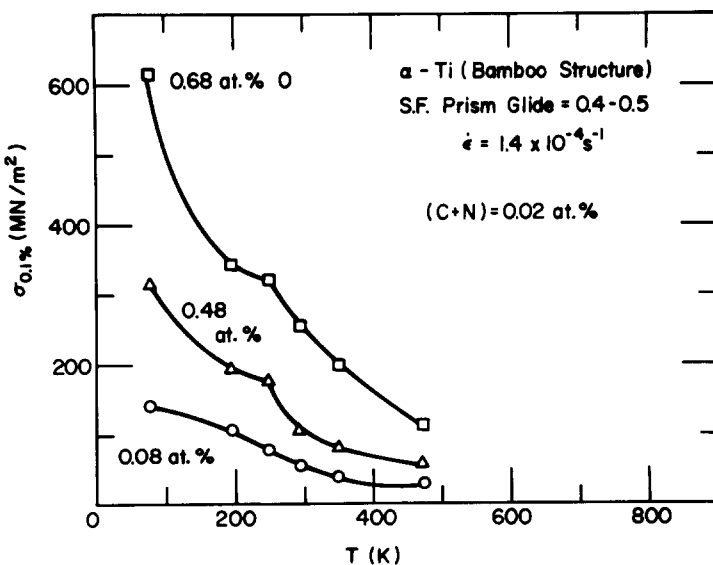


Fig. 4.11. Yield stress versus temperature as a function of oxygen content for Ti wire specimens with a bamboo structure. Data from Elssner, Krohn and Ruano (Ref. 145)

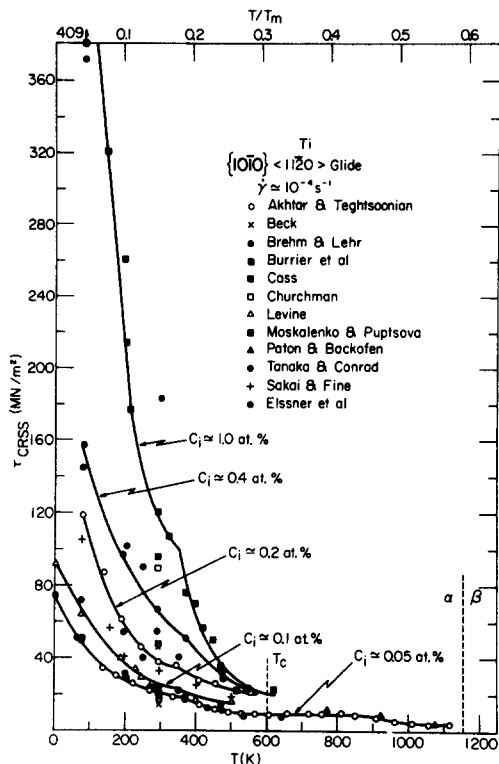


Fig. 4.12. Effects of temperature and interstitial solute content on the critical resolved shear stress for prism slip in Ti. Data from references of Table 4.2.

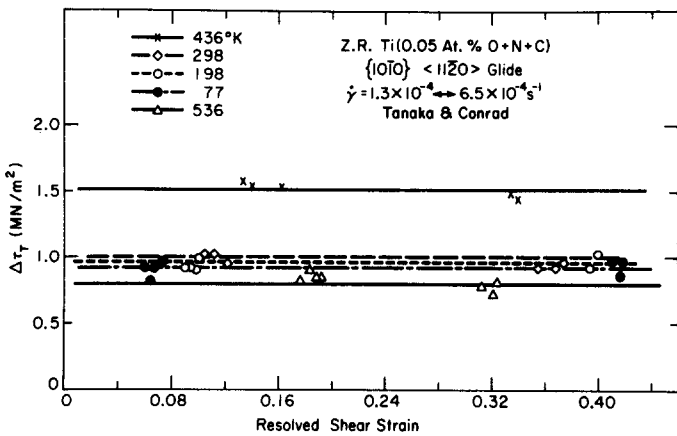


Fig. 4.13. Effect of strain on the change in stress ($\Delta \tau_T$) produced by 5:1 strain rate cycles during prism slip of Ti single crystals at various temperatures. Data by Tanaka and Conrad (Ref. 138).

TABLE 4.2. Effects of Temperature and Interstitial Solute Content on the Critical Resolved Shear Stress for Prism Glide in Titanium

Material	0 ppm [†]	N ppm [†]	C ppm [†]	H ppm [†]	0+N+C at.%	0eq ^{††} at.%	$\dot{\gamma}$ 10^{-4} s^{-1}	τ_{77} MN/m^2	τ_{300} MN/m^2	τ_{500} MN/m^2	Ref.
van Arkel	---	---	---	---	-0.03	-0.03	0.4	---	17.2	---	a
van Arkel	---	---	---	---	-0.3	-0.3	0.4	---	90.1	---	a
MARZ ZR	50	25	50	<0.1	0.04	0.05	26	63.7	19.6	16.2	b
C.P. 75A	2600	170	250	50	0.94	0.97	14	410	---	---	c
Battelle Ti	370	80	40	62	0.15	0.19	1	---	48.3	---	d,e
C.P. Ti	---	---	---	---	-0.3	-0.3	1	---	95.1	---	d
Iodide	200-250	10-15	---	---	-0.07	---	10	---	21.8	11.5	f
Electrolytic	130	84	160	---	0.13	0.14	8.4	51.0	23.5	11.8	g
Electrolytic	320	15	210	---	0.19	0.17	8.4	145	66.6	31.4	g
MARZ ZR	63	6	78	4	0.5	0.5	1.3	50.3	24.2	7.8	h
Ti	---	---	---	---	-0.2	-0.2	5	---	120.5	21.6	i
MARZ ZR	63	6	78	4	0.05	0.05	5	50.0	20.5	10.5	j
Ti	---	---	---	---	-0.15	-0.15	5	120.0	37.8	22.0	j
MARZ ZR	60	35	40	0.1	0.05	0.05	5	---	13.9	---	k
C.P. Ti	665	51	150	2	0.28	0.28	5	---	42.6	---	k
Battelle Ti	(270)	(120)	(170)	---	0.19	0.21	4	102	32.0	18.0	l

Material	0 ppm [†]	N ppm [†]	C ppm [†]	H ppm [†]	O+N+C at.%	0eq ^{††} at.%	$\dot{\gamma}$ 10^{-4} s^{-1}	τ_{77} MN/m^2	τ_{300} MN/m^2	τ_{500} MN/m^2	Ref.
Iodide	580-1800	20	500	---	0.54-0.75	0.50-0.70	10	---	49-115	---	m
MRC, Eching	210-3600	20	40	---	0.09-1.08	0.09-1.09	1	68-350 ^{†††}	23-165 ^{†††}	---	n

Notes: [†] ppm in weight

^{††} 0eq = 1.0 x at. % N + 2.0 x at. % C: H. Conrad, Acta Met. 14, 1631, 1966.

^{†††} Bamboo structure; τ was taken as 0.45 the tensile stress σ .

References:

- a. A. T. Churchman, Proc. Roy. Soc. A226, 216, 1954.
- b. E. Levine, Trans AIME, 236, 1558, 1964.
- c. M. Burrier, M. Amateau and E. Steigerwald, "The Relationship Between Plastic Deformation and Fracture in Alpha Titanium", Rept. AFML-TR-65-239, 1965.
- d. T. R. Cass and W. R. Spencer, "Deformation and Strengthening Mechanisms for Solid Solution Phases of Titanium", Contract No. AF 33(615)-3863, Tech. Repts., Martin Marietta Corp., 1967, 1968.
- e. T. R. Cass, The Science, Technology and Application of Titanium, Pergamon Press, 459, 1970.
- f. N. E. Paton and W. A. Backofen, Met. Trans. 1, 2839, 1970.
- g. C. Brehem and P. Lehr, Mem. Sci. Rev. Metallurg. 68, 277, 1971.
- h. T. Tanaka and H. Conrad, Acta Met. 20, 1019, 1972.
- i. V. A. Moskalenko and V. A. Puptsova, Fiz. Metal. Metalloved. 34, 1264, 1972.
- j. A. Akhtar and E. Tehtsoonian, Met. Trans. 6A, 2201, 1975.
- k. F. H. Beck, "Effect of Hydrogen Content on the Mechanical Properties of Titanium and Its Alloys", NASA-Lewis Grant No. NGL-36-008-051, Ohio State University, 1975.
- l. T. Sakai and M. E. Fine, Acta Met. 22, 1359, 1974.
- m. E. A. Anderson, D. C. Jillson and S. R. Dunbar, Trans. AIME 197, 1191, 1953.
- n. G. Elssner, U. Krohn and O. Ruano, Z. f. Metallkde. 67, 311, 1976.

where both τ^* and τ_μ may depend on structure, i.e. on the type, number and distribution of the crystal defects which are present. As pointed out in Sec. 3.3 the thermal component is also known as the effective stress $\tau^*(=\tau-\tau_\mu)$ and is considered to be associated with short-range (low energy) obstacles to dislocation motion which can be overcome with the aid of thermal fluctuations, whereas τ_μ is considered to be associated with long-range (high energy) obstacles, the overcoming of which is by stress alone.

The results of Fig. 4.12 indicate that interstitial solutes in titanium influence both τ^* and τ_μ for prism slip, the effect on τ^* increasing markedly with decrease in temperature. On the other hand, strain has no significant effect on the temperature dependence of the flow stress, nor its strain rate sensitivity (Refs. 137-139, 147-149) (see, for example, Fig. 4.13), indicating that the effect of strain is primarily on τ_μ , with little, if any, effect on τ^* . One can therefore expand Eq. 4.2 to give for the flow stress for prism slip at temperatures below ~800K

$$\tau \approx \tau^*(T, \dot{\gamma}, C_i) + \tau_\mu(\mu, \gamma, C_i) \quad (4.4)$$

Insufficient data are available at temperatures above 800K to be able to say anything definite about the effects of interstitial solutes on τ in this temperature regime. However, from work on polycrystalline titanium specimens to be discussed below, it appears that the interstitial solutes have little effect on the flow stress at high temperatures ($T > 0.4 T_m$).

Worthy of note regarding Fig. 4.12 is that rather good agreement occurs in the results obtained by the various investigators for the highest purity titanium materials available, which have a total interstitial content of about 0.05 - 0.10 at. %, and which include zone-refined material. On the other hand, the values of τ_{CRSS} by Moskalenko and Puptsova (Ref. 149) suggest a higher interstitial content than the 0.2 at. % reported by them. Of further note regarding Fig. 4.12 is that an abrupt change in slope of the τ_{CRSS} versus temperature curve seems to occur for most compositions at about 350-375K, which is at a higher temperature than for the data of Elssner, Krohn and Ruano (Ref. 145) in Fig. 4.11. Such kinks have also been noted by others (Refs. 98, 150) for zirconium and hafnium single and polycrystals and, as will be seen below, occurs as well for titanium polycrystals.

The effect of oxygen content on the yield stress of the titanium specimens with a bamboo structure is presented in Fig. 4.14. To be noted is that the curve is parabolic at 77K, but is nearly linear at 300K. Further, the rate of solid solution strengthening increases with decrease in temperature. A plot of τ_{CRSS} at 78, 300 and 500K versus the total $O + \{N+C\}$ interstitial content (mainly oxygen) taken from Table 4.2 is given in Fig. 4.15. Included in this plot are the data by Elssner, Krohn and Ruano (Ref. 145) on bamboo specimens, for which a Schmid factor of 0.45 was used to convert the tensile yield stress to the critical resolved shear stress. The values of τ_{CRSS} so obtained agreed (within the scatter of the data) with those obtained by others on larger single crystal specimens. The form of the curves as drawn in Fig. 4.15 is parabolic at all temperatures; however, because of the scatter in the data, the form cannot be positively identified at 300 and 500K. The average values of $\Delta\tau/\Delta C_i$ for C_i in the range of 0.05 to 0.5 at. % are 0.67μ , 0.39μ and 0.17μ respectively for 77, 300 and 500K, taking $\mu = \sqrt{K_e K_s}$. Conversion of the total interstitial content into an oxygen equivalent, O_{eq} (Ref. 151) yielded values for O_{eq} nearly the same as taking $C_i = O + N + C$ (see Table 4.2) and therefore essentially the same values for the solid solution strengthening coefficient $\Delta\tau/\Delta C_i$ were obtained for the two methods of expressing the total interstitial content.

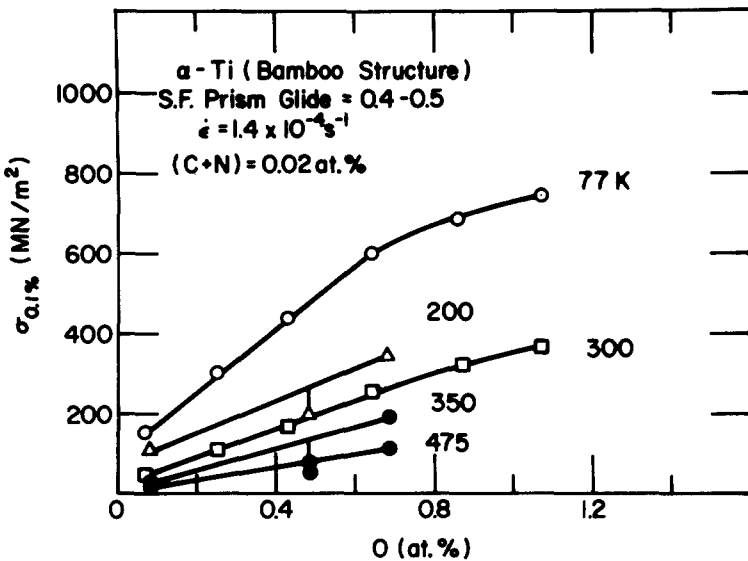


Fig. 4.14. Effect of oxygen on the yield stress of Ti wire specimens with a bamboo structure. Data from Elssner, Krohn and Ruano (Ref. 145).

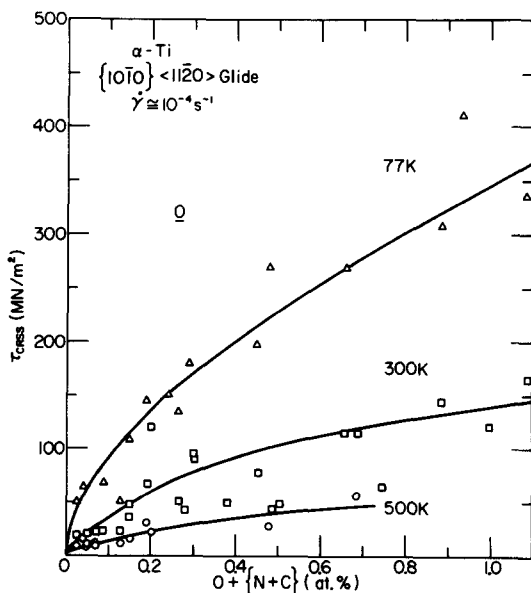


Fig. 4.15. Effect of interstitial content on the critical resolved shear stress for prism slip in Ti at several temperatures. Data from Table 4.2. A Schmid factor of 0.45 was used for data from Elssner, Krohn and Ruano (Ref. 145).

The principal interstitial solute in the materials considered in Figs. 4.14 and 4.15 is oxygen. The influence of nitrogen on the yield stress of bamboo specimens is given in Fig. 4.16, the effect again being parabolic at 77K and nearly linear at 300K. Further, similar to oxygen, the effect of nitrogen on the yield stress increases appreciably with decrease in temperature. The values of $\Delta\tau/\Delta C_1$ (taking $\tau = 0.45\sigma$) for the range of 0.05 - 0.5 at. % N at 77 and 300K are now 0.78μ and 0.53μ respectively, indicating that nitrogen is a more potent strengthener than oxygen.

No definitive data for the effect of carbon on the CRSS for prism slip were found. The effect of hydrogen on τ_{CRSS} at 300K for prism slip in titanium single crystals of two purity levels is shown in Fig. 4.17. The slopes of the straight lines yield $\Delta\tau/\Delta C_1$ equal to 0.18μ and 0.08μ respectively for the low purity and high purity materials. Comparing these values with those for the same composition range in Figs. 4.14, 4.15 and 4.16, we find that the strengthening effect of hydrogen at 300K is about 1/4 to 1/8 that due to oxygen and nitrogen.

The effect of strain rate on the flow stress is often defined by the parameter $\Delta\tau/\Delta\dot{\gamma}\eta$, where $\Delta\tau$ is the change in flow stress associated with a change in strain rate $\dot{\gamma}$. Values of this strain rate sensitivity parameter determined for prism slip by strain rate-cycle tests (Refs. 137-139, 147,148) and by stress relaxation (Ref. 149) are presented in Fig. 4.18 as a function of temperature and interstitial content. Evident is that the strain rate sensitivity of the flow stress increases with increasing interstitial content. Also, there exist humps in the curves, one at about 150K and the other at about 400K (with a minimum at ~300K). Such humps also occur for zirconium and hafnium single and polycrystals (Refs. 69,95,98,150) and for titanium polycrystals to be seen below. Finally, it is to be noted that $\Delta\tau/\Delta\dot{\gamma}\eta$ approaches a value of zero at 0K and at a temperature T_c , which is approximately the same as that (~600K) where $\frac{1}{\tau} \left(\frac{d\tau}{dT} \right)$ first becomes equal to $\frac{1}{\mu} \frac{du}{dT}$ in Fig. 4.12, i.e., where τ^* first becomes zero.

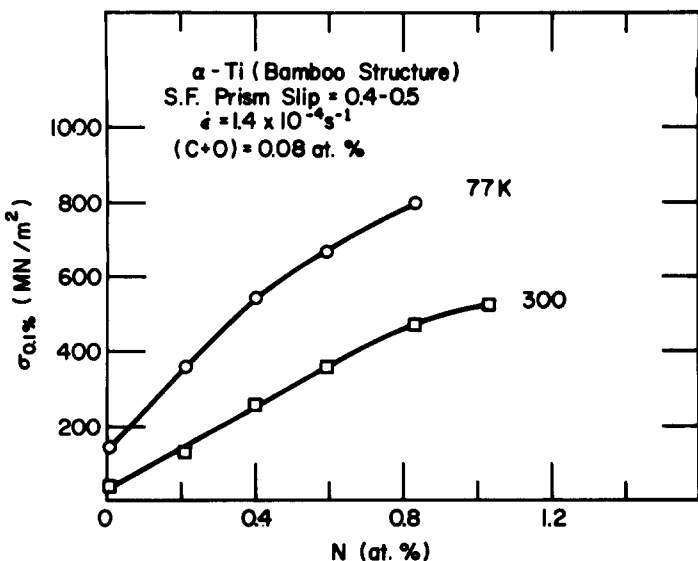


Fig. 4.16. Effect of nitrogen on the yield stress of Ti specimens with a bamboo structure. Data from Elssner, Krohn and Ruano (Ref. 145).

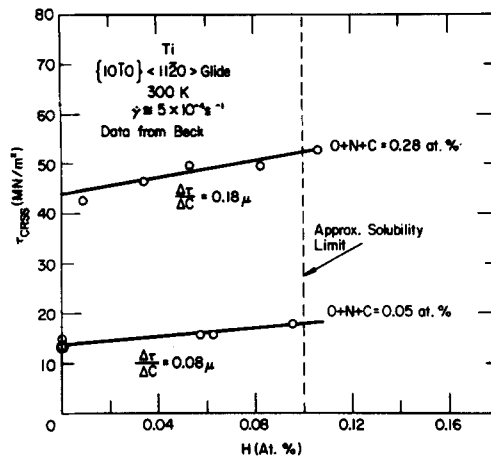


Fig. 4.17. Effect of hydrogen content on the critical resolved shear stress for prism slip in Ti. Data from Beck (Ref. 14).

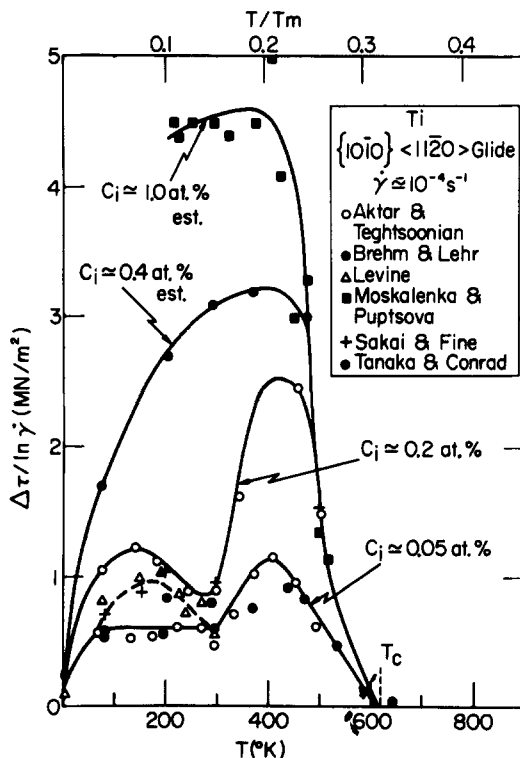


Fig. 4.18. The strain rate sensitivity parameter $\Delta\tau / \Delta \ln \dot{\gamma}$ for prism slip in Ti as a function of temperature and interstitial content. Data from Refs. 137-139, 147-149.

Dislocation Velocity:

Studies were conducted by Tanaka and Conrad (Ref. 152) on the velocity of edge dislocations in zone-refined titanium single crystals ($C_i \approx 0.05$ at. %) oriented for prism slip employing the etch pit technique. The stress required to produce edge dislocation velocities of the order of 10^{-3} cm s $^{-1}$ was found to be approximately the same as the critical resolved shear stress at a strain rate of 10^{-4} s $^{-1}$.

Deformation Kinetics:

The concept of thermally activated deformation discussed in the previous chapter provides a means for evaluating the relationship between the flow stress, strain rate and temperature for prism glide. The two deformation partials important in determining the thermal activation parameters for the plastic flow of single crystals from constant strain rate tests are $(\partial\tau/\partial T)\dot{\gamma}$ and $(\partial\tau/\partial\ln\dot{\gamma})T$. The effect of temperature on the latter has been shown for prism glide in Fig. 4.18, where it is seen that an anomalous behavior occurs in the vicinity of 300K for a total interstitial content of about 0.2 at. % and less. This anomalous behavior also occurs in plots of the apparent activation volume $v (= kT \partial\ln\dot{\gamma}/\partial\tau)$ versus temperature; see Fig. 4.19 (v is here normalized with respect to the Burgers vector b). It is here seen for the lower interstitial content materials ($C_i \leq 0.2$ at. %) that v increases monotonically with temperature to about 300K and then falls sharply with further increase in temperature to about 400K, before increasing again at high temperatures. An anomalous behavior is barely noticeable for interstitial contents greater than about 0.4 at. %; also the maximum in v for the higher interstitial contents occurs

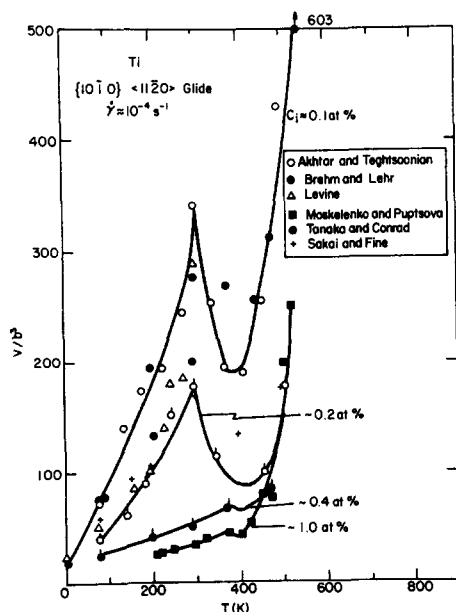


Fig. 4.19. Apparent activation volume versus temperature for prism glide in Ti of various purity levels. Data from references of Table 4.2. The ticks on data points refer to the lower purity materials studied by the referenced authors.

at about 375K rather than 300K. In general, v increases with decrease in interstitial content; however, at ~500K an effect of purity in the range of 0.2 to 1.0 at. % is no longer evident.

The influence of temperature on the deformation partial $(\partial\tau/\partial T)_{\dot{\gamma}}$, obtained by taking the slopes of the τ_{CRSS} versus temperature curves in Fig. 4.12 is presented in Fig. 4.20. In general, $(\partial\tau/\partial T)_{\dot{\gamma}}$ decreases with temperature and with increase in purity level. However, a discontinuity in the curves occurs in the temperature range of 315-420K, the degree or amount of the discontinuity increasing with decrease in interstitial content. Further, the discontinuity tends to occur at a lower temperature as the interstitial content decreases. Also to be noted in Fig. 4.20 is that $(\partial\tau/\partial T)_{\dot{\gamma}}$ becomes essentially zero at ~600K, remains at this value to about 850K; thereafter it increases slightly, reaching a maximum at ~900K before decreasing again at higher temperatures.

A plot of the apparent activation energy $Q (= -T\tau(\partial\tau/\partial T)_{\dot{\gamma}})$ for prism slip derived from the data of Figs. 4.19 and 4.20 is presented in Fig. 4.21. In general, Q increases with temperature, relatively independent of the interstitial content. This is indicated by the solid line through the data points, which represents the average curve of Q versus temperature. However, the results for interstitial contents <0.2 at. % suggest an anomalous temperature dependence of Q in the same temperature region as that for the apparent activation volume v . (This anomalous temperature dependence of Q has also been reported by Akhtar and Tehtsoonian (Ref. 137). The value of Q in the vicinity of 600K is of the order of 2.5-3.0eV.

In addition to $Q (= \Delta H_{\tau})$ and $v (= \partial\Delta G/\partial\tau)$ we are interested in the values of the pre-exponential γ_0 and the entropy $\Delta S_{\tau} (= \partial\Delta G/\partial T|_{\tau})$. Expanding Eq. 3.57 we obtain

$$\Delta G_{\tau} = \Delta H_{\tau} - T\Delta S_{\tau} = kT \ln(\dot{\gamma}_0/\dot{\gamma}) \quad (4.5)$$

Taking $\Delta H_{\tau} = kT^2 (\partial\ln\dot{\gamma}/\partial T)_{\dot{\gamma}} (\partial\tau/\partial T)_{\dot{\gamma}}$, substituting into Eq. 4.5 and rearranging gives

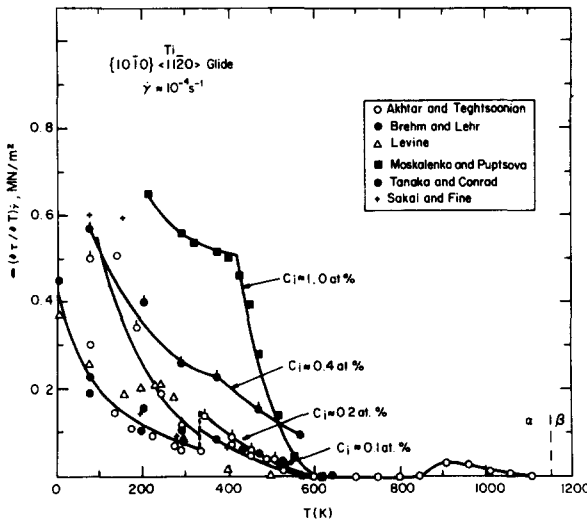


Fig. 4.20. $(\partial\tau/\partial T)_{\dot{\gamma}}$ versus temperature for prism glide in Ti of various purity levels. Data from references in Table 4.2.

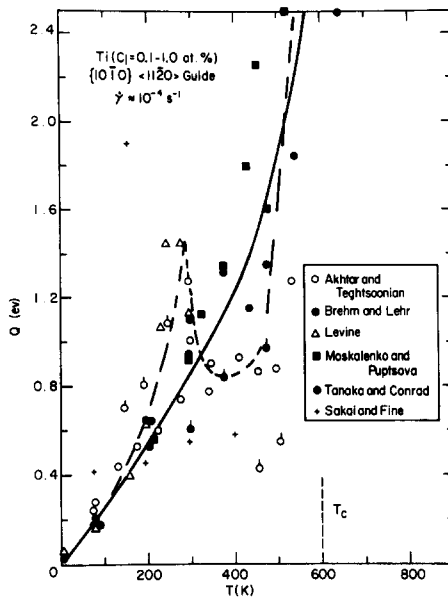


Fig. 4.21. The apparent activation energy versus temperature for prism glide in Ti of various purity levels. Data from references of Table 4.2. Ticks on data points refer to the lower purity materials by the referenced authors.

$$-T \left(\frac{\partial \tau}{\partial T} \right)_\gamma = [\ln(\dot{\gamma}_0 / \dot{\gamma}) + \frac{\Delta S_\tau}{k}] \left(\frac{\partial \tau}{\partial \ln \dot{\gamma}} \right)_T \quad (4.6)$$

If $\dot{\gamma}_0$ and ΔS_τ are constant, then a plot of $-T(\partial\tau/\partial T)_\gamma$ versus $(\partial\tau/\partial \ln \dot{\gamma})_T$ should yield a straight line through the origin of slope $[\ln(\dot{\gamma}_0 / \dot{\gamma}) + (\Delta S_\tau / k)]$. Such a plot is given in Fig. 4.22 for prism slip in the temperature range of 4.2 - 535K. The results scatter about a straight line of slope 36.5, which, if our assumptions are correct, provides the value of the sum of the two terms in the brackets. Further separation of $\dot{\gamma}_0$ and ΔS_τ is only possible with a knowledge of the temperature dependence of ΔG .

4.1.2 (0001) <11-20> Basal Glide

Stress-Strain Behavior:

Basal slip has been reported for specimens tested in shear along the basal plane (Refs. 148,153) and in axial loading for specimens oriented such that the basal plane makes an angle of ~50-72 deg. with the tensile axis (Refs. 143,147,153,154). Resolved shear stress versus resolved shear strain curves observed for basal glide in zone-refined titanium deformed in tension are given in Fig. 4.23. They are parabolic at the lower temperatures; however, strain hardening decreases with increase in temperature, leading to essentially no strain hardening at 1023K.

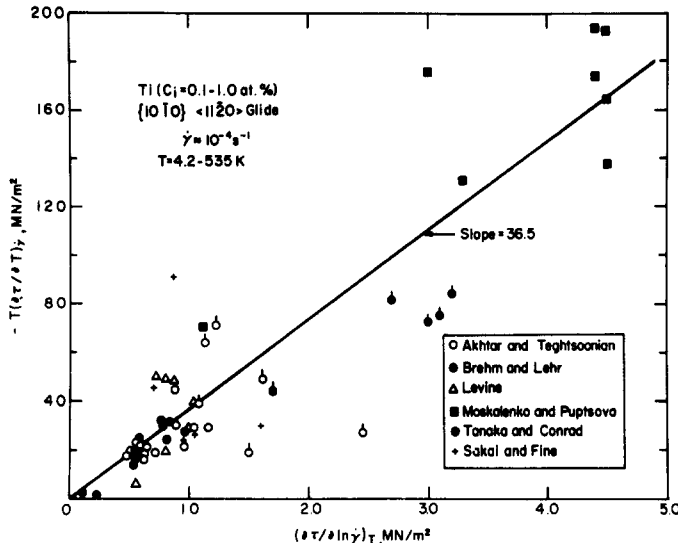


Fig. 4.22. $-T(\partial\tau/\partial T)_\gamma$ versus $(\partial\tau/\partial \ln\dot{\gamma})_T$ for prism glide in Ti of various purity levels. Data from references in Table 4.2.

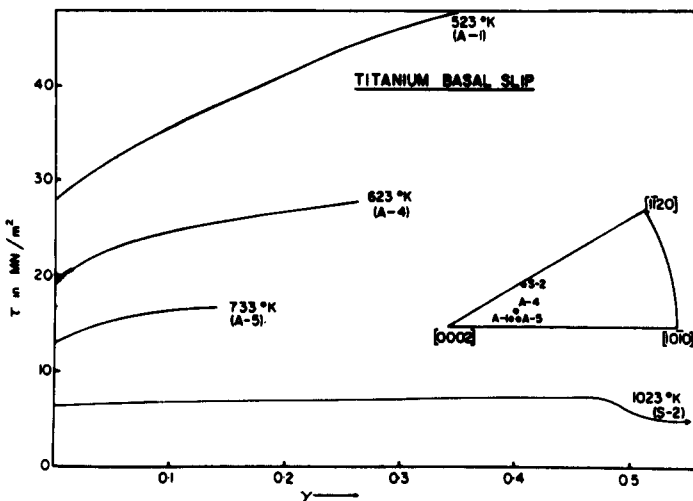


Fig. 4.23. Resolved shear stress versus shear strain curves for basal glide in Ti crystals. From Akhtar (Ref. 143).

Slip Line Appearance and Dislocation Structure:

The appearance of slip lines for basal glide at 623K is shown in Fig. 4.24. The waviness of the slip lines was characteristic for the entire temperature range (500-1073K) investigated (Ref. 143). The dislocation structure observed by TEM for a specimen deformed 15% at 198K in basal glide is shown in Fig. 4.25. Similar to prism glide, the dislocations are near screw orientation and there is no tendency for pairing or tangling of the long dislocations. However, in contrast to prism glide the isolated debris is in the form of approximately circular loops rather than elongated ones.

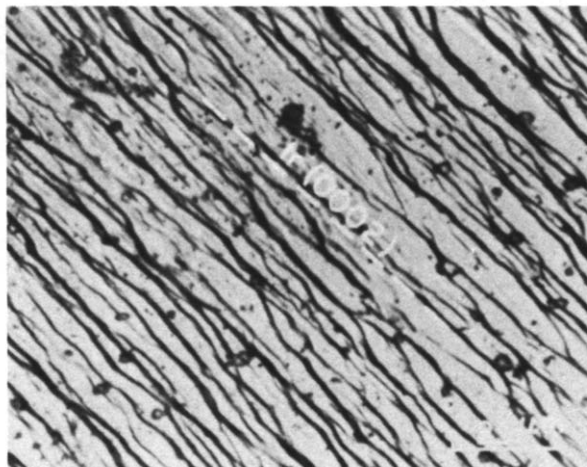


Fig. 4.24. Slip markings on the surface of a Ti crystal deformed to fracture ($\gamma = 0.26$) in basal glide at 623K. From Akhtar (Ref. 143).



Fig. 4.25. Dislocation structure in a Ti specimen deformed 15% by shear at 198K by basal glide. Section is parallel to a basal plane. From Cass (Ref. 45).

Effects of Temperature, Strain Rate and Interstitial Content on the Critical Resolved Shear Stress:

The effects of temperature and strain rate on the critical resolved shear stress for basal slip in high purity titanium are shown in Fig. 4.26. Also included are the results from Fig. 4.12 for prism slip on similar purity material. Similar to prism slip, the strain rate sensitivity parameter $\Delta\tau/\Delta\ln\dot{\gamma}$ for basal glide approaches

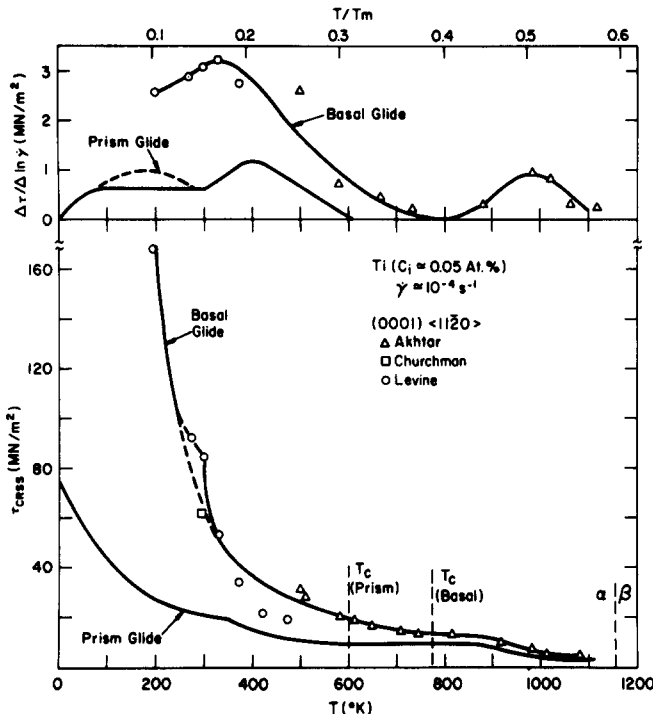


Fig. 4.26. Effects of temperature and strain rate on the critical resolved shear stress for basal slip in Ti. Also included are the average curves for prism slip in high purity titanium taken from Fig. 4.12. Data for basal slip from Refs. 43, 143, 148.

zero at a temperature T_c where the temperature dependence of the flow stress is that of the modulus (plateau stress). The temperature at which the plateau stress terminates (~900K) is approximately the same for basal slip as for prism slip.

Comparing further the results for basal slip with those for prism slip, one finds that basal slip exhibits a stronger temperature and strain rate dependence of the flow stress, but a weaker dependence on interstitial content, Fig. 4.27. Here $\Delta\tau/\Delta C_i = 0.21\mu$ for the initial rate of strengthening ($C_i = 0.05$ to 0.5 at. %) for basal slip at 300K compared to 0.39μ for prism slip (Fig. 4.12). Similar to prism slip, the τ_{CRSS} versus temperature curve for basal slip seems to have a kink at low temperatures. The temperature at which this occurs for basal slip is ~300K. Although no mention is made of the fact in Refs. 143 and 148, it appears that the strain rate sensitivity parameter $\Delta\tau/\Delta\ln\gamma$ for basal glide is relatively independent of strain, similar to the case for prism glide. Assuming this to be so, and considering the results of Fig. 4.26, one is led to the conclusion that basal glide at temperatures below about 850K may also be described by Eq. 4.4.

At temperatures above 900K specimens deforming by basal glide showed little or no strain hardening and it was possible to perform strain rate-cycle tests of various ratios without altering the original flow stress (Ref. 143). This permitted the measurement of the flow stress τ at different strain rates $\dot{\gamma}$, and a linear relation was found to exist between $\log\tau$ and $\log\dot{\gamma}$, the slope of which was 0.25 (Ref. 143).

Deformation Kinetics:

Plots of the apparent activation volume v and the deformation partial ($\partial\tau/\partial T$) $\dot{\gamma}$ for basal glide as a function of temperature derived from the data in Fig. 4.26 are

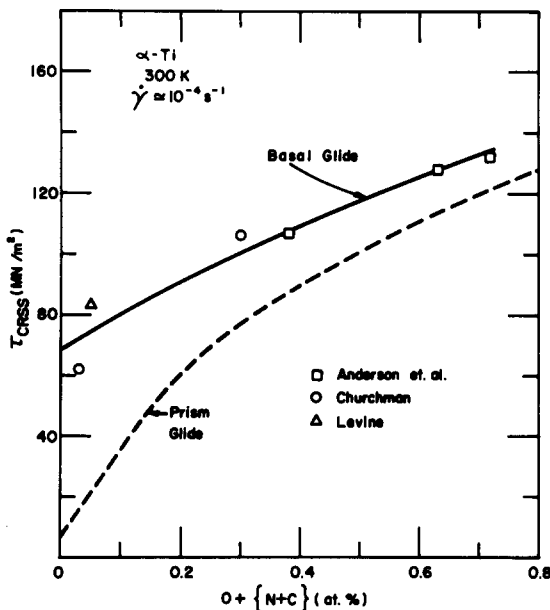


Fig. 4.27. Effect of interstitial solute content on the critical resolved shear stress for basal slip in Ti at 300K. Also included is the average curve for prism glide taken from Fig. 4.15. Data for basal slip from Refs. 43, 143, 148, 154.

given in Fig. 4.28. (The kink in the τ_{CRSS} versus temperature curve suggested in Fig. 4.26 is here neglected). In general, the values of v for basal glide are lower, and those of $(\partial\tau/\partial T)_\gamma$ higher, than for prism glide, there being about an order of magnitude difference at 300K. Worthy of note is that a discontinuity in v for basal glide seems to occur near 800K. The behavior of $(\partial\tau/\partial T)_\gamma$ in this temperature region is similar to that for prism glide.

The effect of temperature on Q for basal glide derived from the data in Fig. 4.26 is shown in Fig. 4.29. Also included are the results for prism glide taken from Fig. 4.21 for single crystals of the same low interstitial content. To be noted is that the first anomaly in the temperature dependence of Q for basal glide occurs in approximately the same temperature region (300-400K) as for prism slip. However, the values of Q are in general higher for basal glide. The second anomaly in the temperature dependence of Q for basal glide begins at about 700K. Whether a second anomaly also exists for prism glide has not been ascertained.

4.1.3 $\{10\bar{1}1\} <11\bar{2}0>$ Pyramidal Glide and $\vec{c} + \vec{a}$ Dislocations

Only little information is available on pyramidal glide in titanium. Its occurrence was first reported by Rosi and coworkers (Refs. 155,156), who observed it in coarse-grained specimens of commercial titanium at room temperature and at elevated temperatures. Churchman (Ref. 43) reported a resolved shear stress of 97 MN/m^2 for pyramidal slip in single crystals with $C_i \approx 0.3 \text{ at. \%}$, this stress being intermediate between that for prism and basal slip. Cass (Ref. 45) found pyramidal slip lines on a specimen whose orientation was near the $(1\bar{1}04)$ pole and which had been deformed

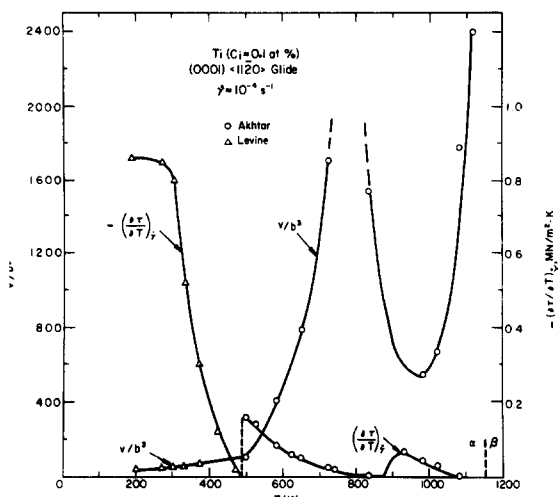


Fig. 4.28. Apparent activation volume V and the deformation partial $(\partial\tau/\partial T)_\gamma$ versus temperature for basal glide in high purity Ti. Data from Refs. 143, 148.

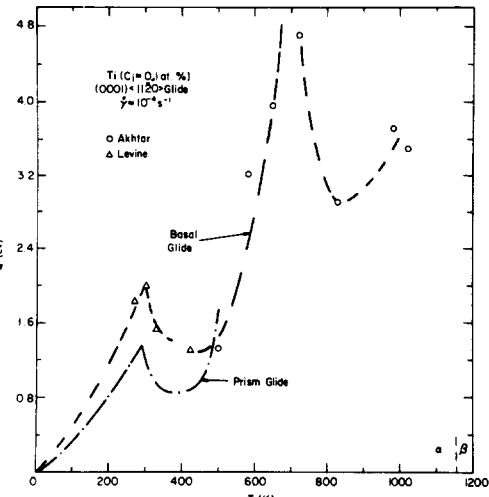


Fig. 4.29. Apparent activation energy Q versus temperature for basal glide in high purity Ti. Data from Refs. 143, 148.

in compression. The dislocation structure on a section parallel to the prism plane of this specimen is shown in Fig. 4.30. The faint dislocations on the prism plane have an \vec{a} vector. The strong images have a slip direction with a component out of the basal plane and is presumed to be $\vec{c} + \vec{a}$. The occurrence of $\vec{c} + \vec{a}$ dislocations in deformed titanium single crystals has also been reported by other investigators (Refs. 44, 46, 142). Paton and Backofen (Ref. 46) conclude that $\vec{c} + \vec{a}$ slip is important for accomodating shear ahead of a propagating twin at low temperatures and as a contributing deformation mode at elevated temperatures.

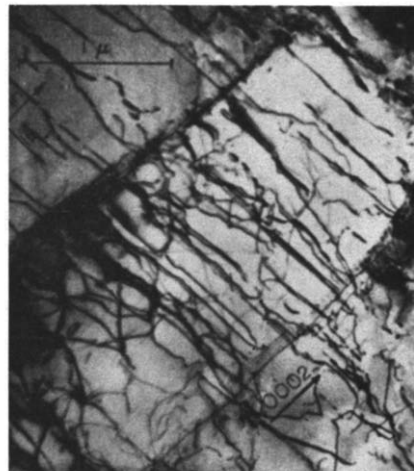


Fig. 4.30. Dislocation structure in a Ti crystal of (1014) orientation deformed in compression at 300K. Dislocations with $\vec{c} + \vec{a}$ Burgers vector are shown gliding on a pyramidal plane, ($g=00\cdot2, 11\cdot0$). From Cass (Ref. 45).

4.1.4 Twinning

The twins most commonly observed during the deformation of zone-refined titanium single crystals are the $\{10\bar{1}1\}$, $\{10\bar{1}2\}$, $\{11\bar{2}1\}$ and $\{11\bar{2}2\}$ twins (Refs. 14, 46, 143, 154 - 159). Examples of the morphology of these twins are given in Fig. 4.31. To be noted is that the $\{10\bar{1}1\}$ and the $\{11\bar{2}1\}$ twins are appreciably thinner than the other two types, there being however no direct correlation between the thickness and the shear strain; see Table 4.3. A high dislocation density generally exists at the twin-matrix interface; an example of which is found in Fig. 4.32, which also shows that an even higher density occurs when two twins interact. Although the four twinning modes listed above are the most common during the deformation of titanium single crystals, $\{11\bar{2}3\}$ and $\{11\bar{2}4\}$ twins have also been observed (Refs. 46, 156, 157, 159), especially at low temperatures (Ref. 156).

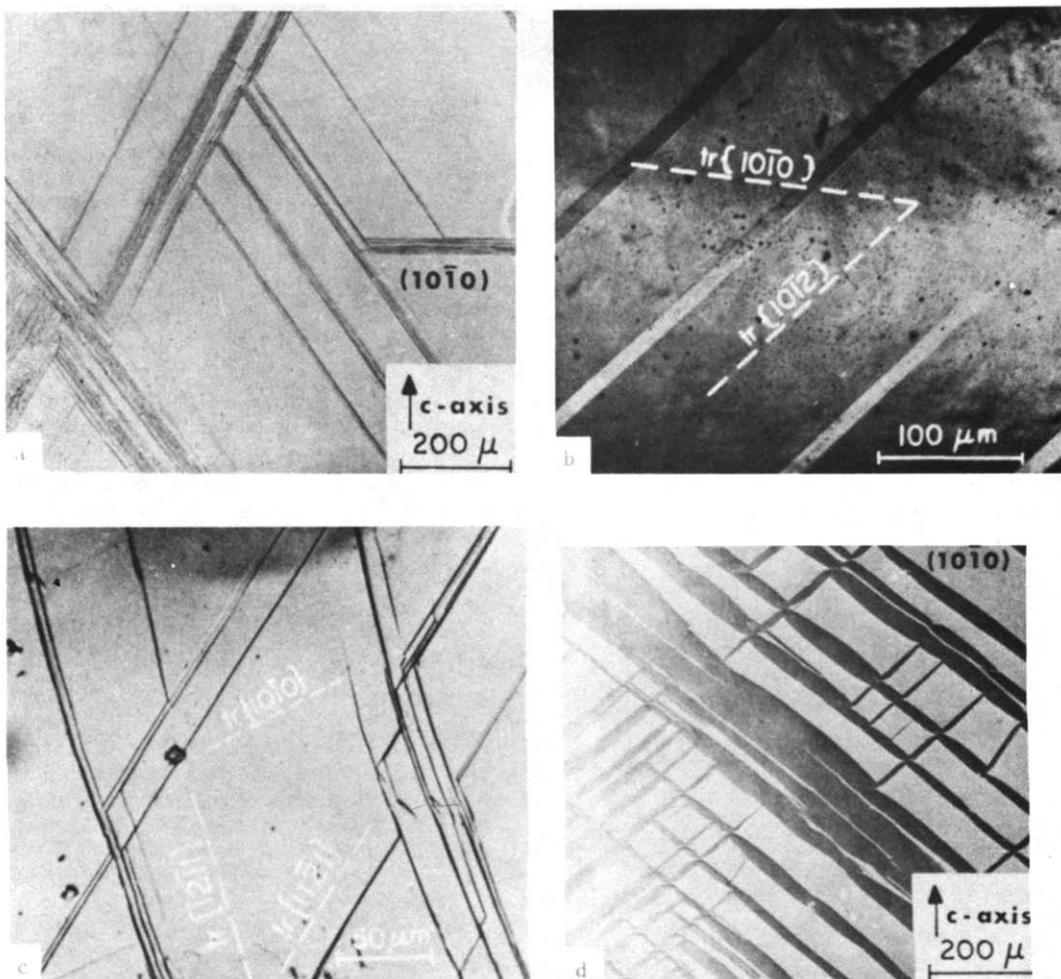


Fig. 4.31. Morphology of the four most common twinning modes observed during the deformation of zone-refined Ti single crystals: (a) $\{10\bar{1}1\}$ twins formed after 3.2% strain in *c*-axis compression at 923K (Ref. 46); (b) $\{10\bar{1}2\}$ twins formed after 0.2% strain in tension ($\chi_B = 78$ deg) at 295K (Ref. 143); (c) $\{11\bar{2}1\}$ twins formed after 0.2% strain in tension ($\chi_B = 47$ deg) at 78K (Ref. 143); (d) $\{11\bar{2}2\}$ twins formed after 3.7% strain in *c*-axis compression at 563K (Ref. 46).

TABLE 4.3 Typical Twin Width and the Resolved Shear Stress for Twinning on Various Systems in Zone-Refined Titanium as a Function of Temperature

Temp °K	Test Method	Orientation [†]	Twin Type	Theoretical Twin Shear ^{††}	Typical Twin Width	Resolved Shear Stress ^{†††} MN/m ²	Ref.
78	Tension	$x_B = 78^\circ$	$10\bar{1}2$	0.17	10-15	99.0	a
78	Compression	S.F.=0.5	$10\bar{1}2$	0.17	1-200	20.1	b
300	Compression	S.F.=0.5	$10\bar{1}2$	0.17	1-200	49.4	b
78	Tension	$x_B = 60^\circ$	$11\bar{2}1$	0.63	2-3	191.0	a
78	Compression	S.F.-0.5	$11\bar{2}1$	0.63	1-5	5.9	b
300	Compression	S.F.=0.5	$11\bar{2}1$	0.63	1-5	40.6	b
295	Compression	$x_B = 90^\circ$	$11\bar{2}2$	0.96	10-50	72.5	c
295	Compression	$x_B = 90^\circ$	$11\bar{2}2$	0.96	10-50	75.8	d
573	Compression	$x_B = 90^\circ$	$11\bar{2}2$	0.96	10-50	185.7	d
773	Compression	$x_B = 90^\circ$	$10\bar{1}1$	0.10	0.1-10	109.0	d
973	Compression	$x_B = 90^\circ$	$10\bar{1}1$	0.10	0.1-10	90.9	d
1023	Compression	$x_B = 90^\circ$	$10\bar{1}1$	0.10	0.1-10	80.2	d
1023	Compression	$x_B = 90^\circ$	$10\bar{1}1$	0.10	0.1-10	65.7	d

Notes: [†] x_B = angle between basal plane and specimen axis

 S.F. = Schmid factor

^{††} From Table 2.10

^{†††} Resolved on the twinning plane

References:

- A. Akhtar, Met. Trans. 6A, 1105, 1975.
- S. Fujishiro and J. W. Edington, "Mechanical Twinning of Titanium Single Crystals", Tech. Rept. AFML-TR-70-176, 1970.
- F. H. Beck, "Effect of Hydrogen on the Mechanical Properties of Titanium and Its Alloys", NASA Grant No. NGL-36-008-051, Ohio State University, 1972.
- N. Paton and W. Backofen, Met. Trans. 1, 2839, 1970.

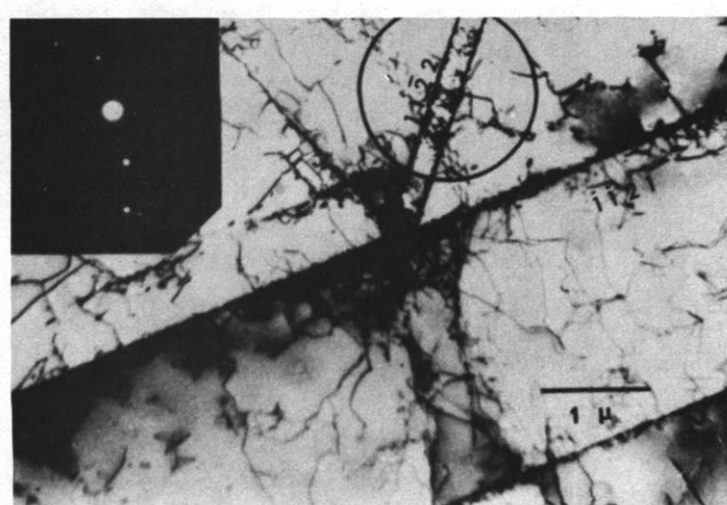


Fig. 4.32. Dislocation structures observed at $\{1\bar{1}21\}$ twin-matrix interface and at the intersection of $\{1\bar{1}21\}$ and $\{11\bar{2}2\}$ twins in Ti. From Fujishiro and Edington (Ref. 158).

Typical tensile stress-strain curves for specimens which exhibited $\{10\bar{1}2\}$ twins are depicted in Fig. 4.33. Irregularities in the curves only occur at the higher temperatures. However, for specimens which exhibited $\{11\bar{2}1\}$ twins in tension, irregularities in the stress-strain curves occurred at temperatures as low as 78K (Ref. 143); see Fig. 4.34. Also, pronounced yield drops occurred for certain orientations (Fig. 4.34), indicating that the stress for the nucleation of $\{11\bar{2}1\}$ twins is higher than that for their propagation. Yield drops were also observed during the c-axis compression of specimens which exhibited $\{11\bar{2}2\}$ twins (Ref. 46), the amount of the drop increasing with increase in temperature. On the other hand, no yield drops existed for specimens similarly loaded at temperatures where $\{10\bar{1}1\}$ twinning occurred (Ref. 46), although negative strain hardening took place at the higher temperatures (~923K) investigated.

The effect of temperature on the resolved shear stress for twinning on various systems is presented in Table 4.3. For most systems the stress for twinning increases with temperature, the exception being the $\{10\bar{1}1\}$ system where the stress decreases with temperature (Ref. 46). Fujishiro and Edington (Ref. 158) and Akhtar (Ref. 143) concluded from their studies that a critical resolved shear stress law did not hold for twinning in titanium. Further, although it is generally accepted that slip is a prerequisite for twinning, Akhtar (Ref. 143) concluded that slip did not precede $\{10\bar{1}2\}$ twinning. He was however of the opinion that the nucleation of $\{11\bar{2}1\}$ twins may possibly have been preceded by prismatic slip. Paton and Backofen (Ref. 46) suggested that the increase in stress for $\{11\bar{2}2\}$ twinning with increase in temperature was evidence that slip is a prerequisite for this twinning mode, since the increase in temperature encourages cross slip and climb and thereby decreases the effectiveness of the stress concentration at possible nucleation sites.

The effect of interstitial content on the resolved stress for twinning is not clear. Liu and Steinberg (Ref. 159) proposed that the twinning mechanism adopted may be controlled by the presence of oxygen and other impurities as an explanation for the fact that $\{11\bar{2}3\}$ and $\{11\bar{2}4\}$ twinning occurred in their single crystal titanium flakes of low oxygen content, whereas these systems were not observed by

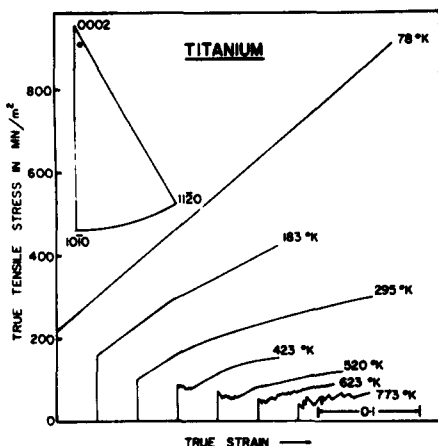


Fig. 4.33. Typical tensile stress-strain curves for Ti crystals which exhibited $\{10\bar{1}2\}$ twins. From Akhtar (Ref. 143).

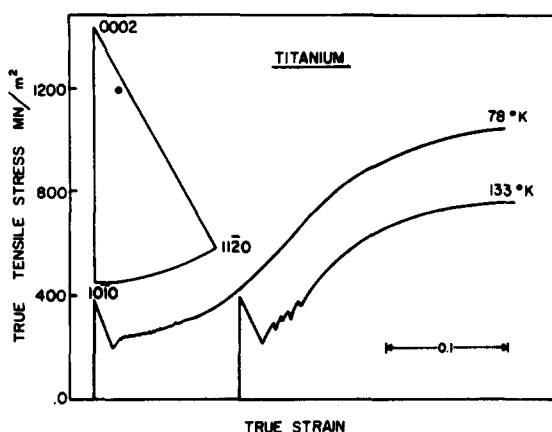


Fig. 4.34. Typical tensile stress-strain curves for Ti crystals which exhibited $\{11\bar{2}1\}$ twins. From Akhtar (Ref. 143).

others (Refs. 154,155) in material with a higher interstitial content. On the other hand, the results of Beck (Ref. 14) indicate that the stress for $\{11\bar{2}2\}$ twinning decreases with increase in O+N content and with increase in H content (Fig. 4.35), the relative effect of each impurity becoming less with increasing amounts of the other. This effect of interstitial content on the $\{11\bar{2}2\}$ twinning stress is similar to the effect of a decrease in temperature, namely both produce an increase

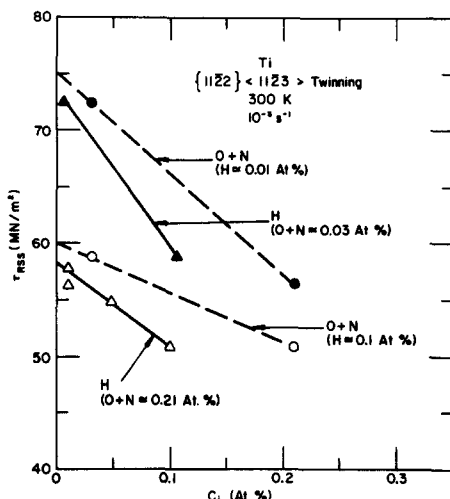


Fig. 4.35. Effect of O+N concentration on the resolved shear stress for $\{11\bar{2}2\}$ $\{11\bar{2}3\}$ twinning in Ti as a function of H content and the effect of H concentration on the twinning stress as a function of the O+N content. Data from Beck (Ref. 14).

in the glide stress and a decrease in the twinning stress. Thus both effects tend support to the idea that slip is a prerequisite for {1122} twinning.

4.1.5 Influence of Substitutional Solute

The addition of aluminum to titanium does not appreciably influence the effect of interstitial solutes on the thermal component of the critical resolved shear stress τ^* (Fig. 4.36) nor the strain rate sensitivity parameter $\Delta\tau/\Delta\ln\dot{\gamma}$ for prism slip at low temperatures (Fig. 4.37).[†] In Fig. 4.36 the influence of aluminum on the athermal component has been eliminated by subtracting from τ_{CRSS} at 77 and 300K that at 500K corrected for the change in modulus (Youngs modulus from Ref. 32) with temperature. It is seen from Figs. 4.36 and 4.37 that the results for the Ti-Al alloys (Ref. 147) fall to a large extent within the scatter of those for titanium without aluminum additions. The effect of aluminum is thus principally on the athermal component of the flow stress, having only little, if any, influence on the thermal component, which is determined mainly by the interstitial solutes.

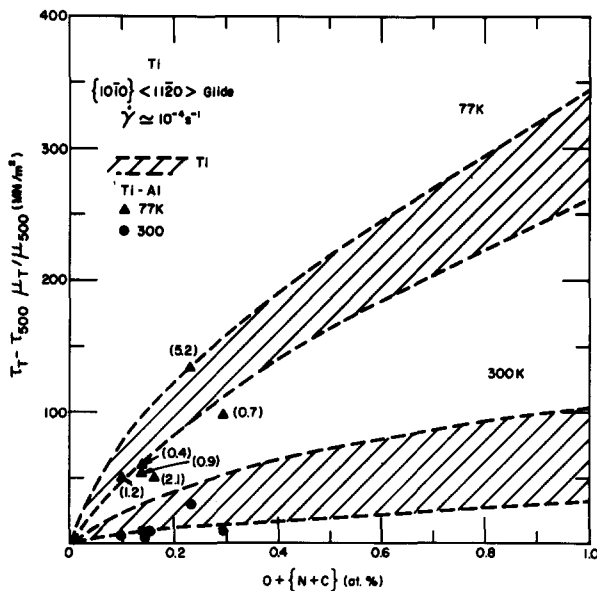


Fig. 4.36. Effect of interstitial solute content on the thermal component of the critical resolved shear stress for prism slip at 77 and 300K as a function of Al content. Data for Ti taken from Fig. 4.15, that for Ti-Al alloys from Sakai and Fine (Ref. 147). Numbers in parentheses refer to the Al content of the Ti-Al alloys.

[†]The interstitial content given in Figs. 4.36 and 4.37 is the average of those reported by Sakai and Fine (Ref. 147) for each alloy.

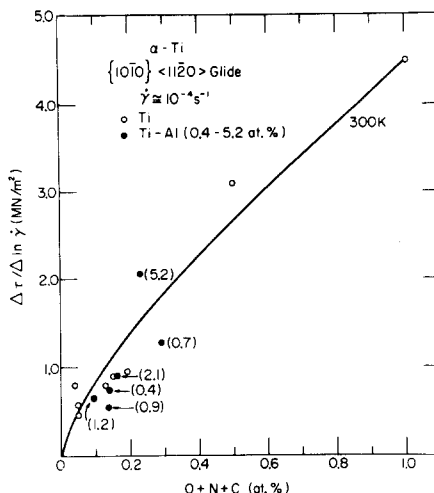


Fig. 4.37. Effect of interstitial content on the strain rate sensitivity parameter $\Delta\tau/\Delta\ln\dot{\gamma}$ for prism slip at 300K as a function of Al content. Data for Ti taken from Fig. 4.18, that for Ti-Al alloys from Sakai and Fine (Ref. 147). Numbers in parentheses refer to the Al content of the Ti-Al alloys.

The results of Figs. 4.36 and 4.37 suggest that the initial decrease in τ_{CRSS} for prism slip noted by Sakai and Fine (Ref. 147) upon alloying with aluminum (Fig. 4.38) may be due to a lower interstitial content originally present in the alloys containing around 1 at. % Al rather than a scavenging effect due to the aluminum, as proposed by them. An appreciably lower oxygen content is indicated in at least one of the two chemical analyses reported for each of the lower aluminum content alloys. Of interest in this regard is that no initial decrease in flow stress was found by Okazaki, Eguchi and Conrad (Ref. 160) for the addition of similar amounts of aluminum (up to 1.9 at. %) to polycrystalline titanium. Of significance in regard to this subject is that large differences in interstitial solute content have been obtained by Okazaki and Conrad (Ref. 161) for separate chemical analyses on unalloyed (with respect to substitutional solutes) polycrystalline titanium. The large variation in interstitial solute content which present-day chemical analyses yields is no doubt an important factor in the scatter in results generally obtained when considering the effects of interstitials on the mechanical properties of titanium and makes interpretation of the results difficult.

Because of the small amount of data, it is difficult to reach any conclusion regarding the influence of aluminum on the effect of interstitial solutes on τ_{CRSS} for basal slip. However, the results of Sakai and Fine (Ref. 162) suggest that, similar to prism slip, the addition of up to 5 at. % Al does not appreciably alter the effect of interstitial solutes on τ_{CRSS} for basal slip, nor its temperature and strain rate dependence. Additions of aluminum do however have a significant influence on the dislocation structure and strain hardening (Ref. 147). For prism slip, as the aluminum content is increased the ratio of screw to edge dislocations increases and the screws become longer. Moreover, strain hardening decreases with increase in aluminum content, becoming negative for the addition of 5.2 at. % Al.

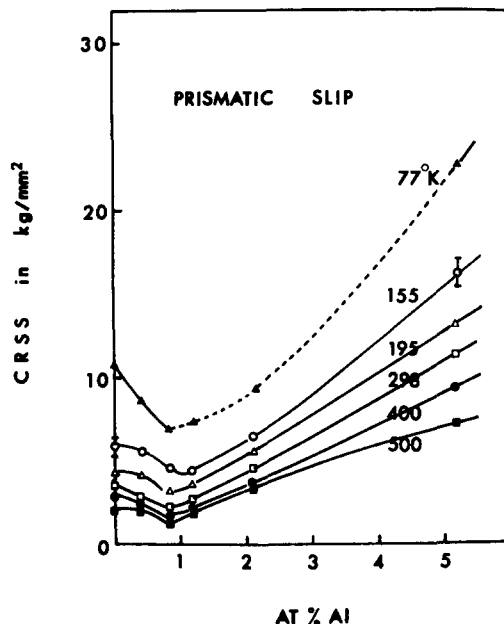


Fig. 4.38. CRSS for prism slip versus Al content for various temperatures.
From Sakai and Fine (Ref. 147).

4.2 Polycrystals

4.2.1 Characterization of Materials

In the present paper the term "titanium" will refer to all the various titanium materials which do not contain intentional additions of substitutional solute atoms. The term "titanium alloys" will be restricted to this latter group of materials and will not include (as is often done) those titanium materials containing appreciable amounts of interstitial solutes acquired during processing or by intentional additions. As mentioned in the Introduction, the present paper is concerned mainly with the effects of interstitial solutes on the mechanical properties of titanium and only to a lesser degree with their effects in titanium alloys. Coupled with the effects of the interstitial solutes are those due to texture and grain size, and other crystal defects which may be present. Therefore, to understand the influence of interstitial solutes on the mechanical behavior of polycrystalline titanium it is important to have as complete a characterization of the material as possible regarding chemical composition, texture, grain size and morphology and other crystal defects which may be present. Hence, in this section a brief review is given of the "character" of the structure of the titanium materials which have been investigated most extensively.

Chemistry:

Many of the experimental investigations into the mechanical behavior of titanium polycrystals to be referred to in the remainder of this section have been carried out on a few select commercial materials. A list of the form and chemical composition of these materials is given in Table 4.4. The total C+N+O interstitial content is given in terms of an oxygen equivalent, O_{eq} (Ref. 151) as well as simply the sum

TABLE 4.4 Form, Chemical Composition and Grain Size of Titanium Materials Employed by Various Investigators.

Material	Form	Composition in ppm [†]							Grain Size	Ref.
		0	N	C	H	Fe	0+N+C	O _{eq} ⁺⁺		
Iodide	sheet	100	50	300	---	<400	0.17	0.15	25	a
Iodide	sheet	100	50	300	---	<400	0.17	0.15	100	b
Z.R.(FIRL)	wire	30	73	20	20	---	0.04	0.06	3	c
Iodide	wire	30	110	18	18	---	0.05	0.09	3	c
MARZ Z.R.(MRC)	wire	(63)	(6)	(78)	(4)	(50)	(0.05)	(0.05)	1-29	d,e,f
		182-790	4-130	58-85	4-26	---				
	{406}	{64}	{69}	{17}			0.17	0.19		d
Battelle	wire	(370)	(40)	(80)	(62)	(90)	(0.16)	(0.16)	1.5-22	d
		330-569	16-140	25-80	17-62	90				d
	{420}	{53}	{53}	{36}	{90}		0.17	0.18		d
A-50 (50A)	wire	1100	90	250	44	500	0.46	0.48	2.22	g
Comm. Ti(A)	plate	1360	100	200	54-92	1600	0.52	0.54	16	e,h
Comm. Ti(B)	?	1200	80	140	50-100	2000	0.44	0.46	25	h

Material	Form	Composition in ppm [†]						Grain Size μm	Ref.	
		O	N	C	H	Fe	O + N + C	O_{eq} ^{††}		
A-70 (Lot 1)	wire	(2800)	(200)	(80)	(68)	(3700)	(0.94)	(1.00)	0.8-19	c
		2830	250	25	67	---	0.94	1.03		c
A-70	wire	(2800)	(200)	(500)	(31)	---	(1.11)	(1.12)	1.5-16	d
		2263-2875	52-200	80	17-51	1200				d
{2646}		{103}	{180}	{32}	{1200}	{1200}	0.86	0.89		d

Notes: [†] Number in parentheses is nominal composition or chemical analysis provided by supplier.
 Number in brackets is average of all analyses by investigator when a range was obtained.
 Number without brackets is the actual chemical composition indicated by investigator.

^{††} $O_{eq} = O + 2N + 0.75C$ in at. %: H. Conrad, Acta Met. 14, 1631, 1966.

References:

- a. W. L. Finlay and J. A. Snyder, Trans. AIME 188, 277, 1950.
- b. R. I. Jaffee, H. R. Ogden and D. J. Maykuth, Trans. AIME 188, 1261, 1950.
- c. H. Conrad and R. Jones, The Science Technology and Application of Titanium, Pergamon Press, 459, 1970.
- d. K. Okazaki and H. Conrad, Acta Met. 21, 1117, 1973.
- e. A. Garde, A. Santhaman and R. Reed-Hill, Acta Met. 20, 215, 1972.
- f. K. Okazaki and H. Conrad, Trans. JIM 13, 205, 1972.
- g. C. Yin, M. Doner and H. Conrad, Met. Trans. 6A, 1901, 1975.
- h. V. Arunachalam, S. Pattanaiak, S. Monteiro and R. Reed-Hill, Met. Trans. 3, 1009, 1972.

of the atomic fractions of these solutes. It is seen that for most of the materials O_{eq} does not differ appreciably from the simple addition of the atomic fractions. Of particular importance regarding the results of Table 4.4 is that large variations in the interstitial solute content for a given material may be obtained for separate chemical analyses by the same and different laboratories (Ref. 161). Thus, any quantitative assessment of the effects of interstitial solutes on mechanical properties will include the possibility of the large scatter in interstitial content indicated in Table 4.4. Of interest in this regard is that Elssner, Krohn and Ruano (Ref. 145) found that the resistivity ρ_r at 293K of titanium specimens with a bamboo structure increased linearly with oxygen and nitrogen content (up to 1.2 at. %) giving $\rho_r = \rho_{r,0} + \alpha_r C_i (\mu\Omega\text{cm})$. Their initial high purity starting material of $C_i = 0.08$ at. % total interstitial content had $\rho_{r,0} = 43 \mu\Omega\text{cm}$; α_r had values of 8.2 and $8.5 \mu\Omega\text{cm}$ for the addition of oxygen and nitrogen respectively, when C_i was expressed in at. %. Resistance measurements thus would seem to offer a means for determining or checking the interstitial content in titanium.

Worthy of mention is that the term "commercial titanium" is often used by investigators for material with an intermediate interstitial content, similar to that listed for A-50 in Table 4.4. It should, however, be recognized that titanium materials of both lower and higher interstitial content are available commercially and that an investigator may in fact have studied some material other than the equivalent of A-50 when he lists his material as "commercial titanium".

Texture:

The textures commonly exhibited by titanium rod or wire and sheet are illustrated in Fig. 4.39 (Refs. 163-167). The texture of drawn or swaged titanium wire consists of the $<10\bar{1}0>$ direction along the wire axis. Upon recrystallization this texture initially sharpens for fine grain sizes ($1-2\mu\text{m}$) and then decreases in intensity as the grain size increases, splitting into two components (each approximately 15 deg. from the wire axis) for grain sizes larger than about $5\mu\text{m}$. In zone-refined material a similar rotation occurs for the basal plane with respect to the wire axis; however, this rotation is restricted by an increase of the interstitial content, for it does not occur in less pure A-50 and A-70 titaniuns (Ref. 167).

The texture of cold-rolled titanium sheet is most generally one with the $<10\bar{1}0>$ direction parallel to the rolling direction and the basal plane tilted 20 to 40 deg. to the plane of the sheet. Upon recrystallization, the texture initially sharpens for the finer grain sizes ($1-2\mu\text{m}$). For larger grain sizes ($>5\mu\text{m}$) there occurs a rotation of the basal plane about its normal so that the $<11\bar{2}0>$ direction becomes more nearly parallel to the rolling direction, although this direction may still be inclined to the rolling plane. For both the cold-rolled and the recrystallized sheet textures, interstitial and substitutional solutes tend to reduce the angle γ (Fig. 4.39) between the basal plane and the plane of the sheet, yielding in the extreme case a texture with the basal plane in the plane of the sheet. Hot working yields sheet textures similar to those of recrystallized material with a large grain size; it can also yield textures with the basal plane parallel to the plane of the sheet.

Grain Structure:

A detailed characterization of the recrystallized structure of swaged and annealed titanium ($C_i = 0.1$ to 1.0 at. % O_{eq}) wires of 1 to $20\mu\text{m}$ grain size employed in many of their studies was carried out by Conrad and coworkers (Ref. 161,167-169). Quantitative optical microscopy (including serial sectioning) established that: (a) the grains are relatively equiaxed in all three dimensions, (b) the three-dimensional grain size distribution is approximately log-normal, (c) the grains become more regular in shape with increase in grain size and (d) the grain size, morphology and distribution are independent of the time and temperature used to

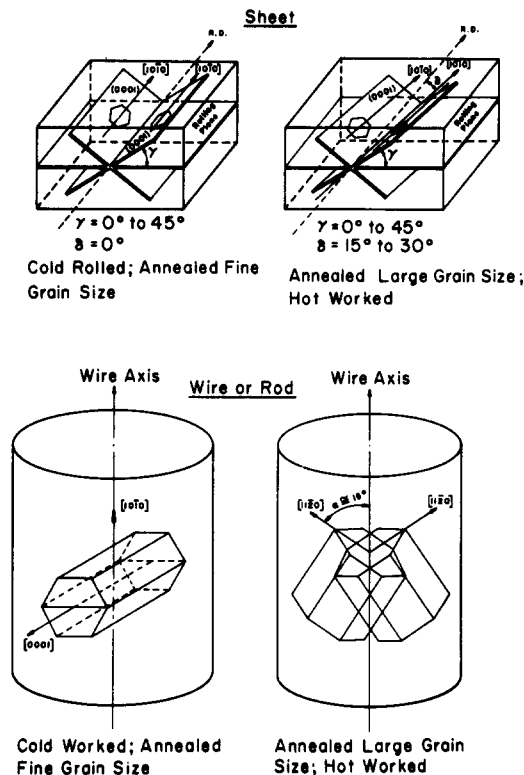


Fig. 4.39. Common textures in Titanium sheet and rod or wire. From Conrad, Doner and DeMeester (Ref. 2).

obtain a given average grain size. The effect of interstitial content was on the degree of these various properties but not their substance. TEM studies indicated that the initial dislocation density tended to increase with decrease in grain size and increase in interstitial content, ranging between 10^7 and 10^8 cm^{-2} for completely recrystallized specimens. Small precipitates (mostly globular in form) were observed in many specimens examined, their amount increasing with decrease in purity of the material. These precipitates tended to disappear when the annealing temperature was above 1000K. Limited microprobe analysis detected a high nitrogen content in the particles in zone-refined material and high iron content in those in A-70 material.

4.2.2 General Deformation Behavior

Stress-Strain Curves:

Typical true stress-true strain ($\sigma-\epsilon$) curves for commercial titanium wire specimens with an intermediate interstitial solute content of ~0.5 at. % (Ti-50A) and a grain size of $22\mu\text{m}$ tested in tension at a nominal strain rate of 10^{-4}s^{-1} over the temperature range of 4.2 to 1000K are depicted in Fig. 4.40.^f These curves and others for similar tests (Refs. 163, 170-175) exhibit the following general features. Yield-point phenomena occur for initial plastic deformation at temperatures below about 800K. The stress-strain curves after about 1-2% strain are nearly linear below about 200K, parabolic between about 200 and 850K and nearly flat above 850K.

^fThe true stress-strain curves are only valid up to the maximum stress.

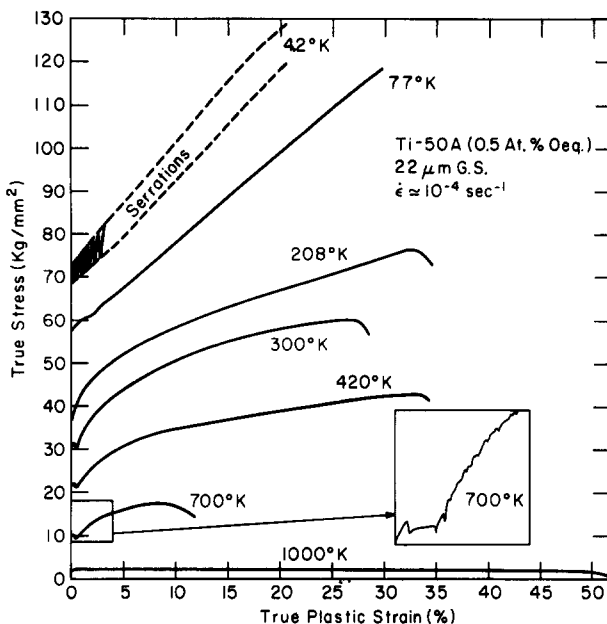


Fig. 4.40. True stress-true strain curves for commercial titanium (0.5 at. % O_{eq}) with 22 μm grain size as a function of temperature. Data from Refs. 163 and 170. From Conrad, Doner and DeMeester (Ref. 2).

Pronounced serrations or stress drops occur during deformation at very low temperatures (4.2K); less marked serrations or irregularities occur in the temperature range of 700-800K; otherwise the stress-strain curves are smooth. In the temperature region below 600K both the stress level and the shape or form of the stress-strain curve are influenced to a marked degree by the grain size and the interstitial solute content.

Effects of Temperature and Strain Rate on the Flow Stress:

The effects of temperature on the flow stress at 1% strain and on the strain rate sensitivity parameter $\Delta\sigma/\Delta\ln\dot{\epsilon}$ (obtained by strain rate cycling tests) for the Ti-50A material are presented in Fig. 4.41. The strain rate sensitivity parameter was relatively independent of the strain (Ref. 170). The deformation behavior portrayed in Fig. 4.41 exhibits three distinct regions. Below about 600K ($T < 0.3T_m$), the flow stress is strongly dependent on the temperature and strain rate (with a maximum strain rate sensitivity at about 400K); between 600 and 800K ($0.3 < T/T_m < 0.4$) it is very weakly dependent (if at all) on temperature and above 800K ($T > 0.4T_m$) it again becomes strongly dependent.

The effect of strain rate on the yield stress versus temperature behavior of titanium (0.5 at. % O_{eq}) is shown in Fig. 4.42. Typically, the effect of an increase in strain rate is to raise the level of the flow stress and to shift to higher temperatures the transition from one deformation region to another. Log-log plots of the yield stress versus strain rate at a constant temperature gave straight lines whose slope $m = \partial\log\sigma/\partial\log\dot{\epsilon}$ varied with temperature in the manner shown in Fig. 4.43.

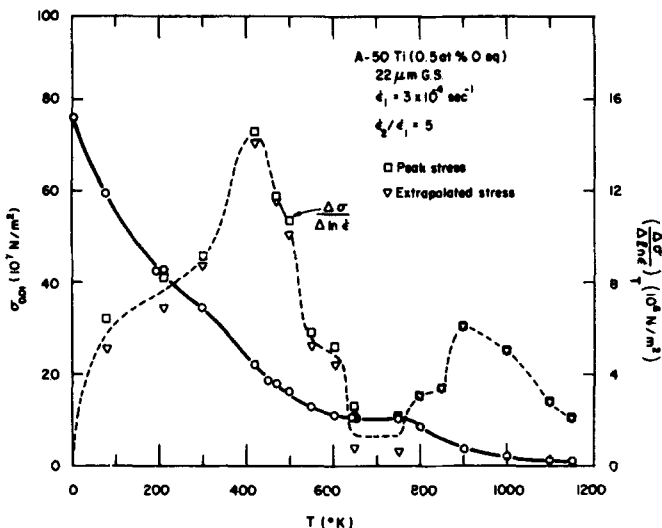


Fig. 4.41. The flow stress and strain rate sensitivity parameter $\Delta\sigma/\Delta\ln\dot{\epsilon}$ at 1% strain versus temperature for Ti-50A (0.5 at. % Oeq) with $22\mu\text{m}$ grain size. From Yin, Doner and Conrad (Ref. 176).

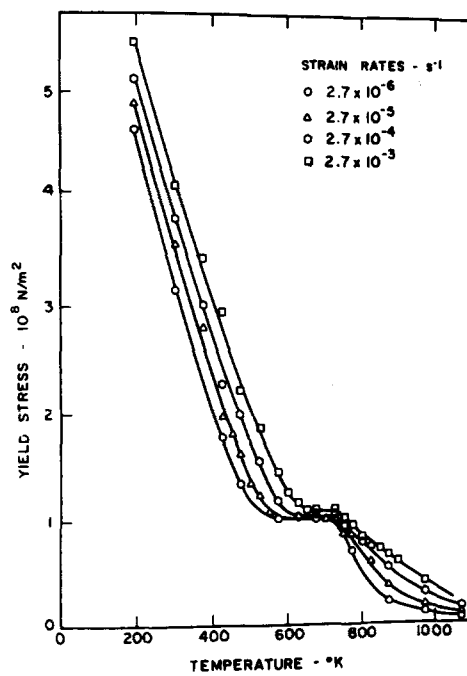


Fig. 4.42. The yield stress of commercial titanium (0.5 at. % Oeq) as a function of strain rate and temperature. Data from Santhanam (Ref. 177) given by Reed-Hill (Ref. 178).

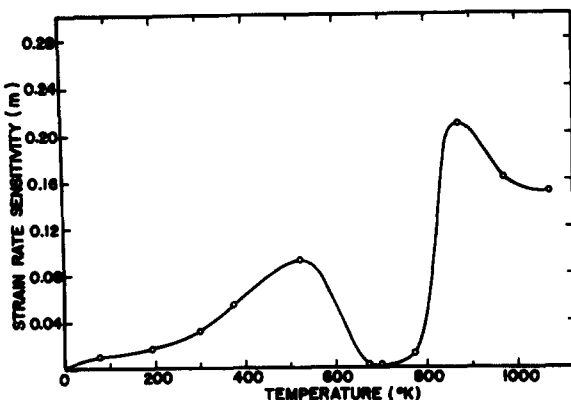


Fig. 4.43. The effect of temperature on the strain rate sensitivity exponent $m = \partial \log \sigma / \partial \log \dot{\epsilon}$ for commercial titanium (0.5 at. % O_{eq}) and 16 μm grain size. From Santhanam and Reed-Hill (Ref. 179).

The effect of a wide range in strain rate (10^{-5} to 10^3 s^{-1}) on the yield stress of commercial titanium (0.5 at. % O_{eq}) at low temperatures is shown in Fig. 4.44. To be noted is that a marked change in the slope of the semi-log plot occurs at a strain rate of about 10^2 s^{-1} at each temperature.

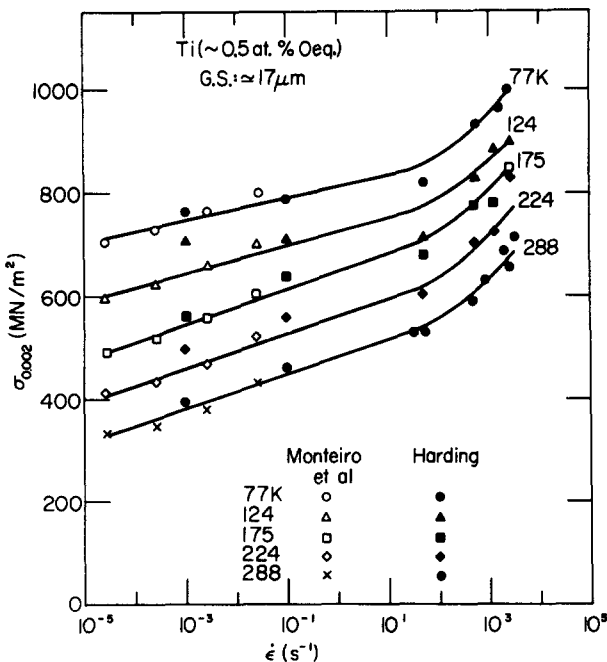


Fig. 4.44. The effect of strain rate on the yield stress of commercial titanium (0.5 at. % O_{eq}) of 17 μm grain size at various temperatures. From Monteiro, Santhanam and Reed-Hill (Ref. 180) and Harding (Ref. 181).

The effect of temperature on the average strain hardening rate for commercial purity and high purity titanium deformed from 0.5 to 5% strain is depicted in Fig. 4.45; the influence on the uniform and total elongation of the commercial purity material is shown in Fig. 4.46. For the commercial purity material a maximum in strain hardening rate and a minimum in ductility occurs in the range 700-800K. No such pronounced effects occur for the high purity iodide titanium.

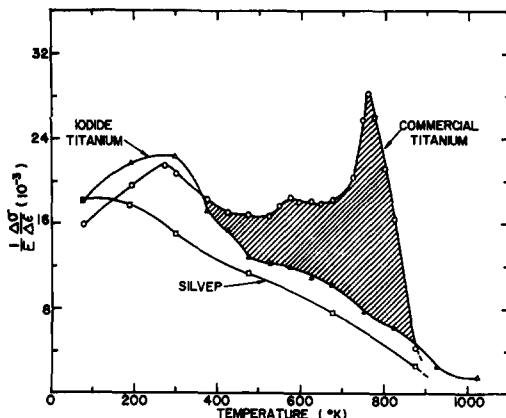


Fig. 4.45. Average modulus reduced strain hardening rate between 0.5 and 5% strain for commercial titanium, high purity iodide titanium and high purity silver versus temperature. E is Young's modulus. From Garde, Santhanam and Reed-Hill (Ref. 171).

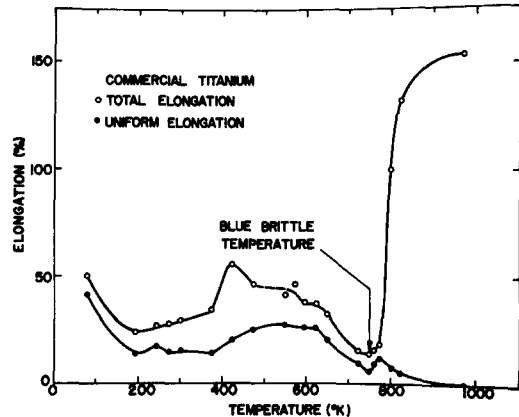


Fig. 4.46. Uniform and total elongations of commercial titanium as a function of temperature. From Garde, Santhanam and Reed-Hill (Ref. 171).

Lii, Ramachandran and Reed-Hill (Ref. 182) found that the original cross section of cylindrical specimens machined from commercial titanium plate of $16\mu\text{m}$ grain size became elliptical during deformation (in accord with the earlier observations of Rosi and Perkins (Ref. 183)), the amount of ellipticity increasing with increasing temperature of deformation in the range 77-1000K. The effect of temperature on the anisotropy of deformation is portrayed in Fig. 4.47, which gives a plot of $[|\epsilon_x| - |\epsilon_y|]/\epsilon_z$ versus temperature, where ϵ_y and ϵ_x are the strains in directions perpendicular to the surface and to the longitudinal cross section planes, respectively, and ϵ_z is that in the axial direction. For a specimen which deforms isotropically, the ratio $[|\epsilon_x| - |\epsilon_y|]/\epsilon_z$ would be zero. Evident from Fig. 4.47 is that the deformation becomes more isotropic as the test temperature is decreased.

Creep and Stress Relaxation:

In keeping with the dependence of the flow stress on strain rate and temperature, titanium exhibits creep and stress relaxation over all of the temperature regions mentioned above. At low temperatures (77-530K), Zeyfang, Martin and Conrad (Ref. 184) found for incremental loading and temperature-change creep tests on Battelle titanium (0.2 at. % O_{eq}) that the creep rate decreased linearly with creep strain (Fig. 4.48), indicative of logarithmic creep. On the other hand, Stetina (Ref. 185) reported the time laws for the creep of titanium of similar interstitial content in the temperature range of 303-373K to be parabolic in form, with a change in the time law occurring at about 400K, becoming in the range 423-473K of the form

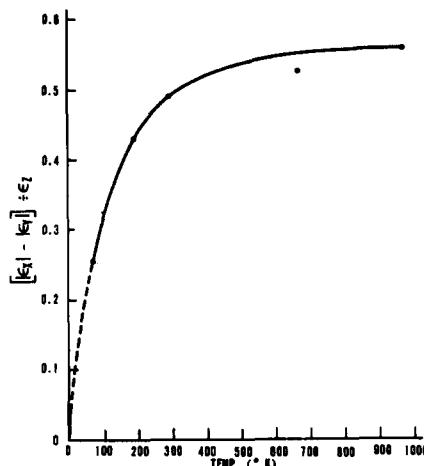


Fig. 4.47. Anisotropy of strain in commercial titanium of 0.5 at. % Oeq and 16 μm grain size as a function of temperature. From Lii, Ramachandran and Reed-Hill (Ref. 182).

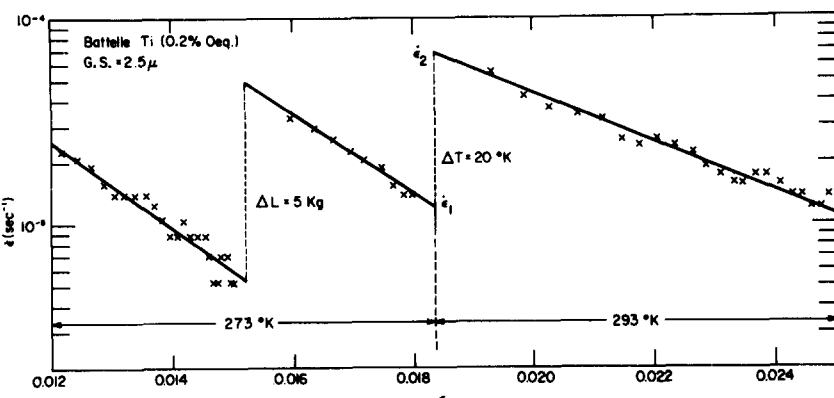


Fig. 4.48. Creep behavior of Battelle titanium during incremental loading and incremental temperature change tests. From Zeyfang, Martin and Conrad (Ref. 184).

$$1/\epsilon = 1/a + 1/bt^m \quad (4.7)$$

where a , b and m are constants. Kiessel and Sinnot (Ref. 186) had earlier also observed a change in the creep behavior of commercial titanium beginning about 400°K; see Fig. 4.49. It is here seen that the stress to cause a creep rate of $3 \times 10^{-10} \text{ s}^{-1}$ decreases as the temperature is raised from room temperature to about 350K, then increases with further rise in temperature reaching a maximum at about 475K, decreasing again at higher temperatures. This anomalous effect of temperature on the creep strength of titanium in the range 400-700K has also been reported by others (Ref. 187,188). The creep behavior of titanium above about 700K (Ref. 187) is similar to that normally observed for metals.

The stress relaxation of Battelle titanium (0.2 at. % O_{eq}) was investigated by Agrawal, Sargent and Conrad (Refs. 189,190) over the temperature range of 77 to 623K. The decrease in stress during relaxation $\Delta\sigma$ varied in a linear fashion with the logarithm of the time at low temperatures ($T \leq 300$ K), but at higher temperatures ($T > 523$ K) plots of $\Delta\sigma$ versus $\ln t$ exhibited a positive curvature. These authors pointed out that the effect of temperature on the form of the $\Delta\sigma$ versus $\ln t$ curves was analogous to that on the σ versus $\ln \dot{\epsilon}$ curves for conventional, constant strain rate tension tests. Curvature in plots of $\Delta\sigma$ versus $\ln t$ is also indicated in stress relaxation tests by others (Refs. 191-193) on titanium at temperatures of 300K and above.

Twinning:

Twining commonly occurs during the plastic deformation of titanium polycrystals, the amount generally increasing with decrease in test temperature (Refs. 47,176, 182,183,194-197). The twinning modes identified in specimens from commercial titanium (0.5 at. % O_{eq}) plate of 16μm grain size deformed to fracture in tension at 77 to 973K were primarily {1124} and {1122}, with occasional {1012} (Ref. 182). The {1124} and {1122} modes were also found in wire specimens of similar composition and grain size (22μm) tested at 78K (Ref. 176). On the other hand, Williams, Sommer and Tung (Ref. 196) have reported {1012} type twinning as the major mode in titanium sheet of similar composition and only slightly larger grain size (25-30μm) deformed at 77-540K.

The effects of strain and temperature on the volume fraction of twins in zone-refined iodide titanium of 22μm grain size are given in Fig. 4.50, where it is seen that the volume fraction increases significantly with increase in strain and decrease in temperature. Moreover, the amount generally increases with increase in purity (Ref. 195). Employing TEM, Conrad (Ref. 197) studied the effects of purity (0.05-1 at. % O_{eq}), grain size (1-23μm) and temperature (78-650K) on the frequency

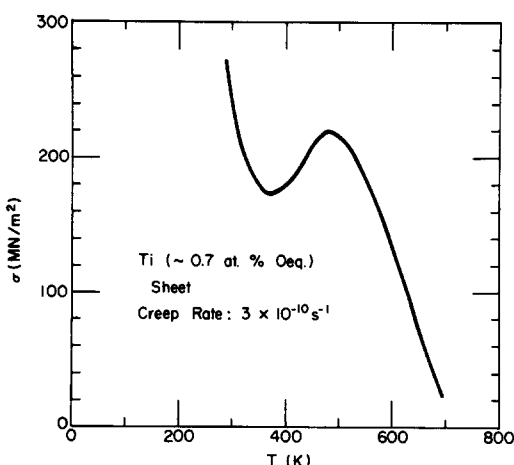


Fig. 4.49. Effect of temperature on the stress to produce a creep rate of $3 \times 10^{-10} \text{ s}^{-1}$ in commercial titanium sheet. Data from Kiessel and Sinnott (Ref. 186).

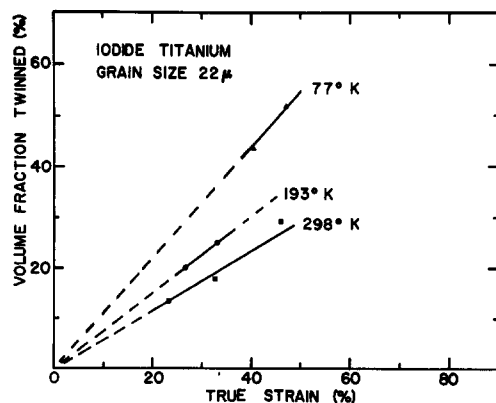


Fig. 4.50. Volume fraction of twins in zone-refined iodide titanium as a function of strain at 77, 193 and 298K. From Garde and Reed-Hill (Ref. 194).

of twinning in wire specimens strained 5-10% in tension. He found that over this temperature range the frequency increased with increase in purity and grain size and decrease in temperature. For zone-refined titanium of $1-2\mu\text{m}$ grain size no twins were observed for tests at 300K and above, while for larger grain sizes a temperature of 500K was required before twins were no longer detected. For commercial Ti-70A (~1 at. % O_{eq}) of grain size $\leq 6\mu\text{m}$, no twins were detected for tests at 200K and above, while for larger grain sizes none were observed at 300K and above. On the other hand, the work of Paton, Williams and Rauscher (Ref. 47) suggests that the effects of purity and temperature on the frequency of twinning may not be as straightforward as first appears; see, for example, Fig. 4.51. The behavior exhibited here suggests that several twinning modes with different temperature and purity dependencies may have been active over the wide temperature range considered.

According to Guimaraes and De Angelis (Ref. 198) the volume fraction of twins f_v^T is related to the total plastic strain by an expression of the form

$$f_v^T = 1 - \exp(A\epsilon^q) \quad (4.8)$$

where A and q are constants. The fit of data by Garde, Aigeltinger and Reed-Hill (Ref. 195) to this relation is illustrated in Fig. 4.52. Reed-Hill, Buchanan and Calfwell (Ref. 200) have proposed the following relation for the contribution of twinning to the tensile strain:

$$\epsilon_T = \phi f_v^T \quad (4.9)$$

where $\phi = \gamma_T/\bar{M}$; γ_T is the twinning shear and \bar{M} the orientation factor. Taking average values of $\gamma_T = 0.22$ and $\bar{M} = 2.5$, Garde, Aigeltinger and Reed-Hill (Ref. 195) deduced that about one-third of the total strain is due to twinning in high purity titanium deformed at 77K. More recently, Guimaraes and De Angelis (Refs. 201,202) have pointed out that a more accurate expression for the contribution of twinning to the total strain is

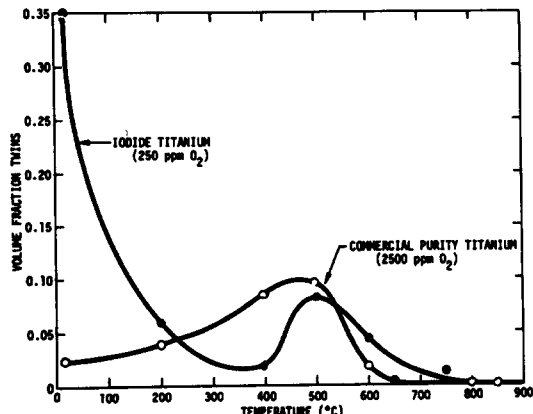


Fig. 4.51. Effects of temperature and purity on the volume fraction of twins at 5% strain. From Paton, Williams and Rauscher (Ref. 47).

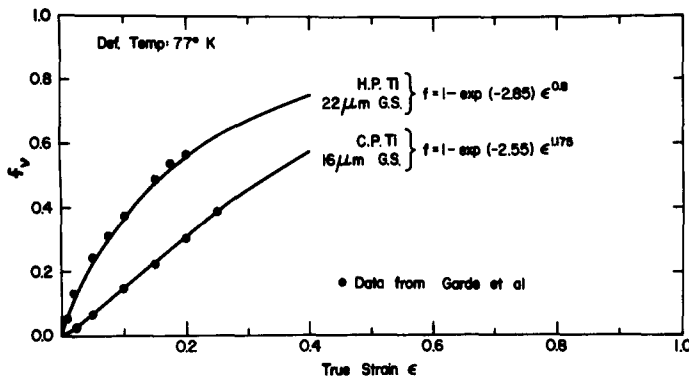


Fig. 4.52. Volume fraction of twins as a function of strain at 77K for high purity titanium and commercial purity titanium. From Keshavan, Sargent and Conrad (Ref. 199) using data of Garde, Aigeltinger and Reed-Hill (Ref. 195).

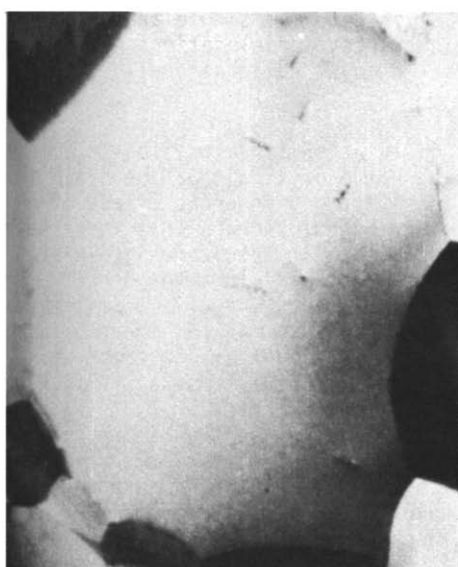
$$\epsilon_T = \ln(1 + \phi f_V^T) \quad (4.10)$$

For a volume fraction of twins less than about 10%, Eqs. 4.9 and 4.10 yield essentially the same values for ϵ_T ; however, smaller values are obtained from Eq. 4.10 at larger volume fractions.

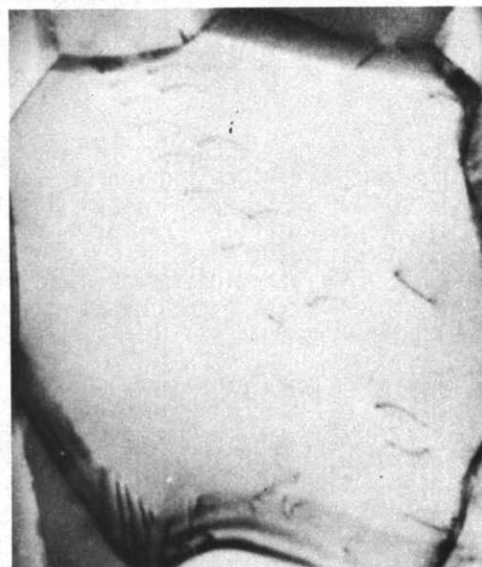
Dislocation Structure:

A detailed study of the dislocation structure of titanium wire specimens with a range in interstitial content (0.1-1.0 at. %) and grain size (1-23 μm) deformed over the temperature range 77-650K was conducted by Conrad, Okazaki, Gadgil and Jon (Ref. 169). Typical dislocation structures as a function of strain for Battelle titanium (0.2 at. % O_{eq}) with a 2 μm grain size deformed at 200K are presented in Fig. 4.53. For strains less than about 1% the significant features included the generation of dislocations from sources both within the grains and from grain boundaries and the subsequent motion, multiplication and interaction of these dislocations with each other and with the grain boundary. The interaction occasionally consisted of classical pile-ups similar to those in Fig. 4.53b; however, more often they consisted of localized entrapments or entanglements and jog formation, similar to those in Fig. 4.53c.

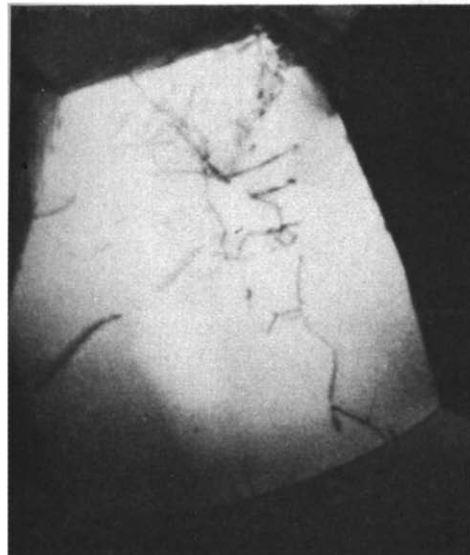
With increase in strain beyond about 1% the dislocation density continued to increase; also, the dislocations became more jogged and tangled, and more uniformly distributed throughout the grain. The structure now consisted of jogs, small loops, and entanglements, with no clear evidence of pile-ups. The entanglements within the grains exhibited some clustering, which tendency increased with increase in strain, so that at strains of the order of 10%, regions of high and low dislocation density developed, giving a "banded" or "cellular" structure; see, for example, Fig. 4.53d. This structure has somewhat the character of the cellular structure generally observed for deformed cubic metals; however, the cell walls are generally broader and less sharp in titanium and there exists a relatively high density of dislocations between the walls. Neither extended nodes nor splitting of the dislocation was observed, indicating a relatively high stacking fault energy in titanium, as proposed by others (Refs. 146,203). Limited electron diffraction studies indicated that: (a) most dislocations lay on the first order prism planes with a $\langle 11\bar{2}0 \rangle$ Burgers vector and (b) there was a preference for single dislocations

2 μ

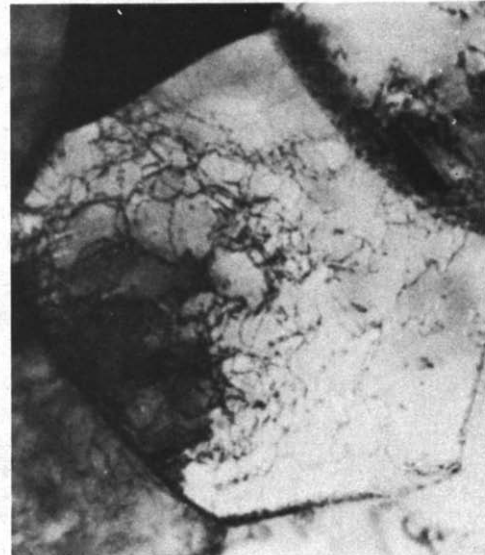
a.

2 μ

b.

2 μ

c.

2 μ

d.

Fig. 4.53. Dislocation structures of Battelle titanium (0.2 at. % O_{eq}) wire of 2 μ m grain size deformed at 200K. (a) as-annealed, (b) $\epsilon = 0.01\%$, (c) $\epsilon = 0.1\%$, (d) $\epsilon = 9.4\%$. From Conrad, Okazaki, Gadgil and Jon (Ref. 169).

to lie along or near the pure screw orientation. These dislocation structures are in accord with those observed by Cass (Ref. 45) on deformed single and polycrystals of titanium. In addition, he reported the occurrence of dislocations with the $\langle 11\bar{2}0 \rangle$ vector on the basal and $\{10\bar{1}\}$ pyramidal planes and occasionally dislocations with the $\vec{c} + \vec{a}$ Burgers vector.

The principal effect of grain size on the dislocation structure was to cause an increase in the dislocation density for a fixed value of strain as the grain size became smaller. For a constant dislocation density, no pronounced effect of grain size on the dislocation arrangement was detected, except perhaps that there was a slightly greater tendency to form the banded structure in the larger grain size specimens. There occurred only a slight decrease in the dislocation density at a given strain and grain size as the temperature increased. The effect of temperature on the arrangement of dislocations was however more marked, there being a greater tendency for dislocations to be uniform and straight at low temperatures and to exhibit more pronounced clustering and grouping as the temperature increased.

The effect of increasing interstitial content was to cause the dislocations to be more restricted to their glide plane, especially at small strains and low temperatures. Also, direct evidence of generation from grain boundaries and classical pile-ups was more frequently observed. Moreover, there was more debris on the slip plane in the form of small dislocation loops. For strains greater than about 2% the dislocation structure in impure A-70 (1.0 at. % O_{eq}) specimens was similar to that for the higher purity materials, except that more debris in the form of small loops was present and there was less tendency for clustering to take place.

In addition to the changes in dislocation structure which occurred within the grains during straining, the grain boundaries experienced appreciable alteration; notably the boundaries became darker, thicker and more fuzzy with strain, indicating an increasing accumulation of dislocations in the boundary and a general disruption of the grain boundary structure. When twinning occurred, a high dislocation density always existed at the twin boundary and especially at its tip.

The effects of interstitial content (~0.2 - 1.6 at. % O_{eq}) and temperature (200-550K) on the dislocation structure of titanium sheet of 25-30μm grain size deformed 2-3% were investigated by Williams, Sommer and Tung (Ref. 196). They found that the deformation had occurred almost exclusively by $\langle 11\bar{2}0 \rangle$ (\vec{a} vector) slip. Appreciable numbers of $\vec{c} + \vec{a}$ vector dislocations were also present; however, these dislocations were confined to regions near twin-matrix interfaces. All of their materials showed a trend toward more uniform distribution of dislocations with increasing temperature (see, for example, Fig. 4.54) or with decreasing oxygen concentration at low temperatures. For interstitial contents of ~0.6 at. % O_{eq} and above, there occurred a transition from planar to wavy glide, the temperature at which the transition took place increased with increasing interstitial content. The preferred glide planes for planar glide were $\{10\bar{1}0\}$ and $\{10\bar{1}1\}$, with essentially no well-developed basal slip bands. Specimens deformed at temperatures within the transition range exhibited increased numbers of dislocations cross slipping out of the slip bands and large, square-ended loops were frequently observed, which had the same \vec{a} vector as the dislocations. In the planar arrays most of the dislocations were jogged screws. The number of jogs and the size of the jogs increased with increasing temperature. There also occurred large numbers of dipoles and loops at all temperatures, their size increasing with temperature. The dipoles were frequently aligned along [0001], suggesting that they lay on the $\{10\bar{1}0\}$ planes.

The effect of tensile strain at 300K on the density of dislocations as a function of grain size and interstitial content is given in Fig. 4.55. The dislocation

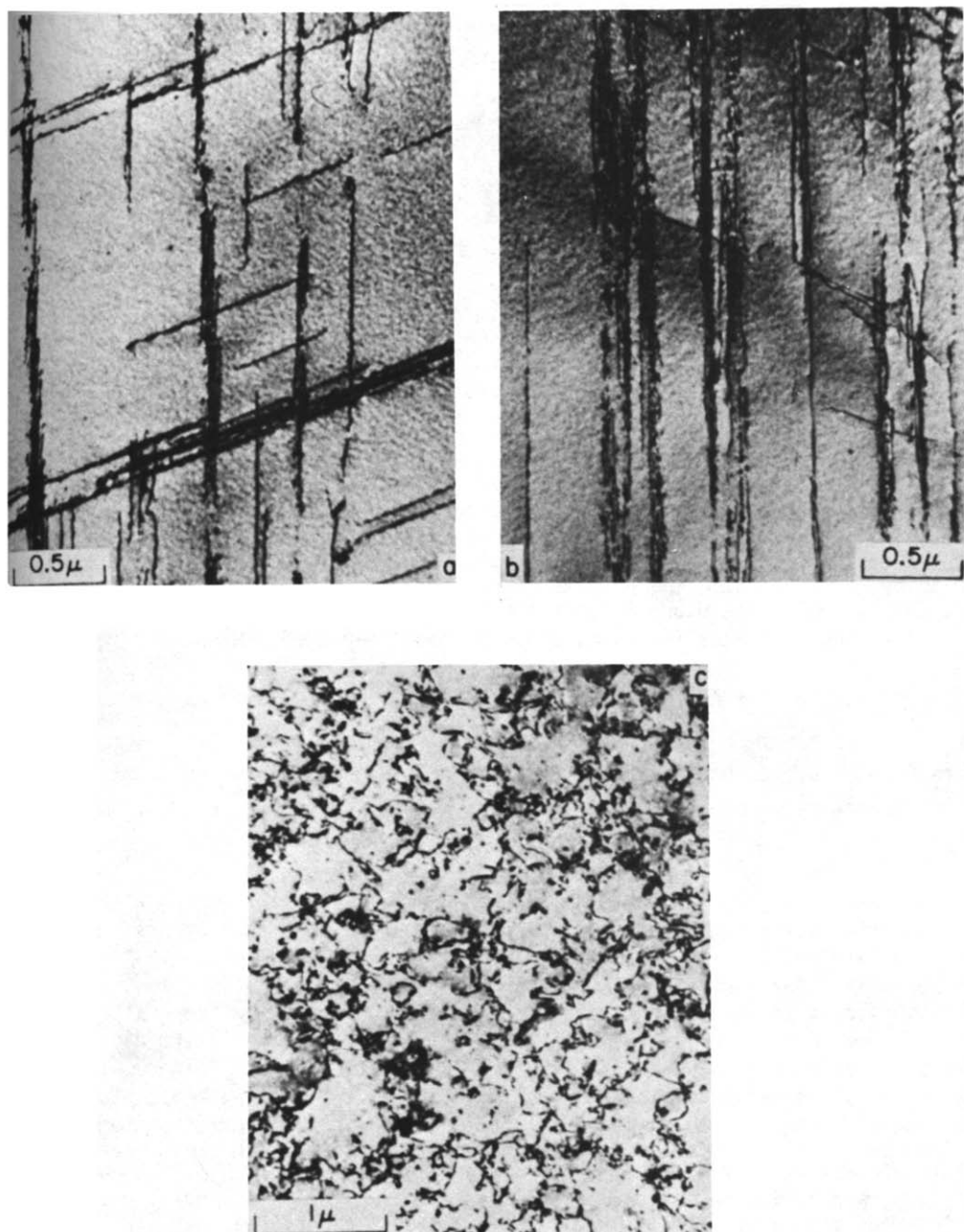


Fig. 4.54. Dislocation structure in titanium of ~1.6 at. % O_{eq} and 25 μm grain size deformed 2-3% at (a) 77K, (b) 300K and (c) 500K. From Williams, Sommer and Tung (Ref. 196).

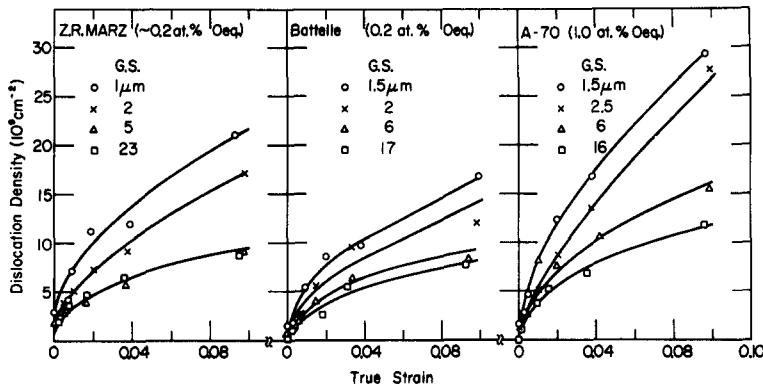


Fig. 4.55. Variation of dislocation density with strain in titanium deformed at 300K as a function of grain size and purity. From Conrad, Okazaki, Gadgil and Jon (Ref. 169).

density increases with strain, with decrease in grain size and with impurity content. Similar results were noted for tests in the range 77-650K, with a tendency for the dislocation density to decrease slightly with temperature when the other variables are constant. The effects of strain, temperature (through the shear modulus μ), grain size d and interstitial content C_i on the dislocation density ρ were approximated by the following empirical equation (Ref. 169)

$$\rho^{1/2} = A\mu^{1/2} [1 + 7C_i^{1/2}] [3 \times 10^2 \epsilon^{1/2} + Bd^{-1/2}], \text{ cm}^{-1} \quad (4.11)$$

where A and B are constants equal to approximately one and have units of $\text{kg}^{-1/2}$ and $\text{cm}^{1/2}$ respectively, $\mu (= C_{66})$ is in units of kg/cm^2 , C_i in atomic fraction and d in cm .

Summary:

The plastic deformation of titanium can be classified into at least four general categories according to the temperature region in which each occurs: (a) very low temperatures, (b) low temperatures, (c) intermediate temperatures and (d) high temperatures. For a strain rate of approximately 10^{-4}s^{-1} the very low temperature behavior occurs in the vicinity of 4.2K ($T/T_m \approx 0.002$), the low temperature behavior begins at $\sim 4.2\text{K}$ and extends to 650K ($0.002 < T/T_m < 0.33$), the intermediate temperature behavior occurs between approximately 650 and 800K ($0.33 < T/T_m < 0.4$) and the high temperature behavior above 800K ($T/T_m > 0.4$). The limiting temperatures of each region increase with increase in strain rate. These deformation temperature regimes can be related to the relative mobility of the titanium and interstitial solute atoms deduced from the diffusion coefficients given in Tables 2.5 and 2.6. At very low, and at low temperatures both species of atoms are essentially immobile, at intermediate temperatures the interstitials become mobile and at high temperatures both are quite mobile.

The very low temperature behavior is characterized by pronounced serrations or stress drops in the stress-strain curve, whose envelope is nearly linear after the first few percent strain. The low temperature behavior is characterized by a strong effect of temperature and strain rate on the flow stress with approximately linear strain hardening at the low temperatures of the region and parabolic at the higher end. Further, the deformation becomes more isotropic as the temperature is decreased

in this regime. The intermediate temperature behavior is characterized by a very weak or nil effect of temperature and strain rate on the flow stress, slight serrations or irregularities in the stress strain curves, a maximum in strain hardening and creep resistance and a minimum in ductility. High temperature behavior is characterized by a strong effect of temperature and strain rate on the flow stress and very low or nil strain hardening. With the exception of the high temperature region, the characterizing features of each region are markedly influenced by the interstitial content. Microstructural features of significance in the various temperature regimes include: (a) the tendency for twinning generally increases with decrease in temperature, increase in grain size and decrease in interstitial content and (b) dislocations tend to be more planar and produce more debris and loops as the deformation temperature decreases and the interstitial content increases.

Further details regarding the deformation behavior in each of the four temperature regimes will now be given.

4.2.3 Very Low Temperatures ($T \approx 0.002T_m$)

Pronounced load drops or serrations in the stress-strain curves of polycrystalline titanium tested at 4.2K similar to those in Fig. 4.56 have been observed by a number of investigators (Refs. 2,172-175). Such serrations occur in compression as well as in tension and at approximately the same stress (Ref. 174). Audible clicks have been heard during the load drops (Refs. 173-175). The amount of the stress drop has been found to increase with strain, increase in interstitial content and decrease in grain size; see Fig. 4.57. Conversely, the frequency of the serrations tends to decrease with the conditions which lead to an increase in the

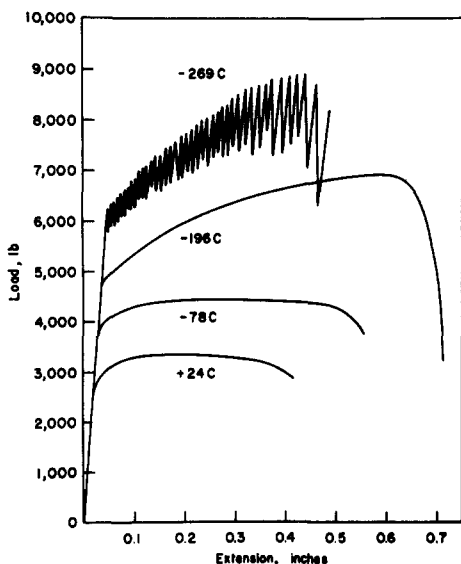


Fig. 4.56. Load-extension curves of commercially pure Ti showing serrations at 4.2K. From Kula and Desisto (Ref. 173).

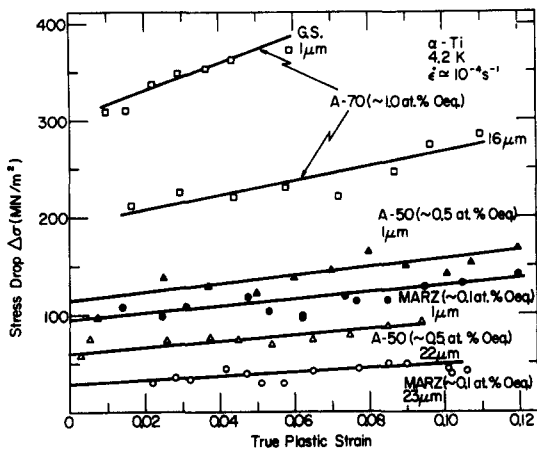


Fig. 4.57. Effect of strain on the stress drop $\Delta\sigma$ associated with the serrations in the stress-strain curves of titanium deformed at 4.2K as a function of purity and grain size. Data points do not include all stress drops. From Conrad, Tanaka and Yin (Ref. 175).

stress drop (Refs. 173,175); see, for example, Fig. 4.56. Fig. 4.58 shows that the size of the stress drop increases with increase in applied stress σ , relatively independent of the cause for the stress increase, i.e. whether it is due to straining, decrease in grain size or increase in impurity content.

4.2.4 Low Temperatures ($0.002 < T/T_m < 0.3$)

Effects of Grain Size, Interstitial Content, Temperature and Strain Rate on the Flow Stress and Hardness:

The effect of temperature on the flow stress of polycrystalline titanium given in Fig. 4.41 is typical of that for many metals in that the flow stress is sensitively dependent on temperature at low temperatures, becoming relatively independent of temperature at intermediate temperatures, before decreasing again at higher temperatures. Similar to single crystals, one can then consider the flow stress of polycrystals at low temperatures to consist of the sum of two components: a thermal component σ^* which is sensitively dependent on temperature T and strain rate $\dot{\epsilon}$ and an athermal component σ_μ which varies with temperature only as the modulus μ and which is given by the plateau region of the flow stress at intermediate temperatures. Considering the effect of temperature on the yield stress in terms of this concept, along with the results from temperature-cycle and strain rate-cycle tests, Conrad and coworkers (Refs. 161,172,193,204-220) found for both commercial titanums and synthesized titanium-interstitial alloys that σ^* is strongly dependent on the interstitial content C_i but to a lesser degree on strain ϵ , grain size d and substitutional solute content C_S ; whereas the reverse situation prevails for σ_μ ; see for example, Figs. 4.41, 4.42, 4.59-4.62^t. Hence, to a first approximation one

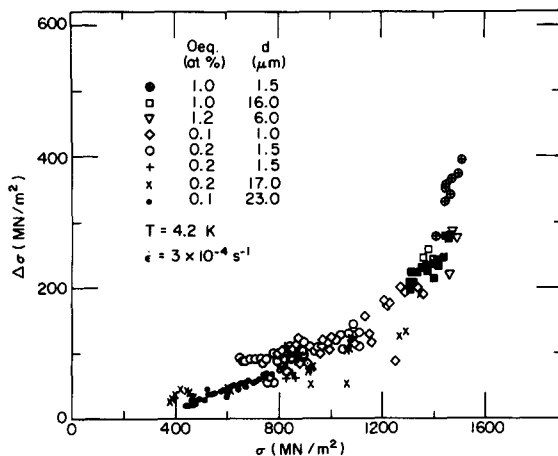


Fig. 4.58. Decrease in stress $\Delta\sigma$ associated with serrations in the stress-strain curves of titanium versus the applied stress σ as a function of strain, grain size and interstitial content.
From Conrad, Tanaka and Yin (Ref. 175).

^t μ used to get σ_μ as a function of temperature in Figs. 4.59, 4.60 and 4.62 is the polycrystalline shear modulus μ_p (Ref. 2), whose temperature dependence is the same as Young's modulus E and is ≈ 0.9 that of $\sqrt{K_e K_s}$ over the range 0-700K.

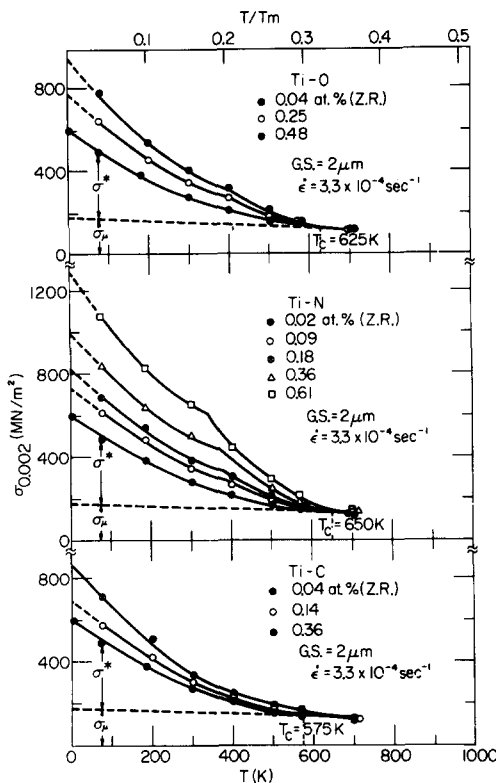


Fig. 4.59. Effect of temperature on the 0.2% yield stress of synthetic titanium-interstitial alloys of $2\mu\text{m}$ grain size. After Conrad, Doner, de Meester and Okazaki (Ref. 3).

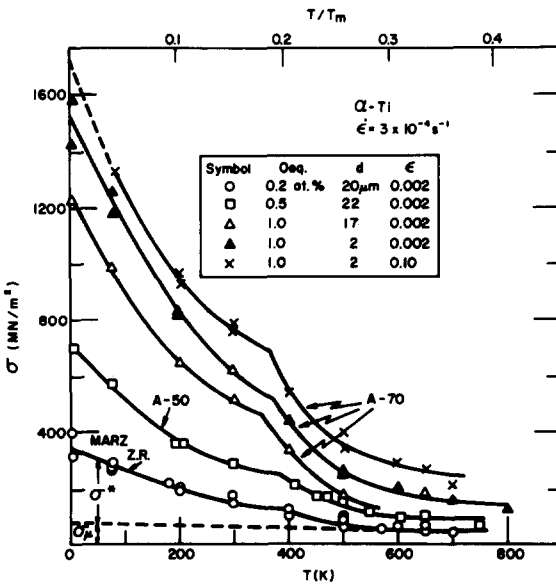


Fig. 4.60. Effect of temperature, interstitial content, grain size and strain on the flow stress of commercial titaniuns. Data from Refs. 172, 175, 197 and 207.

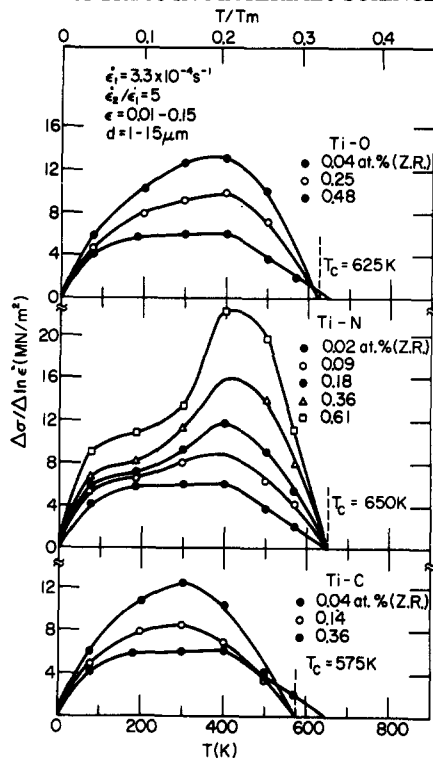


Fig. 4.61. Strain rate sensitivity parameter $\Delta\sigma/\Delta\ln\dot{\epsilon}$ versus temperature as a function of interstitial content for polycrystalline titanium. After Conrad, Doner and de Meester and Okazaki (Ref. 3).

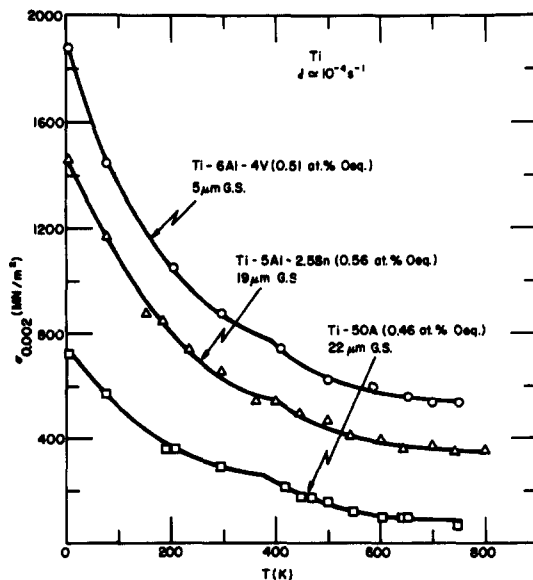


Fig. 4.62. Effect of temperature on the 0.2% yield stress of A-50 titanium and Ti-5Al-2.5Sn and Ti-6Al-4V alloys. Data from Refs. 176, 219, 220.

may write for the flow stress of titanium

$$\sigma \approx \sigma^*(T, \dot{\epsilon}, C_f) + \sigma_\mu(\mu, \epsilon, d, C_s) \quad (4.12)$$

it being recognized that σ^* depends to some degree on ϵ , d and C_s , and that σ_μ depends slightly on C_f . Further, the effects of ϵ and d on σ_μ will depend on the temperature and strain rate at which the deformation is performed. The temperature where σ^* is first zero, i.e. where $d\sigma/dT = d\mu/dT$, is designated as T_c and is in the range of 575-650K. Hence, σ_μ at temperature T is taken as the flow stress at T_c (or in the plateau region) corrected for the change in shear modulus μ , i.e.

$$\sigma_{\mu_T} = \sigma_{T_c} \mu_T / \mu_{T_c} \quad (4.13)$$

As mentioned above, under certain conditions a yield point occurs during the initial plastic deformation of polycrystalline titanium. The influence of grain size and interstitial content on the difference between the upper yield stress and the lower yield stress in titanium deformed at 300K is presented in Fig. 4.63. To be noted is that a yield point does not occur for grain sizes larger than some critical value, which is about 16 μm for A-70 (1.0 at. % Oeq) and about 4 μm for

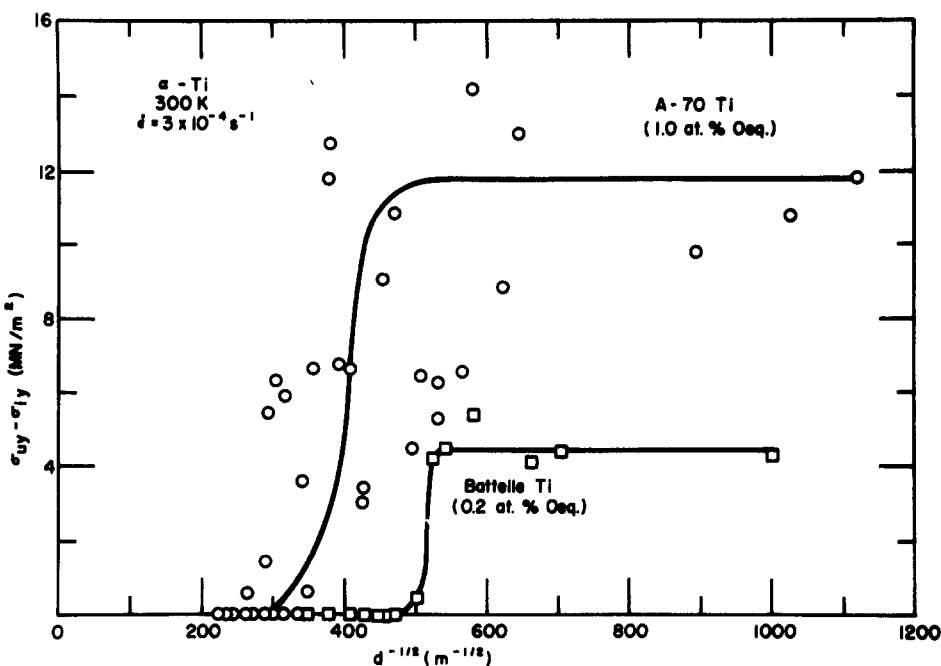


Fig. 4.63. Effect of grain size on the difference between the upper and lower yield stresses at 300K for two purities of titanium. Data from Conrad (Ref. 221).

Battelle titanium (0.2 at. % O_{eq}) at 300K. For grain sizes smaller than these critical values, the difference between the upper and lower yield stresses initially increases very rapidly and then remains relatively constant as the grain size is further decreased, the plateau value increasing with increase in interstitial content. When a yield point occurred, the effect of grain size on the upper and lower yield stresses was given by the Hall-Petch relation.

$$\sigma = \sigma_i + Kd^{-1/2} \quad (4.14)$$

σ_i was slightly higher for the upper yield stress compared to the lower yield stress and increased significantly with interstitial content, whereas K was relatively constant. The values of σ_i and K for the upper and lower yield stresses were similar in magnitude to those to be presented below for the 0.2% offset yield stress.

Worthy of mention at this time is that positive and negative yield points often occurred following the temperature or strain rate changes during cycling tests (Refs. 170,173,176,204-207,222). The degree or sharpness of such yield points increased with increase in interstitial content and decrease in grain size.

The effect of grain size on the 0.2% yield stress at 300K of titanium materials with various oxygen contents is shown in Fig. 4.64. It is seen that the data follow the Hall-Petch relation reasonably well over a rather wide range of grain sizes (0.5 - 29 μm). To be noted is that σ_i increases markedly with interstitial content, whereas K is relatively independent of the purity level.

The effect of temperature on Hall-Petch plots for the 0.2% yield stress of two materials representing extremes in oxygen content is depicted in Fig. 4.65, where it is seen that both σ_i and K increase with decrease in temperature. Similar behavior has been found for synthesized titanium-interstitial alloys (Ref. 224). A summary plot of the effect of the grain size on the yield stress of high purity titanium at various temperatures is presented in Fig. 4.66. Fig. 4.67 shows that the effect of temperature on σ_i ($\epsilon = 0.2\%$) as a function of interstitial content is similar to that for the yield stress shown in Figs. 4.59 and 4.60, except that the level of the stress for each temperature and interstitial content is lower. A summary plot of the effects of temperature and oxygen content on σ_i is given in Fig. 4.68.

The effect of temperature on K ($\epsilon = 0.2\%$) is presented in Fig. 4.69. Any effect of interstitial solutes on K was lost in the scatter of the data and hence only average values are given for the Ti-O, Ti-N and Ti-C alloys. The temperature dependence of K is larger than that of the polycrystalline shear modulus μ_p , being even greater than that of the most temperature dependent modulus C_{66} . For reasons which will become clear subsequently, K can be considered to consist of two components: one, K^U , which is the value at 650-700K corrected for the change in shear modulus μ_p with temperature, the other, K^* , which represents the additional temperature (and possibly strain rate) dependent component.

The effect of strain on the Hall-Petch plot for high purity titanium (MARZ zone-refined and Battelle) is illustrated in Fig. 4.70. It is seen that σ_i increases significantly with strain, whereas K remains relatively constant. However, in the strain range of 0.01 to 0.08, there was a tendency for the slope of the Hall-Petch plots for grain sizes greater than about 15 μm to be less than that for the smaller sizes. An example of this is the plot for the strain of 0.02. At strains ≥ 0.08

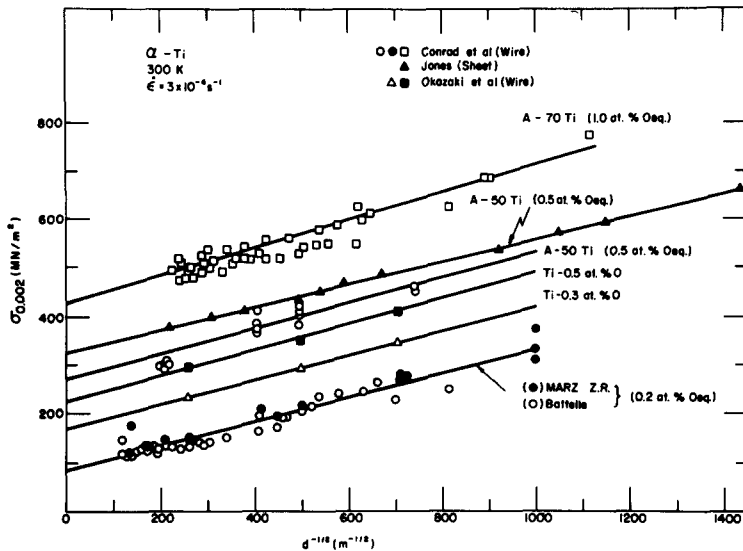


Fig. 4.64. Effect of grain size on the 0.2% yield stress at 300K of titanium materials with various oxygen contents. Data from Refs. 172,207,221,223-225.

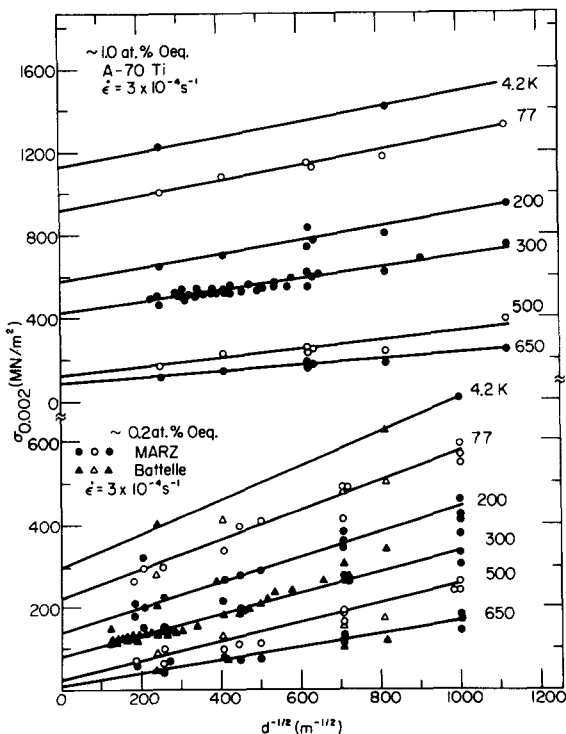


Fig. 4.65. Effect of grain size on the 0.2% yield stress of two purity levels of titanium as a function of temperature. Data from Refs. 172,197,207,221.

α -Ti (~0.2 at. % Oeq.)
 $\dot{\epsilon} = 10^{-4} \text{ s}^{-1}$

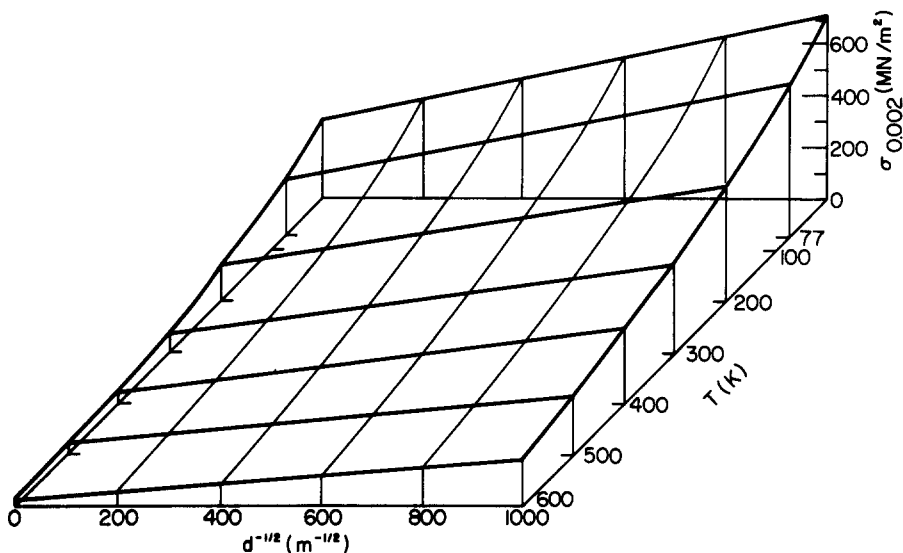


Fig. 4.66. Summary plot of the effect of grain size on the yield stress of high purity titanium as a function of temperature.

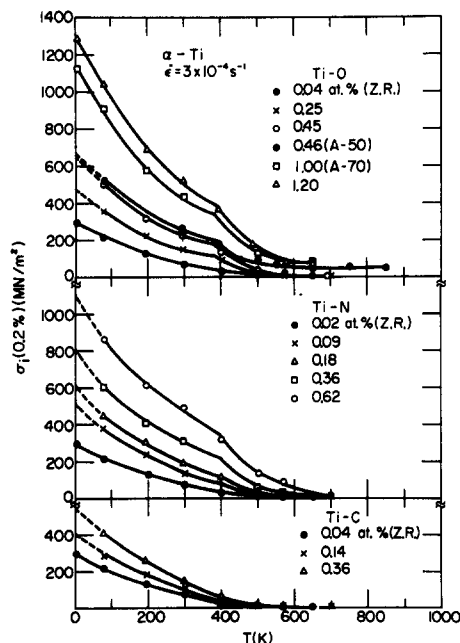


Fig. 4.67. Effect of temperature on the Hall-Petch constant σ_i as a function of interstitial content. Data from Refs. 172, 176, 197, 207, 221, 224, 225.

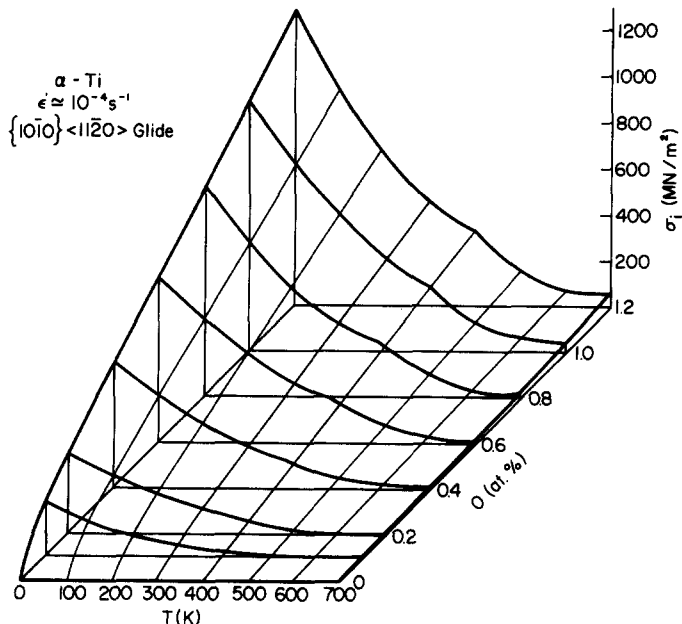


Fig. 4.68. Summary of the effects of temperature and oxygen content on σ_i for yielding of titanium polycrystals.

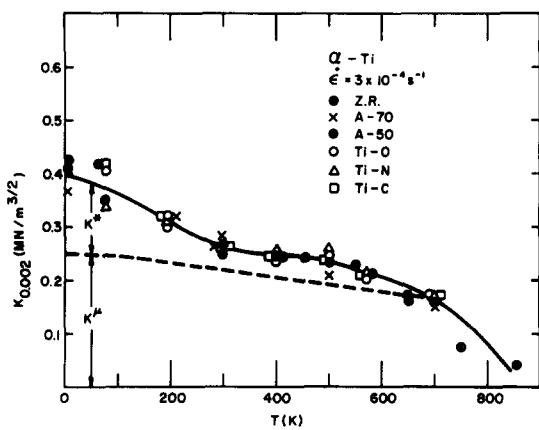


Fig. 4.69. Effect of temperature on the Hall-Petch constant K as a function of interstitial species and content. Data from Refs. 172, 176, 197, 207, 221, 224, 225.

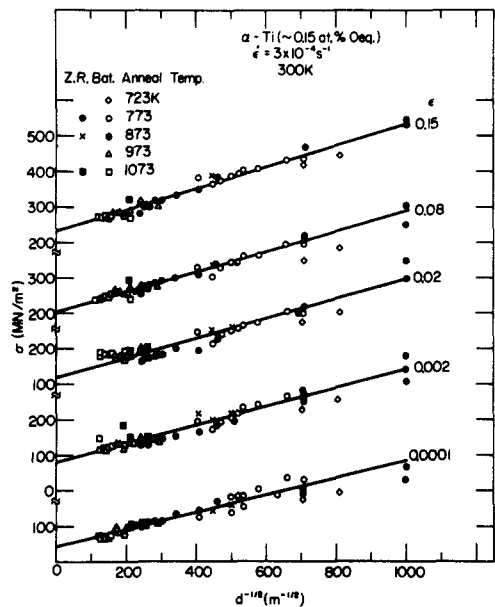


Fig. 4.70. Hall-Petch plots of the effect of grain size on the flow stress of MARZ zone refined (Z.R.) and Battelle (Bat.) titanium at 300K as a function of strain. Data from Ref. 197, 221.

this irregularity disappears again. Also evident in Fig. 4.70 is that the flow stress associated with a given grain size is essentially independent of the annealing temperature (and accompanying time) used to produce it. Results similar to those depicted in Fig. 4.70 were also found for A-70 (1.0 at. % O_{eq}) titanium at 300K (Ref. 221).

The results of Figs. 4.64 - 4.70 thus indicate that the effect of grain size on the flow stress of titanium is approximated by

$$\sigma \approx \sigma_i^*(T, \dot{\epsilon}, C_i, \epsilon) + \{K^*(T, \dot{\epsilon}) + K^\mu(\mu)\} d^{-1/2} \quad (4.15)$$

Employing the concept of Eq. 4.12, σ_i^* can be further broken down to yield

$$\sigma_i^* = \sigma_i^*(T, \dot{\epsilon}, C_i) + \sigma_i^\mu(\mu, \epsilon) \quad (4.16)$$

so that

$$\sigma \approx \{\sigma_i^*(T, \dot{\epsilon}, C_i) + \sigma_i^\mu(\mu, \epsilon)\} + \{K^*(T, \dot{\epsilon}) + K^\mu(\mu)\} d^{-1/2} \quad (4.17)$$

In keeping with Eq. 4.17, σ^* of Eq. 4.12 determined in the conventional manner (i.e. by employing Eq. 4.12 with the polycrystalline shear modulus μ_p to obtain σ_μ) was found to increase with decrease in grain size; see, for example, Fig. 4.71.

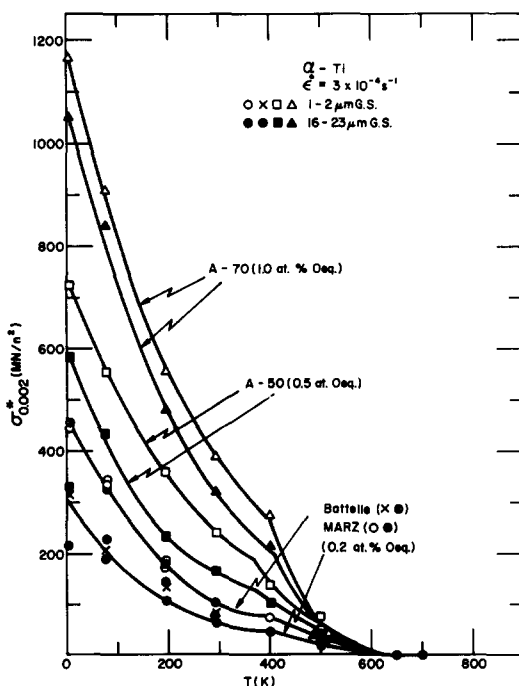


Fig. 4.71. The thermal component of the flow stress σ^* versus temperature as a function of grain size. Data from Refs. 170, 172, 176, 204, 207.

This occurred even when the most temperature dependent shear modulus C_{66} was employed, although, of course, to a lesser degree. This effect can be considered as the contribution of $K^* d^{-1/2}$ to σ_i^* , as illustrated in Fig. 4.72. There also existed some tendency for the strain rate sensitivity parameter $\Delta\sigma/\Delta\ln\dot{\epsilon}$ to increase with decrease in grain size (see Figs. 4.73 and 4.74); however, this effect is not as clear as that for σ^* .

Considering the results of Figs. 4.71 - 4.74 along with Eqs. 4.12 and 4.17 we can then write for the flow stress of titanium at low temperatures

$$\sigma \approx \{\sigma_i^* + K^* d^{-1/2}\} + \{\sigma_\mu^* + K^\mu d^{-1/2}\} \quad (4.18)$$

whereupon

$$\sigma^* \approx \sigma_i^* + K^* d^{-1/2} \quad (4.19)$$

and

$$\sigma_\mu \approx \sigma_\mu^* + K^\mu d^{-1/2}, \quad (4.20)$$

where the starred terms are temperature (and presumably strain rate) dependent and the μ terms vary only as the modulus.

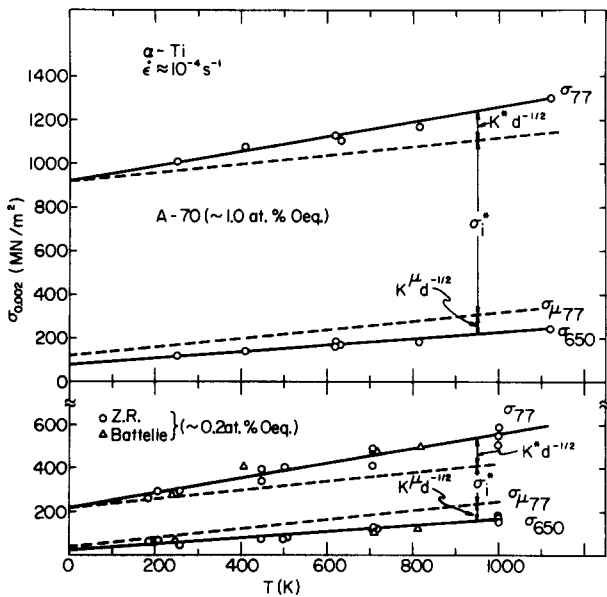


Fig. 4.72. Hall-Petch plot of the effect of grain size on the yield stress at 650 and 77K for two purity levels of titanium showing the contribution of $K^* d^{-1/2}$ to σ^* . Data from Refs. 172, 204, 207.

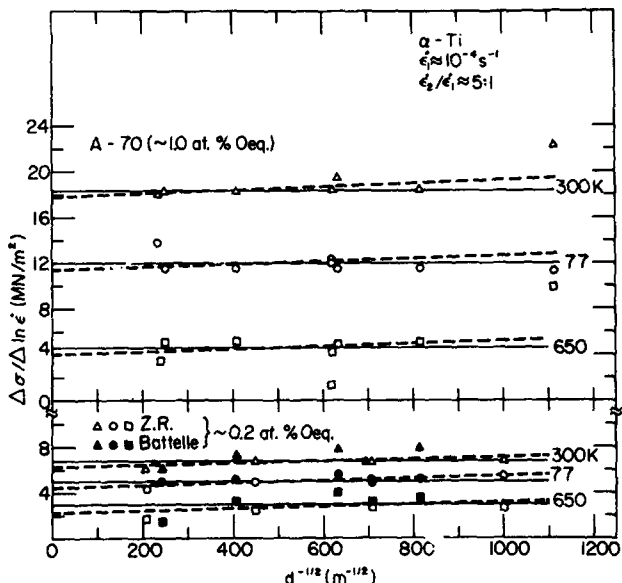


Fig. 4.73. The strain rate sensitivity parameter $\Delta\sigma/\Delta\ln\dot{\epsilon}$ versus $d^{-1/2}$ for two purity levels of titanium. Data from Refs. 171,207.

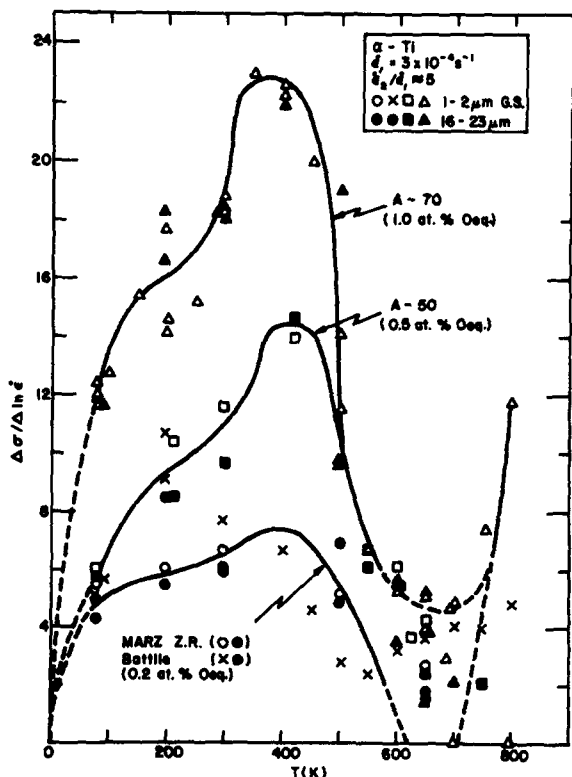


Fig. 4.74. $\Delta\sigma/\Delta\ln\dot{\epsilon}$ versus temperature as a function of grain size and interstitial content. Data from Refs. 169,171,196,204,221.

The effect of the total interstitial content on σ_i as a function of temperature is depicted in Fig. 4.75. Included are results for prism glide by Tanaka and Conrad (Ref. 138) and by Elssner, Krohn and Ruano (Ref. 145)[†]. Each set of curves is for the predominant interstitial solute considered. The filled circles at 4.2K are extrapolated values from the data of Okazaki and coworkers (Refs. 208-212,215). The data of Finlay and Snyder (Ref. 19), Jaffee, Ogden and Maykuth (Ref. 12) and that for the Ti-1.2 at. % O alloy (Ref. 197) have been corrected to $d^{-1/2} = 0$ by using the K values in Fig. 4.69. Evident in Fig. 4.75 is the strong effect of the interstitials on σ_i , which effect increases with decrease in temperature and is in the order C, O, N. Moreover, the results for prism glide are in good agreement with the polycrystalline data when a Taylor orientation factor of 2.5 is used to convert τ_{CRSS} for prism glide^{††} to σ_i . Further, the curves are parabolic at temperatures up to about 300K, nearly linear at about 400K and tend to be hyperbolic

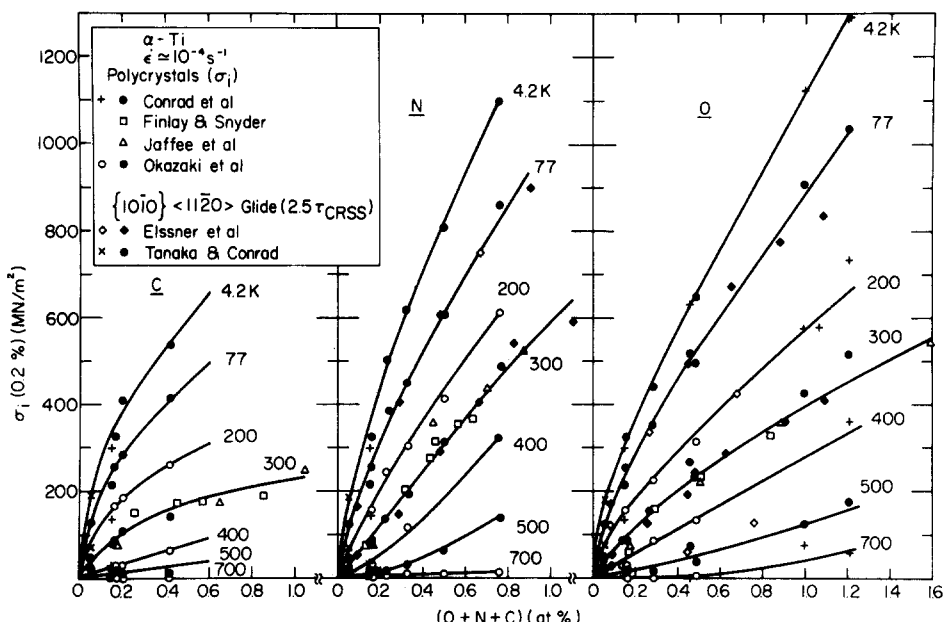


Fig. 4.75. σ_i versus the total O+N+C interstitial solute content as a function of temperature. Data from Refs. 12, 19, 138, 145, 172, 197, 221, 223-225.

[†] It is assumed that the yielding of the bamboo specimens by Elssner, Krohn and Ruano (Ref. 145) is by prism glide and that $\tau_{CRSS} = 0.45\sigma$.

^{††} Earlier limited data suggested that σ_i was 5 times the τ_{CRSS} for prism slip (Refs. 138,172). However, the present ratio of 2.5 seems more reasonable in view of the strong texture exhibited by the titanium materials considered. The earlier value of 5 was based mainly on a comparison of results on polycrystalline, zone-refined MARZ material with those on zone refined single crystals of the same designation. It now appears that the interstitial content of the MARZ polycrystalline material was significantly higher than that of the single crystals, thus leading to the erroneous, larger ratio.

at higher temperatures. Log-log plots of σ_i versus interstitial content yielded reasonably straight lines whose slopes in the temperature range of 4.2-300K ranged between 0.5 and 0.7, were of the order of one at 400K, and slightly greater than one at 500 and 700K.

The average rate of solid solution strengthening $\Delta\sigma_i/\Delta C_i$ in the composition range of 0.1 to 0.6 at.% for the three interstitial solutes C, N and O is depicted in Fig. 4.76. Again evident is the increase in strengthening with decrease in temperature. Also, for the composition range considered, the strengthening is in the order C, O, N, the values of $\Delta\sigma_i/\Delta C_i$ being 0.58E, 0.84E and 1.06E respectively at 4.2K (E = Young's modulus). The strengthening ratio of nitrogen and carbon compared to oxygen varies with temperature, being of the order of 1.2 to 1.5 for N:O and 0.5 to 0.7 for C:O. Also included in Fig. 4.76 are results for hardness measurements, which will be discussed below. Finally, of additional note regarding Fig. 4.76 is that an abrupt change in the slope of the curves of $\Delta\sigma_i/\Delta C_i$ versus temperature occurs at about 360-370K for N and O. No such change is clearly evident in the curve for C.

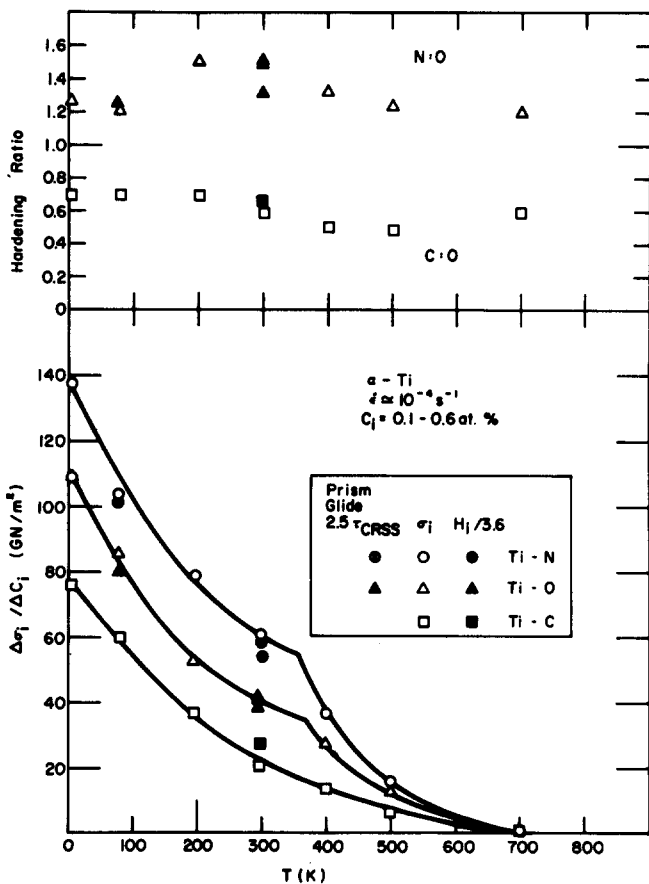


Fig. 4.76. The average rate of solid solution strengthening in the composition range of 0.1 to 0.6 at.% for C, N and O in titanium as a function of temperature. Also included are the results for prism glide in single crystals and hardness measurements.

As mentioned above, the flow stress σ of polycrystalline titanium can be considered to consist of a thermal component σ^* and an athermal component σ_μ , both increasing with decrease in grain size, as indicated by Eqs. 4.19 and 4.20. A Hall-Petch plot of the effect of grain size on σ^* for two extremes in interstitial content (mainly oxygen) is presented in Fig. 4.77. σ_μ at temperature T is here taken as $\sigma_{650} E_T / E_{650}$, where E is Young's modulus. It is seen in Fig. 4.77 that the data points for both interstitial contents lie reasonably well along straight lines in accord with Eq. 4.19. A plot of K^* and the ratio $\sigma^*(d=1\mu\text{m})/\sigma^*(d=\infty)$ taken from Fig. 4.77 is given in Fig. 4.78. Evident is that K^* decreases with temperature for both interstitial contents, being however larger for the A-70 material than for the high purity MARZ and Battelle materials. On the other hand, the ratio of stresses is relatively independent of temperature and is larger for the higher purity materials.

Let us now consider the effect of interstitial content on each of the two components σ^* and σ_μ at two extremes of grain size. The effect of interstitial content on σ_μ for a very large grain size is essentially that given by σ_i at 700K in Fig. 4.75. The effect on σ^* for a very large grain size is then the difference between σ_i at a specified temperature and the quantity $\sigma_i 700 E_T / E_{700}$. (It is of course also given by the effect of interstitial content on the intercept at the stress axis in plots such as those of Fig. 4.77). The effect of interstitial content on σ^* for a fine grain size ($1-2\mu\text{m}$) is presented in Fig. 4.79; it is similar to that for σ_i in Fig. 4.75. The effect of interstitial content on σ_μ is

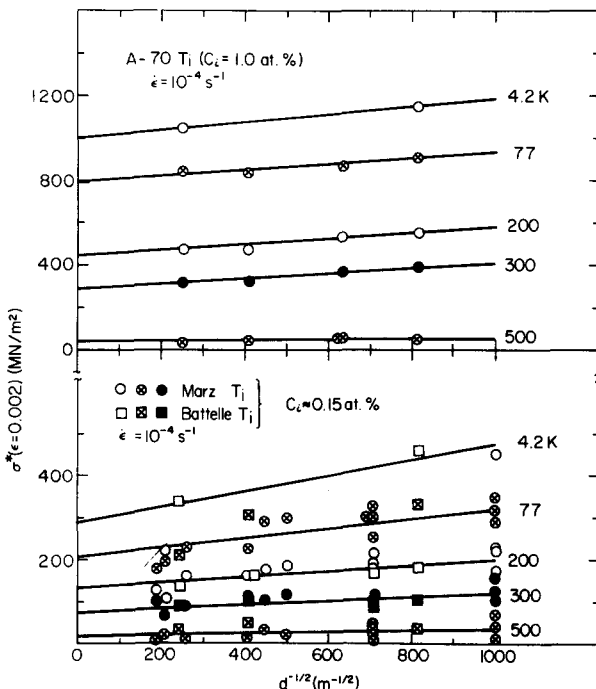


Fig. 4.77. Hall-Petch plot of the effect of grain size on $\sigma^*(0.2\%)$ for two extremes in interstitial content. Data from Refs. 172,224.

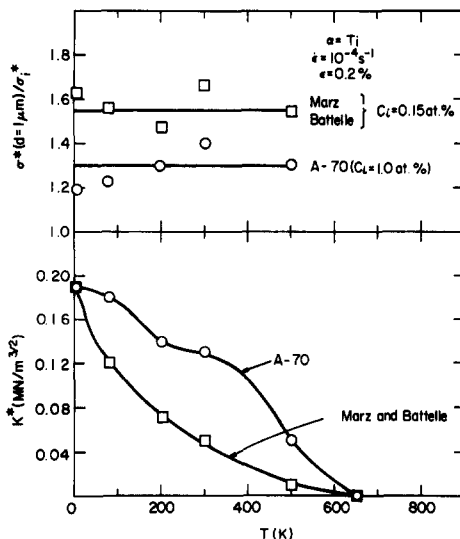


Fig. 4.78. K^* and the ratio $\sigma^*(d=1\text{ }\mu\text{m})/\sigma^*(d=\infty)$ versus temperature for two extremes in interstitial content.

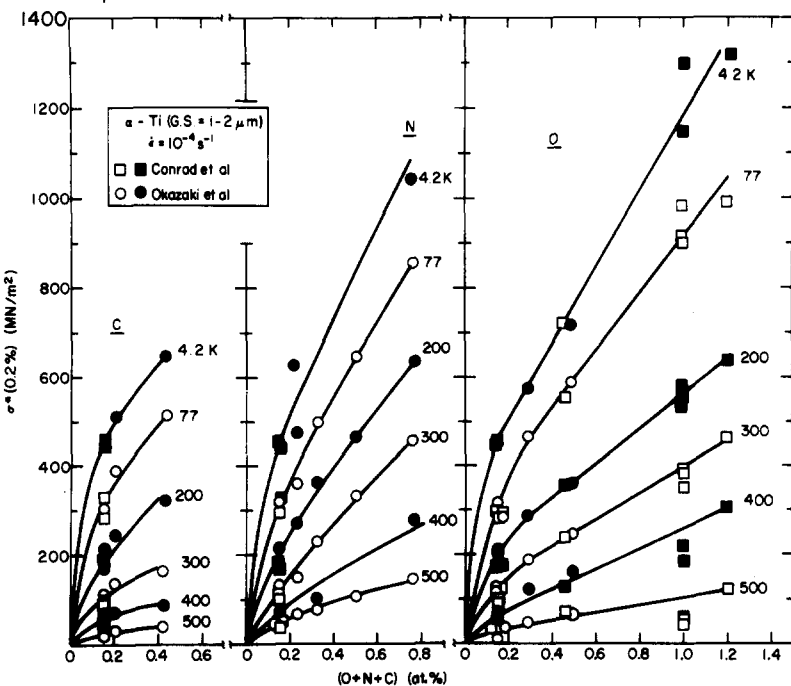


Fig. 4.79. σ^* versus the total interstitial content as a function of temperature. Data from Refs. 172, 197, 221, 224, 225.

shown in Fig. 4.80, which indicates an approximately linear increase beyond about $C_i = 0.1\text{ at. \%}$, giving $\Delta\sigma_\mu/\Delta C_i \approx 0.05 E$, where E is Young's modulus. Thus, the effect of interstitial solutes on σ_μ at 300K and below is considerably smaller than on σ^* .

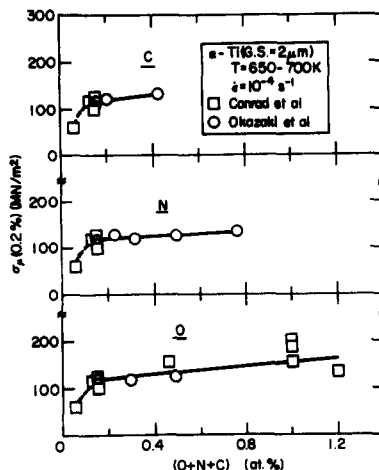


Fig. 4.80. σ_μ versus the total interstitial content. Data from Refs. 172, 197, 221, 224 and 225.

The effect of the interstitial solute content on the peak value (Ref. 204) of the strain rate sensitivity parameter $\Delta\sigma/\Delta\ln\dot{\epsilon}$ as a function of temperature is presented in Fig. 4.81. Since there were insufficient data to establish the effect

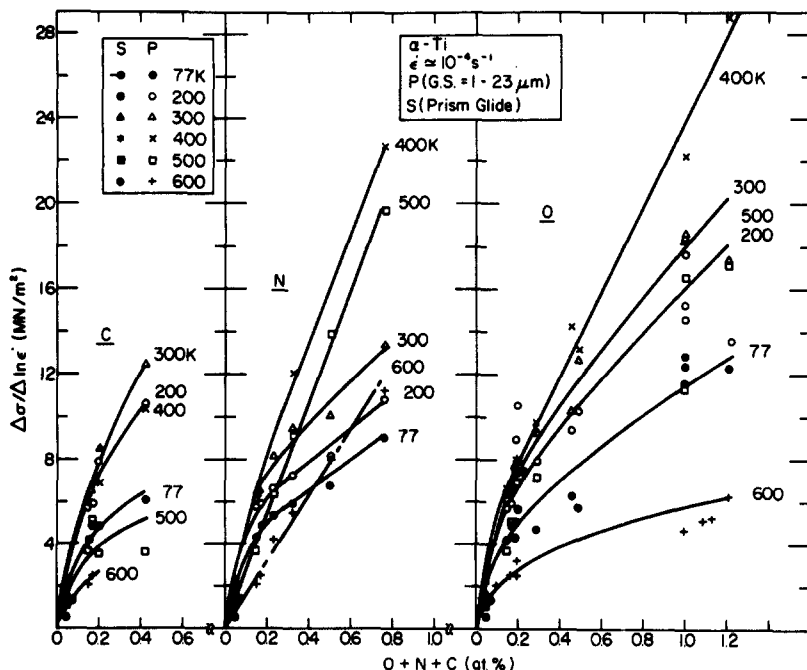


Fig. 4.81. The effect of interstitial content on the strain rate sensitivity parameter $\Delta\sigma/\Delta\ln\dot{\epsilon}$ as a function of temperature. P denotes polycrystals; S denotes single crystals. Data from Refs. 135, 138, 170, 172, 206-212, 215, 224.

of grain size on $\Delta\sigma_i/\Delta\ln\dot{\epsilon}$ accurately, the average value of $\Delta\sigma/\Delta\ln\dot{\epsilon}$ for the range of grain sizes considered is plotted. Also included are the values of $2.5(\Delta t/\Delta\ln\dot{\gamma})$ for prism glide taken from Tanaka and Conrad (Ref. 138) and Brehm and Lehr (Ref. 139), which lie along the curves for the polycrystalline specimens. Evident in Fig. 4.81 is that the curves are slightly parabolic, with the largest effect of the interstitials on the parameter $\Delta\sigma/\Delta\ln\dot{\epsilon}$ occurring at about 400K for O and N and at about 300K for C.

The relative effects of the three interstitials C, N and O on $\Delta\sigma/\Delta\ln\dot{\epsilon}$ for the composition range of 0.1 to 0.6 at. % (data for carbon has been extrapolated to 0.6%) is given in Fig. 4.82. To be noted is that the parameter $\delta(\frac{\Delta\sigma}{\Delta\ln\dot{\epsilon}})/\Delta C_i$ for the composition and temperature range considered peaks at about 300K for C, about 400K for O and about 450K for N. The ratios of this parameter for C and N with respect to O is given in the upper part of Fig. 4.82. It is seen that the values of these ratios and their temperature dependence differ from those for σ_i given in Fig. 4.76.

Similar to the yield and flow stresses, the effect of grain size on the hardness H of titanium is described quite well by the Hall-Petch relation (Refs. 221,226, 227) (see Fig. 4.83) giving

$$H = H_i + K_H d^{-1/2} \quad (4.21)$$

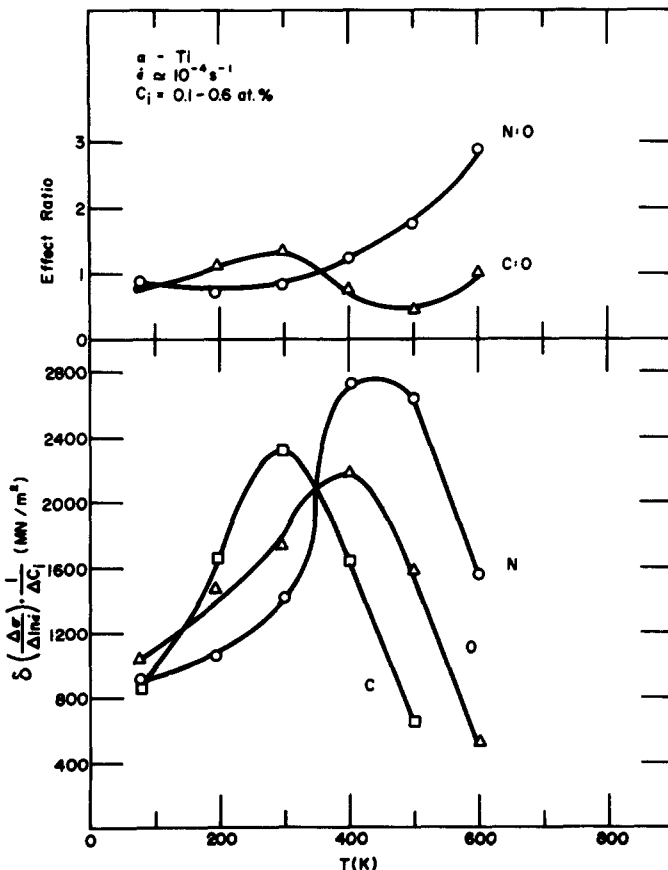


Fig. 4.82. $\delta \frac{\Delta\sigma}{\Delta\ln\dot{\epsilon}} / \Delta C_i$ versus temperature for the concentration range of 0.1-0.6 at. % C, N and O.

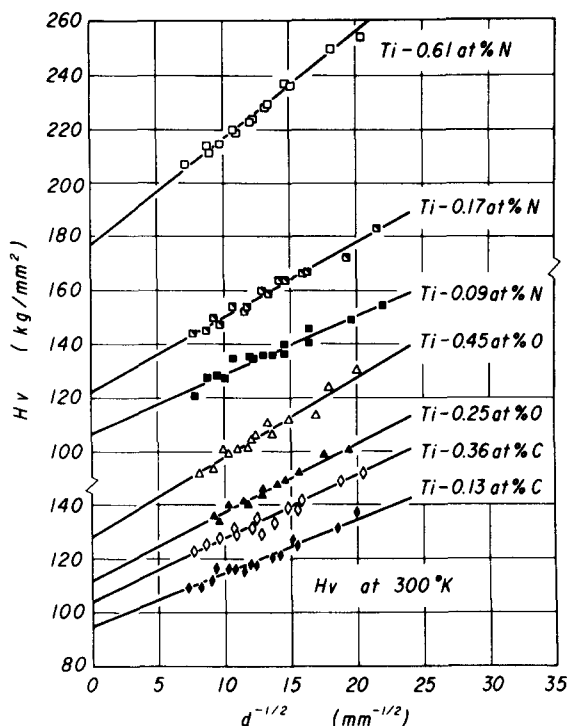


Fig. 4.83. Hall-Petch plots of the effect of grain size on the hardness of titanium at 300K as a function of interstitial content. From Okazaki and Conrad (Ref. 228).

That in fact this relationship applies over a very wide range of grain sizes (even though for sizes smaller than about $1\mu\text{m}$ the material was incompletely recrystallized) is illustrated in Fig. 4.84. Also to be noted from Fig. 4.84 is that H_i is in good accord with the hardness of single crystals of titanium of the same purity level.

The variation of H_i and K_H at 300K with interstitial content is depicted in Fig. 4.85. It is seen that both H_i and K_H increase with interstitial content, the effect being parabolic and in the order C, O, N. Moreover, H_i is in accord with the hardness of single crystals of the same interstitial content.

Jaffee, Ogden and Maykuth (Ref. 12) found that the Vickers hardness of titanium-interstitial alloys was proportional to the ultimate tensile strength, the proportionality constant being 3.5. The results of Finlay and Snyder (Ref. 19) were also in reasonable agreement with this proportionality, although some curvature was indicated in their plot. Fig. 4.86 shows that H_i increases in a linear fashion with σ_i for the 0.2% yield stress giving

$$H_i = 650 + 3.6\sigma_i(0.2\%) \quad (\text{MN/m}^2) \quad (4.22)$$

Further, it is found that $\frac{\Delta H_i}{3.6}/\Delta C_i$ is in accord with $\Delta\sigma_i/\Delta C_i$ for the same composition

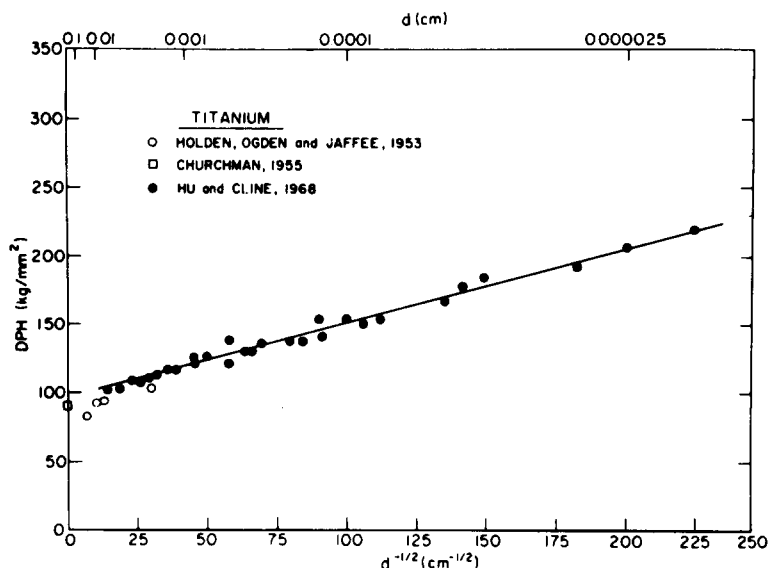


Fig. 4.84. Effect of grain size on the hardness of titanium at 300K. From Armstrong (Ref. 227).

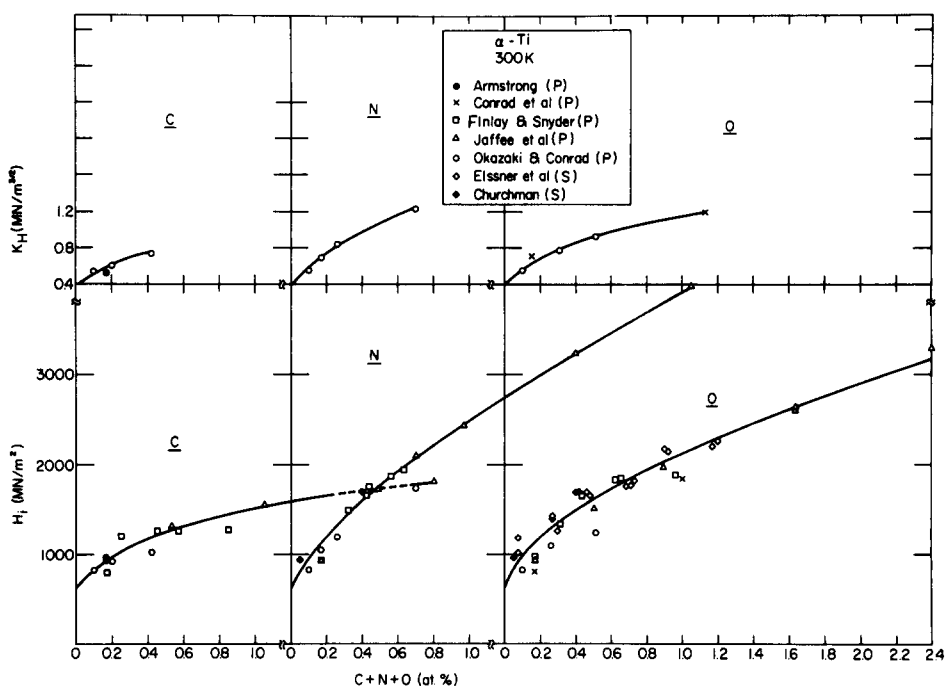


Fig. 4.85. H_V and K_H at 300K versus interstitial content in titanium. P denotes polycrystals; S denotes single crystals. Data from Refs. 12, 19, 43, 145, 197, 221, 227, 228.

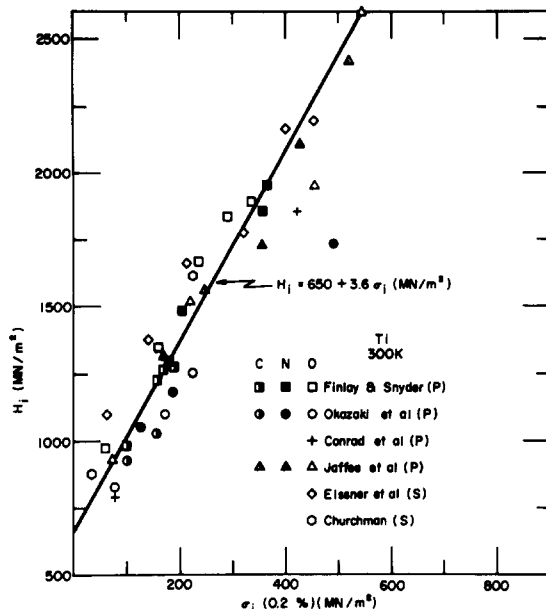


Fig. 4.86. H_B versus σ_y (0.2% at 300K.) P denotes polycrystals; S denotes single crystals. Data from Refs. 12, 19, 43, 145, 197, 224.

range (see Fig. 4.76); also $K_H/3.6$ is in accord with K determined in uniaxial tension (Fig. 4.69). However, K_H shows a variation with interstitial content, whereas this could not be discerned for K determined by tension tests. This difference is probably due to the magnifying influence produced by the factor 3.6 in the hardness tests. Finally, worthy of note regarding Fig. 4.86 is that the data for single crystals are in reasonable accord with the polycrystalline results when a Taylor factor of 2.5 is used to convert τ_{CRSS} for prism slip to σ_y .

An interpretation of Eq. 4.22 is that the term $3.6\sigma_y$ represents the hardness equivalent of the critical resolved shear stress for prism slip, while the quantity 650 measures the strain hardening produced by the hardness indentation. The factor of 3.6 is larger than the value of 3.0 relating hardness to tensile properties found by Tabor (Ref. 229) and Nunes and Larson (Ref. 230) for a large number of metals. The higher value for titanium may be due to the smaller number of equivalent slip systems. However, values greater than 3.0 have also been reported by Abson (Ref. 231) for cubic metals.

The strengthening effect of combined additions of the interstitial solutes C, N and O has been found to be approximately additive (Refs. 1, 12, 19, 232, 233). This led Finlay and Snyder (Ref. 19) to propose the concept of expressing the concentration of all elements present in terms of an equivalent concentration of one element. They chose nitrogen as the standard element and derived the strengthening ratio of N:O:Fe:C to be 1.0:0.82:0.20:0.14 from the effects of these elements in atomic percent on the ultimate tensile strength of titanium. Subsequently, Brown, Folkman and Schussler (Ref. 232) correlated the Brinell hardness with chemical composition (presumably in wt.%) of 152 lots of titanium sponge and obtained

$$BHN = 57 + 196 \sqrt{\%N} + 158 \sqrt{\%O} + 45 \sqrt{\%C} + 20 \sqrt{\%F_e} \quad (4.23)$$

Later, Wood (Ref. 233) proposed that a good approximation to the strengthening

effect, and loss in ductility, of the interstitials in titanium was in the proportion: 3 carbon approximates 2 oxygen approximates 1 nitrogen (again presumably in wt.%). Using these equivalents he found that the Vickers Hardness Number was given by

$$VHN = 65 + 310 \sqrt{O_{eq}(\%)} \quad (4.24)$$

Since then, the concept of an equivalent interstitial concentration has been employed by a number of investigators and a summary of the ratios derived is given in Table 4.5. It is seen that the N:O ratio ranges from 1.31 to 2.29 and the C:O ratio from 0.11 to 0.76, depending on the method by which each is determined. This variation in the value of a given ratio is not surprising, for an accurate determination of the ratio is only possible if the form of the strength versus composition curves for the two solutes considered is the same and if the equation expressing the concentration dependence is known. For example, if the form of the curves

TABLE 4.5 Ratios for Calculating an Oxygen Equivalent
in at. % at 300K of N and C in Titanium

<u>Ref</u>	<u>Basis</u>			<u>Assumed Conc. Dependence</u>
	<u>N:O</u>	<u>C:O</u>	<u>Property</u>	
a	1.60	0.23	UTS	Linear
b	2.29	0.76	UTS	Linear
b	2.29	0.59	R.A.	Linear
c	1.75	0.11	BHN	Square Root
d	2.00	0.75	YS	Linear
e	2.26	0.51	YS	Linear
f	1.96	0.52	VHN (H_i)	Square Root
f	1.96	0.55	VHN (K_H)	Square Root
g	1.50	0.60	YS (σ_i)	Linear
g	1.51	---	CRSS Prism Glide	Linear
g	1.31	0.67	VHN (H_i)	Linear

References:

- a. W. L. Finlay and J. A. Snyder, Trans. AIME 188, 277, 1950.
- b. R. A. Wood, "Titanium Metallurgy Course", New York University, 1965.
- c. C. M. Brown, R. L. Folkman and M. Schussler, "Preliminary Report on the Properties of Sodium Reduced Titanium", AIME Regional Reactive Metals Conf., Buffalo, New York, 1956.
- d. H. Conrad, Acca Met. 14, 1631, 1966.
- e. W. R. Tyson, Canad. Met. Quart. 6, 301, 1968.
- f. K. Okazaki and H. Conrad, Trans. TIM 14, 364, 1973.
- g. Present results, Fig. 4.76.

is parabolic, then the ratio based on a linear dependence will decrease with increase in solute content. For concentrations of the order of 0.1 at. % the ratios of $d\sigma_i/dC_i$ (taken from the slopes of curves of σ_i vs. C_i) for N:O:C is about 1:1:1, while at 1.0 at. % the ratios are more nearly 2:1:0.33.

Hydrogen was not included in the above discussion on the effects of interstitial solutes on the flow stress and hardness of titanium, since this element in solid solution at concentrations considered here (up to 1 at. %) has negligible effect on the tensile properties of titanium (Refs. 1,234). Concentrations of hydrogen greater than the solubility limit lead to the precipitation of the hydride, which has a pronounced detrimental effect on the ductility and toughness of titanium (Ref. 234).

Strain Hardening:

The effects of grain size, interstitial content and temperature on the average rate of strain hardening over the strain range of 0.002 to 0.10 (i.e. on $(\sigma_{0.10} - \sigma_{0.002})/0.098$) are depicted in Figs. 4.87 and 4.88. From Fig. 4.87 it is seen that the average rate of strain hardening decreases as the grain size becomes smaller. The effects of interstitial content and temperature are however not as straightforward; see Fig. 4.88, which shows the effects of these parameters at a constant

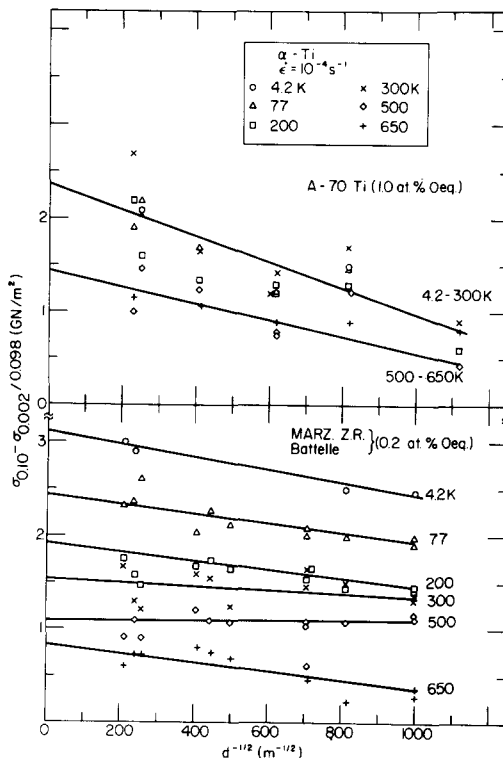


Fig. 4.87. Effect of grain size on the average rate of strain hardening between 0.002 and 0.10 strain as a function of purity and temperature. Data from Ref. 197.

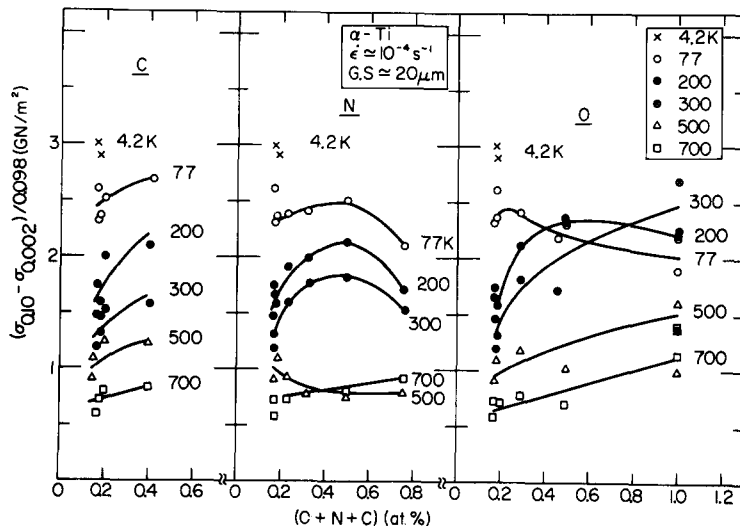


Fig. 4.88. Effect of interstitial content on the average rate of strain hardening between 0.002 and 0.10 strain as a function of temperature for titanium of $\sim 20 \mu\text{m}$ grain size. Data from Ref. 197.

grain size of $20 \mu\text{m}$. At low interstitial contents, the strain hardening increases with increase in interstitial content and decrease in temperature. However, with further increase in interstitial content, the strain hardening may go through a maximum. In the case of oxygen, this maximum varies with test temperature, thereby leading to an anomalous temperature dependence of strain hardening at the higher oxygen contents.

A more detailed description of strain hardening is provided by considering the slope $d\sigma/d\epsilon$ of the stress-strain curve versus the strain ϵ , i.e. by so-called Crussard-Jaoul plots (Refs. 235-237). Such plots are presented in Figs. 4.89 and 4.90 for zone-refined MARZ titanium (0.15 at. % O_{eq}) and A-70 titanium (1.0 at. % O_{eq}) as a function of grain size and temperature. Following Reed-Hill and coworkers (Refs. 195, 240-242a) one can consider the curves to consist of one or more linear regions or stages. The results in Figs. 4.89 and 4.90 suggest three such stages, which appear to have counterparts as the temperature, grain size and interstitial content are varied. The occurrence and extent of Stages I and II are favored by high interstitial content and low temperatures, whereas just the reverse is true for Stage III, especially at the higher temperatures. Thus, Stages I and II are evident for high interstitial content, low temperatures and fine grain size, whereas Stage III becomes predominant at temperatures above 200K in materials of low interstitial content and large grain size. Since Stages I and II are favored by high interstitial content at low temperatures, it does not appear that twinning is primarily responsible for these stages.

The dislocation structures associated with the various stages in the Crussard-Jaoul plots for MARZ and A-70 titaniums are illustrated in Figs. 4.91 and 4.92. Stage I is characterized by a planar, banded dislocation structure, Stage II by a uniform tangled structure and Stage III by the formation of cells. Of interest regarding the presence of cells in Stage III of titanium is that Jaoul (Ref. 237) and Morrison (Ref. 243) had earlier proposed that the occurrence of Stage III in metals was indicative of the development of a cell-type dislocation structure.

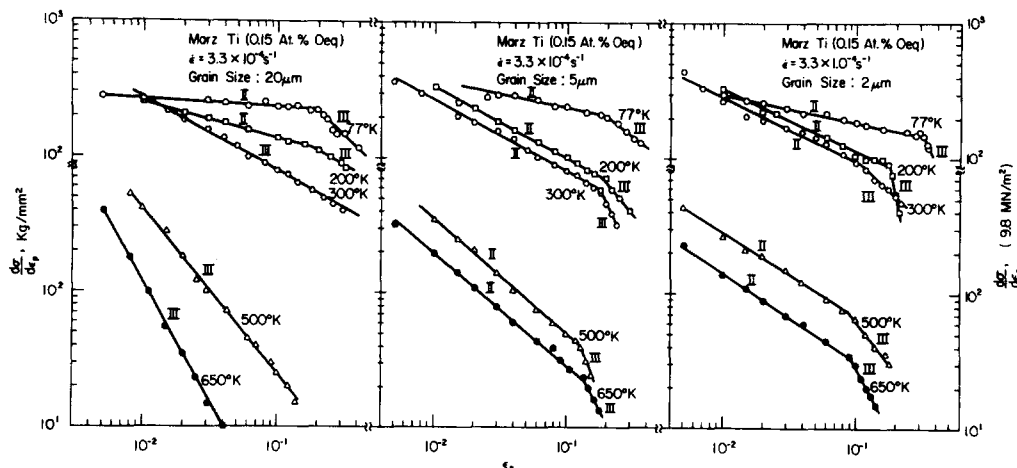


Fig. 4.89. Log $d\sigma/d\epsilon$ versus $\log \epsilon_p$ for zone-refined MARZ titanium as a function of grain size and purity. From Refs. 238 and 239.

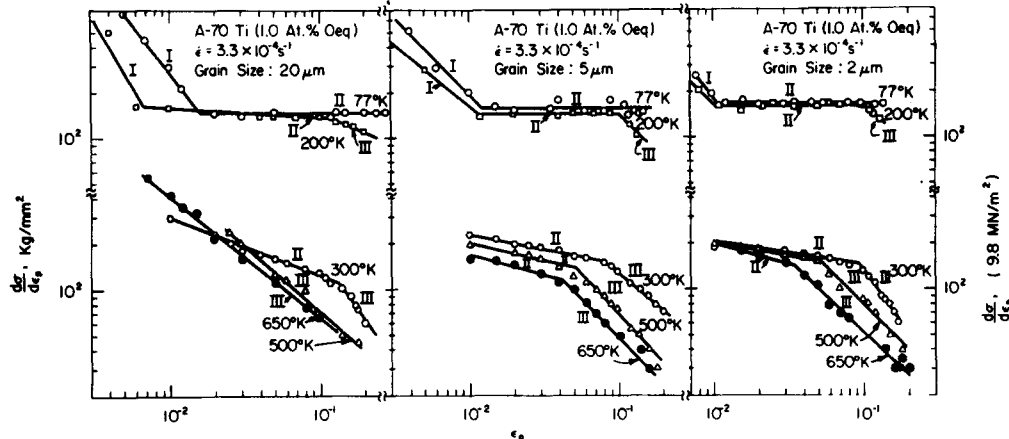


Fig. 4.90. Log $d\sigma/d\epsilon$ versus $\log \epsilon_p$ for A-70 titanium as a function of grain size and purity. From Refs. 238 and 239.

Of additional interest regarding the strain hardening of titanium at low temperatures are the early results of Geil and Carwile (Ref. 244), who found that the stress-strain curve of commercial purity titanium at a given temperature was dependent on the prior deformation history, indicating that the plastic flow of titanium at low temperatures does not obey a mechanical equation of state. The behavior of CPH titanium is intermediate between that of FCC metals and BCC metals (Ref. 245). Of related interest is that work softening occurred upon straining titanium at 300K following a prior deformation of $\epsilon = 0.45$ at 77K (Ref. 244).

A consideration of the strain hardening of titanium in terms of the effect of dislocation density on the flow stress is presented in Figs. 4.93 and 4.94, which

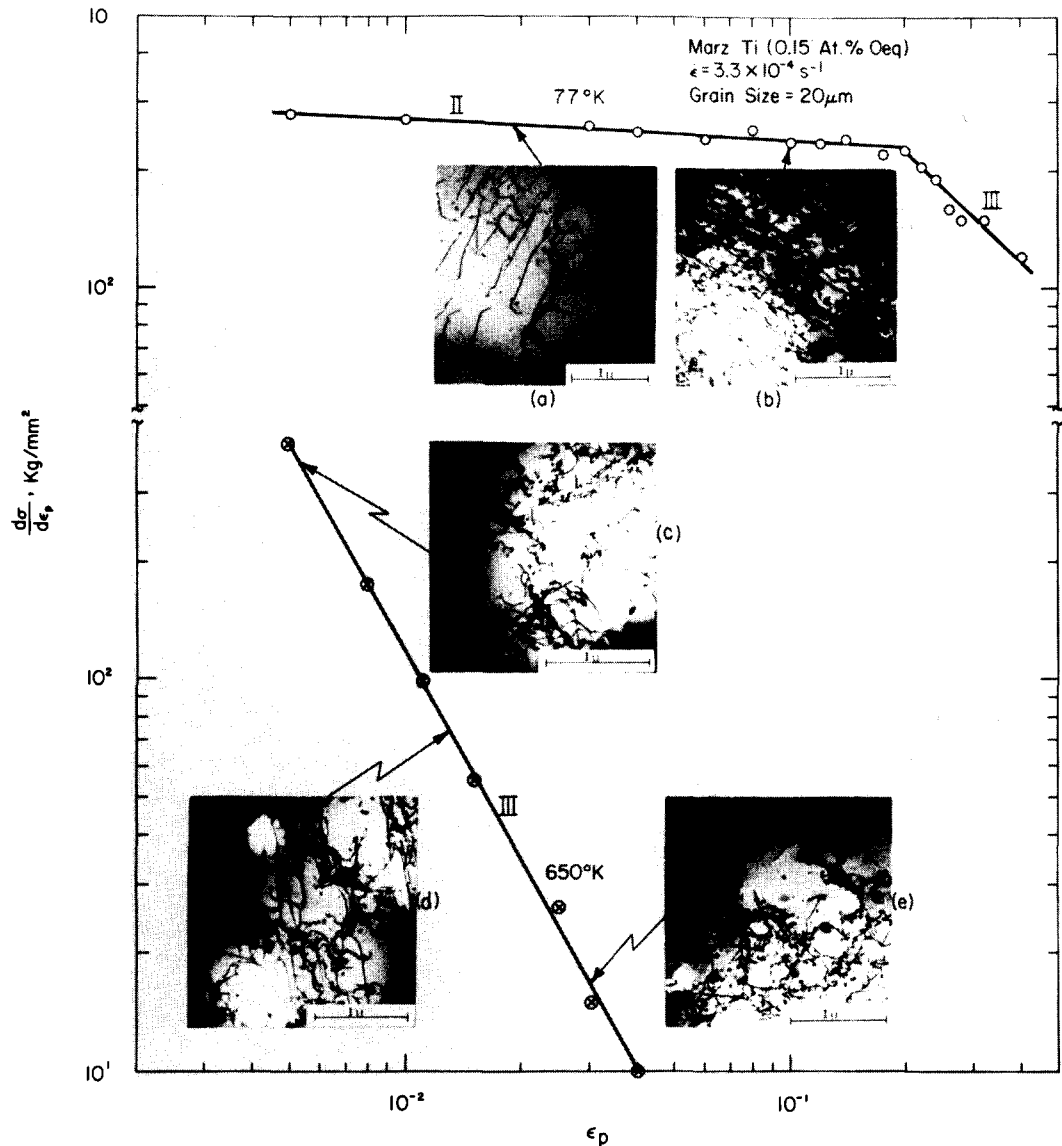


Fig. 4.91. Dislocation structures associated with the various stages in Jaoul-Crussard plots of strain hardening in MARZ titanium of $20 \mu\text{m}$ grain size deformed at 77 and 650K. The average dislocation densities in cm^{-2} at the strains corresponding to the photomicrographs are: (a) 5.8×10^9 ; (b) 38.5×10^9 , (c) 13.2×10^9 ; (d) 30.5×10^9 and (e) 31.3×10^9 . From Refs. 238 and 239.

give the flow stress versus the square root of the dislocation density as a function of grain size for MARZ, Battelle and A-70 titaniums deformed at various temperatures. To be noted is that the data points for the various grain sizes at each deformation temperature lie reasonably well on a single straight line, whose slope B is essentially independent of interstitial content and only weakly dependent on

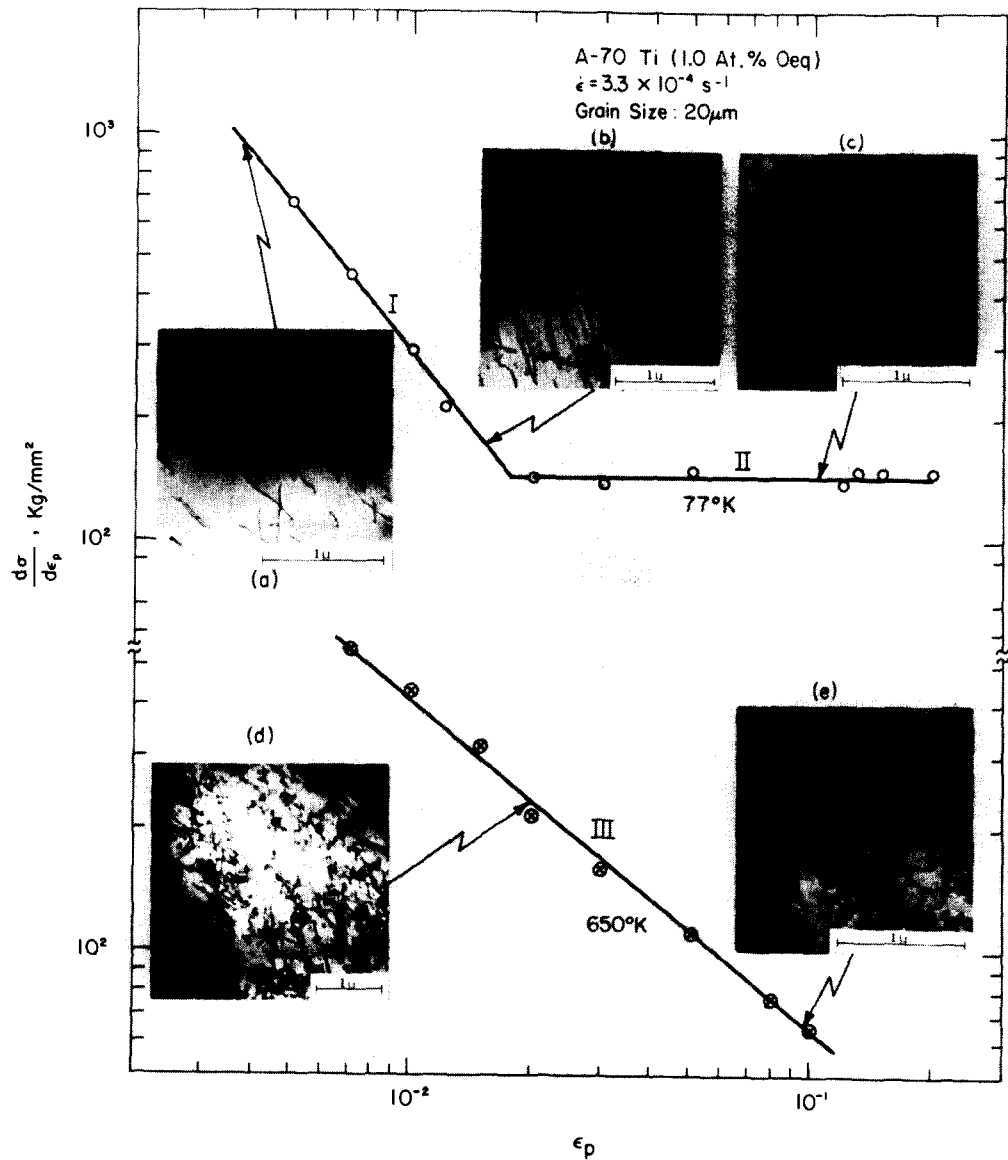


Fig. 4.92. Dislocation structures associated with the various stages in Jaoul-Crussard plots of strain hardening in A-70 titanium of $20\mu\text{m}$ grain size deformed at 77 and 650K. The average dislocation densities in cm^{-2} at the strains corresponding to the photomicrographs are: (a) 2.6×10^9 , (b) 2.7×10^9 , (c) 16.1×10^9 ; (d) 11×10^9 and (e) 18.5×10^9 . From Refs. 238 and 239.

temperature, but whose intercept σ_f increases markedly with interstitial content and with decrease in temperature, yielding

$$\sigma = \sigma_f(T, \dot{\epsilon}, C_i) + B_p^{1/2} \quad (4.25)$$

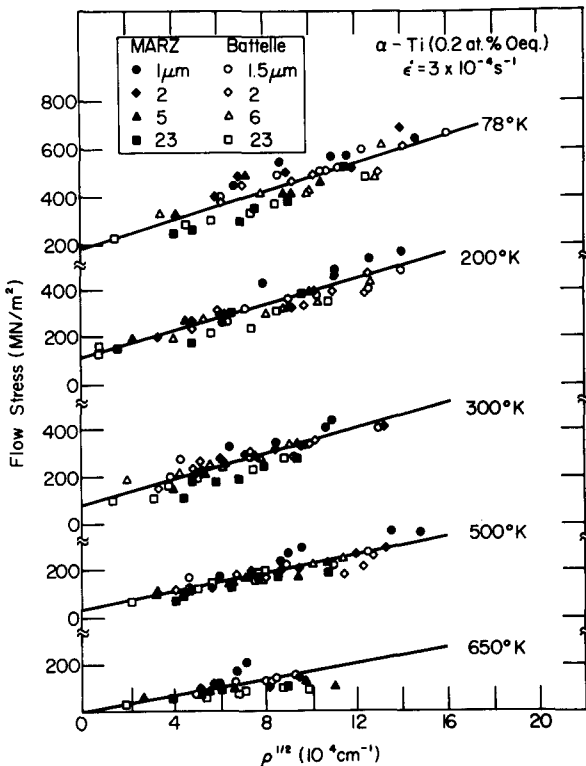


Fig. 4.93. Flow stress versus the square root of the dislocation density for MARZ zone-refined and Battelle titaniums of various grain sizes deformed at 78 to 650K. Data from Refs. 169, 246, 247.

Values of σ_f , B and $\alpha' = B/E_b$ (E is Youngs modulus and b the Burgers vector) derived from Figs. 4.93 and 4.94 and other similar data in the literature for titanium are presented in Table 4.5. Worthy of note is that α' tends to increase slightly with decrease in temperature suggesting that the temperature dependence of B may be greater than that of Youngs modulus. The results of Figs. 4.93 and 4.94 show that: (a) the principal effect of grain size on the flow stress is through its influence on the dislocation density produced at a given strain, and (b) that strain and grain size do not affect σ_f appreciably.

A comparison of the values of σ_f with σ_i , σ^* (for $\epsilon = 0.002$) and $2.5 \tau_{CRSS}$ for prism glide for two extremes in interstitial content is presented as a function of temperature in Fig. 4.95. For the most part, reasonable accord exists between these various flow stress parameters. However σ^* for the coarse grain size ($d \approx 20\mu\text{m}$) tends to be smaller than the other parameters at a given temperature, the difference becoming especially pronounced for the higher purity materials at temperatures below 200K.

Internal Stress:

A number of methods have been employed to determine experimentally the thermal (σ^*) and athermal (σ_u) components of the flow stress of metals at low temperatures. The most common has been the Seeger back-extrapolation method

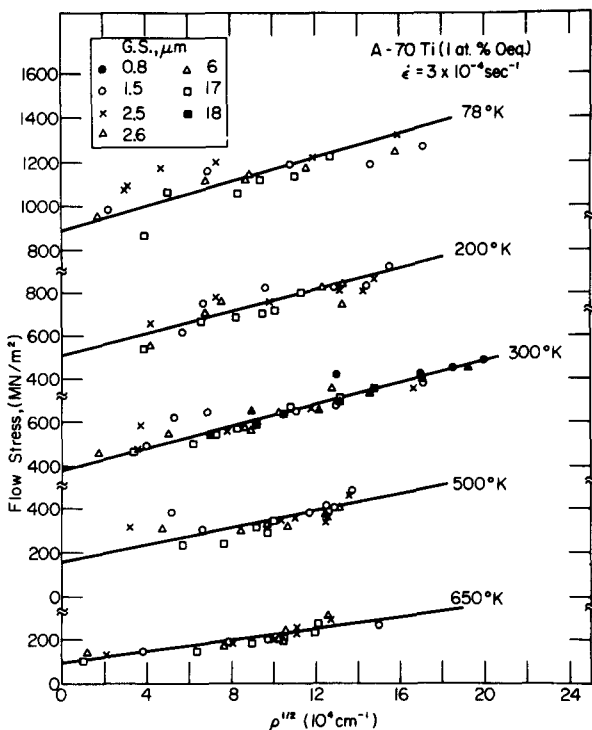


Fig. 4.94. Flow stress versus the square root of the dislocation density for A-70 titanium of various grain sizes deformed at 78 to 650K. Data from Refs. 169 and 246.

(Refs. 146,248), which yields σ_{μ} and in turn σ^* . Other methods which had been employed to determine σ_{μ} up to the year 1970 were reviewed by Conrad (Ref. 249), the most notable being:¹⁴(a) the double strain rate-cycling method, (b) analysis of the stress relaxation curve, (c) the decremental unloading method, and (d) measurements of dislocation density and curvature. Subsequently, Okazaki and Conrad (Ref. 250) showed that σ^* (and in turn σ_{μ}) could also be obtained for titanium by employing single strain rate-cycling tests carried out on specimens representing a range in grain sizes.

In an early study into determining the value of σ_{μ} in titanium, Conrad and Okazaki (Ref. 251) found that the internal stress[†] σ_{int} at the 0.2% yield stress for Battelle titanium wire (0.2 at. % O_{eq}) was essentially the same (within the $\pm 5\%$ scatter of the data) for the following seven techniques: (a) back-extrapolation, (b) double strain rate-cycling, (c) flow stress versus square root of the dislocation density, (d) grain size method, (e) fully relaxed stress, (f) decremental

[†]It is desirable at this point to distinguish σ_{int} as measured by a given experimental technique and the physical quantity σ_{μ} , which represents the maximum amplitude of the long-range internal stress field and is proportional to some modulus. σ_{int} obtained by a given technique may not necessarily be a measure of σ_{μ} .

TABLE 4.6 Values of the Parameters σ_f , B and α' ($= B/E_b$)[†] as a Function of Interstitial Content and Temperature.

Material	$O + N + C$	O_{eq}^{++}	Grain Size	T	σ_f	B	α'	Ref.
	at. %	at. %	μm	$^{\circ}K$	MN/m ²	N/m		
Iodide	0.05	0.09	1.1-3.3	300	88	20.3	0.60	a
			29	300	88	11.5	0.34	
Battelle	0.17	0.19	1.5	300	108	22.3	0.66	b
MARZ Z.R. and Battelle	0.17	0.18	1-23	77	186	29.4	0.77	c
				200	118	27.4	0.75	
				300	88	21.2	0.63	
				500	30	18.5	0.63	
				650	0	17.2	0.65	
A-70 Ti	0.90	1.00	0.8-18	77	882	30.0	0.78	d
				200	510	25.5	0.70	
				300	382	29.9	0.88	
				500	157	19.8	0.67	
				650	88	12.7	0.48	

Notes:

[†] E is Youngs modulus at each temperature; b = 2.95 \AA is the Burgers vector

⁺⁺ $O_{eq} = \text{at. \% } O + 2 \text{at. \% } N + 0.75 \text{at. \% } C$

References:

- a. R. L. Jones and H. Conrad, Trans. TMS-AIME 245, 779, 1969.
- b. H. Conrad and K. Okazaki, Scripta Met. 4, 111, 1970.
- c. Present Fig. 4.93.
- d. Present Fig. 4.94.

unloading, and (g) analysis of the stress relaxation curve. Subsequently, Okazaki and Conrad (Ref. 250) found agreement in the value of σ_{int} obtained by the back-extrapolation method and that by single and double strain rate-cycling methods for zone-refined MARZ titanium wire deformed in the temperature range of 77-500K. Agreement was also obtained between the back-extrapolation method, the single strain rate-cycling and the stress relaxation methods for dilute Ti-N alloys deformed over the range of 77-700K (Refs. 251,252).

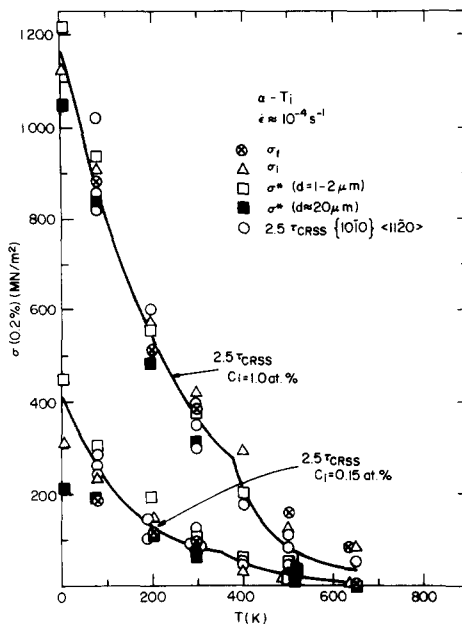


Fig. 4.95. A comparison of σ_f with σ_l , σ^* and $2.5 \tau_{CRSS}$ for prism glide. Data from Table 4.5 and Figs. 4.14, 4.15, 4.75 and 4.79.

On the other hand, Tung and Sommers (Ref. 253) found upon investigating σ_{int} in commercial A-55 titanium sheet (0.5 at. % O_{eq}) over the temperature range of 300 to 500K that σ_{int} determined by the back-extrapolation method (BE) was less than that by the decremental unloading technique (DU) and the fully relaxed stress method (SR) (by approximately 18% at 300K using the polycrystalline shear modulus μ_p), the latter two methods yielding essentially the same values for σ_{int} . Further, the temperature dependence of σ_{int} determined by the latter two techniques was larger than that of the shear modulus. As an explanation, these authors suggested that the stronger temperature dependence of σ_{int} resulted from the fact that the dislocation structure formed during yielding is a function of the deformation temperature.

Subsequently, Williams, Sommer and Tung (Ref. 196) extended the work of Tung and Sommers to include a broader temperature range (200 to 500K) and interstitial content range (0.2 to 1.6 at. % O_{eq}); moreover, they carried out concurrent measurements of the dislocation structure by TEM. They again found that σ_{int} by the DU and SR tests was significantly higher than by the BE method, the difference increasing with increase in oxygen content and decrease in temperature; see Fig. 4.96. To be noted here is that the difference between the DU and BE methods for constant (τ_{int}/G) is small for interstitial contents of the order of 0.2% O_{eq} , in accord with the findings of Conrad and Okazaki (Ref. 251), but increases with increase in interstitial content. Williams, Sommer and Tung (Ref. 196) proposed that: (a) the higher temperature dependence of σ_{int} compared to the modulus correlated with a change in slip transition from planar to wavy (which they noted in their concurrent TEM observations to occur as the temperature was increased) and (b) that a maximum

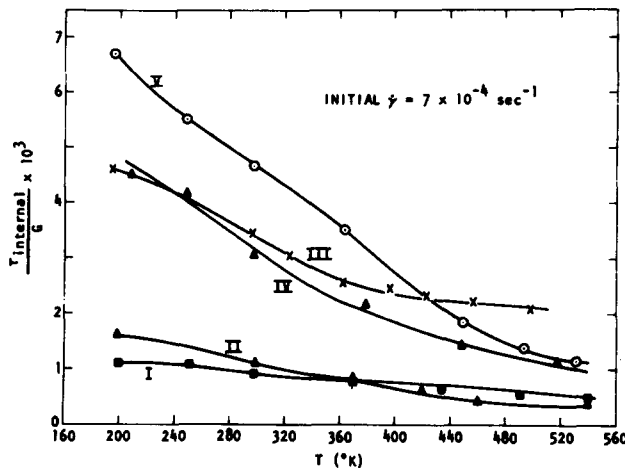


Fig. 4.96. σ_{int} determined by the decremental unloading method versus temperature as a function of impurity content. The O+N contents of the various materials are: Material I (0.15 at. %); Material II (0.17 at. %); Material III (0.56 at. %); Material IV (1.6 at. %). The carbon content is less than 0.12 at. % in all materials. The iron content is 0.04 wt. % in Materials I, II and IV, 0.2 wt. % in Material III and 0.08 wt. % in Material IV. From Williams, Sommer and Tung (Ref. 196).

in σ_e , the difference between the applied stress σ and the internal stress σ_{int} determined by the DU method, occurred at the temperature which corresponded to the onset of planar glide.

To check whether the prior deformation temperature had a significant effect on the internal stress, Yin, Doner and Conrad (Ref. 176) deformed Ti-50A (0.5 at. % O_{eq}) specimens of 2 and 22 μm grain size at predetermined temperatures in the range of 77 to 650K and subsequently conducted decremental unloading tests at 300K on these previously deformed specimens. They found that σ_{int} at 300K determined by both the BE and DU methods was higher for the 2 μm grain size specimens than those with the 22 μm grain size, but was independent of the prior deformation temperature for both grain sizes and both methods. Further, for both grain sizes σ_{int} determined by the DU method had a stronger temperature dependence than the modulus, in accord with the findings of Sommer and coworkers (Refs. 196, 253). However, concurrent TEM observations by Yin, Doner and Conrad (Ref. 176) did not reveal a pronounced difference in dislocation structure (planar versus wavy) as reported by Williams, Sommer and Tung (Ref. 196). Thus, the results of Yin, Doner and Conrad were not in accord with the concept that the stronger-than-modulus temperature dependence of σ_{int} was due to a pronounced effect of temperature on dislocation structure produced during deformation.

More recently, Okazaki, Aono, Kaneyuki and Conrad (Ref. 254) conducted a detailed study into the use of the DU method for measuring the internal stress in three polycrystalline metals: Cu, Fe and A-50 Ti. They found that the stress-time behavior during decremental unloading was of the two types illustrated in Fig. 4.97. The behavior indicated in (a) of Fig. 4.97, which is normally reported for decremental

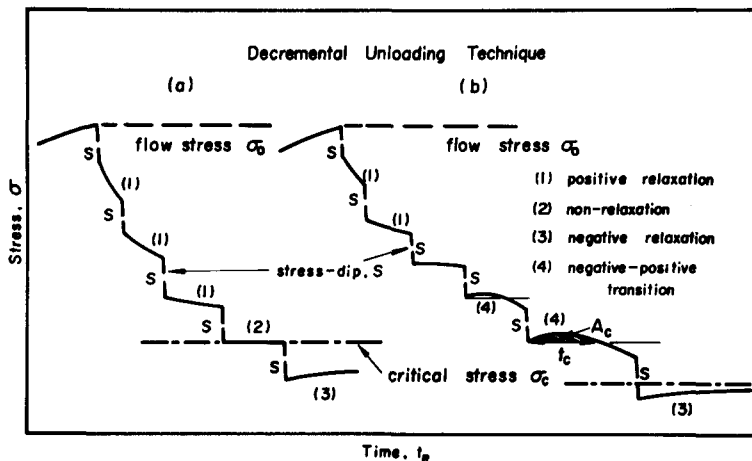


Fig. 4.97. Two types of stress relaxation behavior noted during decremental unloading tests in Cu, Fe and A-50 Ti. From Okazaki, Aono, Kaneyuki and Conrad (Ref. 254).

unloading tests at low temperatures, was only observed for Cu; that indicated in (b) was exhibited by the Fe and A-50 Ti specimens. In the latter case, the relaxation for the initial load decrements is positive (decrease in stress with time); however, below a critical stress the relaxation curve first consists of an increase in stress (negative relaxation), which is later followed by a decrease (positive relaxation). The time t_c for the stress to return to its initial value following a load decrement in this region was found to become longer the lower the value of the applied stress. It was found that the value of the stress for the first evidence of negative relaxation in A-50 Ti ($t_c = 0$ in Fig. 4.97) was similar to the value of σ_{int} reported by others (Refs. 176, 196, 253). Upon further unloading the specimen to a stress where $t_c \rightarrow \infty$, the value of σ_{int} determined by the DU method was in reasonable accord with that obtained by the BE method up to about 400K; see Fig. 4.98. At higher temperatures σ_{int} by the DU method was generally lower than that by the BE method. It was proposed that this was due to recovery occurring during the relaxation test. Finally, similar to Yin, Doner and Conrad (Ref. 176), Okazaki, Aono, Kaneyuki and Conrad (Ref. 254) also found for a strain of about 1% that σ_{int} determined subsequently by the DU method at 300K was independent of the prior deformation temperature in the range of 77-650K.

In summary, the results to date on titanium indicate that of the two most common methods for measuring the internal stress σ_{int} , the decremental unloading (DU) method yields a higher value and a stronger temperature dependence of the internal stress than does the back-extrapolation (BE) method, if the first indication of negative relaxation is used to define σ_{int} . However, at longer relaxation times, the initial negative relaxation following a stress decrement may be followed by positive relaxation. The time for the occurrence of this positive relaxation increases as the stress is lowered. The stress where only positive relaxation occurs for a very long relaxation time is in reasonable accord with σ_u determined by the BE method. The internal stress in Ti-50A produced by a strain of 1% at specific temperatures in the range of 77-650K and subsequently determined at 300K by both the DU and the BE methods was essentially constant, indicating that the prior

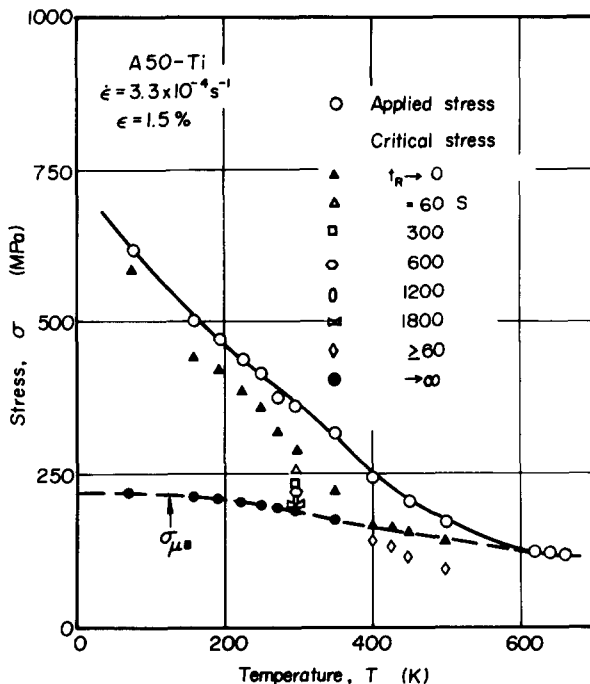


Fig. 4.98. Applied stress (flow stress) and internal stress (σ_{int}) determined by decremental unloading of A-50 Ti specimens previously deformed 1% at the designated temperature. σ_{μ} is σ_{int} determined by the back-extrapolation method; critical stress is σ_{int} determined by the decremental unloading method. The times listed with the critical stress are the relaxation times following a load decrement. From Okazaki, Aono, Kaneyuki and Conrad (Ref. 254).

deformation temperature did not have a significant influence on σ_{int} . This suggests that neither twinning which occurs at low temperatures, nor dynamic strain aging which occurs at the higher temperatures, had a measurable effect on σ_{int} . Finally, worthy of mention regarding the measurement of the internal stress by stress relaxation are the results of Reed-Hill and Donoso (Ref. 255), who showed that the test machine relaxation must be taken into account when determining σ_{int} by the DU or the stress relaxation methods. By subtracting the contribution of the machine relaxation from the total DU relaxation results on commercial Ti (-0.5 at. % O_{eq}) they were unable to detect the occurrence of negative relaxation (i.e. an increase in stress with time) even at loads as low as 5% of the initial applied load. They were thus unable to define σ_{int} positively, but concluded that it was significantly less than the value which was obtained when the machine relaxation was not taken into account.

The curvature of dislocations observed by TEM in deformed specimens offers a direct measure of the local internal stress in metals (Ref. 256). From dislocation line tension considerations, the stress required to bow a dislocation to a radius

of curvature R is

$$\tau = E_L / Rb \quad (4.26)$$

where E_L is the line tension, which is $\approx \mu b^2$ for screw dislocations and $\approx \mu b^2/4$ for edge dislocations when $\mu = K_S$ (Ref. 101). Substituting for E_L in Eq. 4.26 thus gives

$$\tau = \alpha \mu b / R \quad (4.26a)$$

where $\alpha = 1$ for screw dislocations and $1/4$ for edge dislocations. The local long-range internal stress τ_μ following deformation can thus be obtained through Eq. 4.26a by measuring the radius of curvature of the dislocations by TEM, providing the dislocations remain fixed in their position during the unloading and thinning of the specimen for TEM observation. An example of the curvature of dislocations observed in deformed titanium is shown in Fig. 4.99. The values of the local internal stress determined using Eq. 4.26a from the curvature of dislocations in Battelle titanium ($0.2 \text{ at. \% } O_{eq}$) specimens deformed at 77-500K versus the long-range internal stress derived from the dislocation density measurements are plotted in Fig. 4.100. A Taylor factor $M = 2.5$ was here used to convert the tensile stress σ to resolved shear stress τ for the dislocation density measurements so that each value of τ_μ ($= \alpha \mu b \rho^{1/2}$) plotted in Fig. 4.100 was taken to be $(\sigma - \sigma_f)/2.5$ for the specific strain considered. It is seen in Fig. 4.100 that the data points lie for the most part between the two straight lines of slopes $1/4$ and 1 , supporting the proposition that the quantity $\alpha \mu b \rho^{1/2}$ gives the long-range internal stress opposing the motion of dislocations in polycrystalline titanium. Results similar to those of Fig. 4.100 were also obtained for measurements on MARZ zone-refined titanium deformed at 77-500K (Ref. 257), except

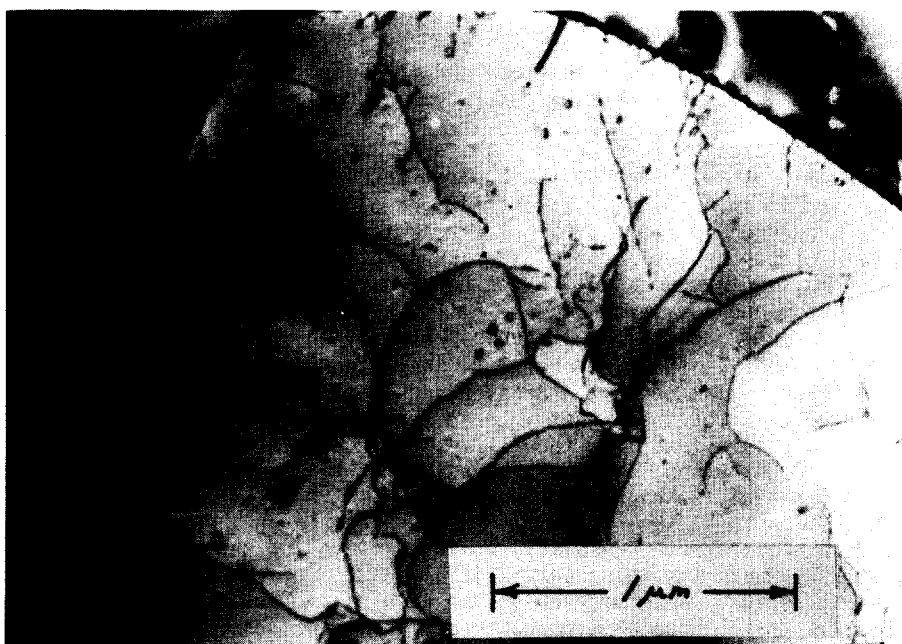


Fig. 4.99. Curvature of dislocations in Battelle titanium deformed 1.3% at 500K. Also shown are dislocations being emitted from a grain boundary. From Jon and Conrad (Ref. 257).

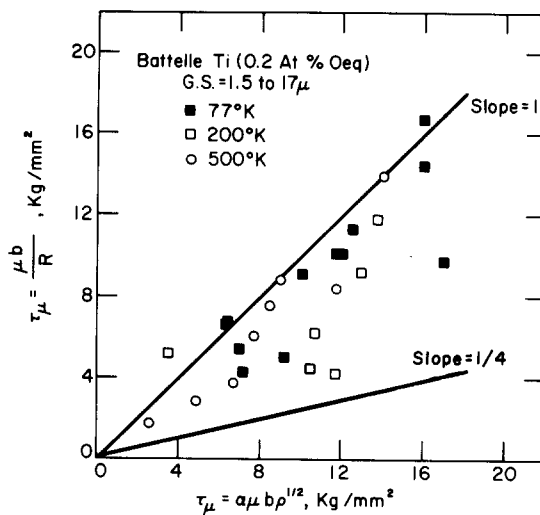


Fig. 4.100. Comparison of the long-range internal stress determined from the curvature of dislocations with that from the dislocation density.
From Conrad, Okazaki, Gadgil and Jon (Ref. 169).

that there was no tendency for the data points to cluster near the line of slope equal to 1 as occurs in Fig. 4.100. It would thus appear that the dislocations considered were not predominantly of one type. Worthy of mention at this point is that since $\sigma_f = 0$ at 650K for these two high purity materials (see Fig. 4.93), the results of Fig. 4.100 support the idea that the flow stress σ at this temperature (i.e. the plateau stress) is the long-range internal stress σ_μ .

Deformation Kinetics:

The effect of temperature on the apparent activation volume v' ($= kT(\partial \ln \dot{\epsilon} / \partial \sigma)_T$) as a function of interstitial content for the plastic flow of polycrystalline titanium is presented in Fig. 4.101. The results given here were obtained by strain rate-cycling tests on synthesized titanium-interstitial alloys and are the average values (normalized with respect to the Burgers vector b) for grain sizes in the range of 1-15 μ m and for strains of 1-15%, since as pointed out above the parameter $(\Delta\sigma / \Delta \ln \dot{\epsilon})_T$ was only slightly dependent, if at all, on grain size and strain. Evident in Fig. 4.101 is that in general v' increases with temperature and with decrease in interstitial content. However, an anomalous temperature dependence occurs at about 400K for the higher interstitial contents in the Ti-O and Ti-N alloys; no such anomaly is evident for the Ti-C alloys. Also to be noted is that v' is approximately proportional to the temperature up to about 300-400K, and then increases more rapidly at higher temperatures.

v' versus temperature curves for strain rate-cycling tests on commercial materials (with oxygen as the major interstitial solute) of various grain sizes are shown in Fig. 4.102. A comparison of the results in Fig. 4.102 with those in Fig. 4.101 reveals that v' for a given commercial alloy has essentially the same value at a given temperature as that for the synthesized Ti-O alloy of equivalent oxygen content. Furthermore, again v' is not sensitively dependent on the grain size.

The values of v' given in Figs. 4.101 and 4.102 were obtained by strain rate-cycling tests and for strains greater than about 1%. Of interest is whether the

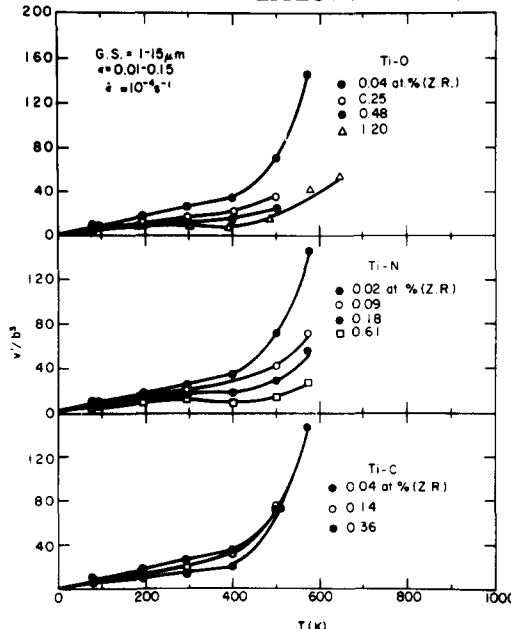


Fig. 4.101. Effect of temperature on the apparent activation volume v' for the plastic deformation of titanium polycrystals as a function of interstitial content. Data from Fig. 4.61.

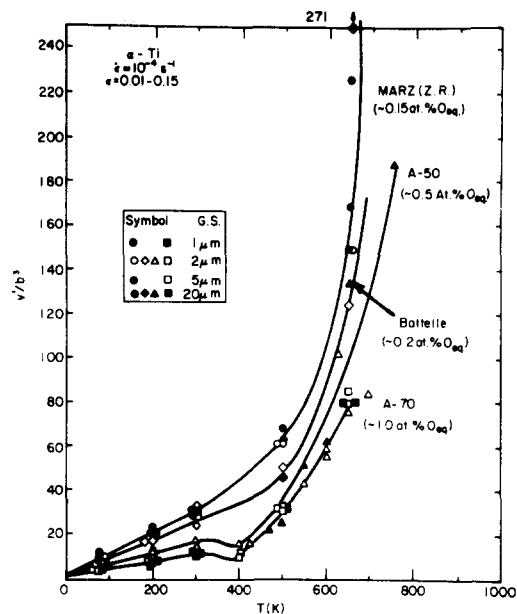


Fig. 4.102. Apparent activation volume v' versus temperature as a function of grain size for various commercial titaniums. Data from the same sources as in Fig. 4.74.

values determined from the effect of strain rate on the yield stress of separate specimens (such as the data of Fig. 4.42) agree with those from the strain rate-cycling tests. That in fact rather good agreement occurs between these two methods for determining v' is shown in Fig. 4.103. Also, the values of v' determined from stress relaxation (Ref. 189) and creep (Refs. 184, 258) tests are in good accord with those from constant strain rate-cycling tests. Furthermore, again rather good agreement is indicated in the value of v' determined for the commercial A-50 alloy and the synthesized Ti-O alloy of the same total interstitial content.

Upon taking slopes of the flow stress versus temperature curves such as those of Figs. 4.59 and 4.60 it was found that the deformation partial ($\partial\sigma/\partial T$) _{ϵ} exhibited discontinuities at 300-400K, similar to what was observed for prism slip mentioned above. Such discontinuities were detected for all titanium materials and alloys except the synthesized Ti-C alloys.

The variation of $Q (= -Tv'(\partial\sigma/\partial T))$ with temperature at a strain rate of 10^{-4} s^{-1} for the synthesized polycrystalline Ti-interstitial alloys of $2\mu\text{m}$ grain size is presented in Fig. 4.104 (data points). It is seen that Q for these alloys increases with temperature (with some indication of an anomaly at 300-400K), relatively independent (within the scatter of the data) of the species and amount of interstitial solute. Also included in Fig. 4.104 for comparison are the results for prism and basal glide taken from Figs. 4.21 and 4.29 (dashed and solid lines). To be noted is that polycrystalline specimens are in better accord with prism glide than basal glide. Worthy of mention is that Q as a function of temperature for commercial polycrystalline materials (Battelle, A-50 and A-70) was essentially the same as that depicted in Fig. 4.104 for the synthesized Ti-interstitial alloys of equivalent oxygen content.

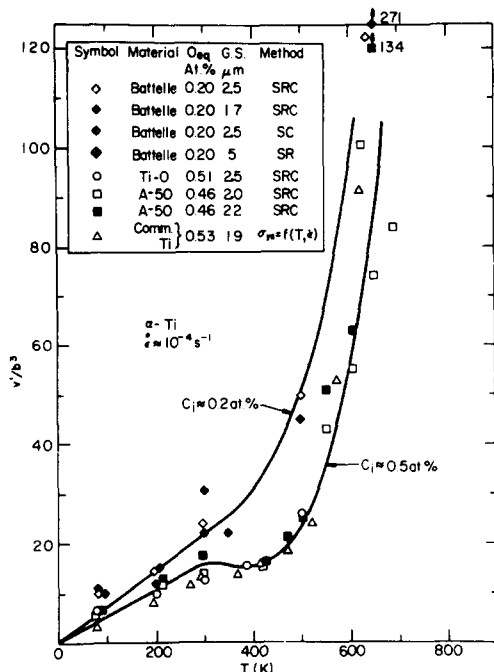


Fig. 4.103. Comparison of v' versus temperature determined from the following test methods: (a) strain rate cycling (SRC), (b) stress cycling during creep (SC), (c) stress relaxation (SR) and (d) effect of strain rate on the yield stress ($\sigma_{ys} = f(T, \dot{\epsilon})$). Data from Refs. 170, 172, 180, 184, 189, 209.

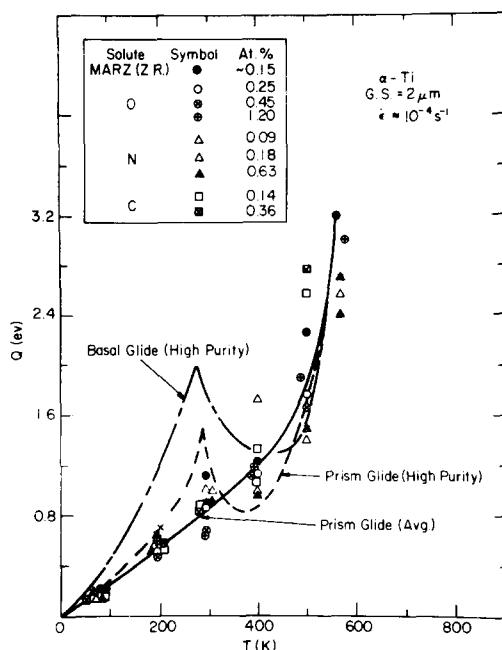


Fig. 4.104. $Q = -T v' (\partial \sigma / \partial T)_\epsilon$ versus temperature as a function of interstitial content for polycrystalline titanium of $2\mu\text{m}$ grain size (data points). Data from Figs. 4.59 and 4.61. Also included are the results (dashed and solid lines) for prism and basal glide taken from Figs. 4.21 and 4.29.

Of special interest is whether or not the value of Q depends on the particular equation employed to obtain it (i.e. $-Tv'(\partial \sigma / \partial T)_\epsilon$ or $-k(\partial \ln \dot{\epsilon} / \partial(1/T))_\sigma$; also, whether or not it depends on the method used to obtain a desired deformation partial (i.e. strain rate or temperature cycling, effects of strain rate and temperature on the yield stress, stress relaxation or creep). Previous work (Refs. 184, 189, 259) has indicated that within the scatter of the data the value of Q is independent of the equation or the method employed to obtain the deformation partial. This is confirmed in Fig. 4.105 where Q obtained by various methods on several materials is plotted versus the temperature. The values of $Q = -k(\partial \ln \dot{\epsilon} / \partial(1/T))_\sigma$ presented here were derived from the effects of temperature and strain rate on the yield stress, similar to that indicated in Fig. 4.42, by first making cross-plots of $\ln \dot{\epsilon}$ versus the reciprocal of the absolute temperature at a constant stress; see, for example, Fig. 4.106. Such plots generally exhibit a slight positive curvature, especially at the higher stresses, indicating that Q increases with temperature. The values of Q plotted in Fig. 4.105 were derived from the slopes of such curves taken at the constant strain rate of 10^{-4}s^{-1} .

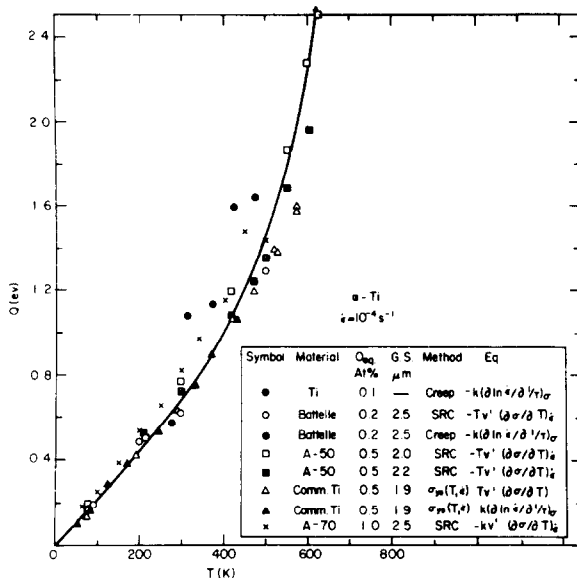


Fig. 4.105. A comparison of the values of Q obtained by various methods. Data from Refs. 170, 172, 180, 184, 185.

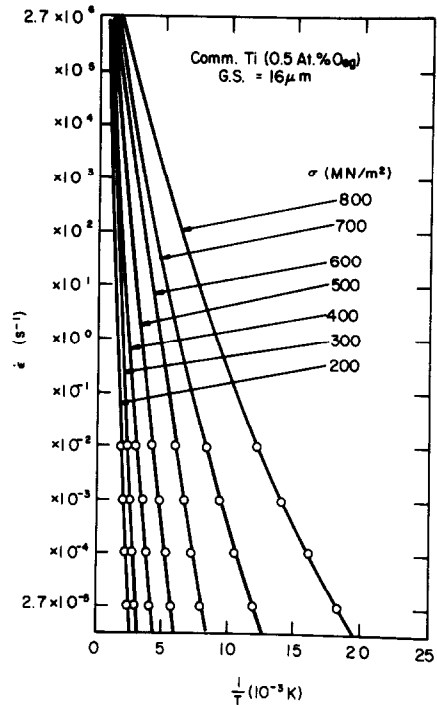


Fig. 4.106. Log $\dot{\epsilon}$ versus $1/T$ as a function of applied stress for commercial titanium. Data from Monteiro, Santhanam and Reed-Hill (Ref. 180).

The fact that Q in Fig. 4.105 is independent of the equation employed and the method used to obtain a given deformation partial gives

$$-kT^2 \left(\frac{\partial \ln \dot{\epsilon}}{\partial \sigma} \right) \frac{(\partial \sigma)}{T} = -kT^2 \left(\frac{\partial \ln \dot{\epsilon}}{\partial T} \right) \sigma \quad (4.27)$$

which in turn yields

$$\left(\frac{\partial \ln \dot{\epsilon}}{\partial \sigma} \right) \frac{1}{T} \cdot \left(\frac{\partial \sigma}{\partial T} \right) \frac{1}{\dot{\epsilon}} \cdot \left(\frac{\partial T}{\partial \ln \dot{\epsilon}} \right) \sigma = -1 \quad (4.28)$$

and thereby indicates that the quantity $\ln \dot{\epsilon}$ is a single-valued function of stress and temperature for the conditions considered.

Moreover, the results of Fig. 4.105 indicate that Q is relatively independent of interstitial content for the range considered (i.e. $C_i = 0.1 - 1.0$ at. % O_{eq}) and grain size ($d = 2 - 19 \mu m$). Thus, any decrease in the deformation partial $(\partial \sigma / \partial T)_{\dot{\epsilon}}$ which results from an increase in grain size is balanced by an increase in $(\partial \ln \dot{\epsilon} / \partial \sigma)_T$ to yield an essentially constant value of Q .

A plot of $-T(\partial \sigma / \partial T)_{\dot{\epsilon}}$ versus $(\partial \sigma / \partial \ln \dot{\epsilon})_T$ for strain rate-cycling tests on polycrystalline titanium of $2 \mu m$ grain size with interstitial contents of $0.1 - 1.2$ at. %

tested over the temperature range of 77-600K is presented in Fig. 4.107. The data scatter about a straight line through the origin with slope 34.5, which according to Eq. 4.6 gives the value of the quantity $\{\ln(\dot{\epsilon}_0/\dot{\epsilon}) - \Delta S/k\}$. The slope of 34.5 is similar in magnitude to that (36.5) obtained for prism glide (see Fig. 4.22).

It is evident in Fig. 4.105 that a curvature occurs in the plot of Q versus temperature. This curvature is reduced upon taking $Q^*(= -T v' (\partial \sigma^*/\partial T)^* = Q - \alpha_1 v \sigma_\mu)$ versus temperature; see Fig. 4.108. Again, Q^* is relatively independent of grain size and interstitial content; there is however some tendency for Q^* , similar to Q , to increase slightly with interstitial content and decrease in grain size for the materials considered.

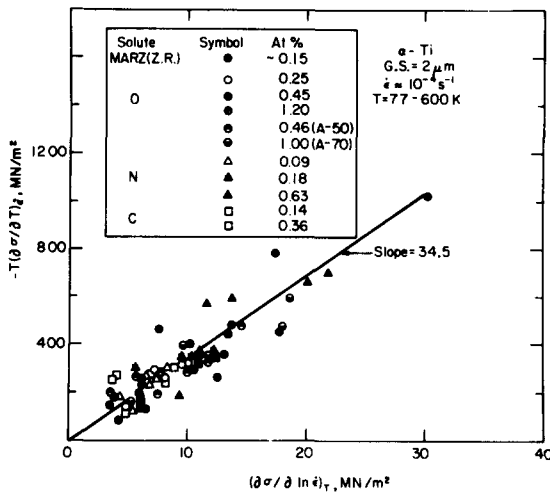


Fig. 4.107. $-T(\partial\sigma/\partial T)_\varepsilon$ versus $(\partial\sigma/\partial\ln\varepsilon)_T$ as a function of interstitial content. Data from Refs. 3, 170, 172, 175.

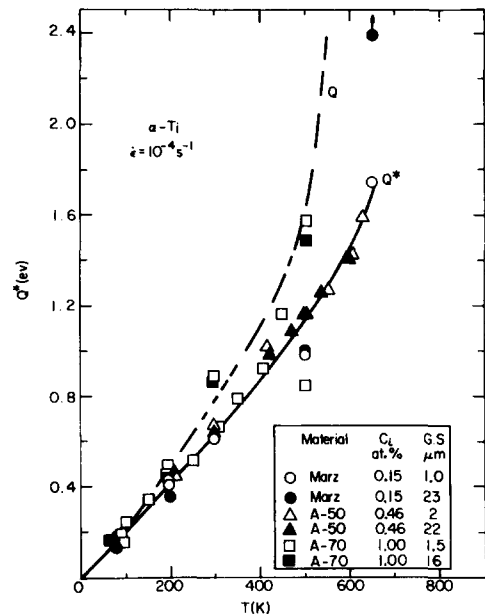


Fig. 4.108. $Q^*(= Q - \alpha_1 v \sigma_\mu)$ versus temperature as a function of grain size and interstitial content. The dashed line gives the average value of Q for the materials considered. Data from Refs. 170 and 172.

Fracture and Ductility:

In a detailed study of the effects of interstitial content (0.1-1.0 at. % O_{eq}), grain size (1-20 μm) and temperature (77-650K) on the fracture behavior of titanium wire specimens (1.6 mm dia.) tested in tension at low temperatures, Conrad, Keshavan and Sargent (Ref. 260) found that in all cases fracture was of the ductile type, i.e. necking preceded fracture and the fracture surface had a dimpled appearance; see, for example, Figs. 4.109 and 4.110 for zone refined titanium of 1 μm grain size and A-70 Ti of 20 μm grain size, respectively. The mode of fracture was cup-cone, except for zone-refined MARZ material of 1-2 μm grain size tested at 650K, which failed by so-called rupture, i.e. by pulling to a point. The dimples at the bottom of the cups tended to be equiaxed, while those on the sides were elongated due to the shear involved in the fracture at this location. The mean linear intercept dimple size at both locations ranged between 2 and 33 μm and increased with increase in temperature and grain size and decrease in interstitial content, which same factors also led to an increase in the fracture stress; see Table 4.7. Dark spots or inclusions were often observed within the dimples, suggesting that they may have been caused by the presences of fine precipitates or inclusions. Only rarely was there indication of a twin within a dimple.

The effect of grain size on the average true fracture stress ($= P_F / A_F$, where P_F is the fracture load and A_F the cross sectional area of the fracture surface) of titanium materials representing extremes in impurity content is depicted in Fig. 4.111. Allowing for the large scatter in the data, the results can be considered to follow a Hall-Petch relation, giving

$$\sigma_F = (\sigma_i)_F + K_F d^{-1/2} \quad (4.29)$$

Conrad, Keshavan and Sargent (Ref. 260) also reported that the effect of grain size on the average true fracture stress of titanium determined over the temperature range 77-650K could be considered to follow a Hall-Petch relation. A summary of the effects of temperature and interstitial content on $(\sigma_i)_F$ and K_F is presented in Fig. 4.112. For comparison, the average values of these parameters for the 0.2% yield stress $(\sigma_i)_y$ and K_y are also included. It is seen that $(\sigma_i)_F$ has a stronger temperature dependence than $(\sigma_i)_y$ for both purity levels of titanium considered. The curve representing the temperature dependence of K_F for the high purity titanium (0.2 at. % O_{eq}) is similar in form to that for the average K_y of the various purity titaniuns, the value of K_F being however for the most part about twice K_y . On the other hand, K_F for A-70 Ti (1.0 at. % O_{eq}) increases with temperature, rather than decreasing as it does for the higher purity materials.

As pointed out by Bridgman (Ref. 262), once necking occurs in a tension test, the stress state is no longer uniaxial but becomes triaxial, which in turn leads to an increase in the average tensile stress required to continue plastic flow. To obtain the true, corrected flow stress, one must multiply the average tensile stress by a correction factor, which contains as the principal term the ratio of the cross-section radius a to the neck contour radius R . Following Bridgman (Ref. 262), Conrad, Keshavan and Sargent (Ref. 260) plotted the ratio of the radius of the fracture cross-section a_F to the radius of the curvature of the neck R_F of fractured titanium wire specimens versus the true fracture strain; see Fig. 4.113.

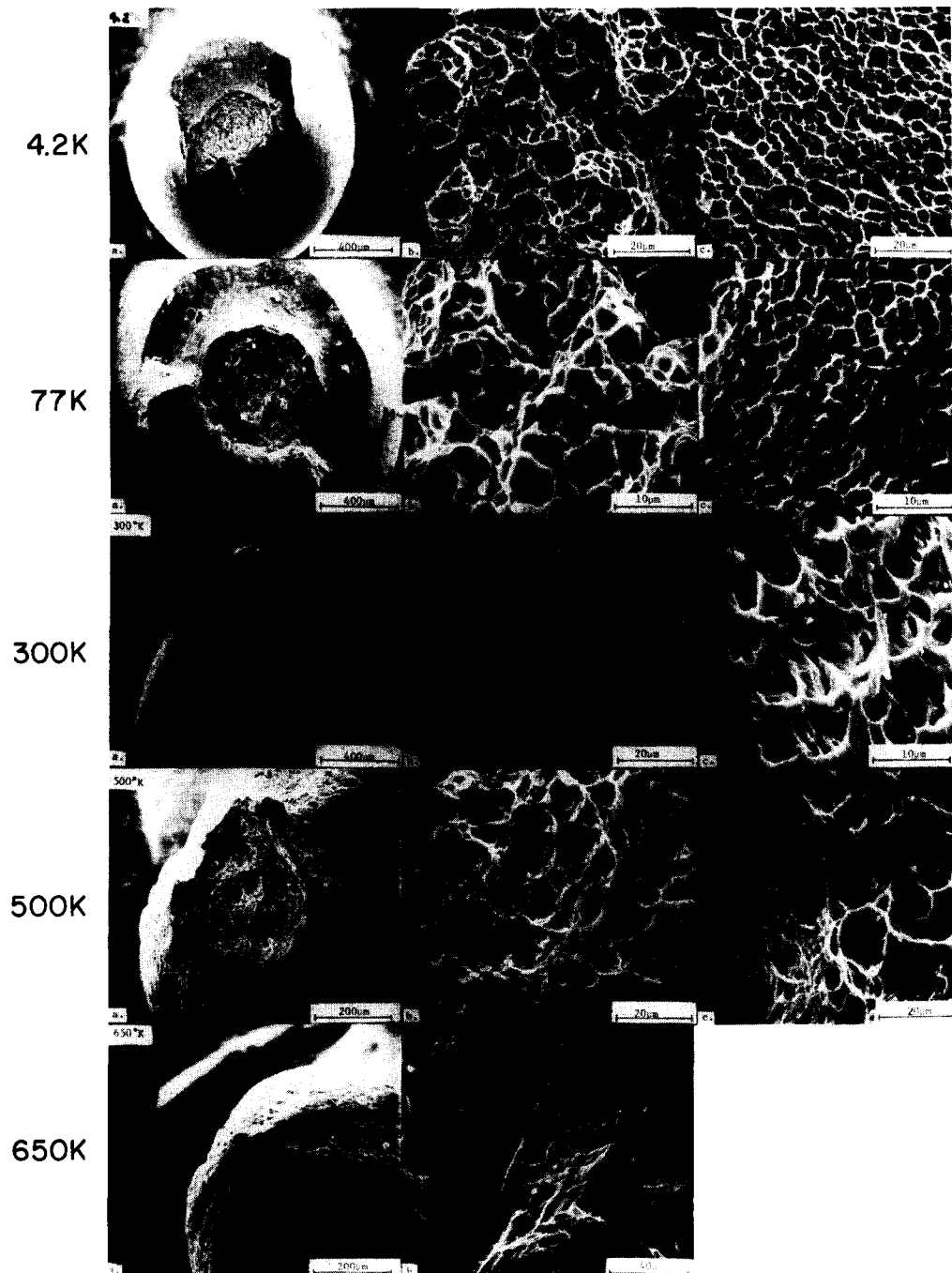


Fig. 4.109. SEM photomicrographs of the fracture surface of zone-refined MARZ titanium (0.15 at. % O_{eq}) of 1 μm grain size deformed to fracture at 4.2 to 650K. (a) entire fracture surface, (b) center region and (c) lip region. From Conrad, Keshavan and Sargent (Ref. 260).

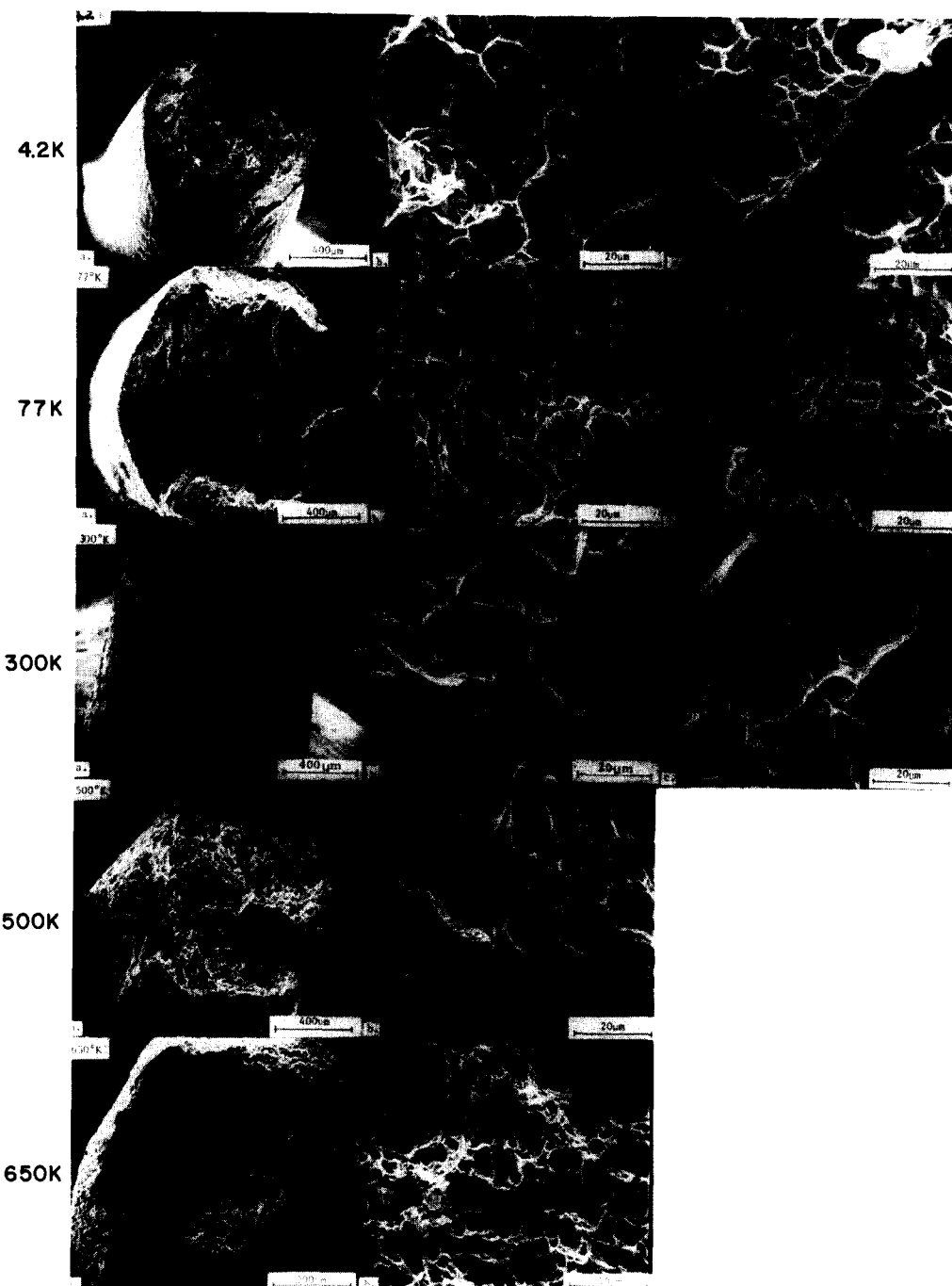


Fig. 4.110. SEM photomicrographs of the fracture surface of A-70 Ti (1.0 at. % O_{eq}) of 20μm grain size deformed to fracture at 4.2 to 650K: (a) entire fracture surface, (b) center region and (c) tip region. From Conrad, Keshavan and Sargent (Ref. 260).

TABLE 4.7 Mean Linear Intercept Dimple Size at the Fracture Surface of Titanium Wire Specimens as a Function of Test Temperature, Grain Size and Purity. Data From Conrad, Keshavan and Sargent (Ref. 260).

Material	Grain Size (μm)	Temperature ($^{\circ}\text{K}$)	Avg. True Fracture Stress (GN/m^2)	Dimple Size (μm)
MARZ Zone-Refined ($C_i = 0.15 \text{ at. \%}$)	1-2	77	2.36	2.1
		300	1.29	2.9
		500	0.49	7.1
		650	0.21	26.0
	20	4.2	2.13	2.7
		300	0.95	6.0
		500	0.26	32.5
A-70 Ti ($C_i = 1.0 \text{ at. \%}$)	1-2	4.2	----	2.1
		77	2.70	2.9
		300	1.74	3.0
		500	1.63	3.6
		650	1.72	5.7
	20	4.2	----	4.9
		77	2.16	4.5
		300	1.04	9.0
		500	0.87	10.9
		650	1.09	15.1

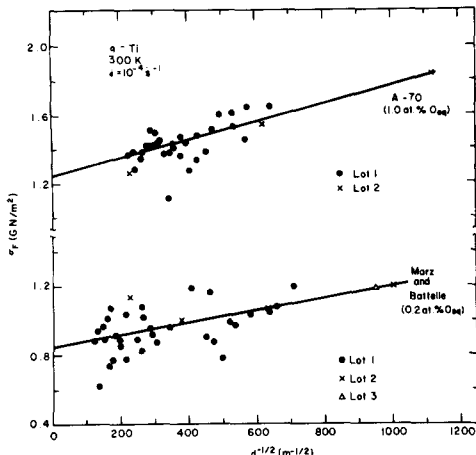


Fig. 4.111. Effect of grain size on the average true fracture stress of titanium at 300K as a function of interstitial content. Data from Refs. 221 and 261.

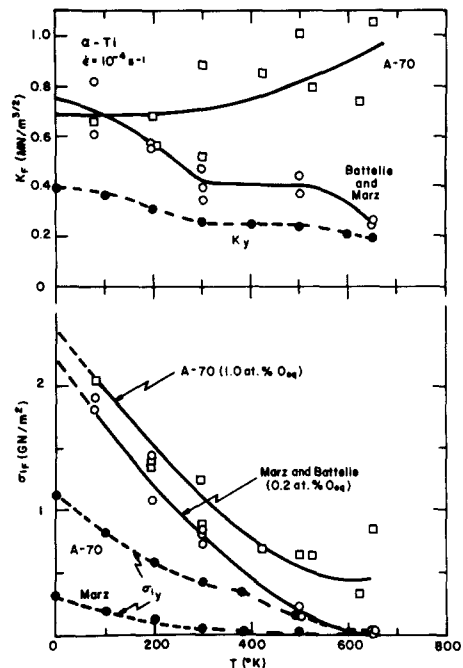


Fig. 4.112. Effect of temperature on $(\sigma_i)_F$ and K_F as a function of interstitial content. Also included for comparison are $(\sigma_i)_y$ and K_y for the 0.2% yield stress. Fracture data are from Refs. 221, 260, 261; yield stress data are from Figs. 4.65 and 4.68.

To be noted is that the results for the various titanium materials can be considered to fall on a single curve; however, it is below the common curve obtained by Bridgman (Ref. 262) for a number of metals, being in better accord with the results of Marshall and Shaw (Ref. 263) for copper and steel. Thus, Bridgman's concept of a single contour factor curve for all metals is not generally applicable.

The effects of temperature, purity and grain size on the true fracture strain ϵ_F ($= \ln(A_0/A_F)$, where A_0 and A_F are the original and final cross section areas respectively) are presented in Fig. 4.114. Below about 400K, ϵ_F is relatively independent of temperature and grain size, although there is some tendency for ϵ_F to become larger with increase in grain size for the highest purity MARZ material. Above about 400K, ϵ_F tends to increase with temperature and with decrease in grain size. Worthy of note is that a significant decrease in ϵ_F occurs for the largest grain size (20μm) between about 300 and 500K for the highest purity materials before the subsequent increase at the higher temperatures. This leads to a cross-over of the curves for the various grain sizes in these higher purity materials at about 400K giving ϵ_F essentially independent of grain size in this temperature region. Also to be noted is that ϵ_F decreases again below 77K for the MARZ material. Regarding the effect of interstitial content, in general ϵ_F decreases with increase in interstitial content.

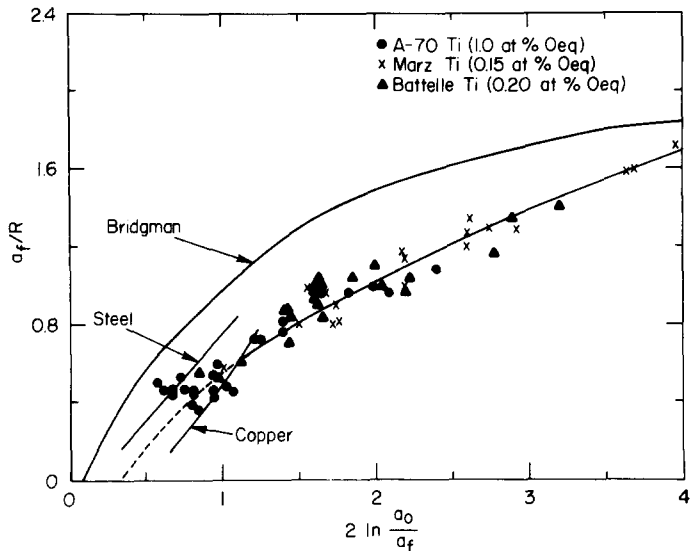


Fig. 4.113. Average neck contour factor α_f/R_f as a function of true fracture strain for titanium with interstitial contents ranging from 0.15 to 1.0 at. % O_{eq} and grain sizes of 1 to 20 μm . Also included are the results of Bridgman (Ref. 262) for a number of metals and of Marshall and Shaw (Ref. 263) for copper and steel. From Conrad, Keshavan and Sargent (Ref. 260).

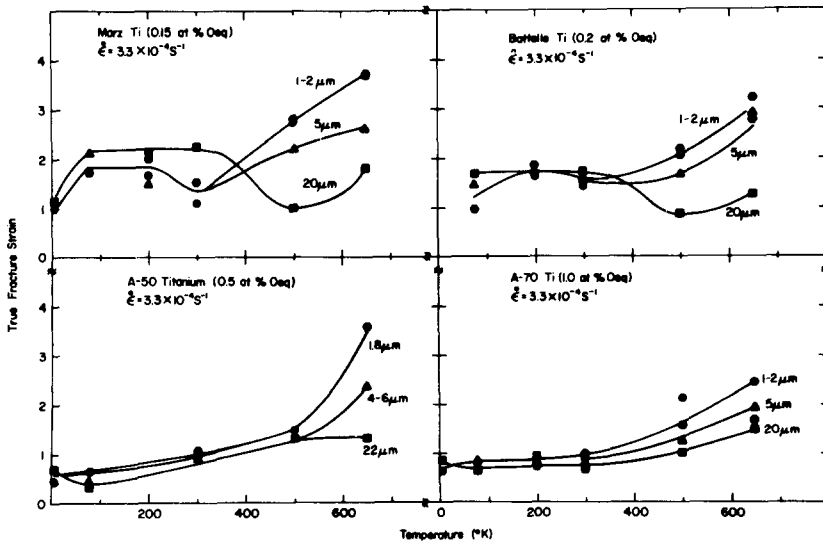


Fig. 4.114. Effects of temperature, purity and grain size on the true fracture strain of titanium wire specimens. From Conrad, Keshavan and Sargent (Ref. 260).

Conrad, Keshavan and Sargent (Ref. 260) also determined the effects of grain size, interstitial content and temperature on the work W required to produce fracture, i.e. on the area under the stress-strain curve. Their results are plotted in Fig. 4.115. Also included is W^* , the work due to the thermal component of the flow stress. In general, W decreases with increase in temperature to about 400K and then remains relatively constant to 650K. At temperatures higher than 300K, W increases significantly with decrease in grain size, whereas at lower temperatures there appears to be a slight increase in W as the grain size becomes larger. In regard to interstitial content, there is a tendency for W to decrease slightly with increase in interstitial content.

The effects of temperature, purity and grain size on the uniform elongation e_u^+ and the total elongation e_t (both as engineering strain) of titanium wire specimens (for which fracture stress data are given in Figs. 4.111 and 4.112) are presented in Figs. 4.116 and 4.117. As a general trend, both e_u and e_t tend to increase with decrease in temperature for the range considered (650 to 77K), especially for the higher purity materials. However, if tests are conducted at smaller temperature intervals, the elongation versus temperature curves contain humps and valleys (see,

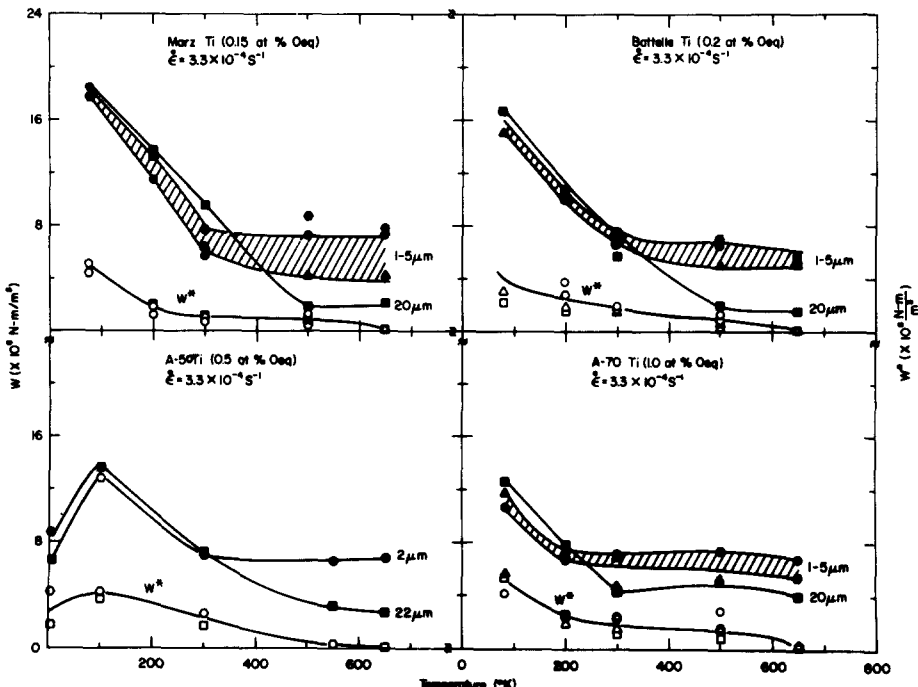


Fig. 4.115. Effects of temperature, purity and grain size on the total work to fracture W and the work W^* due to the thermal component of the flow stress. From Conrad, Keshavan and Sargent (Ref. 260).

te_u also yields the value of the strain hardening exponent $n_u = d\ln\sigma/d\ln e$ at the maximum load in a tension test, for $n_u = \epsilon_u = \ln(1 + e_u)$.

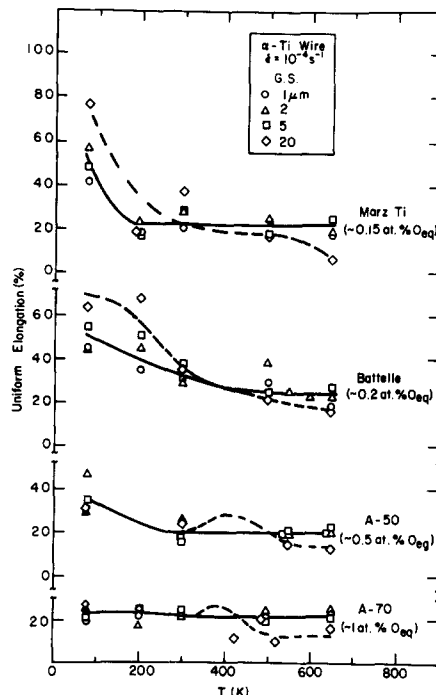


Fig. 4.116. Effects of temperature, purity and grain size on the uniform elongation of titanium wire specimens. Data from Refs. 238 and 260.

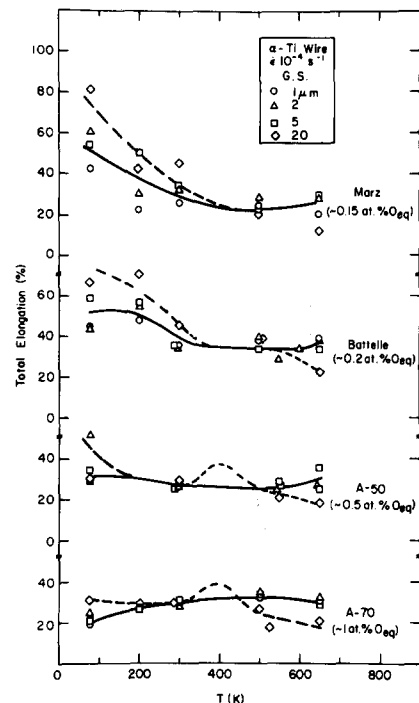


Fig. 4.117. Effects of temperature, purity and grain size on the total elongation of titanium wire specimens. Data from Refs. 238 and 260.

for example, Figs. 4.46 and 4.118) which reflect a more complicated temperature dependence of these ductility indicators. Hence, humps are depicted at ~400K for the A-50 and A-70 titaniuns in Figs. 4.116 and 4.117, based on the data of Garde, Santhanam and Reed-Hill (Ref. 171). In regard to the effect of grain size, the data of Figs. 4.116 and 4.117 can be separated into two groups, one representing grain sizes of 5μm or less and the other the 20μm grain size. At temperatures of 300K and below, the specimens with the larger grain size exhibit the higher elongations, whereas at the higher temperatures just the opposite is true. In regard to the effect of interstitial content, an increase in purity leads to a significant increase in e_u and e_t at temperatures of 300K and below, but has less influence at the higher temperatures.

A detailed consideration of the separate effects of the interstitials C, N and O on the total elongation at 300K is presented in Fig. 4.119. In each case the elongation decreases with interstitial content, the effect being largest at the lowest concentrations. The rate of decrease in elongation with interstitial content increases in the order C, O, N, which is the same as that for their effect on the flow stress.

Finally, although the present review is primarily concerned with unidirectional tensile testing, some mention of the effects of interstitial content on the fatigue strength of titanium seems desirable. Unalloyed titanium exhibits a well defined fatigue limit, which increases with interstitial content (Fig. 4.120) and with decrease in grain size and temperature (Refs. 264-270). The effects of interstitial

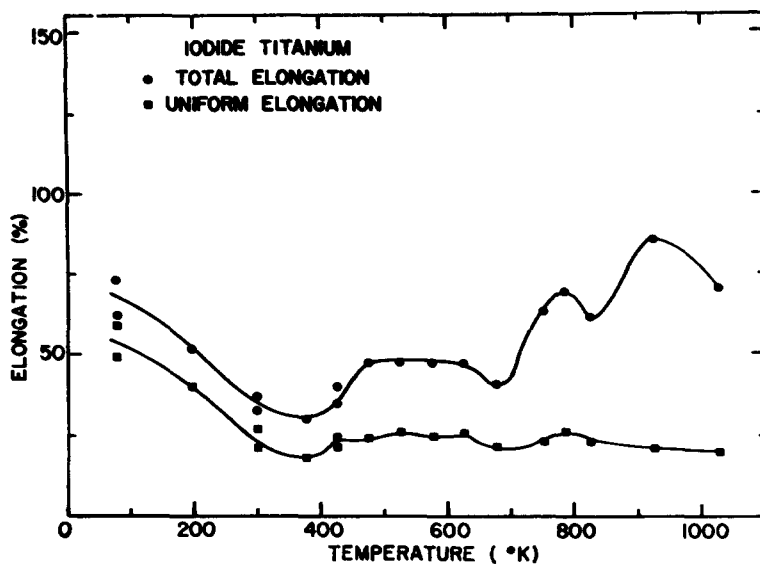


Fig. 4.118. The uniform and total elongation of iodide titanium rod of $22\mu\text{m}$ grain size. From Garde, Santhanam and Reed-Hill (Ref. 171).

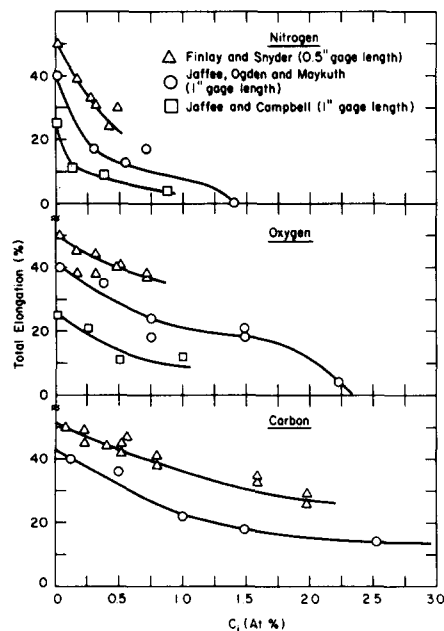


Fig. 4.119. Effects of interstitial content on the total elongation of titanium at 300K. From Conrad, Doner and deMeester (Ref. 2). Data from Refs. 12, 19, 264.

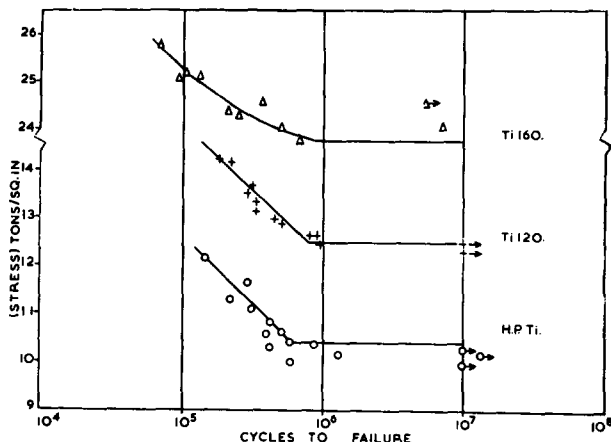


Fig. 4.120. Effect of interstitial content on the S-N curves of titanium with $32\mu\text{m}$ grain size at 300K. Total interstitial contents of the materials are: Ti 160 (1.1 at. %), Ti 120 (0.4 at. %) and H.P. Ti (0.3 at. %). From Turner and Roberts (Ref. 265).

content, grain size and temperature on the fatigue strength are similar to those on the yield strength; see Figs. 4.121 and 4.122. In regard to crack growth rate, Robinson and Bevers (Ref. 271) found for tension-tension tests at room temperature that this property was essentially independent of interstitial content in the range of 0.2 to 0.9 at. % oxygen, but increased about an order of magnitude upon increasing the grain size from 27 to $80\mu\text{m}$ in the material with the lowest interstitial content.

The fracture modes under cyclic deformation in coarse-grained α -titanium have been investigated by Golland and Beevers (Ref. 269). They reported that in the temperature range of 77 to 195K fatigue cracks were associated with $\{11\bar{2}1\}$ type twins, slip bands and grain boundaries, the fracture surfaces exhibiting twin-assisted transgranular and intergranular fracture paths. In the range of 473 to 773K, the failure occurred as a consequence of the transgranular propagation of surface nucleated cracks.

4.2.5 Intermediate Temperatures ($0.3 < T/T_m < 0.4$)

As mentioned above, strain aging phenomena occur in titanium in the intermediate temperature regime, both static and dynamic strain aging having been reported.

Static Strain Aging:

Rosi and Perkins (Ref. 183) were among the first to report the occurrence of static strain aging in commercial purity titanium (~0.8 at. % O_{eq}). They found that a yield point appeared and the level of the flow stress increased slightly following aging treatments of 48h at room temperature and 1h at 473K in specimens which had been previously deformed 4.5% at room temperature. A yield point still occurred after aging 1h at 673K; however, the level of the flow stress had decreased, i.e. softening had taken place. Heating for 1h at 873 and 1073K produced only softening, the amount increasing with increase in temperature.

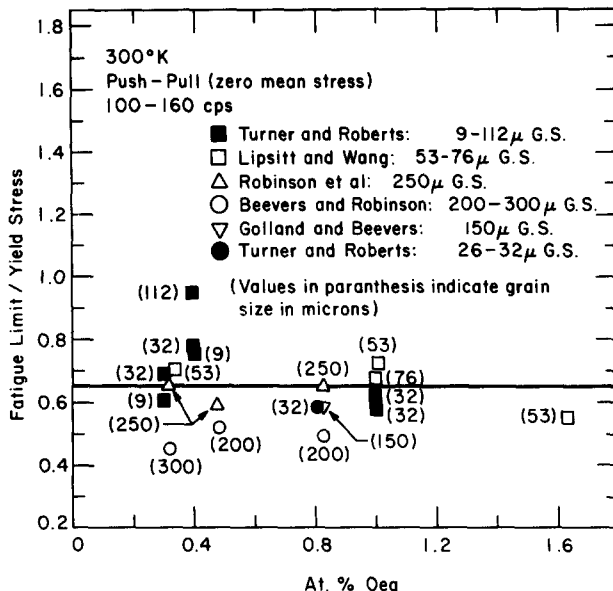


Fig. 4.121. Ratio of the fatigue limit to the yield stress of titanium at 300K as a function of interstitial content and grain size. From Conrad, Doner and deMeester (Ref. 2); Data from Refs. 265-270.

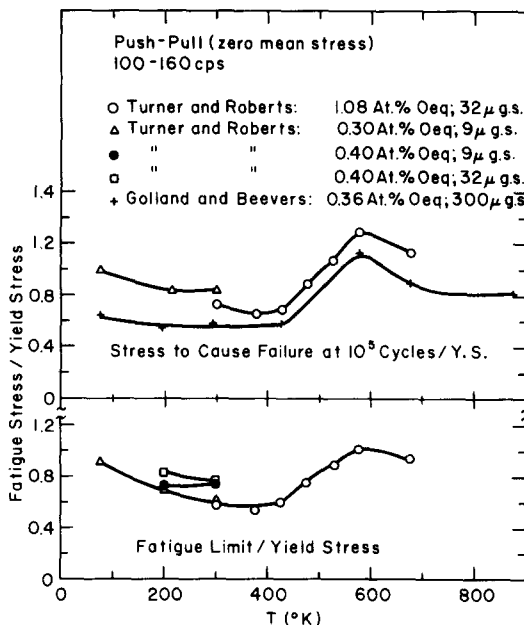


Fig. 4.122. Ratio of the stress to cause failure at 10⁵ cycles to the yield stress and the ratio of the fatigue limit to the yield stress of titanium as a function of temperature. From Conrad, Doner and deMeester (Ref. 2); Data from Refs. 167, 265, 270.

More recently, Donoso and Reed-Hill (Ref. 272) investigated in some detail the static strain aging which occurred in a commercial titanium (0.5 at. % O_{eq} and 0.14 at. % Fe) upon heating under a small load for times of 150s to 68h in the temperature range of 555-630K following a prestrain of 2% at room temperature. They found a yield point to return for all of the aging treatments considered, the upper and lower yield point stress increments increasing with time; see for example, Fig. 4.123 for the increase in stress associated with the upper yield points. Their results suggested that the aging occurred in the four stages depicted in Fig. 4.124. In Stage 1 the appearance of a yield point was essentially time independent. The aging behavior in Stage 2 was time dependent and could be described by the relation (see, for example, Fig. 4.125)

$$\Delta\sigma = \Delta\sigma_0 + \gamma t^{2/3} \quad (4.30)$$

where $\Delta\sigma$ is the difference between the designated yield point and the flow stress prior to aging, $\Delta\sigma_0$ the difference due to Stage 1, γ a constant which increased with temperature and t the time of aging.

Dynamic Strain Aging:

The following features of the deformation of commercial purity titanium in the intermediate temperature range have been identified by Reed-Hill and coworkers (Refs. 171,178,179,180,222,272,273) as evidence for the occurrence of dynamic strain aging:

- (1) Serrations in the stress-strain curves, i.e. the Portevin-Le Chatelier effect,
- (2) A plateau in the yield stress versus temperature curve,
- (3) An abnormally low strain rate sensitivity of the flow stress,

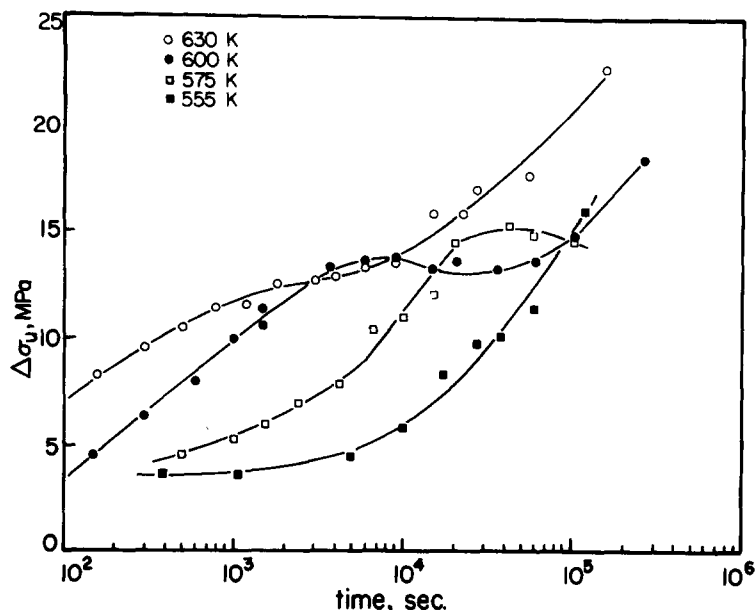


Fig. 4.123. The influence of aging time and temperature on the difference between the upper yield stress and the prior flow stress. From Donoso and Reed-Hill (Ref. 272).

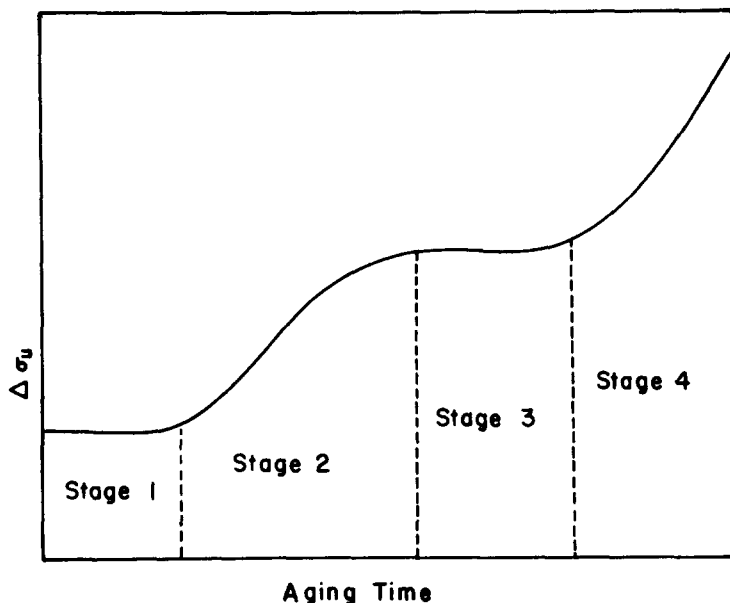


Fig. 4.124. Hypothetical strain aging behavior of commercial purity titanium. From Donoso and Reed-Hill (Ref. 272).

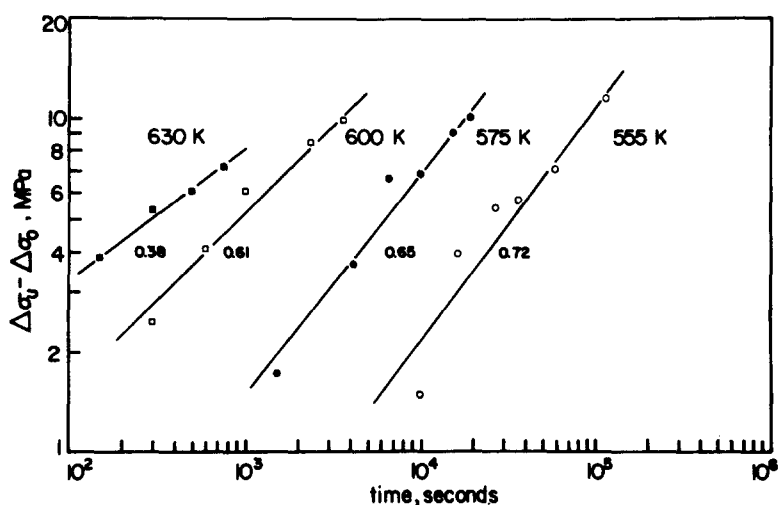


Fig. 4.125. Log-log plot of the return of the upper yield stress corrected for the initial time independent stress. The slope of each line is listed alongside of it. From Donoso and Reed-Hill (Ref. 272).

- (4) The appearance of flow stress transients when the strain rate is suddenly altered,
- (5) Abnormally high strain hardening and an abnormal strain rate dependence of this hardening,
- (6) Abnormally low ductility and an abnormal strain rate dependence of the ductility.

Examples of some of these phenomena are found in Figs. 4.40 to 4.43, 4.45 and 4.46. Examples of the occurrence of flow stress irregularities when the strain rate is altered in the intermediate temperature regime are given in Fig. 4.126 and 4.127. Abnormally high strain hardening is revealed by the appearance of a pronounced hump in the flow stress versus temperature curves in the plateau region; see, for example, Fig. 4.128. Anomalous effects of temperature and strain rate on the strain hardening and ductility of titanium are illustrated in Fig. 4.129. Garde, Santhanam and Reed-Hill (Ref. 171) and Reed-Hill (Ref. 178) point out that all of these phenomena are more pronounced in commercial purity compared to high purity titanium and attribute them to the presence of the interstitial solutes. Other manifestations of dynamic strain aging in titanium are the anomalous temperature dependence of the creep stress (Fig. 4.49) and of the fatigue stress (Fig. 4.122).

Recent studies by Donoso, Watson and Reed-Hill (Ref. 274) and Donoso, Santhanam and Reed-Hill (Ref. 275) have shown that decreasing the grain size in commercial purity titanium reduces the strength of the various manifestations of dynamic strain aging in titanium. Reductions in the work hardening peak and in the "blue brittle" effect by decreasing the grain size are clearly evident in Figs. 4.130 and 4.131 taken from their papers. Additional evidence for the occurrence of an increase in elongation (reduction in the "blue brittle" effect) with decrease in grain size at temperatures within the plateau region is depicted in Figs. 4.116 and 4.117. Donoso, Watson and Reed-Hill (Ref. 274) also found that decreasing the grain size led to reductions in the extent of the yield stress plateau, in the Portevin-

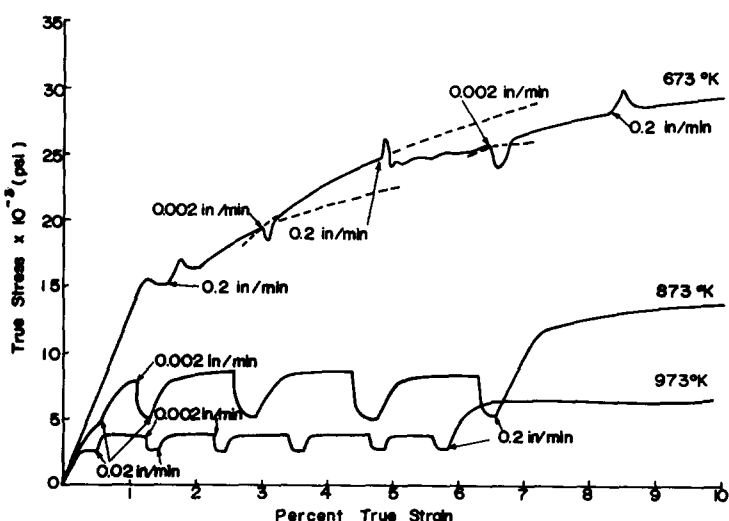


Fig. 4.126. Flow stress transients in commercial titanium when the strain rate is altered during tests at 673K. From Santhanam, Ramachandren and Reed-Hill (Ref. 222).

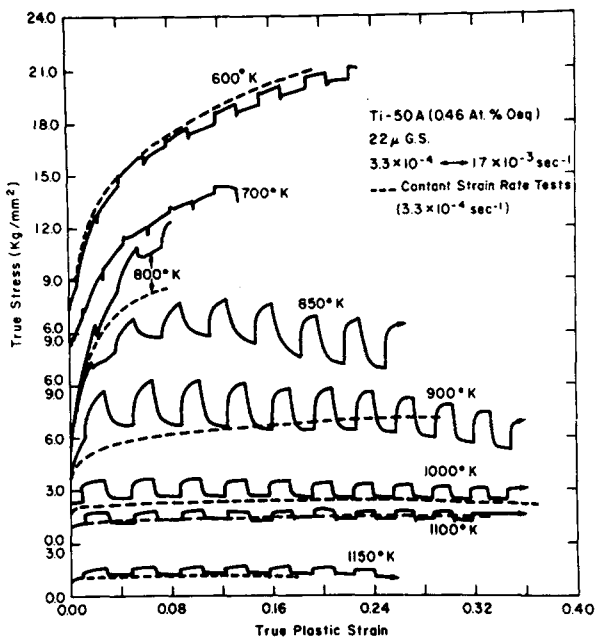


Fig. 4.127. Changes in stress due to strain rate cycling at 600-1150K, indicating flow stress transients at 600-800K. From Doner and Conrad (Ref. 163).

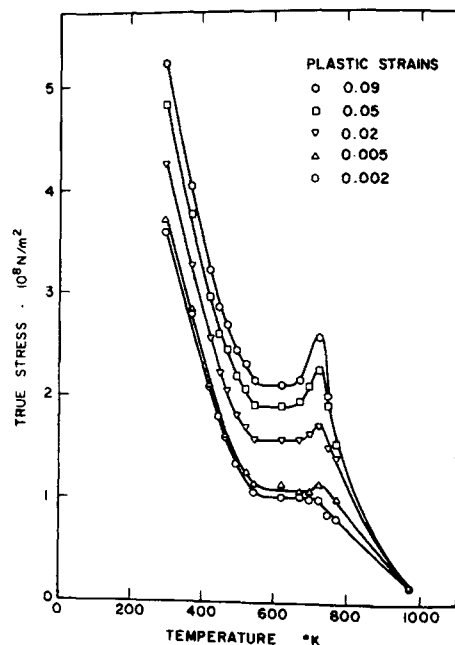


Fig. 4.128. Flow stress versus temperature as a function of strain for commercial purity titanium deformed at a strain rate of $2.7 \times 10^{-5} \text{ s}^{-1}$. Data of Santhanam (Ref. 177). From Reed-Hill (Ref. 178).

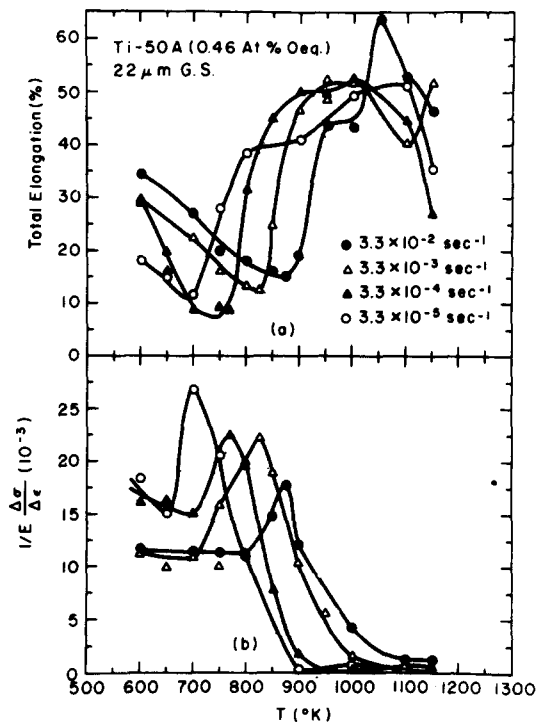


Fig. 4.129 Effects of temperature and strain rate on (a) the total elongation and (b) strain hardening of Ti-50A (~ 0.5 at. % O_{eq}). From Doner and Conrad (Ref. 163).

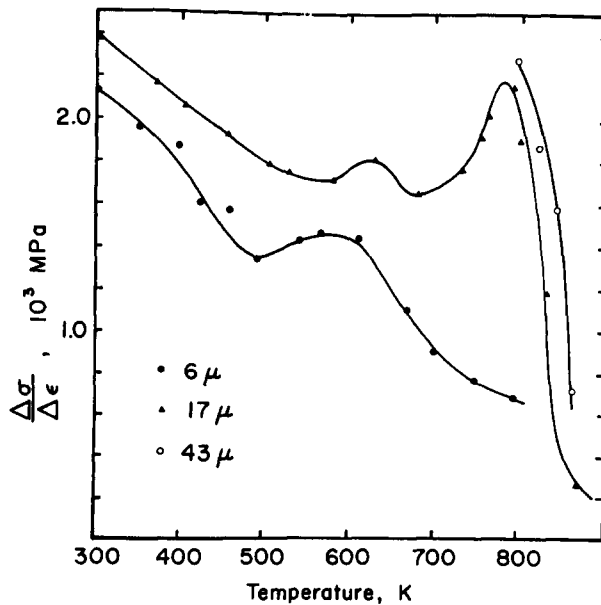


Fig. 4.130 Effect of grain size on the average work hardening rate ($\sigma_{0.05} - \sigma_{0.005}/0.045$) in commercial purity titanium (~ 0.5 at. % O_{eq}) as a function of temperature. From Donoso, Watson and Reed-Hill (Ref. 274).

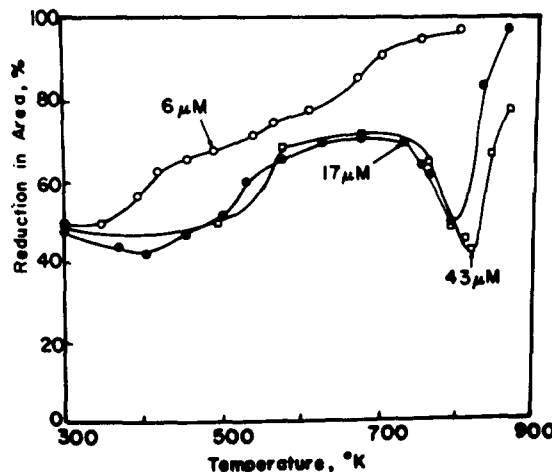


Fig. 4.131. Effect of grain size on the reduction in area in commercial purity titanium (~ 0.5 at. % O_{eq}) as a function of temperature strain rate = 5×10^{-4} s⁻¹. From Donoso, Santhanam and Reed-Hill (Ref. 275).

Le Chatelier effect, in the strain rate sensitivity index minimum (see also Fig. 4.74 of the present text) and in the flow stress transients following a strain rate change.

Sasano and Kimura (Ref. 276) report that the serrations observed in stress-strain curves of α -titanium are not necessarily due to the presence of interstitial solutes alone, but may be produced by substitutional solutes as well; see, for example, Fig. 4.132. They found that as the concentration of the substitutional solute was increased the amplitude of the serrations increased, especially at high strain rates. On the other hand, as the concentration of oxygen was increased in alloyed titanium, the amplitude also increased, but at low strain rates. Thus, they concluded that both substitutional and interstitial solute atoms affect serrated flow in titanium. In regard to the substitutional solutes, the serrations tended to be more pronounced the greater the size difference between the solute atoms and the titanium atoms. The magnitudes of the plateau yield stress and of the work hardening peak (Fig. 4.133) also increased in the order of the strength of the serrations and the atomic size difference.

Deformation Kinetics:

Arrhenius plots of the relationship between aging time and temperature to achieve given values for the yield point return during static strain aging of titanium are presented in Fig. 4.134. The data points for the lowest three temperatures lie on parallel straight lines whose slopes give $Q = 50.5 \pm 1.1$ Kcal/mole (2.19 ev). Donoso and Reed-Hill (Ref. 272) proposed that the reason that the data points at the highest temperature (630K) did not fit those for the lower three temperatures could be due to the fact that at 630K aging was very rapid and hence may have occurred during unloading and reloading, thereby biasing the results.

Arrhenius plots of the relationship between strain rate and temperature for various dynamic strain aging phenomena reported by Doner and Conrad (Ref. 163) are given in Fig. 4.135. The activation energy Q derived for (a) start of serrations,

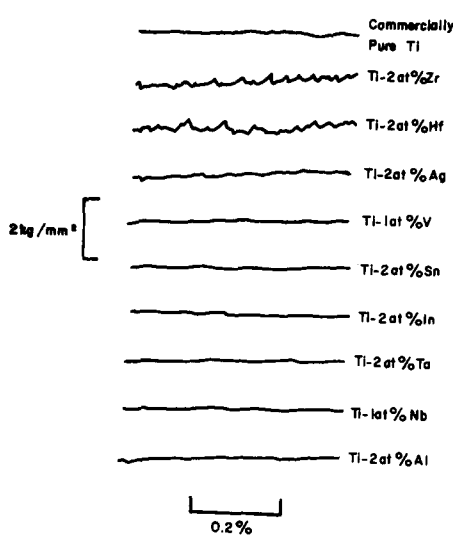


Fig. 4.132. Portions of the stress-strain curves of -titanium alloys (0.2-0.3 at.% O) at about 4% strain for tests at 663K. $\dot{\varepsilon} = 2.2 \times 10^{-4} \text{ s}^{-1}$. From Sasano and Kimura (Ref. 276).

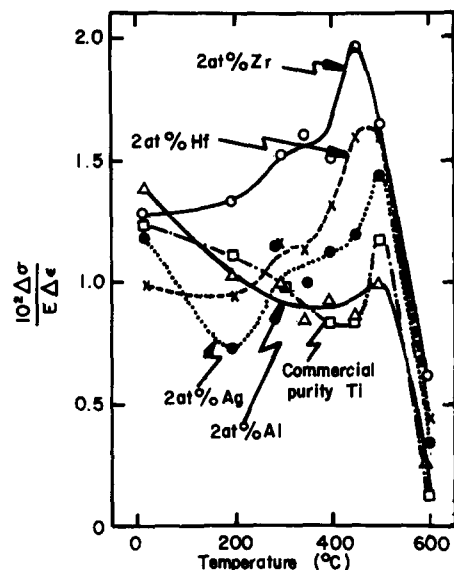


Fig. 4.133. Effect of substitutional solutes in titanium on the strain hardening rate as a function of temperature From Sasano and Kimura (Ref. 276).

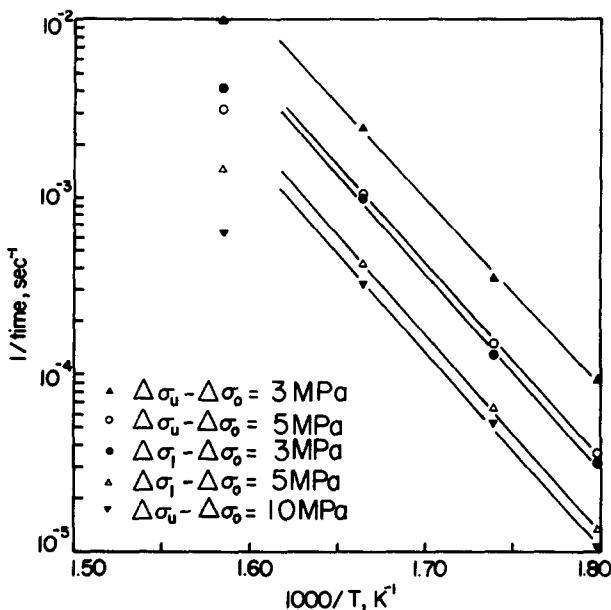


Fig. 4.134. Arrhenius plots of the times to achieve given values of the parameters $\Delta\sigma_u - \Delta\sigma_0$ and $\Delta\sigma_g - \Delta\sigma_0$ during the static strain aging of titanium. From Donoso and Reed-Hill (Ref. 272).

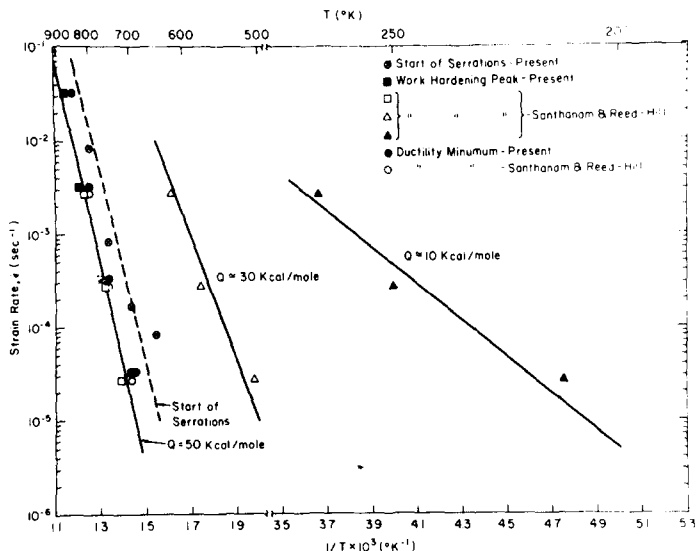


Fig. 4.135. Arrhenius plots for various dynamic strain aging phenomena in commercial purity titanium. From Doner and Conrad (Ref. 163).

(b) the high temperature work hardening peak and (c) ductility minimum is 50 Kcal/mole (2.17 ev). In comparison, Donoso, Santhanam and Reed-Hill (Ref. 275) reported $Q = 60$ Kcal/mole (2.60 ev) for their studies of the effects of strain rate and temperature on the ductility minimum in commercial purity titanium. Also included in Fig. 4.135 are two other strain hardening peaks located at 575 and 250K respectively for a strain rate of 2.7×10^{-4} s⁻¹. The values of Q associated with these peaks are approximately 30 and 10 Kcal/mole (1.30 and 0.43 ev) respectively.

An example of the relationship between strain rate and temperature for the appearance (lower critical temperature T_L) and the disappearance (upper critical temperature T_H) of serrations in stress-strain curves of dilute titanium alloys reported by Sasano and Kimura (Ref. 276) is given in Fig. 4.136. It is seen that both T_L and T_H increase with increasing strain rate. However, each critical temperature regime is divided into two segments, i.e. T_{L-1} and T_{L-s} and T_{H-1} and T_{H-s} , with T_{L-1} being essentially parallel to T_{H-1} and T_{L-s} parallel to T_{H-s} , yielding a parallelogram which encloses the region for the occurrence of serrations. The two sets of parallel lines yield activation energies of 7.1 and 59.4 Kcal/mole, (0.31 and 2.58 ev) respectively.

Fracture:

Donoso, Santhanam and Reed-Hill (Ref. 275) found that the fracture mode as observed by SEM was the same in fine grained specimens which did not exhibit a ductility minimum at a given temperature and strain rate as it was for coarse grained specimens which did. In both cases the fracture mode was microvoid coalescence. Further, they reported that most of the pores occurred at triple lines or at the junctions of three grain boundaries. They concluded that the voids had apparently nucleated at grain boundaries. They however did not determine whether the voids were nucleated by precipitates or inclusions along the grain boundaries.

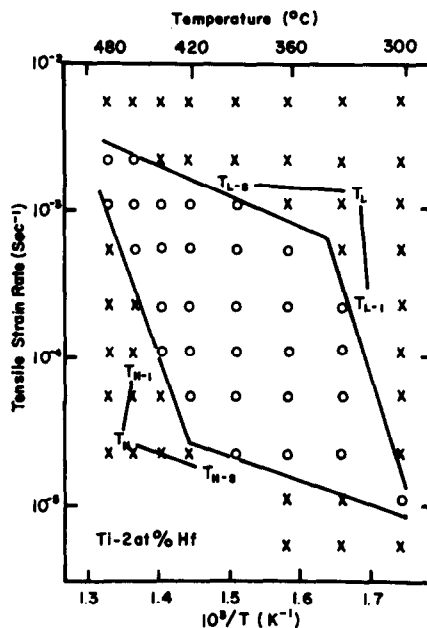


Fig. 4.136. Critical conditions for serrations in Ti - 2 at. % Hf alloy.
 O: Serrations are observed. X: Serrations are not observed. From Sasano and Kimura (Ref. 276).

4.2.6 High Temperatures ($T/T_m > 0.4$)

General:

As shown by Doner and Conrad (Ref. 163), high temperature deformation of titanium is characterized by small strain hardening (Fig. 4.40), high values of the strain rate sensitivity index $m = \partial \ln \sigma / \partial \ln \dot{\epsilon}$ (Fig. 4.137) and a strong effect of temperature on the flow stress, or on the strain rate for a constant flow stress (Figs. 4.42 and 4.138). These characteristics are typical of the high temperature deformation and rupture behavior of titanium (Refs. 186, 187, 277-280), and of other metals as well. Details regarding the inter-relationships between strain rate (or time to rupture), stress and temperature are covered in the section to follow on deformation kinetics at high temperatures.

In general, the ductility increases appreciably with temperature upon entering this temperature region; see, for example, Figs. 4.46 and 4.131. However, the results of Doner and Conrad (Ref. 163) reveal that a decrease may occur just below the $\alpha \rightarrow \beta$ transition (Fig. 4.129). The results of stress rupture tests (Refs. 187, 280) indicate that the ductility in such tests is similar to that for standard constant crosshead speed tension tests at the same test temperature.

Deformation Kinetics:

A log-log plot of the effect of stress on the minimum creep rate $\dot{\epsilon}_s$ of A-75 Ti (~1.0 at. % Oeq) in the temperature range of 644 to 922K is presented in Fig. 4.139. In the temperature range of 644-755K the curves exhibit some curvature, but are reasonably straight at 811K and above, with a slope of 4. An Arrhenius plot of

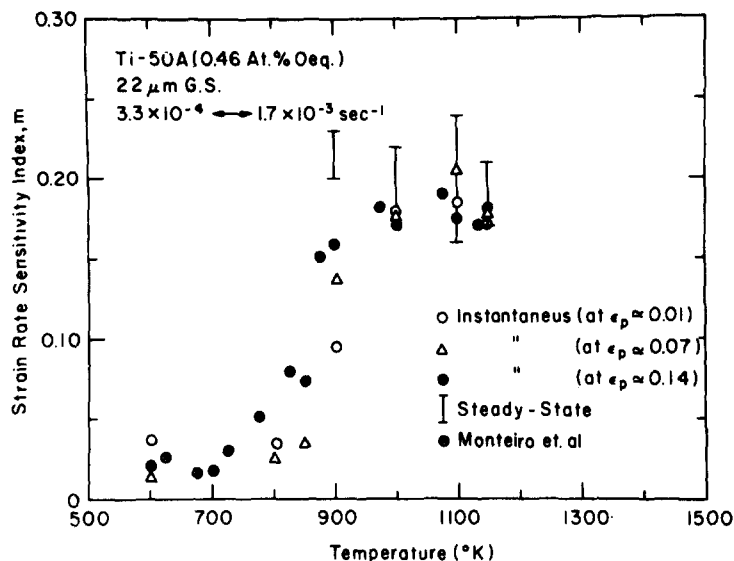


Fig. 4.137. Effect of temperature on the strain rate sensitivity index $m = (\partial \ln \sigma / \partial \ln \dot{\epsilon})_T$. From Doner and Conrad (Ref. 163).

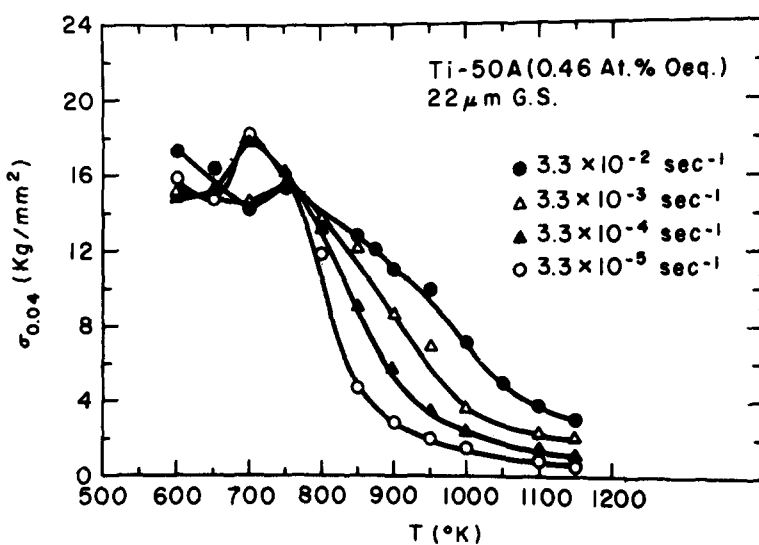


Fig. 4.138. Effect of temperature on the flow stress at 4% strain for commercial purity titanium at various strain rates. From Doner and Conrad (Ref. 163).

the creep rate at several stresses taken from Fig. 4.139 is presented in Fig. 4.140, giving parallel straight lines whose slopes yield an activation energy $Q = 71 \text{ Kcal/mole}$ (3.1 eV). In their studies on the minimum creep rate in commercial titanium of ~0.5 at. % O, Kehoe and Broomfield (Ref. 279) found the stress exponent to decrease with stress from 6 at low stresses to 4.5 at high stresses. The value of Q obtained by them ranged between 68 - 72 Kcal/mole (2.95 - 3.12 eV), decreasing slightly with increasing stress.

Orr, Sherby and Dorn (Ref. 280) have shown that stress-rupture data for titanium over the temperature range of 700-1033K correlate through the relation

$$\sigma_F = f(t_r \exp. - \frac{Q}{RT}) \quad (4.31)$$

where t_r is the time to rupture and Q ranged from 60 to 80 Kcal/mole (2.6 - 3.5 eV), the higher value of Q being associated with less pure material. Their plot of σ_F versus $\log(t_r \exp. - \frac{60,000}{RT})$ for the stress-rupture data of Cuff and Grant (Ref. 187) is shown here in Fig. 4.141.

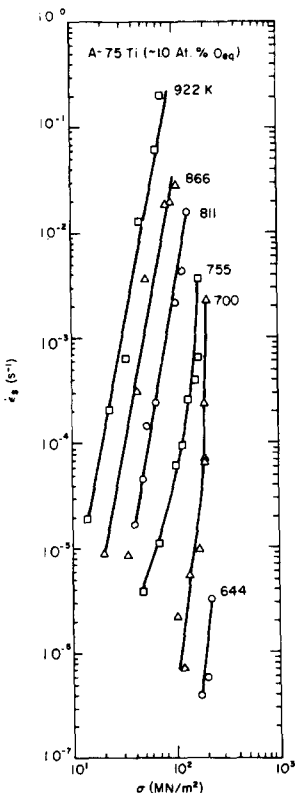


Fig. 4.139. Log-log plot of minimum creep rate versus stress of A-75 Ti at 700-922K. Data from Cuff and Grant (Ref. 187).

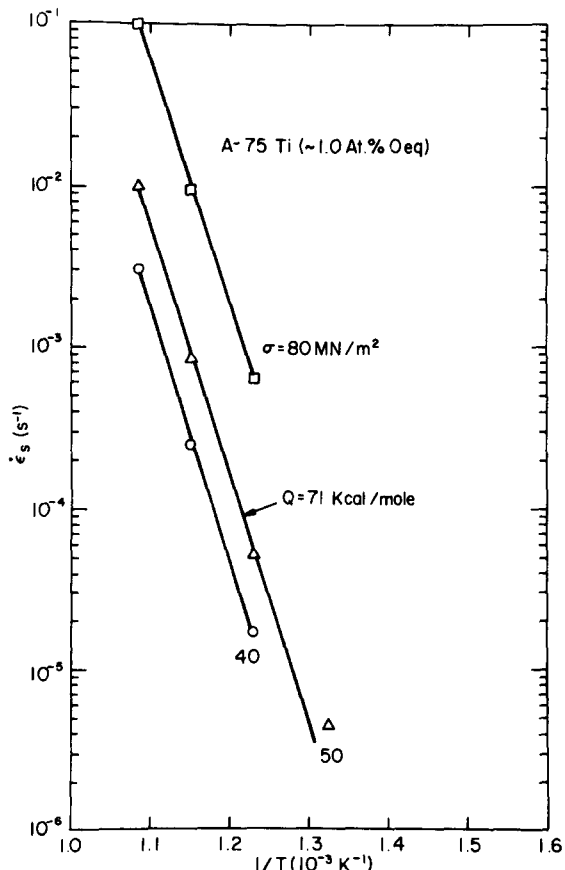


Fig. 4.140. Arrhenius plot of minimum creep rate of A-75 Ti for three stresses. Data from Cuff and Grant (Ref. 187).

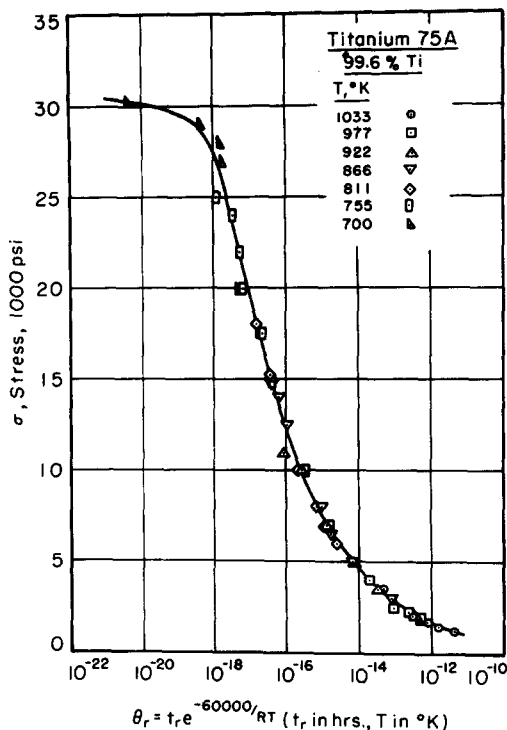


Fig. 4.141. Correlation of the stress rupture data of Cuff and Grant (Ref. 187) through the relation $\theta_r = f(\sigma)$. From Orr, Sherby and Dorn (Ref. 280).

4.2.7 Summary of Deformation Kinetics

A summary plot of Q versus temperature for the plastic flow of α -titanium at a strain rate of $\sim 10^{-4} \text{ s}^{-1}$ in the temperature range of 4.2–925K is presented in Fig. 4.142. The shaded region gives the range in values obtained, some of which appears to be related to interstitial content, especially for $C_i \leq 0.2 \text{ at. \%}$ in the region of 300–400K. Otherwise, no clear consistent effect of interstitial content on Q was evident, suggesting that a good part of the scatter results from the determination of the deformation partials $\partial \ln \dot{\epsilon} / \partial \sigma$, $\partial \sigma / \partial T$ and $\partial \ln \dot{\epsilon} / \partial (1/T)$.

It is seen in Fig. 4.142 that starting from absolute zero, Q increases with temperature (with a positive curvature), reaching a value of about 3.0–3.2 eV at 600–650K ($\sim 0.3 T_m$), and then appears to remain constant with further increase in temperature to the $\alpha \rightarrow \beta$ transition (1156K). However, data are lacking in the range of 600–800K, and above 975K, to be sure of the constancy of Q over the entire temperature range of 600K to the α – β transition temperature. Also to be noted in Fig. 4.142 is that the curve representing the average values of Q for prism glide in the temperature region of 0–600K lies wholly within the range of values for the plastic deformation of polycrystalline titanium, suggesting that the rate controlling deformation mode in polycrystalline titanium is prism glide. Finally, it should be noted that over the entire temperature range the curve of Q versus temperature representing the various dynamic strain aging phenomena lies below (or

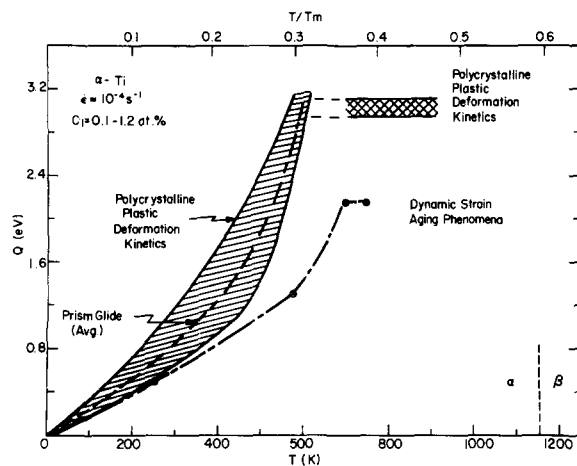


Fig. 4.142. Summary plot of Q versus temperature for the plastic deformation of polycrystalline α -titanium.

on the low side) of that for deformation which presumably does not include strain aging effects.

5. MODELS AND MECHANISMS

This chapter deals with the interpretation of the experimental data presented in Chapter 4 in terms of current models and mechanisms for the mechanical behavior of crystalline solids.

5.1 Low Temperatures ($T < 0.3 T_m$)

5.1.1 Serrations in Stress-Strain Curves at 4.2K

Criterion for Plastic Instability:

Similar to the behavior of many metals, load drops or serrations occur in the stress-strain curves of polycrystalline titanium deformation at 4.2K. Serrations have been found to occur both at the first indication of plastic flow at 4.2K and after some strain at this temperature (Refs. 173-175). The individual load drops vary in magnitude but outline an upper and a lower envelope whose separation (difference in stress) increases with strain. The difference in stress between the envelopes also increases with decrease in grain size and increase in interstitial content (Fig. 4.57). It has been found that twinning occurs both before and after the onset of serrations in polycrystalline titanium specimens (Refs. 173, 174), indicating that twinning alone is not responsible for the load drops in this material. This has also been found to be the case for polycrystalline zirconium (Ref. 281).

It is now generally agreed that the load drops which occur during the plastic deformation of metals at 4.2K are caused by localized adiabatic heating and result from the peculiar conditions of low heat capacity and large temperature dependence of the flow stress which exist at very low temperatures (Refs. 282, 283). Supporting this concept is the experimental observation that the temperature starts to rise when the load drops (Refs. 283-285). Also, reasonable agreement has been found between calculated and experimental values of the temperature rise and the magnitude of the load drops (Ref. 283). Further, Bazinski (Ref. 283) has shown that the load drop occurs in about 1.5×10^{-4} s and that reasonable agreement between the calculated load drop and that measured experimentally is obtained for a plastic zone length which is about 1 to 3 times the diameter of the specimen.

Kula and DeSisto (Ref. 173) expanded the analysis by Chin, Hosford and Backofen (Ref. 286) for the initiation of adiabatic shear and arrived at the following equation for the occurrence of localized plastic flow

$$dP = Ad\dot{\epsilon}[(\partial\sigma/\partial\epsilon) - \sigma + (\partial\sigma/\partial\dot{\epsilon})d\dot{\epsilon}/d\epsilon + (\partial\sigma/\partial T)dT/d\epsilon] \quad (5.1)$$

where P is the load on a bar undergoing uniaxial straining and A the instantaneous area; the other symbols have their usual meaning. Plastic instability occurs when dP first becomes zero, and then sufficiently negative so that it is equal to the relaxation of the load by the test machine, which is given by

$$dP_M = -K_M d\epsilon \quad (5.2)$$

where K_M is the combined spring constant of the specimen and machine and $d\ell$ is the length change associated with the strain $\delta\epsilon$. The increase in temperature with strain is given by

$$dT/d\epsilon = \alpha\sigma/\rho_s c \quad (5.3)$$

where α is the fraction of the work of plastic deformation which is converted into heat and retained in the deforming region, ρ_s the density of the specimen and c its specific heat.

Kula and DeSisto (Ref. 173) took as the condition for the initiation of plastic instability that $dP = 0$. Neglecting strain rate effects (which are expected to be negligibly small at 4.2K), one then obtains from Eq. 5.1

$$(\partial\sigma/\partial\epsilon) - \sigma \leq - (\partial\sigma/\partial T)(\alpha\sigma/\rho_s c) \quad (5.4)$$

as the criterion for the occurrence of load drops at very low temperatures. In a more recent analysis of the onset of thermal instability, Culver (Ref. 287) took $d\sigma/d\epsilon = (1/A)(dP/d\epsilon) = 0$ as the criterion for instability, giving

$$\partial\sigma/\partial\epsilon < - (\partial\sigma/\partial T)(\alpha T/\partial\epsilon) \quad (5.5)$$

Rearranging Eq. 5.1 and again neglecting the strain rate hardening term, one obtains for the stress at which discontinuous flow first occurs

$$\sigma_c \geq \frac{[(\frac{\ell_z}{\ell_g}) E_M + \frac{\partial\sigma}{\partial\epsilon}]}{[-(\frac{\partial\sigma}{\partial T})(\frac{\alpha}{\rho_s c}) + 1]} \quad (5.6)$$

which is equivalent to that by Chin, Hosford and Backofen (Ref. 286). Here ℓ_z is the plastic zone length, ℓ_g the specimen gage length and E_M the effective machine-specimen modulus ($= (dP/A)/d\epsilon$).

A comparison of available experimental data for the deformation of titanium at 4.2K with the conditions set forth in Eqs. 5.4 to 5.6 is presented in Table 5.1. It is seen that in every case the conditions are already favorable by several orders of magnitude for discontinuous yielding to occur at the yield stress in both single crystals and polycrystals of titanium deformed at 4.2K (Refs. 173-175, 288). The fact that load drops do not necessarily occur at the yield stress even though the conditions of Eqs. 5.4 to 5.6 are met has been attributed to the difficulty of nucleating a region of plastic instability. For example, Bazinski (Ref. 283) and Chin, Hosford and Backofen (Ref. 286) found that a load drop could be induced, when none occurred otherwise, by gently tapping the test machine.

Magnitude of Stress Drop:

A check on Eq. 5.1 can be made by expressing it in the following form

$$\Delta\sigma = [(\frac{\partial\sigma}{\partial\epsilon}) \beta_1 \Delta\epsilon + (\frac{\partial\sigma}{\partial \ln\dot{\epsilon}}) \Delta\ln\dot{\epsilon}] + [-\sigma\beta_2 \Delta\epsilon + (\frac{\partial\sigma}{\partial T}) \Delta T] \quad (5.7)$$

where $\Delta\sigma = \Delta P/A = (\sigma_1 - \sigma_2)$ is the drop in stress; β is the ratio of specimen gage length ℓ_g to the length of the plastic zone ℓ_z ; $\Delta\epsilon = -\Delta\sigma/E_M$ is the plastic strain associated with the load drop, where $E_M = P\ell_g/A\Delta\ell$ is the combined specimen-machine modulus; $\Delta\ln\dot{\epsilon} = \ln(\dot{\epsilon}_2/\dot{\epsilon}_1)$ represents the increase in the strain rate of the plastic

TABLE 5.1 Experimental data relating to the criterion for load drops during the plastic deformation of Ti at 4.2K.

Mater.	σ_{eq}	Spec.	G.S.	$\sigma(0.2\%)$	$\frac{\partial \sigma}{\partial \epsilon}$	(a)	(b)	(c)	(c)	(f)
	at.-%	Dia. d mm	μm	MN/m^2	MN/m^2	MN/m^2	$MN/m^2 -K$	$10^5 MN/m^2$	σ_c	Ref.
MARZ	0.05	3x1.5	Single Crystal	210 (d)	696	486	0.62	1.9	5.2	(1)
	0.15	1.61	1	711	3185	2474	2.16	22.2	2.3	(2)
	0.15	1.55	23	319	2858	2539	0.32	1.5	14.8	(2)
A-50	0.46	1.25	2	947	2613	1666	2.20	30.0	2.1	(2)
		1.30	22	725	3103	2378	1.94	30.3	2.5	(2)
A-70	1.0	1.24	1	1421	1307	-114	3.18	65.5	1.2	(2)
		1.31	16	1225	1782	557	3.18	56.5	1.3	(2)
Comm.Ti	0.5 (e)	6.35	-	869	2840	1971	2.48	31.2	1.9	(3)
A-50 (e)	0.5 (e)	2.55	500	715	2571	1856	2.0 (e)	20.7	2.3	(4)

Notes:

- (a) $\frac{\partial \sigma}{\partial \epsilon}$ = slope of best straight line through upper envelope of the stress serrations.
 (b) $\frac{\partial \sigma}{\partial T} = (\sigma_{4.2} - \sigma_{78})/74$.
 (c) $\alpha = 0.5$; $\frac{E_z}{E_g} \approx \frac{1}{2} d/l_g \approx 0.1$; $E_m = 4 \times 10^4 MN/m^2$; $\frac{Q_c}{T} = 3.45 \times 10^2 N/m^2 -K$, based on value at 15K in A.D. McQuillan and M.K. McQuillan, Titanium, Academic Press, New York (1956) p. 143, and taking c proportional to T.
 (d) Yield stress at 4.2K after prior deformation at 298 and 77K.
 (e) Estimated values based on yield stress.
 (f) Sources for the data used:
 (1) T. Tanaka and H. Conrad, Acta Met. 20 1019 (1972)
 (2) H. Conrad, T. Tanaka and C. Yin, Unpublished research, University of Kentucky (1978)
 (3) E. B. Kula and T.S. De Sisto, ASTM STP 387 Behavior of Materials at Cryogenic Temperatures (1966) p.3.
 (4) N. M. Madhava and R. W. Armstrong, Met. Trans. 5 1517 (1974).

zone ℓ_2 compared to the overall specimen strain rate $\dot{\varepsilon}_1$. $\dot{\varepsilon}_2 = \beta_2(-\Delta\sigma/E_M)/t$, where t is the time in which the load drop occurs. The first two terms on the right hand side (R.H.S.) of Eq. 5.7 give the hardening associated with a load drop; the last two terms give the softening. Knowing the values of the quantities on the R.H.S., one can calculate $\Delta\sigma$ and compare the calculated value with that determined experimentally.

A comparison between $\Delta\sigma$ calculated using Eq. 5.7 and the experimental value is presented in Fig. 5.1 for various titaniums, reflecting the influence of strain,

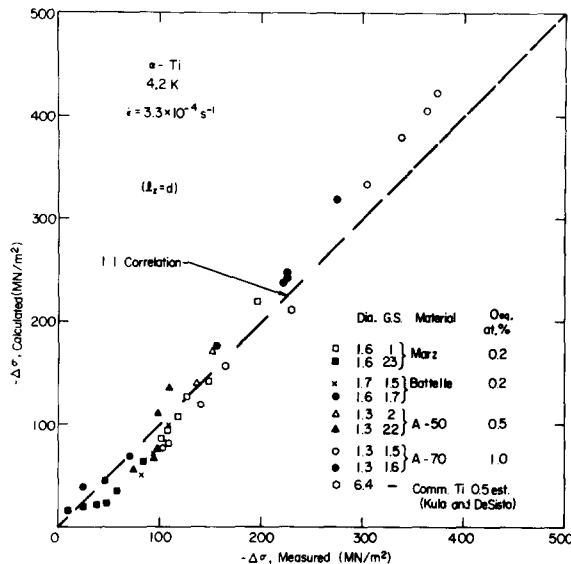


Fig. 5.1 Comparison of calculated values for stress drops in titanium deformed at 4.2K with those measured experimentally. Data from Refs. 173, 175.

grain size, interstitial content and specimen diameter. The values used for the various quantities on the R.H.S. of Eq. 5.7 were the following: $\partial\sigma/\partial\varepsilon$ was taken as the average slope of the upper envelope of the serrated true stress-strain curve. β_1 was taken equal to one and $\beta_2 = \ell_g/d$, where ℓ_g is the instantaneous specimen gage length and d the instantaneous specimen diameter. E_M was taken from the rising portion of the load-displacement curve following a stress drop. $\partial\sigma/\partial T$ was taken from the decrease in the 0.2% yield stress with temperature above 4.2K at the strain rate $\dot{\varepsilon}_1$ (e.g. from curves such as those in Fig. 4.60) and was assumed to be independent of strain, based on the results given in Chapter 4. The value of ΔT was obtained by equating the plastic work ΔW converted to heat and retained in the specimen during a load drop to the thermal energy ΔQ required for a temperature rise ΔT and then solving for ΔT . ΔW was taken to be

$$\Delta W = \alpha \sigma_e \beta_2 \Delta \varepsilon = \alpha \beta_2 \sigma_e (-\Delta\sigma/E_M) \quad (\text{N/m}^2) \quad (5.8)$$

where α ($=0.5$) is the fraction of the total plastic work which is converted to work and retained in the specimen (Ref. 173) and $\sigma_e = (\sigma_1 + \sigma_2)/2$ is the average stress during the load drop. ΔQ is given by

$$\Delta Q = \int_{4.2}^T c dT \quad (5.9)$$

In the range 4.2-100K the heat capacity c for titanium is approximated by (see Fig. 5.2)

$$c = 1.75 \times 10^4(T - 24) \quad (\text{N/m}^2\text{K}) \quad (5.10)$$

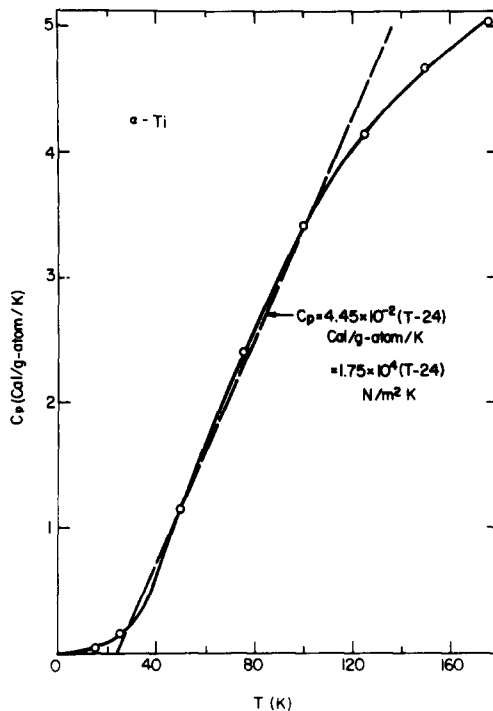


Fig. 5.2 Specific heat of titanium versus temperature.
Data from McQuillan and McQuillan (Ref. 9).

Substituting Eq. 5.10 into Eq. 5.9 and integrating gives

$$\Delta Q = 0.875 \times 10^4(T - 24)^2 \quad (\text{N/m}^2) \quad (5.11)$$

Setting $\Delta Q = \Delta W$ and solving for ΔT then gives

$$\Delta T = 24 + (1.14 \times 10^{-4} \Delta W)^{1/2} \quad (5.12)$$

The values of ΔT so obtained for the materials of Fig. 5.1 ranged from 33-136K.

The three remaining quantities in Eq. 5.7 are σ , $\partial\sigma/\partial\ln\dot{\epsilon}$ and $\dot{\epsilon}_2$. σ was taken to be σ_e and the value of t to obtain $\dot{\epsilon}_2$ was taken to be $1.5 \times 10^{-4}\text{s}^{-1}$ based on the measurements of Bazinski (Ref. 283). Using this value of t , the values of $\dot{\epsilon}_2$ for the various titanium specimens ranged between 3×10^1 and $1 \times 10^3\text{s}^{-1}$. The values of $\partial\sigma/\partial\ln\dot{\epsilon}$ were taken from the strain rate cycling test results presented in Fig. 4.74 at the temperature $(4.2 + \Delta T)$. This quantity was assumed to be independent of strain and grain size for a given interstitial content, which on the basis of

the results in Chapter 4 is a reasonable assumption. Also, it was assumed to be constant over the entire strain rate range considered, namely 10^{-4} to 10^3 s^{-1} ; see Fig. 4.44 for possible errors due to this assumption.

Fig. 5.1 shows fairly good agreement between the calculated and measured values of $\Delta\sigma$ for the various titanium materials, which represent significant differences in specimen diameter, grain size and interstitial content. This provides some support for the validity of Eq. 5.7 and further that the length of the region which undergoes plastic instability is of the order of the specimen diameter, in keeping with Bazinski's calculations for 24S aluminum alloy (Ref. 283). However, there is one aspect of the analysis which is questionable, namely that in order to obtain the agreement indicated in Fig. 5.1, β_1 had to be taken equal to unity rather than to $\ell g/d$, i.e. ($=\beta_2$). Use of $\ell g/d$ for β_1 led to calculated values of $\Delta\sigma$ which were considerably less than those measured, especially for the higher purity materials, which had large values of $\partial\sigma/\partial\epsilon$ and low values of σ_e .

Agreement between calculated and measured values of $\Delta\sigma$ on the order of that indicated in Fig. 5.1 also occurred when the plastic zone length was taken as twice the specimen diameter (i.e. $\ell_z = 2d$), and both strain hardening and strain rate hardening were neglected, i.e. the two terms in the first bracket on the R.H.S. of Eq. 5.7 were neglected. When ℓ_z was taken to be $3d$ or greater, the calculated values of $\Delta\sigma$ became significantly less than those measured even though strain hardening and strain rate hardening were neglected. Thus, to obtain reasonable agreement between the measured and calculated values of $\Delta\sigma$ using Eq. 5.7 the plastic zone length ℓ_z had to be taken between $1d$ and $3d$, and strain hardening in the zone to be relatively small; further, for $\ell_z \geq 2d$, strain rate hardening had to be neglected as well:

Metallographic examination of titanium specimens following discontinuous plastic flow at 4.2K revealed that twinning had occurred in all cases (Refs. 173-175). However, the magnitude of the load drop was not directly related to the amount of twinning, for larger load drops occurred as the grain size was reduced or the interstitial content increased, both of which reduced the amount of twinning (Ref. 175). Further, as mentioned above, in some cases twinning was observed prior to the onset of load drops in titanium (Refs. 173, 174). Nevertheless, twinning appears to play some role in discontinuous flow in titanium at 4.2K, because serrations were not observed in tests at this temperature on a polycrystalline Ti-7.4 at.% Al alloy, in which twinning is significantly inhibited (Ref. 289). Also, Madhava and Armstrong (Ref. 174) attribute anomalous differences in load drops between titanium and steel to the difference in twinning behavior between the two metals. It may be that twinning assists in the nucleation of the avalanche of plastic flow which leads to a load drop. It is not clear why a critical amount of twinning is needed before this nucleating action occurs in titanium and zirconium.

5.1.2 Prism Glide - Solid Solution Strengthening by Interstitials

Nature of Interstitial Solute Obstacles:

The experimental results presented in Chapter 4 revealed that the flow stress of titanium single crystals and polycrystals at low temperatures increases markedly with interstitial solute content, the effect becoming larger as the temperatures is lowered. Concurrent with the increase in flow stress there occurs an increase in the strain rate sensitivity of the flow stress with interstitial content. The influence of interstitials on the flow stress and its strain rate sensitivity is relatively independent of strain, indicating that the interstitial solute atom obstacles are more subject to thermal activation than the forest dislocations. It was also shown in Chapter 4 that there exists rather good accord between the

critical resolved shear stress for prism glide and both the thermal component of the flow stress σ^* and the Hall-Petch lattice friction stress σ_j for the yielding of polycrystals (especially for small grain sizes and/or high interstitial contents) when a Taylor orientation factor $M = 2.5$ is employed to convert the tensile stresses to their respective shear stresses. Further, the deformation kinetics parameters for the plastic flow of polycrystals are in agreement with those for prism glide in single crystals. All of these results lead to the conclusion that the principal deformation mode during the plastic flow of titanium polycrystals is glide on the first order prism planes and that the principal rate controlling mechanism is the thermally activated overcoming of interstitial solute atom obstacles.

It follows from Eq. 3.78 that when a single set of discrete obstacles controls the flow stress, the reciprocal of the activation volume v is proportional to the increase in the thermal component of the flow stress $\tau^* = (\tau - \tau_0)$ produced by the addition of the obstacles. To check this for interstitials in titanium, the parameter $\frac{1}{T} \left(\frac{\Delta \tau}{\Delta \ln v} \right)$, which is equal to k/v (k = Boltzmanns constant), is plotted in Fig.

5.3 versus the increase in $\tau^*(C_i)$ produced by the addition of the interstitial

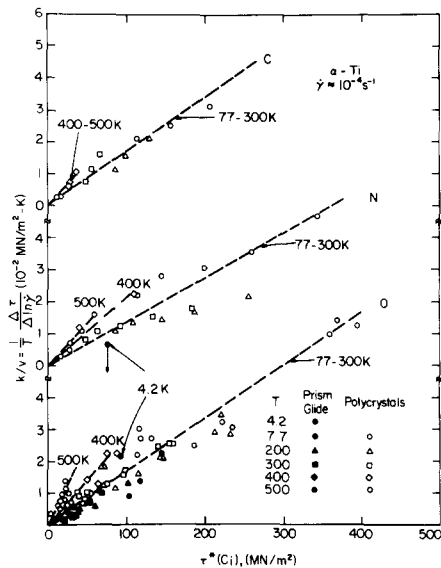


Fig. 5.3 $\frac{1}{T} \frac{\Delta \tau}{\Delta \ln \gamma}$ versus $\tau^*(C_i)$ as a function of temperature for C, N, and O. Data from Chapter 4.

solute C, N and O to titanium. The use of τ^* for this plot rather than the total flow stress τ eliminates the effects of strain and grain size on τ_u . Fig. 5.3 shows that within the scatter of the data the reciprocal of the activation volume can be considered to be proportional to $\tau^*(C_i)$, the proportionality constant being relatively independent of temperature between 77-300K, but increasing at lower and higher temperatures. The results in Fig. 5.3 thus suggest that a single set of obstacles is rate controlling at each temperature. Thermodynamic considerations (Refs. 24, 25) indicate that the interstitial obstacles are randomly dispersed solute atoms. However, Eissner, Krohn and Ruano (Ref. 145) propose that clusters of interstitial solute atoms also exist. Using a weak-beam electron microscopy technique (Refs. 95, 145, 290), they observed clusters in Zr and Hf alloys

containing about 1 at.-% oxygen. In zirconium, roughly 50% of the oxygen was found to be in clusters of about 6 nm diameter separated by 76 nm in the slip plane. In hafnium, the clusters were also about 6 nm diameter but were separated by about 120 nm.

Considering the electron microscopy observations on Zr and Hf and the abrupt changes in the slopes of the yield stress versus temperature curves which occurred in their titanium specimens at ~300K (see, for example, Fig. 4.11), Elssner, Krohn and Ruano (Ref. 145) concluded that there exists a spectrum of obstacles to prism glide in titanium. They further proposed that at high temperatures ($T > 300K$) the flow stress of dilute Ti-O alloys is determined by solute atom clusters, which represent strong obstacles to dislocation glide; the obstacles associated with individual solute atoms being much weaker are transparent to the dislocation motion at these temperatures. At low temperatures ($T < 300K$), the strong obstacles (clusters) become athermal and the flow stress is then controlled by the weaker, individual solute atom obstacles. The results of Fig. 5.3, which indicate that a single set of obstacles is rate controlling at each temperature, do not preclude this idea, because one set of obstacles (individual solute atoms) may be rate controlling at 300K and below, and another set (e.g. clusters) at the higher temperatures.

Thus, the possibility that clusters may exist in titanium and influence the strengthening must be taken into consideration in any analysis of solid solution strengthening by interstitial solutes. It should however be pointed out that, since the flow stress increases with interstitial content both below and above the transition temperature of ~300K, the model proposed by Elssner, Krohn and Ruano (Ref. 145) requires that both the concentration of interstitials in solid solution and that associated with clusters increase continuously as the total interstitial content is increased. The linear increase in electrical resistivity of Ti, Zr and Hf with oxygen content up to ~1 at.-% (Ref. 145) might then suggest that the relative distribution of the oxygen between clusters and matrix remains nearly constant as the concentration is increased.

Concentration Dependence of the Strengthening:

Insight into the mechanism by which solutes strengthen a crystalline solid is obtained from the concentration dependence of the strengthening. The fact that the strengthening of titanium by interstitials appeared parabolic in form had earlier suggested to Conrad, de Meester, Doner and Okazaki (Ref. 3) that the model of Fleischer (Ref. 74) and Friedel (Ref. 77) which leads to $C_i^{1/2}$ dependence (Eq. 3.29), or that of Labusch (Refs. 86, 100) which leads to a $C_i^{2/3}$ dependence (Eq. 3.34) might apply. In an attempt to ascertain which of these two types of models describe the strengthening of titanium by interstitial solutes, they plotted the flow stress versus $C_i^{1/2}$ and versus $C_i^{2/3}$. The data available at the time gave a reasonable fit to a straight line in both cases, so that they were unable to clearly identify the concentration dependence. However, because of the high value of strengthening coefficient $d\tau/dC_i$, these authors concluded that the strengthening was of the Flesicher-Friedel (F-F) type. Assuming the F-F model to apply, they then obtained reasonable agreement between experimentally derived values and theoretical predictions for the dislocation-solute atom interaction energy and force, and for the relative order of the strengthening effect of the three interstitials C, N and O. Additional data on the concentration dependence of the strengthening have become available since the writing of the earlier paper (Ref. 3). It is therefore desirable to look again into the concentration dependence of the strengthening of titanium by interstitials to see whether any further insight into its nature can be obtained.

The effects of the total (O+N+C) content on τ_{crss} for prism glide in single

crystals and on σ_i and σ^* for the yield stress of polycrystals were shown in Figs. 4.75 and 4.76. The total interstitial content was taken in these figures so that materials for which there existed only one (or at most two) additions of a specific interstitial solute could be included in the comparison and because previous studies (Table 4.5) indicated that the relative strengthening of the three solutes did not differ appreciably. However, to identify more rigorously the concentration dependence of the solid solution strengthening the effects of each solute need to be evaluated separately. This is especially important for interstitial solutes in titanium, because we are dealing with relatively low concentrations (<1 at. %) and because the initial, high purity starting materials generally contain significant quantities of residual interstitial solutes in addition to the one being considered. The detailed effects of these residual solutes on the flow stress will depend on the operative solid solution strengthening model. Hence, to eliminate these effects the approach here is to assume a specific model and then see whether the results obtained are consistent with the model.

The concentration dependence of the interstitial solute strengthening of titanium will now be considered in terms of three common solid solution strengthening models:

$$\text{Fleischer-Friedel (F-F): } \tau^* = \alpha_1 \mu k^{*3/2} C_i^{1/2} \quad (3.29a)$$

$$\text{Labusch (L): } \tau^* = \alpha_2 \mu k^{*4/3} C_i^{2/3} \quad (3.34a)$$

$$\text{Friedel-Mott (F-M): } \tau^* = \alpha_3 \mu k^{*n} C_i^n \quad (3.38a)$$

where α is a constant of the order of unity, $k^* = f_i^*/2E_L$ and $n=1-2$. When there exist additional obstacles which act in a similar way as the solute atom species under consideration, the following forms of the above three equations are recommended (Ref. 291):

$$\text{Fleischer-Friedel (F-F): } \tau^{*2} = [\tau^*(C_i=0)]^2 + A_1^2 C_i \quad (5.13)$$

$$\text{Labusch (L): } \tau^{*3/2} = [\tau^*(C_i=0)]^{3/2} + A_2^{3/2} C_i \quad (5.14)$$

$$\text{Friedel-Mott (F-M): } \tau^* = \tau^*(C_i=0) + A_3 C_i \quad (5.15)$$

where A_1 , A_2 and A_3 are the coefficients associated with C_i in Eqs. 3.29a, 3.34a and 3.38a and $\tau^*(C_i=0)$ gives the contribution to the flow stress by the additional obstacles due to the residual solute atoms.

Plots of τ_{crss} and τ_i ($=\sigma_i/2.5$) versus the concentration of a specific interstitial solute according to Eqs. 5.13 to 5.15 for those cases where controlled additions of one solute were made to a single high purity starting material (Refs. 12, 19, 145, 175, 209, 210, 212) are presented in Figs. 5.4 to 5.6. To be noted is that in Fig. 5.5 ($\tau^{3/2}$ versus C_i) the data conform reasonably well to straight lines for all cases. In Fig. 5.4 (τ^* versus C_i), the curves for oxygen and nitrogen show a distinct positive curvature, whereas in Fig. 5.6 (τ versus C_i) those for nitrogen exhibit a negative curvature at low concentrations. Thus, according to Figs. 5.4 to 5.6 the concentration dependence of the strengthening conforms better to a $C_i^{2/3}$ dependence than either a $C_i^{1/2}$ or a C_i dependence, although the difference between a $C_i^{2/3}$ and a C_i dependence is small and may be questioned in view of possible errors in chemical analysis and the flow stress values. A linear regression analysis of the experimental data indicated that a $C_i^{2/3}$ dependence was only slightly better than a linear fit. Worthy of mention is that the concentration dependence of the strengthening of vanadium by oxygen was found to vary with concentration, being a $C_i^{1/2}$ dependence at low concentrations and becoming a linear dependence at high concentrations, with a $C_i^{1/2}$ dependence giving

a reasonable fit over the entire concentration range of 0.004 - 1.0 at. % (Ref. 292).

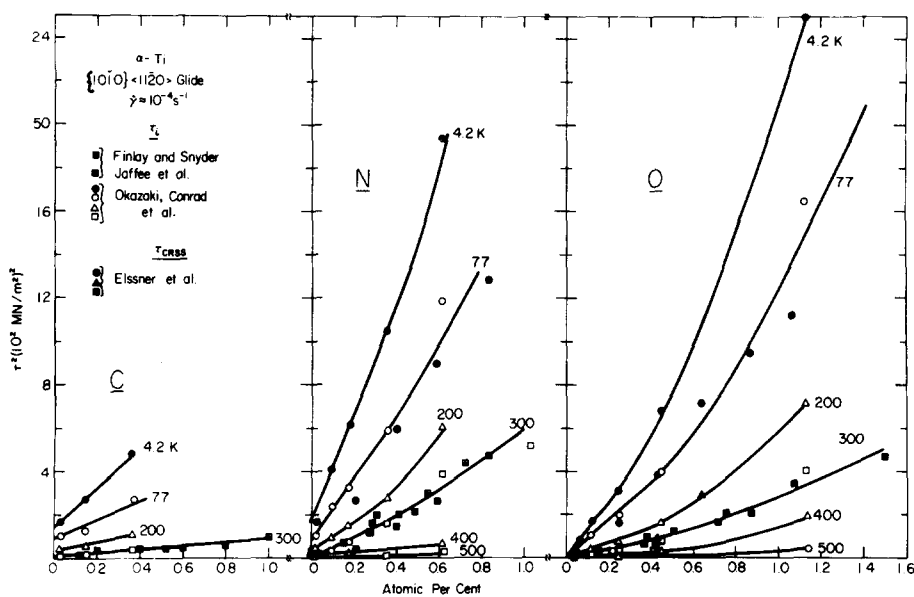


Fig. 5.4 τ^2 versus the concentration of C, N and O (considered separately) as a function of temperature.

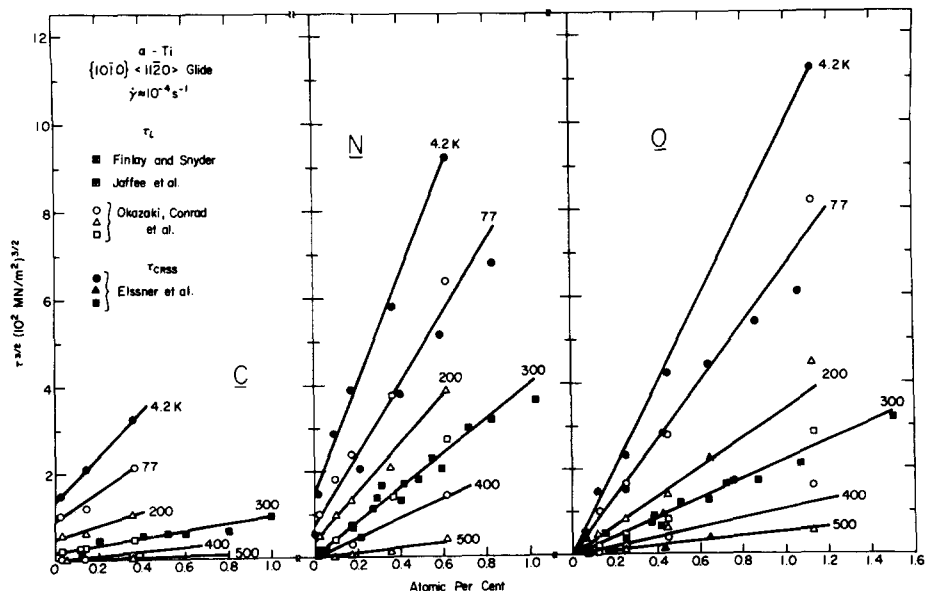


Fig. 5.5 $\tau^{3/2}$ versus the concentration of C, N and O (considered separately) as a function of temperature.

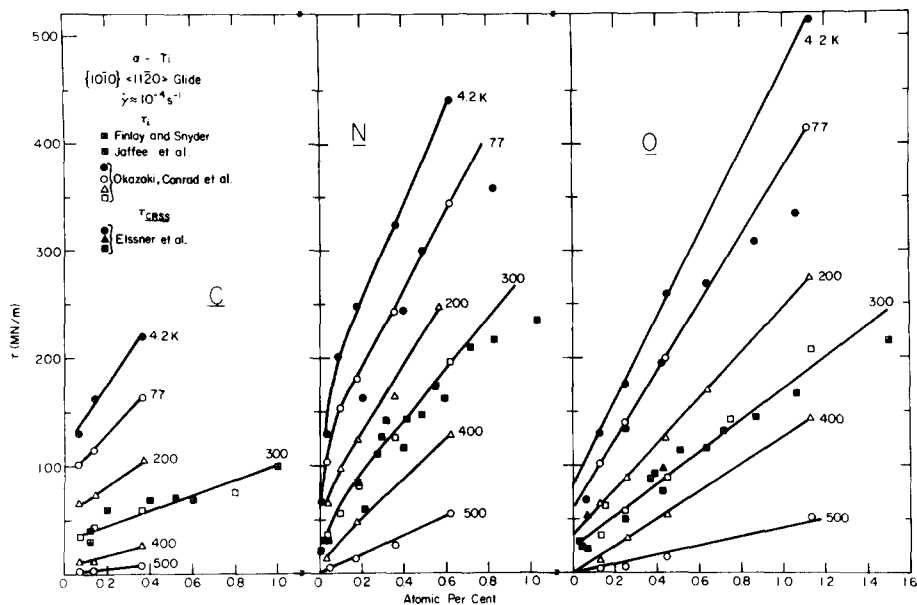


Fig. 5.6 τ versus the concentration of C, N and O (considered separately) as a function of temperature.

The modulus-corrected values of $d\tau/dC_i^{2/3}$ and of $d\tau/dC_i$ derived from the slopes of the linear regions of the curves in Figs. 5.5 and 5.6 are plotted as a function of temperature in Figs. 5.7 and 5.8; also shown are the relative strengthening ratios of nitrogen and carbon to oxygen based on the slopes. Common to both figures is that the strengthening increases in the order C, O, N and that it is sensitively dependent on the temperature, becoming quite small at temperatures in the vicinity of T_c (taken from Fig. 4.59). Further, a marked change in slope appears to occur at 300-400K, which is less pronounced for carbon compared to oxygen and nitrogen. Also of interest is that the strengthening ratio of C:O tends to decrease with temperature, whereas that for N:O tends to increase. The strengthening ratio ranges between 0.3-0.9 for C:O and between 1.0-1.6 for N:O. Finally, worthy of mention is that the values of $d\tau/dC_i$ obtained here for interstitials in titanium at 300K are similar to those for interstitials in other Group IVa metals and in the Group Va metals (Ref. 145).

With the thought that the F-F model is expected to apply at the lowest interstitial solute concentrations considered here, the modulus-corrected values of $d\tau/dC_i^{1/2}$ derived from the initial slopes of the curves in Fig. 5.5 are plotted as a function of temperature in Fig. 5.9. The behavior is qualitatively similar to that in Figs. 5.7 and 5.8.

Concentration Dependence of the Activation Volume:

Additional insight into the solution strengthening mechanism may be obtained from a consideration of the concentration dependence of the activation volume v . Assuming that the deformation kinetics of titanium-interstitial alloys are given by an Arrhenius-type equation (Eq. 3.56), and considering a force-activation distance curve similar to that of Fig. 3.8, it follows that (Ref. 122)

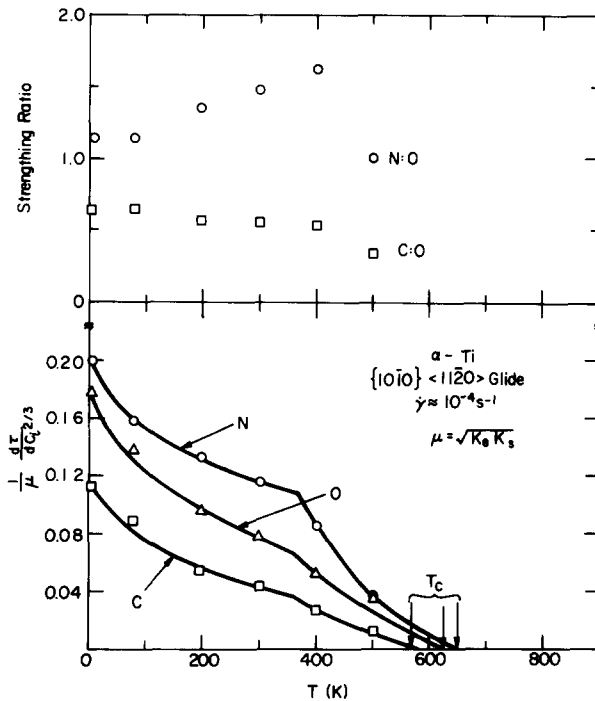


Fig. 5.7 $\frac{1}{\mu} \frac{d\tau}{dc_i^{2/3}}$ versus temperature derived from Fig. 5.5.

$$x^* = -\left(\frac{\partial \Delta G}{\partial f_i^*}\right)_T = -\left(\frac{\partial \Delta G}{\partial \tau^*}\right)_T \left(\frac{\partial \tau^*}{\partial f_i^*}\right)_T \quad (5.16)$$

$$= kT \left(\frac{\partial \ln \dot{\gamma}}{\partial \tau}\right)_T \left(\frac{\partial \tau^*}{\partial f_i^*}\right)_T = v \left(\frac{\partial \tau}{\partial f_i^*}\right)_T \quad (5.16a)$$

For a constant $\dot{\gamma}_0$, temperature and strain rate, ΔG is constant and therefore x^* is constant; Eq. 5.16a then becomes

$$\frac{k}{v} = \frac{1}{T} \left(\frac{\partial \tau}{\partial \ln \dot{\gamma}}\right)_T = \text{const.} \left(\frac{\partial \tau^*}{\partial f_i^*}\right)_T \quad (5.17)$$

Based on these considerations, the concentration dependence of the reciprocal of the apparent activation volume v ($=kT(\partial \ln \dot{\gamma}/\partial \tau) = \bar{M}v'$) resides in the parameter $\partial \tau^*/\partial f_i^*$.

Taking the derivative of Eq. 3.29, 3.34 and 3.38, one obtains

$$F-F: \frac{\partial \tau^*}{\partial f_i^*} = \left(3\alpha_1/2b^2\right) \kappa^{*1/2} c_i^{1/2} \quad (5.18)$$

$$L: \frac{\partial \tau^*}{\partial f_i^*} = \left(4\alpha_2/3b^2\right) \kappa^{*1/3} c_i^{2/3} \quad (5.19)$$

$$F-M: \frac{\partial \tau^*}{\partial f_i^*} = \left(\alpha_3/b^2\right) \kappa^{*n-1} c_i \quad (5.20)$$

These relationships then yield for the concentration dependence of the activation volume

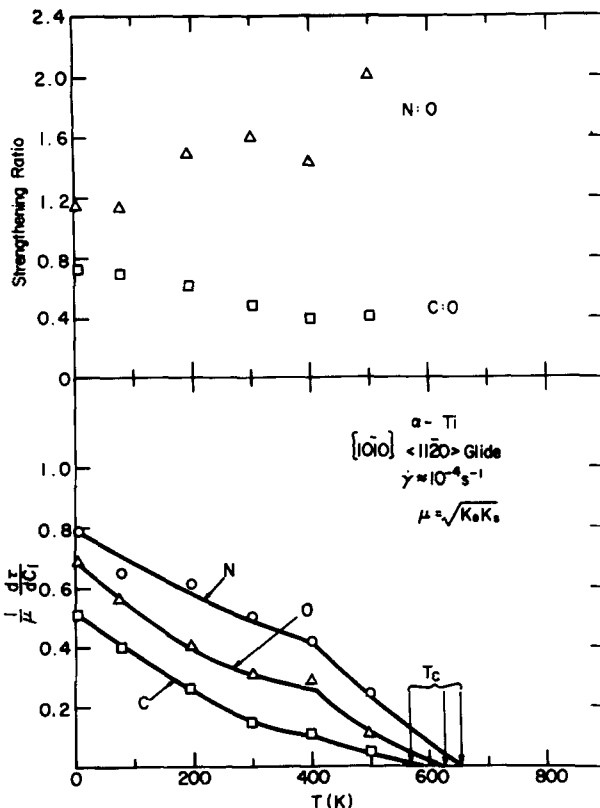


Fig. 5.8 $\frac{1}{\mu} \frac{d\tau}{dC_i}$ versus temperature derived from Fig. 5.6.

$$F-F: (k/v)^2 = \text{const. } \kappa * C_i \quad (5.21)$$

$$L: (k/v)^{3/2} = \text{const. } \kappa^{1/2} C_i \quad (5.22)$$

$$F-M: (k/v) = \text{const. } \kappa^{n-1} C_i \quad (5.23)$$

The variation of the experimental values of $[(1/T) \cdot (\partial\tau/\partial\ln\dot{\gamma})]$ with interstitial content was found to be in reasonable accord with all three of the concentration dependencies given by Eqs. 5.21 to 5.23, with best agreement however occurring for Eq. 5.22 (see Fig. 5.10). The values of the slopes and intercepts derived from the three types of plots for the effect of interstitial content on v are given in Table 5.2.

Søb, Kratochvil and Kroupa (SKK) Model:

The solid solution strengthening models presented above are all based on the interaction of solute atoms with undissociated dislocations. Consideration will now be given to the possibility that the interaction consists of retarding the recombination of sessile screw dislocations, as proposed by Søb, Kratochvil and

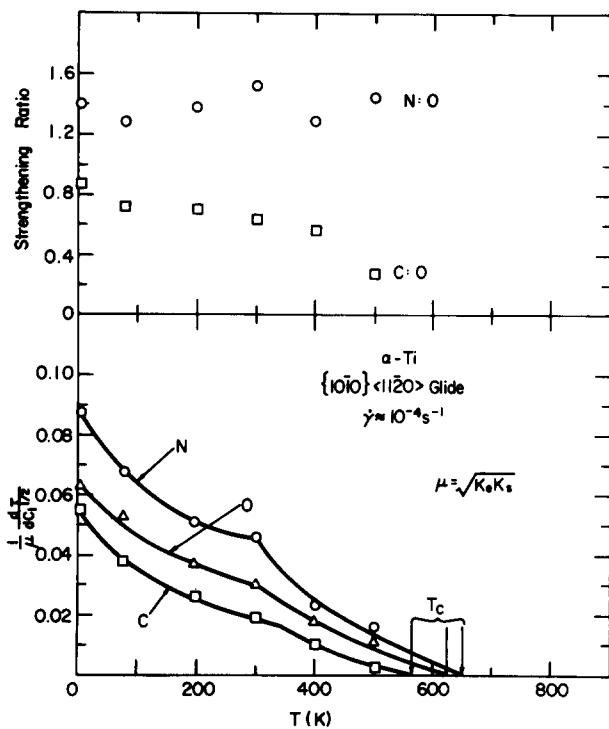


Fig. 5.9 $\frac{1}{\mu} \frac{d\tau}{dC_i^{3/2}}$ versus temperature derived from Fig. 5.7.

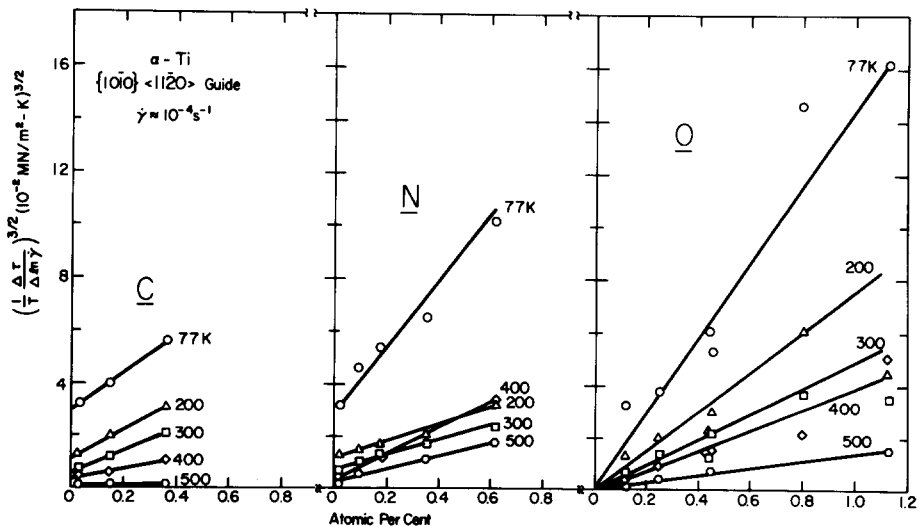


Fig. 5.10 $(\frac{1}{T} \frac{\partial \tau}{\partial \ln \gamma})^{3/2}$ versus the concentration of C, N and O (considered separately) as a function of temperature.

TABLE 5.2 Intercepts a and slopes b of the straight lines obtained in plots pertaining to the concentration dependence of the reciprocal of the activation volume (k/v).

Alloy	Temp.	$\frac{k}{v}$ versus C_i		$(\frac{k}{v})^{3/2}$ versus C_i		$(\frac{k}{v})^2$ versus C_i	
		a (10^{-2} MN/m ² -K)	b (MN/m ²)	a (10^{-2} MN/m ² -K) ^{3/2}	b ($10^{-2/3}$ MN/m ² -K) ^{3/2}	a (10^{-2} MN/m ² -K) ²	b (10^{-1} MN/m ² -K) ²
Ti-0	77	1.4	4.5	0	1.44	0	30.8
	200	0.7	3.0	0	0.75	0	9.5
	300	0.5	2.5	0	0.49	0	4.6
	400	0.4	1.2	0	0.39	0	3.9
	500	0.2	1.0	0	0.14	0	1.6
Ti-N	77	2.2	5.1	3.0	1.24	3.6	29.7
	200	1.1	1.8	1.2	0.32	1.2	5.6
	300	0.9	1.5	0.7	0.30	0.5	4.3
	400	0.6	2.8	0.4	0.50	0.2	7.8
	500	0.3	1.0	0.2	0.26	0	3.8
Ti-C	77	2.1	3.9	3.0	0.70	4.4	15.8
	200	1.2	2.8	1.2	0.53	1.2	9.5
	300	0.7	2.4	0.6	0.41	0.5	6.3
	400	0.5	1.4	0.4	0.20	0.3	2.3
	500	0.3	0	0.1	0	0	0

Kroupa (Refs. 87, 88). The fact that the dislocation structure in titanium observed by TEM is mainly screw in character provides some basis for considering this model.

To facilitate comparison with the experimental data expressions are here derived for the concentration dependence of the flow stress and the activation volume which are based on the concept of Söb, Kratochvil and Kroupa (Refs. 87, 88) that the rate controlling process during the deformation of titanium is the thermally activated recombination of sessile screw dislocations and that interstitial solutes are barriers to this recombination. It is assumed that the elastic interaction between the partials of a disassociated screw dislocation minus that due to the stacking fault energy provide an internal stress τ_b , which must be subtracted from the applied stress τ^* acting to overcome the interstitial solute atom obstacle. τ_b is taken to be

$$\tau_b = \left(\frac{\mu b}{2\pi r} \right) - \left(\frac{\gamma_{sf}}{b} \right) \quad (5.24)$$

where the first term is due to the elastic interaction of the partials and the second due to the stacking fault separating the partials. The effective force acting on a solute atom obstacle is then given by

$$f_i^* = \tau_e b \ell^* = (\tau^* - \tau_b) b \ell^* \quad (5.25)$$

Assuming that ℓ^* is given by Eq. 3.26 with $\tau_e = \tau_0^*$ and rearranging, one obtains

$$\tau^* = \frac{2E_L}{ab^2} \left(\frac{f_i^*}{2E_L} \right)^{3/2} C_i^{1/2} + \tau_b \quad (5.26)$$

Further, let us make the simple assumption that

$$\gamma_{sf} \approx \gamma_0 - \beta C_i \quad (5.27)$$

where β is a constant and $\gamma_0/b \approx \mu/2\pi$. Inserting Eq. 5.27 into Eq. 5.26 one obtains

$$\tau^* = \frac{2E_L}{ab^2} \left(\frac{f_i^*}{2E_L} \right)^{3/2} C_i^{1/2} + \frac{\beta}{b} C_i \quad (5.28)$$

which has a form similar to Eq. 3.36, except that β does not depend explicitly on f_i^* . Differentiating Eq. 5.28 with respect to f_i^* and inserting into Eq. 5.16a gives $1/v$ proportional to $C_i^{1/3}$. The concentration dependence of the flow stress given by Eq. 5.28 and of the activation volume derived therefrom are in qualitative accord with those observed experimentally (and discussed above). Hence, based on the concentration dependence of the flow stress and the activation volume, one cannot rule out the possibility that the strengthening of α -Ti by interstitial solutes may be due to their retarding effect on the recombination of sessile screw dislocations, as proposed by Söb, Kratochvil and Kroupa (Refs. 87, 88).

Solution Strengthening Model:

The above considerations lead to the conclusion that the concentration dependence of the flow stress and of the reciprocal of the activation volume in the range of 0.1-1.0 at.% is best described by a $C_i^{2/3}$ dependence. Theoretical considerations however suggest that the exact concentration dependence may vary with solute content; hence the $C_i^{2/3}$ dependence may only represent the best average fit over the range considered. It is expected that the Fleischer-Friedel statistics will apply at low concentrations and the Labusch-Mott statistics at higher concen-

trations, leading to concentration dependencies ranging from C^2 to a linear dependence. The available experimental data do not permit a critical evaluation of combined concentration dependency concepts as have been proposed by Kocks, Labusch and Schwarz (Refs. 119, 120) and Labusch and Schwarz (Ref. 293) and were obtained above for the Söb, Kratochvil and Kroupa model.

The role of interstitial solute atom clusters in the strengthening of α -Ti is not clear. If they exist and play a significant role, one would expect that the concentration dependence of the flow stress and of the activation volume would vary with concentration as a result of the variation in the number and size of such clusters with solute content and prior thermal history.

Stress Equivalence of Solution Strengthening

Basinski, Foxall and Pascual (Ref. 294) found a stress equivalence regarding the thermal aspects of solid solution strengthening for single crystal alloy systems based on Cu, Ag and Mg. The stress equivalence was manifested in the following ways: (a) the difference in the yield stress at 77 and 298K plotted versus the yield stress at 77K was independent of the specific alloying solute and its concentration, (b) the activation volume was uniquely related to the yield stress at a given temperature irrespective of the type of alloying element and its concentration, and (c) two alloys of a given base metal which had the same yield stress at any selected temperature in the range 4-400K exhibited the same temperature dependence of the yield stress (and of the activation volume) over the entire temperature range. A similar stress equivalence of solid solution hardening was found by Butt and Feltham (Ref. 295) for polycrystalline Cu-Zn alloys in the range of 77-300K. Of interest here is whether Ti-interstitial alloys exhibit similar stress-equivalence correlations.

An evaluation of the stress equivalence concept for Ti-interstitial alloys is made in the plots of Figs. 5.11 and 5.12. It is here seen that the data for the three Ti-interstitial alloys can be considered to be in accord with the stress equivalence concept, although some departure from the concept is suggested by the results at high stresses for the Ti-N alloys in Fig. 5.11. Of interest regarding the stress-equivalence concept for Ti-interstitial alloys is the correlation found by Conrad and coworkers (Refs. 207, 209-212) between the ratio v/v_{T_0}

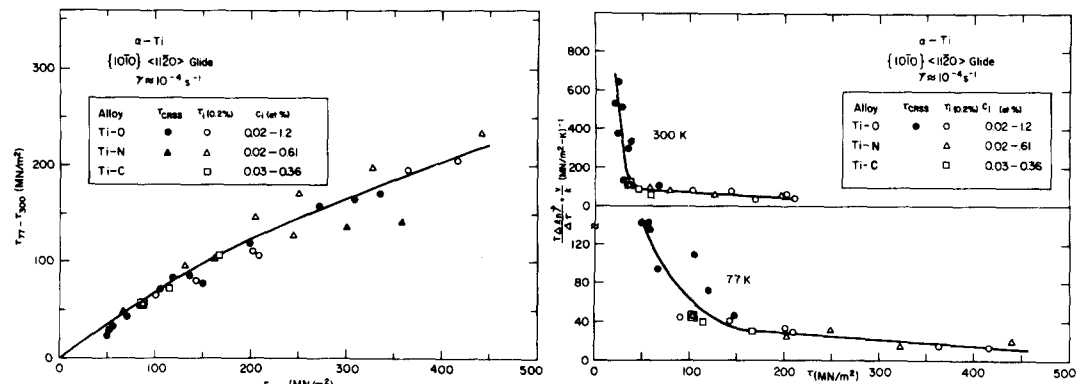


Fig. 5.11 The difference in yield stress at 77 and 300K versus the yield stress at 77K for Ti-interstitial alloys.

Fig. 5.12 The activation volume versus the yield stress for tests at 77 and 300K on Ti-interstitial alloys.

and τ^*/τ_0 (see Figs. 5.13 and 5.14), where v and v_{T_0} are the activation volumes at temperature T and a reference temperature T_0 (515-625K) respectively and τ^* and

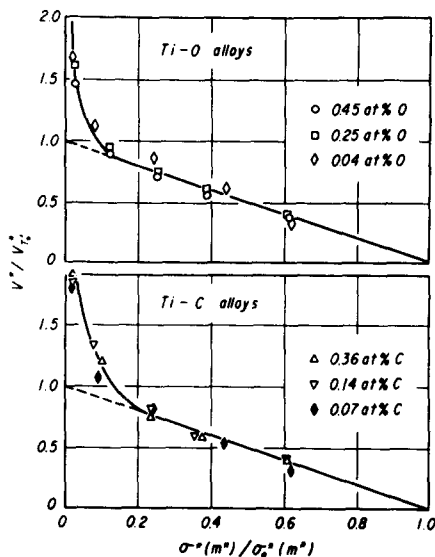


Fig. 5.13 The normalized stress dependence of the activation volume for the plastic flow of Ti-O and Ti-C alloys. From Okazaki, Kanakogi and Conrad (Ref. 211).

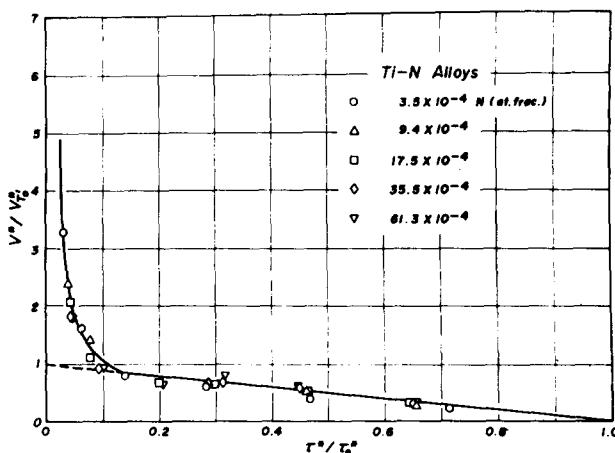


Fig. 5.14. The normalized stress dependence of the activation volume for the plastic flow of Ti-N alloys. From Okasaki, Monochi and Conrad (Ref. 210).

τ^* are the thermal components of the flow stress at T and at 0K. To be noted is that the curves for the three solutes are very similar and would essentially superimpose if all the data were plotted on one graph.

The results of Figs. 5.11-5.14 suggest that the same basic mechanism is

responsible for the strengthening due to all three solutes (C, N, O). Since the solubility of these three solutes in α -Ti differs appreciably, it is expected that the number and size of any solute atom clusters which might exist would also vary significantly. In view of the correlations presented in Figs. 5.11-5.14, it does not appear that solute atom clusters play a significant role in the strengthening of α -Ti by the interstitial solutes C, N, O.

Force-Activation Distance Curve:

Although the above considerations do not permit a positive decision regarding the solid solution strengthening model which applies to interstitials in α -titanium over the entire concentration range of 0.1 to 1.0 at.%, it may be informative to consider the force activation distance ($f_i^* - x^*$) curve which is obtained for the lowest concentrations. Making the reasonable assumption that the F-F model applies at low interstitial concentrations, one can derive the $f_i^* - x^*$ curve by rearranging Eq. 3.29 to give

$$f_i^*/2E_L = \left(\frac{\alpha b^2}{s^2 E_L} \frac{\tau_i^*}{C_i^{1/2}} \right)^{2/3} \approx \left(\frac{\tau_i^*}{C_i^{1/2} \mu} \right)^{2/3} \quad (5.29)$$

and by inserting the derivative of Eq. 5.29 into Eq. 5.16a to give

$$\frac{x^*}{b} = \frac{v}{b} \left(\frac{\partial \tau_i^*}{\partial f_i^*} \right) = \frac{3sv}{2\alpha b^3} \left(\frac{f_i^*}{2E_L} \right)^{1/2} C_i^{1/2} \quad (5.30)$$

$$\approx \frac{3}{2} \frac{v C_i^{1/2}}{b^3} \left(\frac{\tau_i^*}{C_i^{1/2} \mu} \right)^{1/3} \quad (5.30a)$$

s is here taken to be 0.9, $\alpha = 0.89$ and $E_L = \mu b^2/2$. The $f_i^* - x^*$ curves derived from the initial slopes of the plots of τ_i^* versus C_i (Fig. 5.4) and $(k/v)^2$ versus C_i (Table 5.2) are presented in Fig. 5.15. These curves are similar in form and

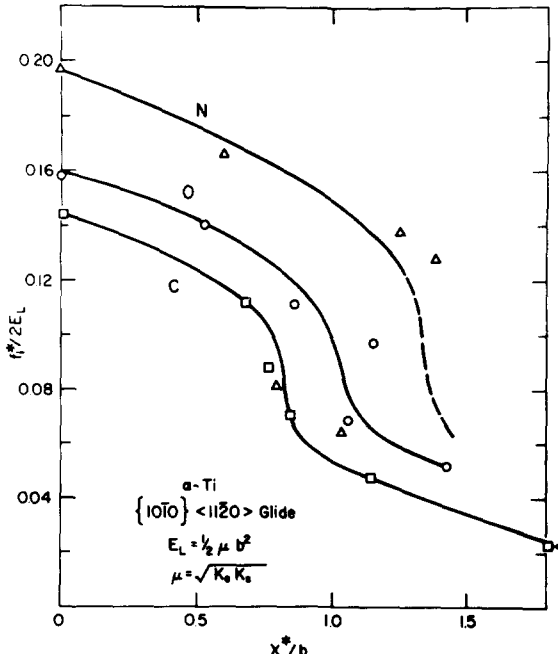


Fig. 5.15 Normalized force - activation distance curve for prism glide in α -Ti with low interstitial content.

value to those derived previously by Conrad and coworkers (Refs. 3, 172), who assumed that the F-F model applies over the entire range of interstitial contents considered by them, namely 0.05 - 1.0 at.%; see for example Figs. 5.16 and 5.17. To be noted in Figs. 5.15-5.17 is that the curves first rise steeply at $x^*/b \approx 1$, i.e. within the core region of the dislocation.

The values of $f_{i,0}^*/2E_L$ ($x^*/b = 0$) in Fig. 5.15 are 0.144, 0.159 and 0.198 respectively for C, O⁺ and N⁺. A comparison of these values with those derived from a consideration of elastic interactions (given in Table 3.4) indicates reasonable agreement for screw dislocations with y (the distance the interstitial solute lies from the slip plane) having a value between $b/3/6$ and $b/3/4$; see Table 5.3. The agreement is probably better than one can rightfully expect in view of: (a) the uncertainty in the experimental values of ϵ_b , ϵ_c and n , (b) the uncertainty in the concentration dependence of the flow stress and the activation volume and (c) the fact that most of the interaction occurs within the core region of the dislocation, where Hooke's law no longer applies. In regard to the last concern, Fleischer (Ref. 68) has pointed out that the agreement may be better than expected because of the cancellation of errors. For example, the assumption that the stress is constant over the defect will lead to the calculated stress being smaller than would arise by considering the stress variation over the defect. On the other hand, Hooke's law is not expected to apply at distances less than about $2.5b$ from

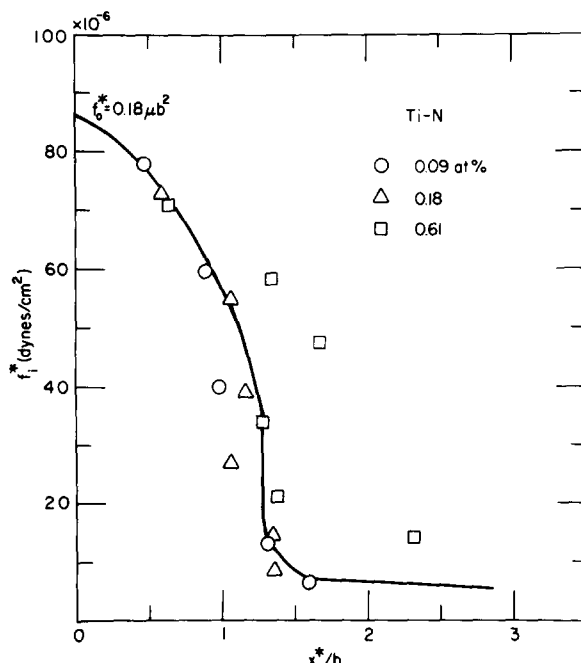


Fig. 5.16 Force-activation distance curve for Ti-N alloys.
From Conrad, deMeester, Doner and Okazaki (Ref. 3).

[†]These values of $f_{i,0}^*/2E_L$ are based on $\ell^* = 0.9b$ (μ/τ^*C_i)^{1/2} and derived using Eqs. 3.26 - 3.28.

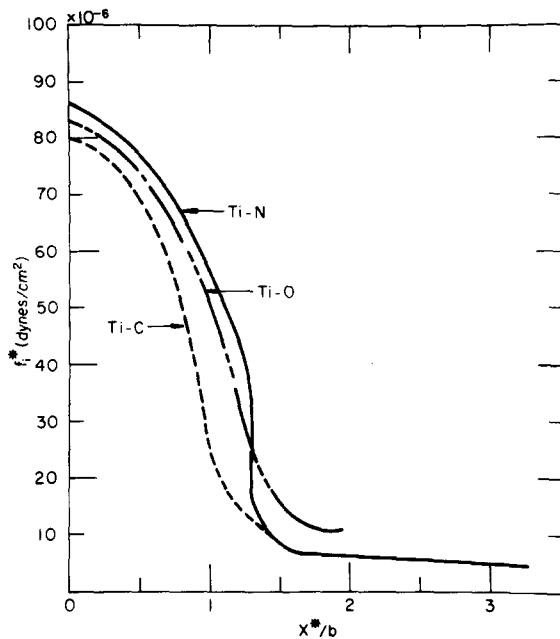


Fig. 5.17 Force-activation curves for Ti-C, Ti-N and Ti-O alloys with interstitial contents ranging between 0.1 and 1.0 at.%. From Conrad, deMeester, Doner and Okazaki (Ref. 3).

TABLE 5.3 Comparison of experimental values of $f_{i,0}^*/2E_L$ with those calculated for elastic interactions between interstitial solutes and prism glide dislocations.

Alloy System	y	edge	$f_{i,0}^*/2E_L$		Experimental $\ell^* = 2.3b(\mu/\tau^*c_i)^{1/3}$
			Calculated	screw	
Ti-O	$b\sqrt{3}/4$	0.26-0.32	0.08	0.16	0.40
	$b\sqrt{3}/6$	0.83-1.08	0.29		
Ti-N	$b\sqrt{3}/4$	0.27-0.31	0.08	0.20	0.50
	$b\sqrt{3}/6$	0.86-1.03	0.27		
Ti-C	$b\sqrt{3}/4$	0.25-0.26	0.03	0.14	0.35
	$b\sqrt{3}/6$	0.74-0.78	0.11		

a dislocation and therefore the use of linear elasticity overestimates the stress.

A detailed comparison of the $f_i^* - x^*$ curve derived from experimental data with that calculated for elastic interactions is given in Fig. 5.18. The calculated (theoretical) curves given here were obtained by first plotting the f_i^* versus distance x curve (similar to Fig. 3.1) and then graphically determining the value of the activation distance x^* as a function of f_i^* . It is seen in Fig.

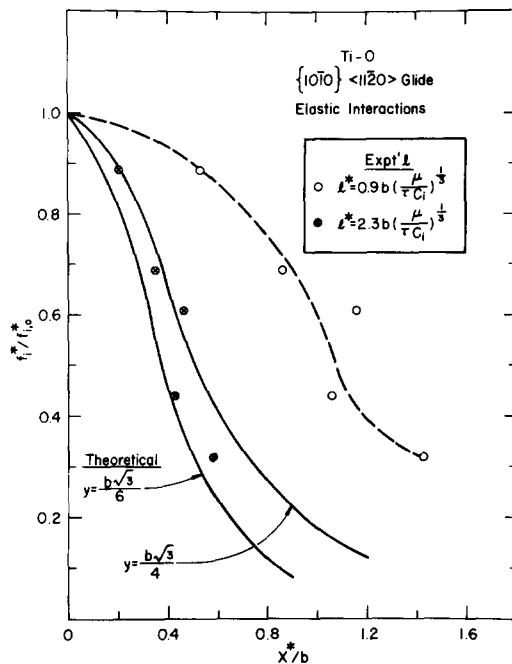


Fig. 5.18 Comparison of experimental force-activation distance curves for the plastic deformation of Ti-O alloys for two values of ℓ^* with that derived for elastic interactions between dislocations and interstitial solute atoms.

5.18 that the experimental curve derived using Eqs. 3.26 to 3.28 for ℓ^* (i.e. $\ell^* = 0.9b(\mu/\tau^*C_i)^{1/3}$) is similar in form to the theoretical curves taking $y = b\sqrt{3}/6$ and $y = b\sqrt{3}/4$. However, for this value of ℓ^* the experimental value of x^* at constant f_i^*/f_i^* is about 2.5 times the theoretical value. Good quantitative agreement between the experimental and theoretical curves is obtained by taking $\ell^* = 2.3b(\mu/\tau^*C_i)^{1/3}$; i.e. 2.5 times the value normally taken for the F-F statistics. Such an increase in ℓ^* however leads to a similar increase in f_i^* , which then brings the experimental values of the maximum interaction force more in accord with those for edge dislocations than screws; see Table 5.3.

Dislocation Kinetics:

Assuming that the Fleischer-Friedel statistics apply to the strengthening of α -Ti at low interstitial concentrations, the Gibbs free energy of activation ΔG associated with surmounting the solute atom obstacles by gliding dislocations may be determined from experimental data using either Eqs. 3.65-3.71 (giving ΔG^0) or Eq. 3.72 (giving ΔG^H). Further, as indicated by Eq. 3.57, ΔG so obtained should be proportional to the temperature for a constant strain rate, providing the pre-exponential factor $\dot{\gamma}_0$ remains constant.

The activation enthalpy ΔH^* ($\equiv \Delta G^0$) versus temperature for prism glide derived from two sets of data on high purity titanium single crystals (Refs. 137, 138) using Eqs. 3.65-3.68 is presented in Fig. 5.19. The data points are the averages of separate determinations by the present author and three of his associates; the error bars show the scatter in such determinations, which is mainly due to inaccuracies in the determination of the deformation partial $\partial\tau/\partial T$, and to some

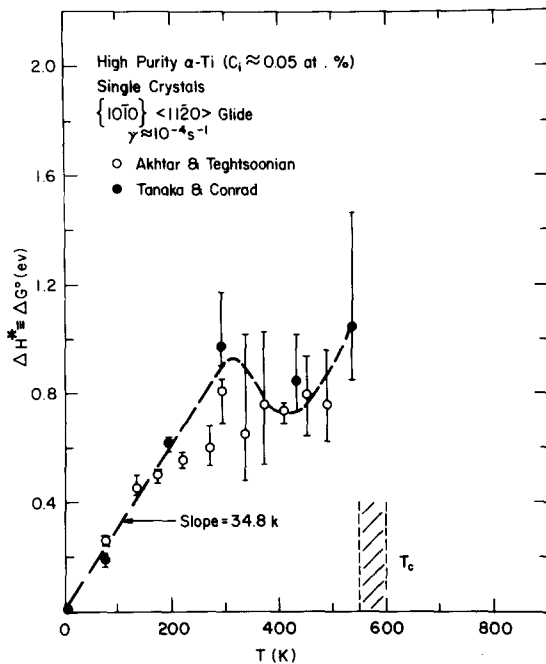


Fig. 5.19 Activation enthalpy $\Delta H^*(\equiv \Delta G^0)$ versus temperature for prism glide in high purity Ti single crystals. Derived from data in Refs. 137 and 138. $\mu = \sqrt{K_e K_s}$

extent in the determination of τ^* . In Fig. 5.19 ΔH^* is approximately proportional to the temperature to about 300K, then decreases with further increase in temperature to about 400K, before increasing again at higher temperatures. The anomaly in the temperature dependence of ΔH^* occurs in the same temperature region as that for the apparent activation volume v (Fig. 4.19) and for the temperature dependence of the flow stress (Fig. 4.20), and in turn in the apparent activation energy Q (Fig. 4.21). The reason for this anomaly is not at all clear. It may reflect changes in the pre-exponential γ_0 , or in the rate controlling mechanism. The anomaly tends to become less pronounced as the interstitial content is increased; see Fig. 5.20. Other than this, no clear effect of interstitial content on ΔH^* could be discerned. By combining the data of Figs. 5.19 and 5.20 onto a single curve, the results are found to scatter about a straight line through the origin with a slope of 32.9 k and with $\Delta H^*(\tau^*=0)=1.7 \text{ eV}$, taking $T_c = 600 \text{ K}$.

The Gibbs free activation energy ΔG^U was also derived (using Eq. 3.72) from the data used in Figs. 5.19 and 5.20 and plots of ΔG^U versus temperature exhibited trends similar to those for ΔH^* . A combined plot of ΔG^U versus temperature for the various data sources (representing interstitial contents ranging from 0.05-1.0 at.%) is presented in Fig. 5.21. The "best" straight line through the data points and passing through the origin has a slope of 23.2 k and yields $\Delta G_U^U(\tau^*=0) = 1.1-1.2 \text{ eV}$. Correction for the change in modulus with temperature gives $\Delta G_U^U(\tau^*=0) = 1.7-1.9 \text{ eV}$ at 0K, which is in agreement with ΔG^0 .

The variation of ΔH^* (Eq. 3.65) with temperature for prism glide in zone-refined single crystals and for the plastic flow of zone-refined polycrystals reported by Conrad, de Meester, Doner and Okazaki (Ref. 3) is presented in Fig. 5.22

Fig. 5.20 Activation enthalpy ΔH^* ($\equiv \Delta G^\circ$) versus temperature for prism glide in low purity Ti single crystals. Derived from data in references of Table 4.2. $\mu = \sqrt{K_e K_s}$

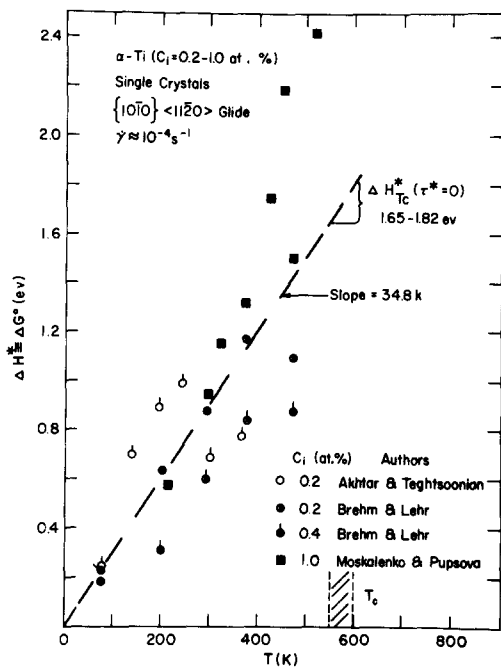
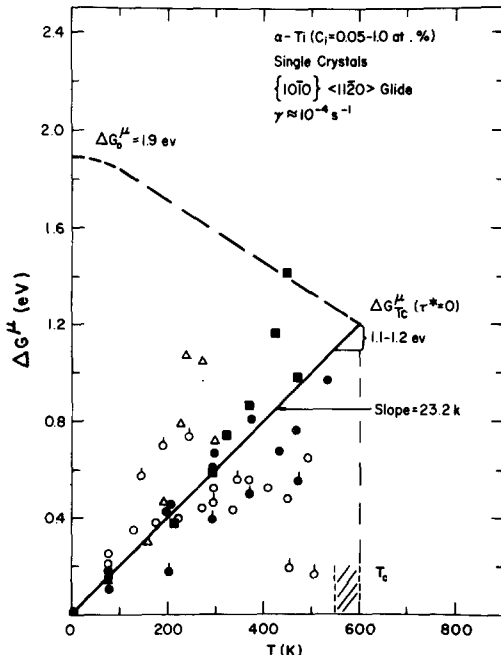


Fig. 5.21 Gibb's free energy of activation ΔG^μ versus temperature for prism glide in Ti single crystals with various purity levels. Derived from data in references of Table 4.2. Data point symbols refer to same authors as in Figs. 4.12 and 4.19. $\mu = \sqrt{K_e K_s}$



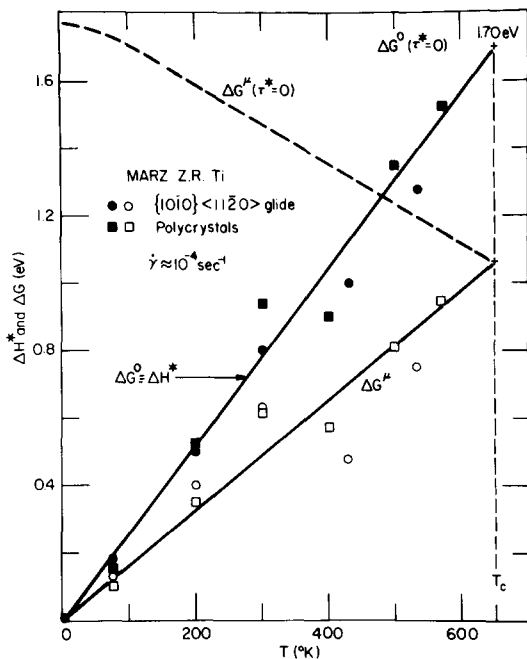


Fig. 5.22 ΔH^* and ΔG^μ as a function of temperature for prism glide in zone-refined Ti single and polycrystals. From Conrad, de Meester, Doner and Okazaki (Ref. 3). $\mu = \sqrt{K_e K_s}$

The data for both materials scatter about a single straight line through the origin (in accord with Eq. 5.37), supporting the idea that the dislocation kinetics for the polycrystals are the same as those for glide on the first-order prism planes.

The experimental values of ΔG^μ are also plotted in Fig. 5.22. Again, both the single crystal and polycrystal data points scatter about a single straight line through the origin. Further, $\Delta G^\mu(T_c=0)$ extrapolated to 0 K by correcting for the change in modulus with temperature is in good accord with the value of $\Delta H^*(\tau^*=0)$, which is assumed to be independent of temperature. Finally, it should be noted in Fig. 5.22 that the anomalous temperature dependence of ΔH^* and ΔG^μ in the region of 300–400 K occurs for polycrystalline specimens as well as for single crystals.

Work by Conrad and coworkers (Refs. 3,172,209,210,212,215) has shown that ΔH^* and ΔG^μ are relatively independent of grain size and interstitial content for polycrystalline Ti specimens with a total C+N+O content >0.1 at.%. An example of the insensitivity to interstitial content is given in Fig. 5.23, which is a plot of ΔH^* and ΔG^μ versus temperature for polycrystalline titanium specimens with nitrogen contents ranging between 0.02 and 0.63 at.%. Again, if one disregards the anomaly at 300–400 K, a proportionality between ΔH^* and temperature (and between ΔG^μ and temperature) is indicated, which is independent of nitrogen content.

Behavior similar to that in Fig. 5.23 for Ti-N alloys was found for polycrystalline Ti-O and Ti-C alloys. A comparison of the results for the three interstitial solutes is given in Fig. 5.24. The data points here for each solute

Fig. 5.23 ΔH^* and ΔG^μ as a function of temperature for polycrystalline Ti-N alloys. From Conrad, de Meester, Doner and Okazaki (Ref. 3). $\mu = \sqrt{K_e K_s}$

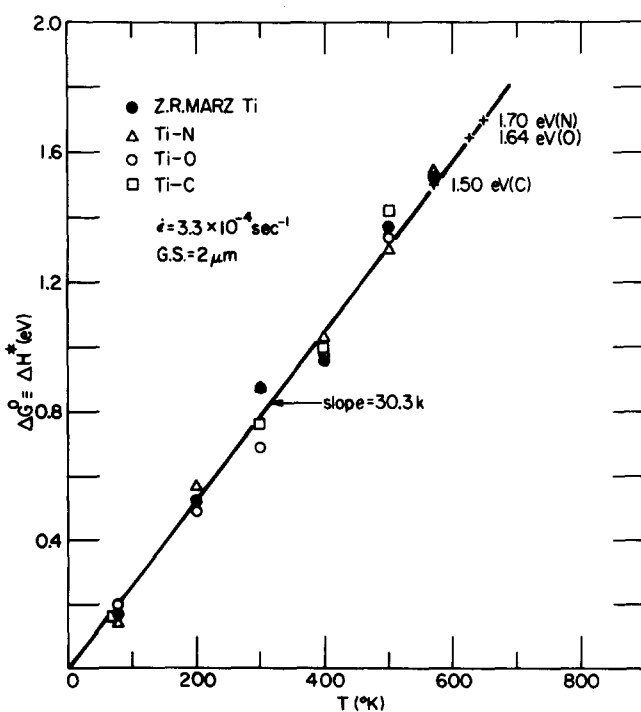
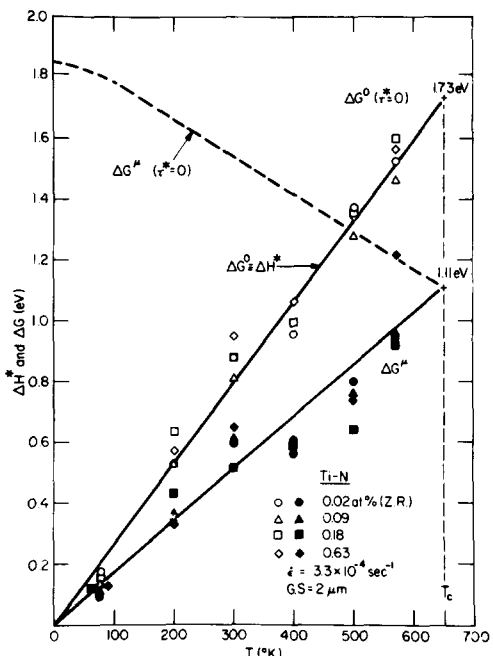


Fig. 5.24 $\Delta G^0 (\equiv \Delta H^*)$ as a function of temperature for polycrystalline Ti-C, Ti-N, and Ti-O alloys. From Conrad, de Meester, Doner and Okazaki (Ref. 3). $\mu = \sqrt{K_e K_s}$

are the averages for the various compositions, since ΔG for a given temperature was essentially independent of interstitial content. To be noted is that they conform reasonably well to a single straight line of slope 30.3k. The values of ΔH^* at $T=T_c$ ($\equiv \Delta G^0 \approx \Delta G^U$) are 1.73, 1.65 and 1.54 eV respectively for N, O and C. Similar behavior of ΔH^* and ΔG^U versus T and values of $\Delta H_{T_c}^*$ ($\equiv \Delta G^0 \approx \Delta G^U$) have been obtained for commercial titaniums of various interstitial contents in both uniaxial tension (Refs. 172,259) and in stress relaxation (Ref. 189).

A comparison of the experimental values of $\Delta H_{T_c}^*$ ($\approx \Delta G^U$) with the values of ΔG^0 calculated from a consideration of elastic interactions (taken from Table 3.4) is made in Table 5.4. Again, there exists reasonable agreement between the experimental values and those calculated for combined elastic interactions, with y having a value between $b\sqrt{3}/6$ and $b\sqrt{3}/4$. Worthy of note is that the experimental values of $\Delta H_{T_c}^*$ ($\approx \Delta G^U$) are similar in magnitude to the chemical bond energies between Ti and the interstitial elements given in Table 2.9.

Typical variation of the apparent activation volume v' with σ^* for zone-refined specimens is illustrated in Fig. 5.25. Here both v' and σ^* have been normalized to OK for the two cases considered, i.e. for

$$\Delta G^0 \left(\text{where } \frac{\partial f_i}{\partial T} \Big|_{T,x} = 0 \right), \quad \text{and for}$$

$$\Delta G^U \left(\text{where } \frac{\partial f_i}{\partial T} \Big|_{T,x} = \left(\frac{T}{\mu} \frac{d\mu}{dT} \right) \left(\frac{f_i^*}{T} \right) \right)$$

where f_i^* is the interaction force between the dislocation and the obstacle and x is the position of the dislocation. In the first case, the normalization consists of (Ref. 259)

$$\sigma^*(OK) = \sigma_T^* \left(\mu_T / \mu_0 \right)^{1/2} \quad (5.31)$$

and

$$v'[OK, \sigma^*(OK)] = v' \left(T, \sigma_T^* \right) \left(\mu_0 / \mu_T \right)^{1/2} \quad (5.32)$$

In the second case, the corrections consist of (Ref. 259)

$$\sigma^*(OK) = \sigma_T^* \left(\mu_0 / \mu_T \right) \quad (5.33)$$

and

$$v'[OK, \sigma^*(OK)] = v' \left(T, \sigma_T^* \right) \quad (5.34)$$

Integration of the area under the v' versus σ^* curve of Fig. 5.25 should yield ΔG ; i.e.

$$\Delta G = \int_{\sigma^*}^{\sigma_0^*} v' d\sigma^* \quad (T=OK) \quad (5.35)$$

Hence, ΔG derived by means of Eqs. 3.65 and 3.72 can be compared with that obtained by Eq. 5.35 to determine whether ΔG^0 or ΔG^U gives the better agreement. This has been done in Fig. 5.26 for the zone-refined polycrystalline material. Slightly better agreement is indicated for ΔG^0 ($\equiv \Delta H^*$) than for ΔG^U , suggesting that the interaction energy may be less temperature dependent than the modulus used here, i.e. $\sqrt{K_e k_b}$. Furthermore, the good agreement between ΔG^0 determined by Eq. 3.65

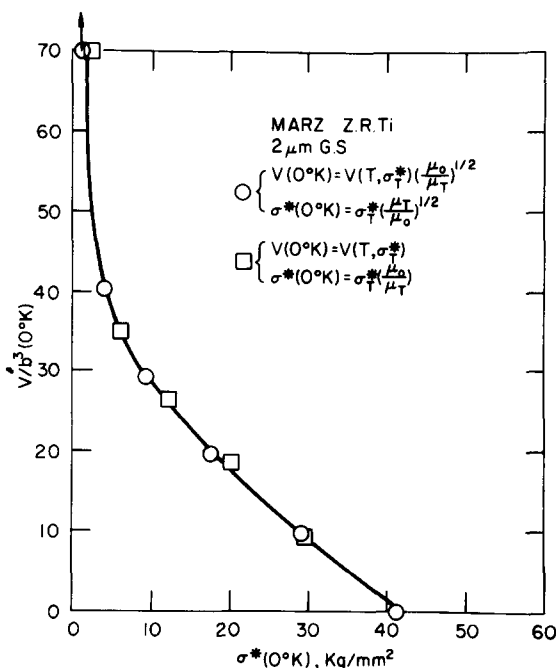


Fig. 5.25 v'/b^3 versus σ^* (both corrected to 0K) for zone-refined Ti. From Conrad, de Meester, Doner and Okazaki (Ref. 3). $\mu = \sqrt{K_e K_s}$

TABLE 5.4 Comparison of experimental values of ΔG with those calculated for elastic interactions between interstitial solutes and prism glide dislocations

Alloy System	y	Calculated		$\Delta G_0/\mu b^3$	Expt'l ($\Delta H_{T_c}^* \approx \Delta G_0^\mu$)
		edge [†]	screw ^{††}		
Ti-O	$b\sqrt{3}/4$	0.17-0.21	0.08	0.18	0.18
	$b\sqrt{3}/6$	0.37-0.48	0.29		
Ti-N	$b\sqrt{3}/4$	0.19-0.21	0.08	0.19	0.19
	$b\sqrt{3}/6$	0.38-0.46	0.27		
Ti-C	$b\sqrt{3}/4$	0.17-0.18	0.03	0.17	0.17
	$b\sqrt{3}/6$	0.32-0.34	0.11		

$${}^{\dagger}\mu_e = K_e = (C_{11}^2 - C_{12}^2)/2C_{11} = 6.65 \times 10^{11} \text{ dynes/cm}^2$$

$$b = 2.95 \text{ \AA}^0$$

$${}^{\ddagger\dagger}\mu_s = K_s = (C_{44} C_{66})^{1/2} = 4.74 \times 10^{11} \text{ dynes/cm}^2$$

$$\mu b^3 = 8.99 \text{ eV}$$

$${}^{\dagger\dagger\dagger}\mu = \sqrt{K_e K_s} = 5.61 \times 10^{11} \text{ dynes/cm}^2$$

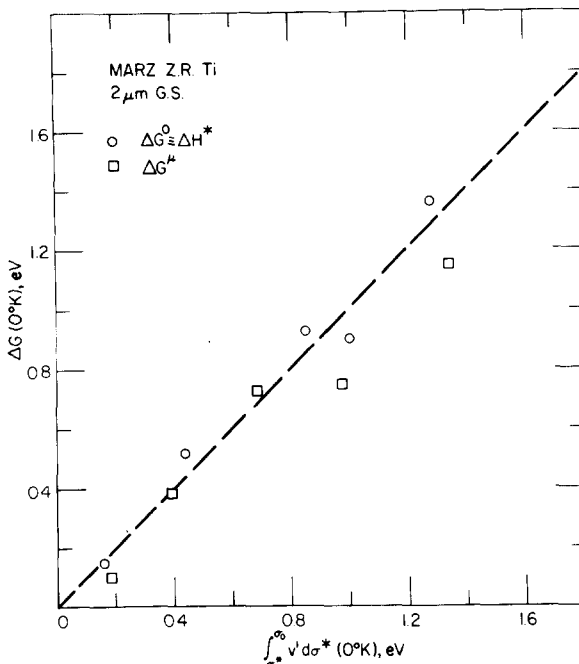


Fig. 5.26 ΔG versus integration of the area under the v' versus σ^* curve (all corrected to 0K) for zone-refined polycrystalline Ti. From Conrad, de Meester, Doner and Okazaki (Ref. 3). $\mu = \sqrt{K_e K_s}$

at a single temperature and from the integration of the activation volume versus σ^* curve (Eq. 5.35) determined from 0K to that temperature supports the concept that a single mechanism (or set of mechanisms) is rate controlling over the entire temperature range considered.

Let us now consider the effect of stress on ΔG , assuming F-F statistics to apply. Rearranging Eq. 3.29 gives for any temperature T above 0K

$$f_i^* = A \tau^{*2/3} \mu^{1/3} / C_i^{1/3} \quad (5.36)$$

where $A = (\frac{ab^3}{\mu})^{2/3}$. Since ΔG will be a constant for a constant value of f_i^* , one can compare the effects of stress on ΔG by substituting the flow stress τ^* at some reference temperature T^0 for the interstitial content C_i in Eq. 5.36. This then gives

$$f_i^* = a^0 [(\tau^*)^0]^{2/3} \mu^{1/3} \quad (5.37)$$

where $a^0 = (\mu^{1/3}/f_i^*)^0$ and $(\tau^*)^0$ are taken at the reference temperature T^0 . Hence, a unique value of ΔG will be associated with each value of the quantity $[(\tau^*/(\tau^*))^{2/3} \mu^{1/3}]$, independent of interstitial content. Fig. 5.27 shows that the data for commercial titaniuns of various interstitial contents (mainly oxygen) are in rather good accord with this concept. The reference temperature taken here is 4.2K, since the proportionality constant relating τ^* to $C_i^{1/2}$ increases with decrease in temperature, giving a more sensitive measure of C_i .

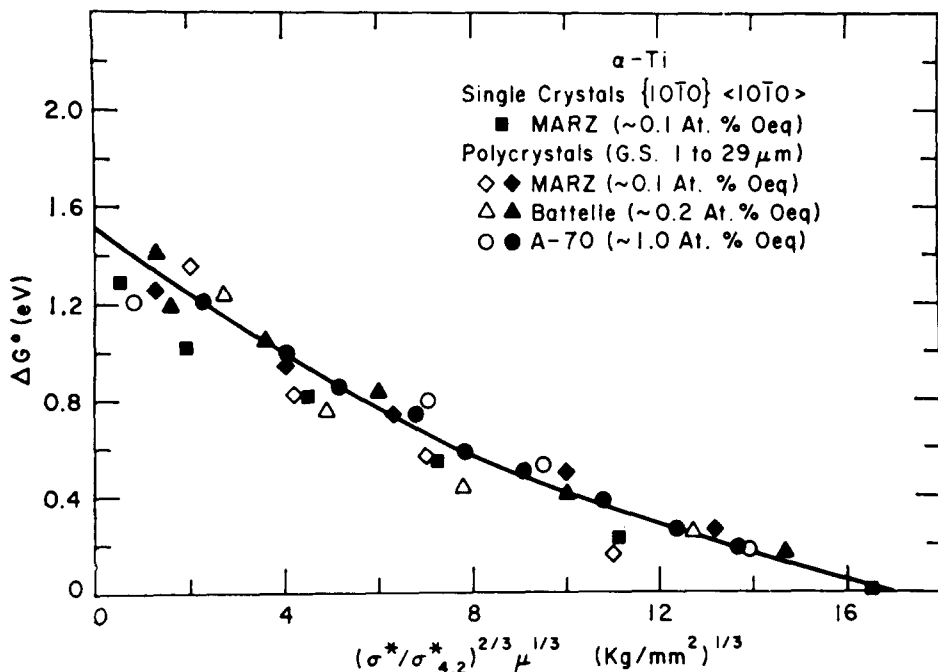


Fig. 5.27 ΔG versus $(\sigma^*/\sigma^*_{4.2})^{2/3} \mu^{1/3}$ for titaniums representing various interstitial contents and grain sizes. From Okazaki and Conrad (Ref. 172). $\mu = C_{66}$.

A detailed study of the application of the concepts and theory of thermally activated deformation to the plastic deformation of titanium at low temperatures was made by de Meester, Doner and Conrad (Ref. 259). Special attention was given to the question whether the Gibbs free energy of activation was independent of temperature (ΔG° , Case 1), or whether it was proportional to the modulus C_{66} (ΔG^μ , Case 2). Two sets of experimental data were considered because of their completeness: those of Conrad and coworkers (Refs. 205, 295) on A-70 Ti (~1.0 at.% Oeq.) rod swaged into wire and those of Reed-Hill and coworkers (Ref. 180) on commercial RMI 55 Ti (0.5 at.% Oeq.) plate. Some of the more important results obtained by de Meester, Doner and Conrad will now be presented.

Eqs. 3.71 and 3.72 above were derived under the condition that ΔG is a constant for a constant force f_i applied to the dislocation pressing it against the short-range obstacle. According to Eq. 5.36, a constant force is obtained for a given interstitial content when the product $\tau^*2/3\mu^{1/3}$ is a constant. Therefore, for Case 1 where $\Delta G^\circ(\tau^*, T) = \Delta G^\circ(\tau^* b l^*)$, plots of $\ln \dot{\epsilon}$ versus $1/T$ for polycrystalline specimens at constant values of $\sigma^*2/3\mu^{1/3}$ should yield straight lines whose slopes equal $-\Delta G^\circ/k$. Such plots are presented in Fig. 5.28 for data on the commercial Ti plate. The straight lines with a common intercept on the ordinate axis are in accord with ΔS^* being independent of temperature. The values of ΔG° derived from the plots of Fig. 5.28 are compared with those determined using Eq. 3.65 in Fig. 5.29. Good agreement occurs over the entire temperature range.

For Case 2, where $\Delta G^\mu(\tau^*, T) = \mu\phi(\tau^* b l^*/\mu)$, a plot of $\ln \dot{\epsilon}$ versus $\mu b^3/kT$ at a constant modulus-reduced effective force f_i^*/μ (or σ/μ) should yield straight lines of slope $-\Delta G^\mu/\mu b^3$. Using the most temperature dependent modulus C_{66} , de Meester, Doner and Conrad (Ref. 259) found that the data of Fig. 5.28 conformed reasonably

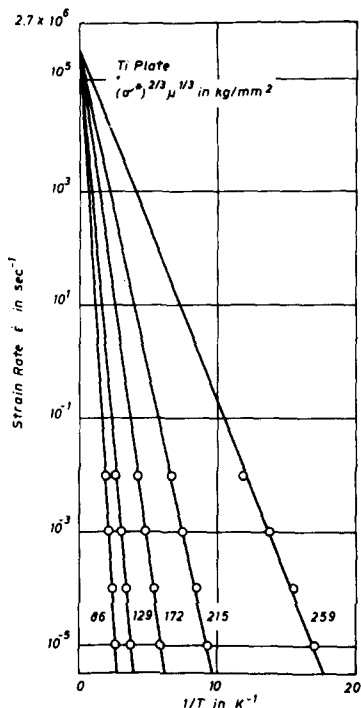


Fig. 5.28 Log strain rate versus reciprocal of the temperature for constant values of $\sigma^*^{2/3} \mu^{1/3}$ for commercial Ti plate. From de Meester, Doner and Conrad (Ref. 259).

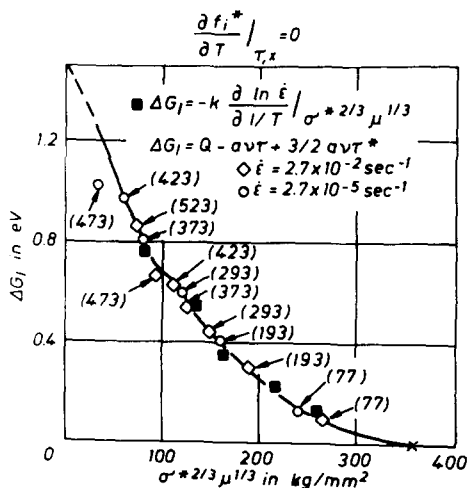


Fig. 5.29 ΔG° (ΔG_1) obtained by two methods versus $\sigma^*^{2/3} \mu^{1/3}$ for commercial Ti plate. From de Meester, Doner and Conrad (Ref. 259).

well to the prescribed behavior, although the plots exhibited some positive curvature at the higher values of σ/μ , indicating that the temperature dependence of ΔG is less than that of C_{66} .

A plot of ΔG^0 versus $\sigma^{2/3}\mu^{1/3}$ for the RMI 55 plate material is given in Fig. 5.29. It is here seen that the data points for the two strain rates and the two methods used for determining ΔG^0 all lie on one curve. The fit to a single curve was not as good as that in Fig. 5.29 when $\Delta G^U/\mu b^3$ was plotted versus σ/μ , indicating again that the temperature dependence of ΔG is less than that of the modulus C_{66} . Additional support for this conclusion regarding the temperature dependence of ΔG was provided by the fact that ΔG determined by integration of the activation volume versus stress curve was in better agreement with ΔG determined directly using Eqs. 3.65-3.72 for ΔG^0 than for ΔG^U .

Also of interest regarding the deformation kinetics is the value of the pre-exponential $\dot{\gamma}_0$. For the case of discrete obstacles (F-F statistics), $\dot{\gamma}_0$ is given by the quantity $\rho_m Abv^*/\ell^*$; see Eq. 3.55. Taking $v^* = v_D b/\ell^*$ and $A = (\ell^*)^2$, one obtains

$$\dot{\gamma}_0 = \rho_m b^2 v_D \quad (5.38)$$

Assuming that ρ_m is approximately equal to the total dislocation density at the critical resolved shear stress for prism slip or at the 0.2% yield stress in polycrystals, one has $\rho_m \approx 10^8 \text{ cm}^{-2}$. A reasonable value for $v_D \approx 10^3 \text{ s}^{-1}$. Inserting these values for ρ_m and v_D into Eq. 5.38 and taking $b = 2.95 \times 10^{-8} \text{ cm}$ gives $\dot{\gamma}_0 \approx 10^6 \text{ s}^{-1}$.

Experimentally, as indicated by Eq. 3.57, $\dot{\gamma}_0$ can be obtained from the slope of the plot of ΔG versus temperature at a constant strain rate. On the other hand, plots of ΔH versus temperature, or of $-T(\partial\tau/\partial T)_Y$ versus $(\partial\tau/\partial\dot{\gamma})_T$ will yield the product $\dot{\gamma}_0 e^{-\Delta S/k}$ (See Eq. 4.6). Values of $\dot{\gamma}_0$, or of the product $\dot{\gamma}_0 e^{-\Delta S/k}$, taken from the literature are given in Table 5.5 for prism slip in Ti single crystals and in Table 5.6 for the plastic flow of polycrystals. The tests were carried out at strain rates in the range of 10^{-5} to 10^{-3} s^{-1} with the exception of those by Harding (Ref. 181), which ranged between 10^{-3} to 45 s^{-1} . To be noted from Table 5.5 is that for prism glide at strain rates of 10^{-3} to 10^{-5} s^{-1} , plots of ΔH versus T or of $-T(\partial\tau/\partial T)$ versus $(\partial\tau/\partial\dot{\gamma})_T$ yield $\dot{\gamma}_0 e^{-\Delta S/k} = 10^7 - 10^{20} \text{ s}^{-1}$, with most values falling between 10^8 and 10^{11} s^{-1} , whereas plots of ΔG^U versus T yield $\dot{\gamma}_0 = 10^4 - 10^6 \text{ s}^{-1}$. For the plastic flow of polycrystals at strain rates of 10^{-5} to 10^{-3} s^{-1} , the quantity $\dot{\gamma}_0 e^{-\Delta S/k}$ ranges between $10^5 - 10^{11} \text{ s}^{-1}$ (with most values falling between $10^8 - 10^{11} \text{ s}^{-1}$), whereas the values of $\dot{\gamma}_0$ from plots of ΔG^U versus T range between $10^1 - 10^5 \text{ s}^{-1}$. The similarity in the values of the pre-exponential for the plastic flow of polycrystals and for prism glide in single crystals is in keeping with the idea that the deformation kinetics in polycrystals are governed primarily by prism glide. Except for one set of results on Ti-C alloys (Ref. 212), no clear effect of interstitial solute species or content on the pre-exponential is evident. The reasons for the large variation in the experimental values of the pre-exponential are not clear, but they are probably due in part to inaccurate measurements of the deformation partials.

A comparison of the experimental values of the pre-exponential with the value of 10^6 s^{-1} calculated above from Eq. 5.38 reveals that those based on ΔG^U are for the most part one to three orders lower than the calculated values, whereas those based on $\Delta G^0 (\equiv \Delta H^*)$ are two to three orders of magnitude higher. A decrease in the calculated value of $\dot{\gamma}_0$ would result if ρ_m were less than the total dislocation density, which is reasonable, and would bring the experimental values based on ΔG^U in better accord with the calculated value. The larger value of the pre-exponential associated with ΔH^* could be due to the fact that the activation entropy ΔS^* is a constant greater than zero. If the difference in the value of the pre-

TABLE 5.5 Experimental Values of the Pre-exponential $\dot{\gamma}_0$ in the Arrhenius Rate Equation for Prism Slip in Ti Single Crystals.

Authors	Ref.	C_i (at.%)	Test Method	$\dot{\gamma}$ (s^{-1})	T (K)	Procedure	Slope [†]	$\dot{\gamma}_{01}$ (s^{-1})
Levine	148	0.05	Shear	10^{-3}	0-200	ΔH_{T^*} vs. T	36.2 k	$10^{13} e^{\Delta S_T^*/k}$
Tanaka & Conrad	152	0.05	Tension	10^{-4}	0-600	$\Delta H_{T^*} \frac{vs.}{-(\partial \tau^*/\partial T)}$ T	28.3 k	$10^8 e^{-\Delta S_T^*/k}$
Akhtar & Teightsoonian	97	0.05 ~0.2	Tension Tension	10^{-4} 10^{-4}	0-300 0-300	ΔH_T vs. ΔH_T vs.	32.9 k 58.8 k	$10^{10} e^{-\Delta S_T^*/k}$ $10^{18} e^{-\Delta S_T^*/k}$
Brehm & Lehr	139	0.1-0.2	Tension	10^{-5}	0-500	ΔH_T vs. T	26.5 k	$10^7 e^{-\Delta S_T^*/k}$
Mokalenko & Puptsova	149	~1.0	Stress Relax. & Tension	10^{-4}	0-400	ΔH_{T^*} vs. T	32.9 k	$10^{10} e^{-\Delta S_T^*/k}$
Saki & Fine	147	0.2	Compression	10^{-4}	0-150	ΔH_T vs. T	54.4 k	$10^{20} e^{-\Delta S_T^*/k}$
Conrad et al	2	0.05-0.2	Tension	10^{-4}	0-600	ΔH_{T^*} vs. T	28.5 k	$10^8 e^{-\Delta S_T^*/k}$
Conrad et al	3	0.05	Tension	10^{-4}	0-600	ΔH_{f^*} vs. T $\Delta G^H(u = \sqrt{K_e K_s})$ vs. T	30.3 k 19.0 k	$10^9 e^{-\Delta S_{f^*}/k}$ 10^4
Present	0.05 0.05-1.0 0.05-1.0 0.05-1.0	Tension Tension Tension Tension	10^{-4} 10^{-4} 10^{-4} 10^{-4}	0-300 0-600 0-600 0-600	ΔH_{f^*} vs. T $\Delta H_{f^*}^{-1}$ vs. T. $-T(\partial \tau/\partial T)$ vs. $\Delta G^H(u = \sqrt{K_e K_s})$ vs. T	34.8 k 34.8 k 36.5 k 23.2 k	$10^{11} e^{-\Delta S_{f^*}/k}$ $10^{11} e^{-\Delta S_{f^*}/k}$ $10^{12} e^{-\Delta S_{f^*}/k}$ 10^6	

[†]Notes

- (1) Slopes of the plots of ΔH versus T equal $k[\ln(\dot{\gamma}_0/\dot{\gamma}) + \Delta S/k]$.
- (2) Slopes of the plots of $-T(\partial \tau/\partial T)$ versus $(\partial \tau/\partial \ln \dot{\gamma})$ equal $[k \ln(\dot{\gamma}_0/\dot{\gamma}) + \Delta S/k]$.
- (3) Slopes of the plots of ΔG^H versus T equal $k \ln(\dot{\gamma}_0/\dot{\gamma})$.

References are listed at end of text.

TABLE 5.6 Experimental Values of the Pre-exponential $\dot{\varepsilon}_0$ in the Arrhenius Rate Equation for the Plastic Flow of Ti Polycrystals.

Authors	Ref.	Major Solute	C_i (at.%)	Test Method	$\dot{\varepsilon}_0$ (s^{-1})	T (K)	Procedure	Slope ⁺	$\dot{\varepsilon}_0$ (s^{-1})
Conrad	205	0	1.0	Tension	10^{-4}	0-600	ΔH_σ^* vs. T $(\partial \sigma / \partial \ln \dot{\varepsilon}) / T$ vs. $-(\partial \sigma^* / \partial T)$	28.3 k	$10^{8 - \Delta S_\sigma^* / k}$
Jones & Conrad	206	0	1.0	Tension	10^{-4}	0-500	ΔH_σ^* vs. T.	27.8 k	$10^{8 - \Delta S_\sigma^* / k}$
Conrad & Jones	207	0	0.06-1.0	Tension	10^{-4}	0-500	ΔH_σ^* vs. T.	28.0 k	$10^{8 - \Delta S_\sigma^* / k}$
Zeyfang et al	184	0	0.2	Creep	10^{-4}	0-500	ΔH_σ^* vs. T	28.0 k	$10^{8 - \Delta S_\sigma^* / k}$
Jones	223	0	0.5	Tension	10^{-4}	0-500	ΔH_σ^* vs. T	27.8 k	$10^{8 - \Delta S_\sigma^* / k}$
Okazaki et al	209	0	0.04-0.45	Tension	10^{-4}	0-500	$\Delta H_{f_i}^*$ vs. T $\Delta G^*(\mu=C_{66})$ vs. T $1/(\partial \sigma / \partial T)$	24.1 k	$10^{6 - \Delta S_{f_i}^* / k}$
Okazaki & Conrad	215	N	0.04-0.61	Tension	10^{-4}	0-500	$\Delta H_{f_i}^*$ vs. T	29.7 k	$10^{9 - \Delta S_{f_i}^* / k}$
Okazaki et al	210	N	0.04-0.61	Tension	10^{-4}	0-500	$\Delta H_{f_i}^*$ vs. T. $(\partial \ln \dot{\varepsilon} / \partial \sigma) / T$ vs. $1/(\partial \sigma / \partial T)$	27.8 k	$10^{8 - \Delta S_{f_i}^* / k}$
Okazaki et al	212	C	0.07-.36	Tension	10^{-4}	0-500	$\Delta H_{f_i}^*$ vs. T	18.0 k	$10^{4 - \Delta S_{f_i}^* / k}$
Agrawal et al	189	0	0.2	Stress Relax.	10^{-4}	0-500	$\Delta H_{f_i}^*$ vs. T $\Delta G^\mu(\mu=E)$ vs. T	26.7 k	$10^{8 - \Delta S_{f_i}^* / k}$
Conrad et al	3	C,N,0	0.05-1.0	Tension	10^{-4}	0-500	$\Delta H_{f_i}^*$ vs. T $\Delta G^\mu(\mu=\sqrt{K_e K_s})$ vs. T	30.3 k	$10^{9 - \Delta S_{f_i}^* / k}$
									$10^{5.5}$

TABLE 5.6 (Con't.)

Authors	Ref.	Major Solute	$C_{i\%}$ (at.%)	Test Method	$\dot{\varepsilon}^{-1}$ (s ⁻¹)	T (K)	Procedure	Slope [†]	$\dot{\varepsilon}_0$ (s ⁻¹)
de Meester et al	259	0	0.5	Tension	10^{-4}	0-500	ΔH_f^* vs. T $\Delta G^{\mu}_{\{i=C_{66}\}}$ vs. T	24.9 k	$10^6 e^{-\Delta S_f^*/k}$
		1.0		Tension	10^{-4}	0-500	ΔH_f^* vs. T $\Delta G^{\mu}_{\{i=C_{66}\}}$ vs. T	14.1 k	$10^1 e^{-\Delta S_f^*/k}$
Harding	181	0	0.6	Tension	10^{-3}	0-240	ΔH_σ vs. T	22.4 k	$10^7 e^{-\Delta S_\sigma/k}$
					10^{-1}	0-273	ΔH_σ vs. T	37.5 k	$10^{15} e^{-\Delta S_\sigma/k}$
					45	0-273	ΔH_σ vs. T	44.9 k	$10^{21} e^{-\Delta S_\sigma/k}$
Gegel & Duvall	296	0	0.1	Tension	10^{-4}	0-573	ΔH_σ^* vs. T $(\partial \sigma / \partial \ln \dot{\varepsilon}) / T$ vs. -($\partial \sigma / \partial T$)	21.2 k	$10^5 e^{-\Delta S_\sigma^*/k}$
					10^{-4}	0-500			$10^6 e^{-\Delta S_\sigma/k}$
Evans	297	0	0.6	Tension	10^{-4}	0-400	ΔH_σ^* vs. T.	29.7 k	$10^9 e^{-\Delta S_\sigma^*/k}$
Present		0	0.1-1.0	Tension	10^{-4}	0-500	$-T(\partial \sigma / \partial T)$ vs. $(\partial \sigma / \partial \ln \dot{\varepsilon})$	34.5	$10^{11} e^{-\Delta S_\sigma/k}$

[†]Note

See bottom of Table 5.5 for significance of slopes.

References are listed at end of text.

exponential between ΔG^U and ΔH^* were entirely due to the activation entropy, one obtains $e^{\Delta S^*/k} \approx 10^4 - 10^5$, which gives $\Delta S^* = 9 - 12k$. The fact that ΔS^* is relatively independent of temperatures is in keeping with the temperature dependencies of the pertinent moduli of Ti (i.e. $d\mu/dT$), which are relatively constant over most of the temperature range considered; see Fig. 2.3.

Other than the inclusion of a significant entropy contribution, the larger values of the pre-exponential associated with ΔH^* might be due to: (a) the area A swept out per successful thermal fluctuation is greater than the dislocation pinning length squared (ℓ^*)² and/or (b) that the dislocation segment vibrational frequency is greater than the product v_{pb}/ℓ^* . That A may in fact be greater than (ℓ^*)² is indicated by the computer calculations of Arsenault and Cadman (Ref. 298), who found for the thermally activated motion of dislocations through a random array of obstacles that the distance between hard spots was $10 - 100 \ell^*$ rather than simply ℓ^* . That v^* may be greater than v_{pb}/ℓ^* is suggested by the work of Frank and Grydman (Ref. 126), which led to the conclusion that v^* may be in the range between $v_{pb}/2\ell^*$ and $v_{pb}/b/2\ell^*$.

Worthy of note in Table 5.6 is that the results by Harding (Ref. 181) show a significant increase in the pre-exponential quantity $\dot{\epsilon}_0 e^{\Delta S/k}$ with increase in strain rate from 10^{-3} to $45 s^{-1}$, suggesting that the pre-exponential may be a function of stress. It is conceivable that stress might influence ρ_m , and perhaps ΔS ; also both A and v^* might increase with stress.

Finally, worthy of mention is that the deformation kinetics behavior of single and polycrystalline Hf-O alloys (Ref. 98) were found to be similar to those of the Ti-interstitial alloys discussed here. Reasonably good straight lines through the origin were obtained for plots of $\Delta H^*(\equiv \Delta G)$ and ΔG^U versus temperature for the Hf-O alloys, even though irregularities existed in plots of the deformation partials $(\partial\tau/\partial\ln\dot{\gamma})_T$ and $(\partial\tau/\partial T)_\gamma$ versus temperature. For these alloys the value of $\dot{\epsilon}_0 e^{\Delta S/k}$ associated with ΔH^* was $10^8 s^{-1}$ and that of $\dot{\epsilon}_0$ associated with $\Delta G^U(\mu=C_66)$ was $10^4 s^{-1}$, in accord with those reported here for the Ti-interstitial alloys.

A summary of the results pertaining to the deformation kinetics for prism slip in single crystals and for the plastic flow of polycrystals at low temperatures ($T < 700K$) and strain rates of 10^{-5} to $10^{-3}s^{-1}$ will now be given.

- (1) The behavior of polycrystals is very similar to that for prism slip in single crystals, indicating rather strongly that the principal rate controlling mechanism(s) during the plastic flow of polycrystals is associated with prism slip.
- (2) Irregularities occur in the deformation partials $(\partial\tau/\partial\ln\dot{\gamma})_T$ and $(\partial\tau/\partial T)_\gamma$ as a function of temperature, the former showing two maxima (one at $\sim 200K$ and the other at $\sim 400K$), whereas the latter shows a sharp discontinuity in the range of $250-500K$. These irregularities are especially pronounced in Ti-N alloys.
- (3) Plots of the enthalpy of activation ΔH^* calculated on the basis that the rate controlling process is overcoming of individual interstitial solute atom obstacles versus the temperature exhibit irregular behavior in the region of $300-400K$, especially for the highest purity materials. This irregularity becomes less pronounced as the total interstitial content exceeds 0.1 at.-%.
- (4) Comparison of the results for ΔH^* (ΔG independent of temperature) with those obtained by taking the Gibbs free activation energy ΔG proportional to a modulus (ΔG^U) indicates that the temperature dependence of ΔG^U is of the order, or slightly less than, Youngs modulus E.
- (5) The values of ΔH^* and ΔG^U obtained from measurements at one specific temperature are equal to those obtained by integration of the activation volume versus stress curve from that temperature to 0K. This indicates rather strongly that a single mechanisms or set of mechanisms is operative over the entire range of 0-700K.

(6) The derived experimental values of the dislocation-obstacle interaction energy and force assuming Fleischer-Friedel statistics are in reasonable quantitative accord with those calculated based on elastic interactions associated with individual interstitial solute atom obstacles.

(7) The fact that similar deformation kinetics behavior occurs for all three interstitial solutes (C, N, O) in Ti (and for O in Hf) suggests that if solute atom clusters are the principal rate controlling obstacles, then their size and spacing are proportional to the interstitial content in each case.

(8) The results of Harding (Ref. 181) suggest that the pre-exponential in the rate equation may be dependent on stress.

Temperature Dependence of the Flow Stress:

The temperature dependence of the flow stress is a reflection of the obstacle profile. However, it is not a critical measure of the obstacle profile, nor the rate controlling mechanism, as first pointed out by Ono (Ref. 300). Conrad and coworkers (Refs. 157, 205, 209, 210, 212, 299) found a rather good fit to a straight line when the thermal component of the flow stress was plotted versus $T^{1/2}$; see, for example, Fig. 5.30. As pointed out by Conrad (Ref. 151), this temperature dependence is in accord with a triangular force-activation distance curve, which leads to the following expression for the variation of ΔG with stress τ^* ,

$$\Delta G = F_0 [1 - (\tau^*/\tau_{00}^*)]^2 \quad (5.39)$$

where F_0 is the Helmholtz free energy and τ_{00}^* is the flow stress at 0K. An approximation to a triangular shape is indicated by the experimental $f_i^* - x^*$ curves of Figs. 5.16 and 5.17 and the theoretical curves of Fig. 5.18.

Eq. 5.39 represents a specific equation of the more generalized expression given by Kocks, Argon and Ashby (Ref. 101)

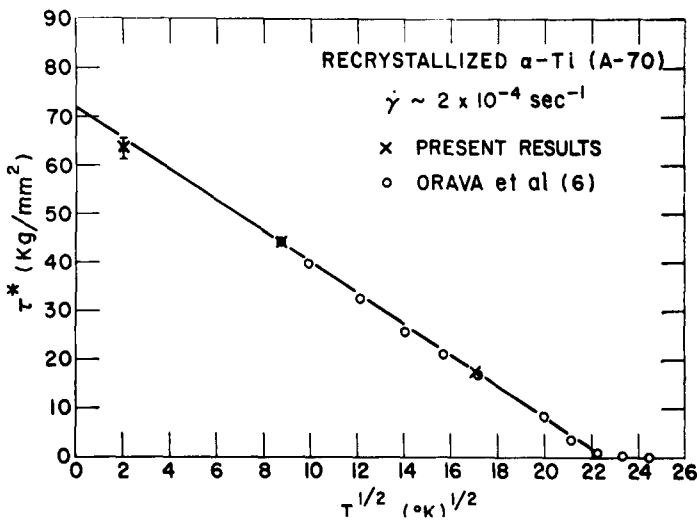


Fig. 5.30. $\tau^* (= \sigma^*/2)$ versus $T^{1/2}$ for polycrystalline A-70 titanium. From Jones and Conrad (Ref. 295).

$$\Delta G = F_0 [1 - (\tau^*/\tau_0^*)^p]^q \quad (5.40)$$

where p has the limits $0 < p < 1$ and $1 < q < 2$. Ono (Ref. 298) has proposed that the following expression is a sufficiently accurate description for many cases, including the case of elastic interactions.

$$\Delta G = F_0 [1 - (\tau^*/\tau_0^*)^{1/2}]^{3/2} \quad (5.41)$$

This gives for the flow stress (starting with Eq. 3.57)

$$(\tau^*/\tau_0^*)^{1/2} = 1 - \left[\frac{kT \ln(\gamma_0/\dot{\gamma})}{F_0} \right]^{2/3} \quad (5.42)$$

and a plot of $(\tau^*/\tau_0^*)^{1/2}$ versus $T^{2/3}$ should yield a straight line. Comparisons of the fit of the temperature dependence of the flow stress of Ti single and polycrystals according to Eqs. 5.39 and 5.41 are presented in Figs. 5.31 to 5.33. It is here seen that the fit is in general better for Eq. 5.39 (τ^*/τ_0^* versus T^2) than for Eq. 5.41 ($(\tau^*/\tau_0^*)^{1/2}$ versus $T^{2/3}$), indicating that the $f_i^* - x^*$ profile associated with interstitial obstacles in Ti is more triangular than that given by Eq. 5.41.

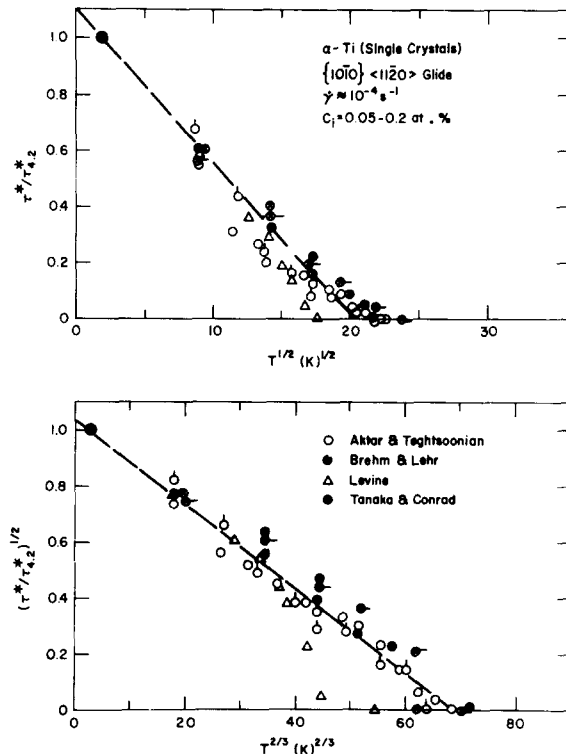


Fig. 5.31 $(\tau^*/\tau_{4.2}^*)^{1/2}$ versus $T^{1/2}$ and $(\tau^*/\tau_{4.2}^*)^{1/2}$ versus $T^{2/3}$ for prism glide in Ti single crystals. Data from Refs. of Table 4.2. Ticks on data points indicate lower purity material.

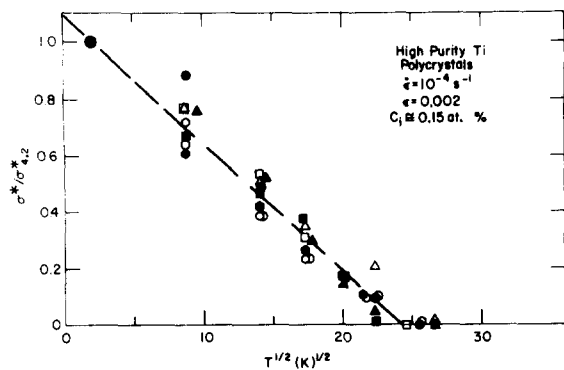


Fig. 5.32. $(\tau^*/\tau_{4.2}^{1/2})$ versus $T^{1/2}$ and $(\tau^*/\tau_{4.2}^{1/2})^{1/2}$ versus $T^{2/3}$ for plastic flow of high purity Ti polycrystals. Data from Refs. 172, 209, 210. Open symbols refer to grain sizes of 1-2 μm ; filled symbols refer to grain sizes of 15-20 μm .

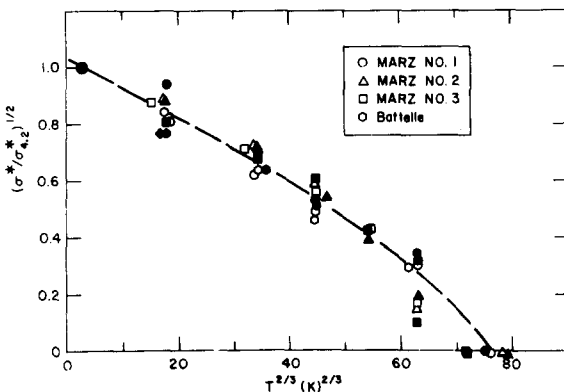
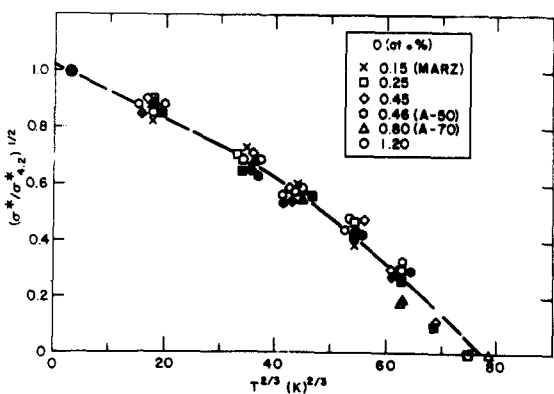
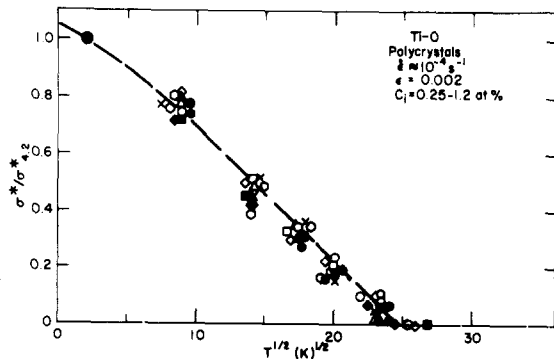


Fig. 5.33. $(\tau^*/\tau_{4.2}^{1/2})$ versus $T^{1/2}$ and $(\tau^*/\tau_{4.2}^{1/2})^{1/2}$ versus $T^{2/3}$ for the plastic flow of Ti-O polycrystals. Open symbols refer to grain sizes of 1-2 μm ; filled symbols refer to grain sizes of 15-20 μm . Data from references in Table 4.3 and from Refs. 197 and 209.



Strengthening Due to Two or More Interstitial Solutes:

Of interest is the strengthening due to the presence of more than one of the interstitial solutes. Since from the above it appears that the values of f_i^* for C, N and O in Ti are not too different, and since the concentration of these solutes in Ti are often of similar magnitude, a reasonable approximation to the combined effect of these interstitials should be given by Eq. 3.47, i.e.

$$\tau^{*2} = \tau_O^{*2} + \tau_N^{*2} + \tau_C^{*2} \quad (5.43)$$

If we now assume that the F-F model of solid solution strengthening applies and we insert for each value of τ^* in Eq. 5.43 the value given by Eq. 3.29, we obtain

$$\tau^* = [\beta f_{i,0}^{*3} C_0 + \beta f_{i,N}^{*3} C_N + \beta f_{i,C}^{*3} C_C]^{1/2} \quad (5.44)$$

$$= \beta^{1/2} f_{i,0}^{*3/2} (C_0 + X_N C_N + X_C C_C)^{1/2} \quad (5.44a)$$

$$= \beta^{1/2} f_{i,0}^{*3/2} O_{eq}^{1/2} \quad (5.44b)$$

where τ^* is the effective stress (thermal component of the flow stress), $\beta = s' / \alpha b^2 (2E_L)^{1/2}$, $X_N = (f_{i,N}^*/f_{i,0}^*)^3$, $X_C = (f_{i,C}^*/f_{i,0}^*)^3$ and O_{eq} is the oxygen equivalent of the total interstitial content. The values of X_N and X_C derived from the values of $f_{i,0}^*$ for O, N and C given in Table 3.4 for elastic interactions are presented in Table 5.7. Comparing these values with the experimental values of the strengthening ratios given in Fig. 5.9, it is seen that reasonable agreement exists for the interaction of edge dislocations with interstitial solute atom obstacles. Previous considerations by Conrad, de Meester, Döner and Okazaki (Ref. 3) yielded better agreement between calculated and experimental values of X_N and X_C for screw dislocations. The difference in the two sets of independent results arises from a difference in the modulus interaction parameter derived from the limited data on the effect of interstitial solute content on the elastic constants; see Figs. 2.5 and 2.6.

TABLE 5.7 Relative Strengthening Ratios $X_N = (f_{i,N}^*/f_{i,0}^*)^3$ and $X_C = (f_{i,C}^*/f_{i,0}^*)^3$ for Edge and Screw Dislocations Based on Elastic Interactions[†]

y	edge		screw	
	$I_e = \sqrt{2}[(n')^2 + (\alpha_e \epsilon_e)^2]^{1/2}$	$I_e = n' + \alpha_e \epsilon_e$	$I_s = n' - \alpha_s \epsilon_s$	
X_N	$b\sqrt{3}/4$	0.91	1.12	1.00
	$b\sqrt{3}/6$	0.87	1.11	0.81
X_C	$b\sqrt{3}/4$	0.54	0.89	0.05
	$b\sqrt{3}/4$	0.38	0.71	0.05

[†]Note

Values for $f_{i,0}^*$, $f_{i,N}^*$ and $f_{i,C}^*$ taken from Table 3.4.

Mott-Labusch Statistics:

The above considerations of the dislocation-solute atom interaction energies and forces are all based on the Fleischer-Friedel solution strengthening model, which seems to apply reasonably well over the entire interstitial content range considered (0.05-1.2 at.%). Considering Eq. 3.33 and the data in Fig. 5.15, this model is expected to apply at the lowest concentrations (~ 0.1 at.%) over most of the temperature range considered, and perhaps even at the higher concentrations. However, the $C_i^{2/3}$ average concentration dependence of the strengthening suggests that the Mott-Labusch statistics may apply at the higher concentrations. The interaction forces can then be calculated by means of Eq. 3.34. Employing the data of Fig. 5.7, Eq. 3.34 yields $f_{i,p}^*/2E_L$ equal to 0.225, 0.354 and 0.415 for the Ti-C, Ti-O and Ti-N alloys respectively. These values are similar to those obtained for the F-F statistics when the dislocation segment length ℓ^* is taken to be 2.5 times that given by Eqs. 3.26 to 3.28 (see Table 5.3) and are in accord with those calculated for the interaction of edge dislocations with the interstitial solutes.

Summary:

Although considerable effort has been spent in the past 15 years investigating the effects of interstitial solutes at concentrations less than 1 at.% on the plastic flow of Ti at low temperatures (4.2 - 700K) and moderate strain rates (10^{-5} - 45s^{-1}), we still are not completely clear on the exact mechanism(s) by which the strengthening occurs. However, two aspects appear to have been established: (a) The interstitial solutes C, N and O provide strong "thermal" obstacles to dislocation motion on the first-order prism planes in Ti and are largely responsible for the temperature and strain rate dependence of the flow stress for glide on these planes, and (b) The deformation kinetics associated with the plastic flow of polycrystals are largely governed by prism glide.

The concentration dependence of the strengthening due to interstitial solutes in Ti has not yet been clearly identified. The available data indicate that for concentrations of 0.05 to 1.2 at.% it is somewhere between a $C_i^{1/2}$ (Fleischer-Friedel model) and a linear dependence (Mott-Nabarro model), with reasonable agreement occurring for a $C_i^{2/3}$ dependence (Labusch model). Theoretical consideration suggest that the exact concentration dependence may vary with solute content; hence the $C_i^{2/3}$ dependence may only represent the best average over the concentration range considered. The available experimental data do not permit a positive resolution of this possibility.

Reasonable success in interpreting the available experimental data is obtained by assuming that the rate controlling mechanism is the overcoming of strong discrete interstitial-solute atom obstacles by dislocations moving on the prism planes, i.e. by employing Fleischer-Friedel statistics. When this is done, qualitative and to some degree quantitative accord is obtained between the experimental values of the dislocation-obstacle interaction energy and force and those calculated theoretically from elastic interactions between individual interstitial solutes and prism glide dislocations. Although the general behavior appears to be in accord with this model, there exist a good number of irregularities which still need to be explained before it can be fully accepted, the concentration dependence of the strengthening being among these. Further, the experimentally deduced interaction energies are also in reasonable accord with a number of chemical interaction energies, so that these types of interaction cannot be completely disregarded. Also, the roles played by sessile-glissile dislocation recombination and by interstitial solute atom clusters need further evaluation.

The concepts and models which have been proposed to explain the physical origin of the interaction between prism dislocations and individual interstitial atoms are summarized in Table 5.8. Considering first the elastic interactions, based on the limited data available on the effect of interstitials on the modulus

TABLE 5.8 History of the development of the concepts for the physical origin of the strengthening of titanium by interstitial solutes

		ELASTIC INTERACTIONS	CHEMICAL INTERACTIONS
1954:	Churchman (Ref. 43)]		
	Interstitial Solutes in Octahedral Sites Are Obstacles to Dislocation Motion Spacing Between Interstitials Greater on (101̄) Plane Than (0001) and (101̄) Planes		
1966:	Tetragonal distortion. [Conrad (Ref. 151)]	1968:	Tetrahedral site at dislocation core. [Tyson (Ref. 69)]
1970:	Size misfit and modulus mismatch deduced from general elastic interaction energy equation. [Kratochvil and Conrad (Ref. 301)]	1968:	Breaking covalent bonds. [Tyson (Ref. 69)]
1973:	Calculation of size misfit and modulus mismatch interaction energies. [Conrad, de Meester, Döner and Okazaki (Ref. 3)]	1969:	Breaking chemical bonds deduced from interatomic potential considerations. [Tyson (Ref. 69)]
1974:	Sessile-Glissile recombination; consider tetragonal distortion and stacking fault energy. [Sob, Kratochvil and Kroupa (Refs. 87, 88)]	1972:	Chemical bond energy for Ti-O deduced from thermodynamic measurements. [Sargent and Conrad (Ref. 38)]
1973:		1973:	BCC structure at dislocation core. [Tyson and Conrad (Ref. 98)]
1973:		1973:	Chemical bond energy for Ti-O, Ti-N, Ti-C deduced from thermodynamic measurements. [Tyson (Ref. 4)]
1980:		1980:	Chemical bond energy for Ti-O, Ti-N, Ti-C deduced from surface energy measurements. [Conrad (present)]

of titanium it appears that the interaction can be described by a Fleischer-type elastic interaction due to the combined size misfit (tetragonal distortion) and the modulus mismatch, with the modulus effect making the larger contribution. However, as mentioned above, before this model can be fully accepted more data are needed, especially on the effect of interstitial solutes on the modulus of titanium. Moreover, a troublesome feature of the model is that agreement with experimental results occurs for an interaction well within the core region of the dislocation, where linear elasticity is not expected to apply. A similar problem occurs for the model by Sob, Kratochvil and Kroupa, who proposed that screw dislocations in CPH titanium are dissociated similar to the situation in BCC metals and that the effect of interstitials is on the recombination of the sessile configuration (through an elastic interaction between the interstitial atoms and the partials on the first-order pyramidal planes) into a glissile configuration. The additional assumptions which must be made to obtain agreement with experimental results regarding the length of the dislocation segment involved in the recombination and the effect of interstitials on the stacking fault energy makes this latter model rather speculative at this time.

The models based on chemical interactions refer to changes in the environment of a solute atom as it enters the core of a dislocation. In the model based on the concept of the breaking of directed atomic bonds (ionic or covalent), reasonable agreement occurs between the values of the bond energy calculated from thermodynamic measurements and those derived from the plastic deformation kinetics. Insufficient thermodynamic data are available for evaluation of the model based on the concept that the interaction energy results from the difference in free energy of an interstitial when it resides in the BCC structure at the core of a dislocation compared to when it resides in the CPH matrix. Likewise, insufficient data are available to determine the increase in energy of the crystal which occurs when the motion of a partial dislocation on the prism plane converts an octahedral site containing an interstitial atom into a tetrahedral site as proposed by Tyson (Ref. 69).

The similarity in the values of the elastic and chemical interaction energies suggests that they may in fact be equivalent, for they both describe electronic energy changes in terms of macroscopic properties. Until we are in a position whereby we can determine directly the electronic energy changes which occur when a dislocation approaches a solute atom, we will need to rely on such indirect measures of these changes. At this time there are insufficient experimental data to decide which of the two approaches (elastic or chemical) yield a more accurate description of these changes.

The deformation kinetics behavior of the Ti-interstitial alloys (and that of Hf-O alloys) suggest that if clusters of interstitial solutes play a dominant role, then there exists a fixed distribution of the solute atoms between the clusters and the matrix as the solute concentration is increased.

5.1.3 Prism Glide - Strain Hardening

As pointed out in Chapter 4 the stress-strain curves for prism glide in Ti single crystals exhibit the three stages characteristic of the deformation of metal single crystals. The values of the strain hardening coefficient $\theta = d\tau/dy$ for Stages I and II listed in Table 4.1 are similar to those reported for metals in general (Refs. 302-309) and it is therefore expected that similar types of dislocation interactions may be responsible for the strain hardening. However, a systematic study into the specific mechanisms responsible for the strain hardening associated with prism slip in Ti single crystals has not yet been performed.

A significant feature of Stage I hardening in Ti noted in TEM studies of lightly deformed single crystal specimens at room temperature is that the dislocation structure is predominantly screw in character (Ref. 45). This was also observed for prism slip in Zr (Ref. 310) and Be (Ref. 309) single crystals. In contrast, lightly deformed Hf (Ref. 311) and Ru (Ref. 312) single crystals contained largely edge dislocations. Based on an analysis of the stress-strain curves for prism glide in Ti obtained by them and the dislocation density measurements of Cass (Ref. 45), Tanaka and Conrad (Ref. 138) suggested that strain hardening in Stage I in Ti might be due to forest dislocations.

Akhtar and Techtsoonian (Refs. 97, 313) proposed that the more rapid Stage II hardening in Ti and Zr may be the result of a sessile lock formed through the interaction of two perfect dislocations lying on the primary and secondary prism planes, namely

$$\frac{a}{3} [11\bar{2}0] + \frac{a}{3} [1\bar{2}10] + \frac{a}{3} [1\bar{1}00] + \frac{a}{9} [1\bar{2}10] + \frac{2a}{9} [11\bar{2}0] \quad (5.45)$$

Additional studies are however needed to evaluate whether this reaction is responsible for Stage II hardening in Ti.

The wavy slip lines associated with Stage III in Ti (Fig. 4.8) are indicative of the occurrence of cross slip. The effects of temperature and strain rate on τ_{III} are described by Eq. 4.1 (see Figs. 4.4 and 4.5). Using the quantitative relationship between the stacking fault energy γ_{SF} and the constant A of Eq. 4.1 proposed by Seeger, Berner and Wolf (Ref. 141), Akhtar and Techtsoonian (Ref. 97) obtained the values of γ_{SF} for the $\{10\bar{1}0\}$ planes listed in Table 5.9. It is here seen that the value of γ_{SF} for Ti at room temperature is 0.145 J/m^2 . Using the same technique, these authors (Ref. 313) obtained 0.056 J/m^2 for Zr.

TABLE 5.9 Stacking fault energy γ_{SF} and related parameters of titanium.
From Akhtar and Techtsoonian (Ref. 97).

T (K)	$\frac{d\ln\tau_{III}}{d\ln\gamma} = \frac{kT}{A}$	A (eV)	$\mu b^3/A$	$10^3 \gamma_{SF}/\mu b$	γ_{SF} (J/m ²)
295	0.090 ± 0.004	0.64	9.9	12.3	0.145 ± 0.025
473	0.066 ± 0.006	0.62	8.9	11.3	0.115 ± 0.015

On the basis of a hard sphere model, the following reaction has been proposed for the dissociation of a perfect $a/3 [11\bar{2}0]$ dislocation lying on a $\{1\bar{1}00\}$ plane (Refs. 51, 89, 314).

$$\frac{a}{3} [11\bar{2}0] \rightarrow \frac{a}{18} [42\bar{6}3] + \frac{a}{18} [24\bar{6}3] \quad (5.46)$$

Since the coordination number is changed from 12 to 11 in the fault and since there is an appreciable increase in the spacing between the corrugated prism planes in the metastable position, Akhtar and Techtsoonian (Ref. 97) concluded that the energy for this fault to be higher than the experimental value of 0.145 J/m^2 . Instead they proposed the alternate dissociation model considered by Regnier and Dupouy (Ref. 89) based on the HCP \rightleftharpoons BCC transformation, in which two sets of $\{10\bar{1}0\}$ planes of the HCP lattice are transformed into two $\{112\}$ BCC planes. The fault which results is of low energy and may be considered to be bound by partials defined by the dissociation

$$\frac{a}{3} [11\bar{2}0] \rightarrow \frac{a}{9} [11\bar{2}0] + \frac{2a}{9} [11\bar{2}0] \quad (5.47)$$

On the basis of the reaction given by Eq. 5.47 Regnier and Dupouy (Ref. 89) proposed that the stacking fault energy will decrease as the ratio T_t/T_m becomes smaller, where T_t is the temperature of the HCP \rightleftharpoons BCC transformation and T_m is the melting temperature. Since the ratio T_t/T_m is 0.6 for Ti and 0.53 for Zr, the lower experimental value of γ_{SF} for Zr compared to Ti is consistent with this model.

5.1.4 Basal Glide and Relative Ease of Basal and Prism Glide

Only limited studies have been carried out on the mechanisms associated with basal glide in Ti at low temperatures. The stronger effects of temperature and strain rate on the yield stress (Fig. 4.26) and the weaker effect of interstitial solute content (Fig. 4.27) suggest that the rate controlling mechanism differs from that for prism glide. Levine (Ref. 148) proposed that overcoming of the Peierls force was the rate controlling mechanism at temperatures below about 400K. Employing the Dorn-Rajnak theory (Ref. 315) he obtained from shear tests on high purity Ti at 195-473K the values listed in Table 5.10 for various Peierls mechanism parameters.

TABLE 5.10 Parameters of the Peierls mechanism for basal slip in titanium using the Dorn-Rajnak theory. From Levine (Ref. 148).

Peierls Stress τ_p^0	:	441 MPa
Kink Energy, E_K	:	0.94 eV
Dislocation Line Energy E_L		
Edge Dislocation	:	$7\mu b^2$
Screw Dislocation	:	$10\mu b^3$

Thermal activation analysis of Levine's data (Ref. 148) by Conrad, Doner and de Meester (Ref. 2) yielded $\Delta H_{T^*}(T_c=400K) = 2.34$ eV and $\dot{\gamma}_0 \exp(\Delta S_{T^*}/kT) = 67.5k$. The unusually large value of 67.5k suggests that the pre-exponential $\dot{\gamma}_0$ may be dependent upon the effective stress T^* .

Worthy of note regarding the thermal activation analysis of basal glide in Ti is the anomalous behavior of $Q(=\Delta H_{T^*})$ versus temperature in the region of 300-400K shown in Fig. 4.28. This anomalous behavior is also indicated in the plot of ΔH_{T^*} versus temperature by Conrad, Doner and de Meester (Ref. 3), their Fig. 5.

The fact that wavy slip lines occurred in Ti crystals oriented for basal slip and tested in uniaxial tension at all temperatures considered by him (500-1100K) led Akhtar (Ref. 143) to conclude that cross slip was the rate controlling mechanism for basal slip in this temperature range. He proposed that in the unstressed crystal the $a/3 [11\bar{2}0]$ screw dislocations split into lower energy partials on the first order prism planes. Upon application of a stress, the partials recombine with the aid of thermal fluctuations and the screw dislocations cross glide onto the basal planes, similar to the Friedel (Ref. 316) cross slip mechanism, which gives for the flow stress τ

$$\dot{\gamma} = A\tau^n \exp(-Q/kT) \quad (5.48)$$

where $\dot{\gamma}$ is the shear strain rate, n the stress exponent whose theoretical value for cross slip is 2, Q the activation energy for cross slip and A a constant. Support for Eq. 5.48 is provided by the results plotted in Figs. 5.34 and 5.35.

The stress exponent n derived from these experimental data is 4 and the activation energy is 2.5eV. The value of n is more nearly those for a diffusion controlled mechanism (Ref. 163) than for a cross-slip mechanism. Also, the value of Q is of the order of that for self-diffusion in titanium; see Table 2.5.

Worthy of note regarding the deformation kinetics of basal glide in titanium is that the activation energy determined by Akhtar (Ref. 143) in the temperature range of 500-1100K is approximately the same as that derived by Conrad, Doner and de Meester (Ref. 3) from Levine's (Ref. 148) data in the range of 195-473K, suggesting that the same mechanism may be rate controlling over the entire temperature range of 195-1100K. On the other hand, the results in Figs. 4.28 and 4.29 suggest that at least two mechanisms may be rate controlling over this temperature range, one below approximately 700K and the other above. Furthermore, the anomalous effect of temperature on Q at 300-500K needs additional consideration.

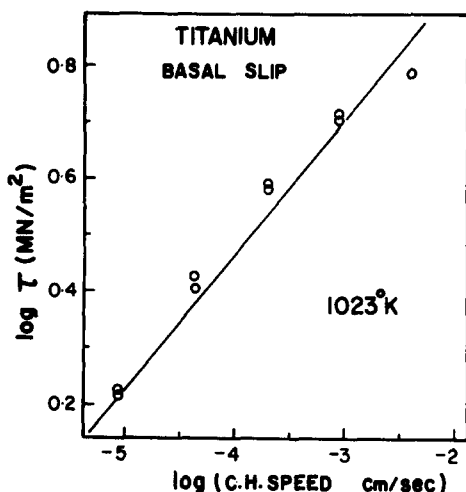


Fig. 5.34. Log-log plot of flow stress for basal glide at 1023K versus cross-head speed. From Akhtar (Ref. 143).

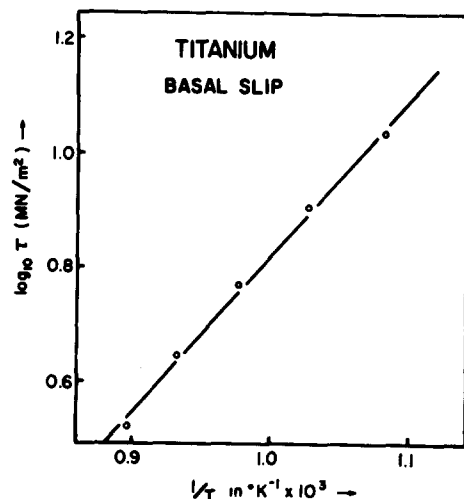


Fig. 5.35. $\log \tau$ versus $1/T$ for basal glide at a strain rate of $1.66 \times 10^{-4} \text{ s}^{-1}$. From Akhtar (Ref. 143).

A list of the primary and secondary slip systems in CPH metals is presented in Table 5.11. Of interest regarding the plastic deformation of titanium (and CPH metals in general) is the relative ease of prism compared to basal slip. Attempts to explain the preference for either the prism or basal plane as the primary slip system in terms of the Peierls stress, elastic anisotropy, strain energy or c/a ratio (Refs. 51,318,319) are found to be inadequate. Also, inconsistencies occur when one attempts to explain the slip plane preference on the basis of the CPH \rightleftharpoons BCC transformation as proposed by Regnier and Dupouy (Ref. 89,320). These authors pointed out that CPH metals which do not undergo a phase transformation (e.g. cadmium, zinc and magnesium), or transform to the FCC structure (e.g. cobalt), have the basal plane as the primary slip plane, whereas those which transform to the BCC structure slip preferentially on the prism plane. Since beryllium (Ref. 309) is an exception to this rule, they argue that metals which undergo the CPH \rightleftharpoons BCC transformation near the melting temperature ($T_t/T_m \approx 1$) have the basal plane as the primary slip plane. However, yttrium (Ref. 321) and gadolinium (Ref. 322) also

TABLE 5.11. Primary and Secondary Slip Systems in HCP Metals[†]. From Aldinger (Ref. 317).

Metal	c/a	T_a/T_f	T_t/T_f	$\Delta F_{\text{hcp-bec}}/\Delta F_{\text{hcp-fcc}}$	Primary slip plane	Secondary slip planes	Twining planes	γ_B (erg/cm ²)	γ_p (erg/cm ²)
Co	1.6235	0.17	0.39	26.6	{0001}	{1122}, {1011}	{1012}, {1121}	26	—
La	2×1.6126	—	—	15.9	{0001}	—	—	—	—
Cd	1.8856	0.50	—	2.22	{0001}	{1122}, {1011}, {1010}	{1012}	15-150	—
Zn	1.8563	0.43	—	1.59	{0001}	{1122}, {1010}, {1011}	{1012}	15-30	—
Re	1.615	0.09	—	1.53	{0001}	{1011}, {1010}, {112n}	—	—	—
Be	1.568	0.19	0.98	1.51	{0001}	{1010}, {1122}	{1012}, {112n}	173-1000	≥ 1190
Mg	1.6235	0.32	—	1.49	{0001}	{1122}, {1010}, {1011}	{101n}	30-60	—
Tb	1.5811	0.19	0.97	—	{0001}, {1010}	—	—	—	—
Y	1.5712	0.17	0.96	—	{1010}	{0001}	{1012}, {112n}	—	—
Gd	1.5904	0.19	0.97	—	{1010}	—	—	—	—
Ru	1.5824	0.12	—	—	{1010}	—	{101n}, {112n}	—	—
Os	1.5790	—	—	—	{1010}	—	{101n}	—	—
Hf	1.5811	0.12	0.88	—	{1010}	{0001}, {1011}, {1122}	{1012}, {112n}	—	—
Ti	1.5873	0.15	0.60	0.95	{1010}	{1011}, {0001}	{1012}, {112n}	300	145
Zr	1.5931	0.14	0.53	0.87	{1010}	{1011}, {0001}, {1122}	{1012}, {112n}	300	56
Tl	1.5984	0.52	0.88	0.49	{1010}	{0001}	—	—	—

[†] T_a = ambient temperature, T_f = melting point, T_t = transformation temperature.

γ_B = stacking fault energy of the basal plane.

γ_p = stacking fault energy of the prism plane.

have a T_t/T_m ratio close to one and slip primarily on the prism plane. Moreover, the primary slip system in ruthenium (Refs. 312,323), which has no stable BCC structure, is the prismatic system.

Somewhat better agreement between observed and predicted slip plane preference is obtained when the stacking fault energies on both the basal and prism planes are considered in terms of the relative phase stability. Aldinger (Ref. 317) proposes that if the formation of stacking faults on prism and basal planes reflects the tendency of the CPH structure to transform into the BCC or FCC modification, respectively, then the ratio of the stacking fault energy on these planes ($\gamma_{\{10\bar{1}0\}}/\gamma_{(0001)}$) should be proportional to the ratio of the free energy difference ($\Delta F_{CPH-BCC}/\Delta F_{CPH-FCC}$). Consequently, the stability of the BCC or FCC structure relative to the CPH structure at a given temperature should determine whether the prism or basal plane has the lower stacking fault energy. He further reasons that glide on either the prism or basal plane is easier the lower the stacking fault energy, because the dislocations can then readily dissociate, making cross slip more difficult. A high stacking fault energy leads to less dissociation and in turn the dislocation can cross slip easily, whereupon if the stacking fault energy of the cross slip plane is lower, the dislocation dissociates on this plane, thereby becoming restrained. Applying this reasoning to titanium, it must be presumed that the stacking fault energy on the prism plane is smaller than that on the basal plane and therefore dislocations on the basal plane can readily cross slip onto the prism plane, where they dissociate and become restrained, causing a higher yield stress. The observation that basal slip lines in titanium were always wavy (Ref. 143) is in accord with this model.

The temperature dependence of the relative phase stability between the CPH and the BCC and FCC structures expressed in terms of the difference in free energy is presented in Fig. 5.36. It is here seen that for titanium $\Delta F_{CPH-BCC} < \Delta F_{CPH-FCC}$ at temperatures above about 250K and therefore $\gamma_{\{10\bar{1}0\}}$ is expected to be less than $\gamma_{(0001)}$, favoring prism glide as the primary system. Further, Fig. 5.37 shows that there seems to be a quantitative relationship between the ratio of the CRSS for prismatic and basal slip ($\tau_{\{10\bar{1}0\}}/\tau_{(0001)}$) and the ratio of the free energy difference. Of special note here is that the model applies to the behavior of CPH alloys as well as to pure metals.

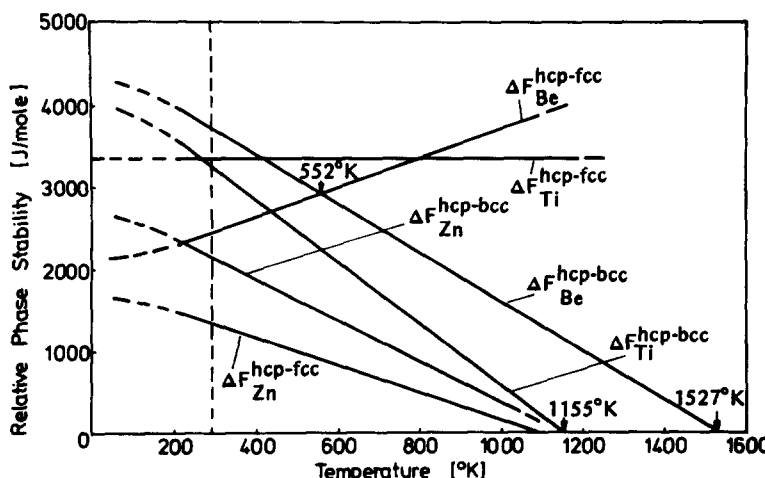


Fig. 5.36. Relative stabilities of the BCC and the FCC structures in some CPH metals. From Aldinger (Ref. 317).

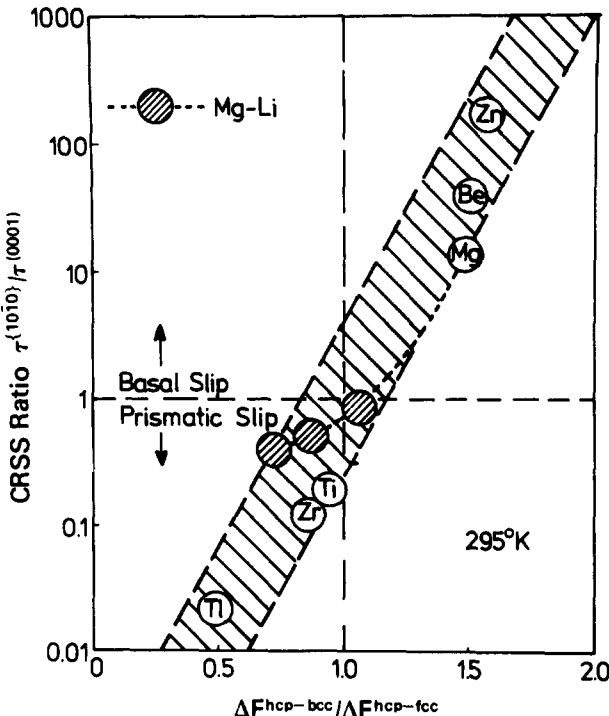


Fig. 5.37. Ratio of the CRSS for prism to basal slip versus the ratio of the relative stabilities of the BCC and FCC structures. From Aldinger (Ref. 317).

That Aldinger's model may be too simple is indicated by the results in Fig. 5.38, where the ratio of the CRSS for basal slip compared to prism slip increases with decrease in temperature for both titanium and zirconium. If this ratio were directly related to the ratio of the free energy change, then from the data in Fig. 5.36 one would expect the basal/prism CRSS ratio to decrease with decrease in temperature, rather than increase as in Fig. 5.38. As pointed out by Aldinger (Ref. 317), a factor which is not taken into account in his model is that the stacking fault energy is not simply a function of the free energy difference of the two structures (Ref. 324), but also depends on the strain energy and the surface energy of the stacking fault-matrix interface (Ref. 325). In general the latter term is small compared to the relative phase stability. However, the strain energy term can be important. For example, employing anisotropic elasticity Regnier and Dupuy (Ref. 320) have found that for equal stacking fault energies, the dissociation of prism-plane dislocations will always occur more readily than the dissociation of dislocations on the basal plane.

In addition to the above, the rate controlling mechanism which is operative on each plane must be taken into account when considering the effect of temperature on the prism/basal CRSS ratio given in Fig. 5.38. For example, since the rate controlling mechanism for prism glide in titanium appears to be the thermally activated overcoming of interstitial solute atom obstacles, the effect of temperature on the CRSS for prism glide will be determined by this mechanism and in turn

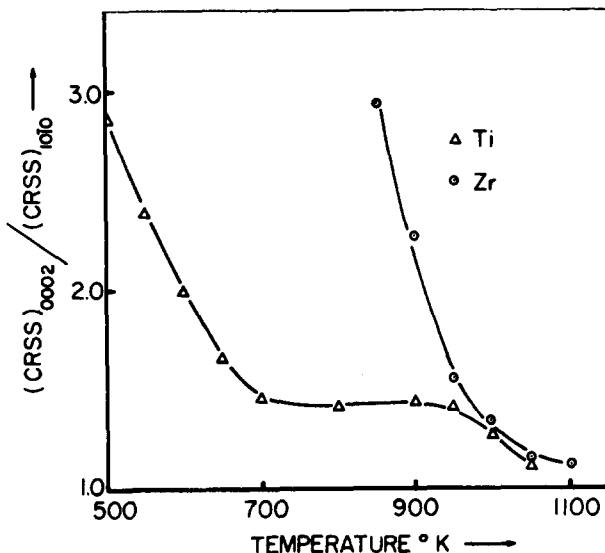


Fig. 5.38. The ratio of the CRSS for basal to that for prism slip in Ti and Zr. From Akhtar (Ref. 143).

will be included in the effect of temperature on the prism/basal CRSS ratio. As a result, the influence of the free energy difference may be masked in titanium, because the interaction between gliding dislocations and solute atom obstacles is different for the prism compared to the basal plane. Hence, interstitial solutes in titanium can influence the effect of temperature on the relative ease of prism/basal glide through their direct interaction with dislocations (which is expected to be strongly temperature dependent) as well as their indirect effect through the stacking fault energy (which is expected to be less temperature dependent). Thus, comparisons of the relative ease of prism/basal glide in CPH metals should be made for those conditions where solute atom obstacles exert either no influence or exactly the same influence on the CRSS of both planes. The former condition is obtained at very high purity or at temperatures where the solute atoms obstacles are essentially transparent to dislocation motion.

5.1.5 $\langle c+a \rangle$ Slip and Twinning

The occurrence of $\langle c+a \rangle$ slip in titanium (Refs. 44-46, 142) is in keeping with the analyses of Rosenbaum (Ref. 314) and Teutonico (Ref. 55). On the basis of a hard sphere crystal model Rosenbaum (Ref. 314) was able to explain slip on the second-order pyramidal {1122} plane along $\langle 11\bar{2}3 \rangle$ directions ($\langle c+a \rangle$ slip) in titanium and zirconium in terms of glissile, twin-like stacking faults with displacements parallel to the slip direction. Subsequently, Teutonico (Ref. 55) derived expressions for the energies of dislocations with $\langle a \rangle$, $\langle c \rangle$ and $\langle c+a \rangle$ Burgers vectors in a hexagonal crystal. These expressions yielded a criterion which defined the orientations for which a $\langle c+a \rangle$ dislocation is stable against dissociation into an $\langle a \rangle$ dislocation and a $\langle c \rangle$ dislocation. It was found that in general a non-basal slip plane will contain sectors for which a $\langle c+a \rangle$ dislocation is stable against dissociation, whereas it is unstable for other sectors. The second-order {1122} pyramidal plane was however the one non-basal plane for which a glissile $\langle c+a \rangle$

dislocation can be stable for all orientations. Worthy of mention is that for the c-axis compression of titanium crystals at elevated temperatures, $\langle c+a \rangle$ slip accounted for up to 60% of the strain at 700K and up to 90% at 1100K (Ref. 46).

Turning to twinning, Rosenbaum (Ref. 314) described a model for twinning on the $\{11\bar{2}2\}$ planes which fit this experimentally observed twinning mode in zirconium. Further, he analyzed twinning on $\{10\bar{1}1\}$ planes in terms of a shear diagram and similarities to twins on $\{1\bar{0}12\}$ and $\{1\bar{0}13\}$ planes were pointed out. Subsequently, Crocker and Bevis (Ref. 326) carried out a detailed analysis of the crystallography of deformation twinning in titanium. They presented fifteen deformation twinning modes which involve shear strains less than unity and rather simple shuffle mechanisms. However, only two of these modes have been observed, namely the $\{10\bar{1}2\}$ and the $\{11\bar{2}1\}$ composition planes. Two additional twinning planes, the $\{11\bar{2}2\}$ and the $\{11\bar{2}4\}$ planes, could be explained by a low shear mode and its conjugate, which also have simple shear shuffles. Crocker and Bevis (Ref. 326) also reviewed the restrictions on the twinning dislocations associated with the operative modes.

Tucker (Ref. 327) has analyzed the interaction between dislocations and twin boundaries in titanium. He calculated the image force f acting on basal slip dislocations due to twin boundaries of five twinning modes to be

$$f = \mu' b_e^2 h \sin^2 2\theta (1-h^2 \cos^2 2\theta) 4\pi(1-\nu') d^{-1} = H_T d^{-1} \quad (5.49)$$

where μ' and ν' are functions of the elastic constants, which when the crystal is isotropic reduce to the shear modulus and Poisson's ratio respectively, b_e is the edge component of the Burgers vector, d is the distance of the dislocation from the boundary and $h = (1-\beta^2)/(1+\beta^2)$ with $\beta = C_{11}/C_{33}$. For the twins observed in titanium, H_T was found to be positive at all temperatures and therefore the boundaries always repel the dislocations. The values of H_T as a function of temperature for five twinning modes are listed in Table 5.12.

TABLE 5.12 Force Factors H_T (in Units of 10^{-7} dyne-cm) for Edge Dislocations of $1/3 \langle 1120 \rangle$ Burgers Vectors Interacting with Twin Boundaries in Titanium. From Tucker (Ref. 327).

T(K)	$\{10\bar{1}2\}$	$\{11\bar{2}1\}$	$\{11\bar{2}2\}$	$\{11\bar{2}3\}$	$\{11\bar{2}4\}$
4.2	7.8	3.4	8.5	10.4	9.9
298	9.3	4.3	10.6	13.0	12.3
1023	11.6	5.1	12.6	15.5	14.8

To be noted from Table 5.12 is that the interactions are appreciably weaker for $\{11\bar{2}1\}$ interfaces than for the other twins. Also, in every case the forces increase significantly with temperature.

As a limiting case, Tucker (Ref. 327) was able to obtain exact expressions for the energies of edge twinning dislocations, which took into account the relative misorientation between matrix and twins. These energies were of the form

$$E_T = A \log(R/r_0) \quad (5.50)$$

where A is a function of the elastic constants, the Burgers vector and the misorientation angle θ ; R and r_0 are the conventional outer and inner radii of the dislocation. The values of A for four twinning modes in titanium are given in Table 5.13.

TABLE 5.13 Elastic Energy Factor A (in Units of 10^{-7} erg) of Unit Edge Twinning Dislocations in Titanium. From Tucker (Ref. 327).

T(K)	{10̄12}	{11̄21}	{11̄22}	{11̄24}
4	5.46	4.56	4.52	2.41
1023	3.36	2.91	2.84	1.49

An interesting feature of the results in Table 5.13 is that they are in accord with the observed frequency of twinning at low temperatures. However, this is not the case for high temperatures, which may be due to the fact that the atomic shuffling which accompanies the dislocation motion may be more important than the elastic effects. Furthermore, as pointed out by Tucker (Ref. 327), his elastic calculations are for individual dislocations rather than zonal dislocations and it may well be that the zonal dislocations are more important in actual twin growth.

The effect of temperature on the maximum shear stress at which twinning occurred on several planes during compression tests on high purity titanium single crystals is shown in Fig. 5.39. To be noted is that the stresses for twinning on

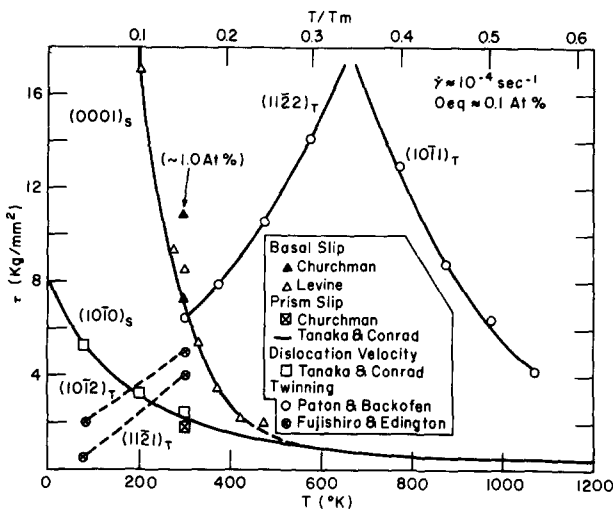


Fig. 5.39 Effect of temperature on the shear stress for twinning on {10̄12}, {11̄22} and {10̄11} planes of titanium crystals tested in compression. Also included are the effects of temperature on the CRSS for prism and basal slip. From Conrad, Doner and de Meester (Ref. 2).

the {10̄12}, {11̄21} and {11̄22} planes increase with temperature, whereas those for {10̄11} twinning decrease. Paton and Backofen (Ref. 46) proposed that the increase in stress for twinning with temperature was in accord with the concept that slip is a prerequisite for twinning (Refs. 328-331). With increase in temperature, cross slip and climb are facilitated and the effectiveness of stress concentrations which nucleate twinning are thereby reduced. They further proposed that the transition from {11̄22} twinning to {10̄11} results because the stress for the nucleation of {11̄22} twins continues to rise with temperature until it exceeds the

stress for $\{10\bar{1}1\}$ twinning.

The large yield stress drops which were observed in compression for $\{11\bar{2}2\}$ (Ref. 46) and $\{10\bar{1}2\}$ (Ref. 158) twinning and in tension for $\{11\bar{2}1\}$ (Ref. 143) twinning indicate that the nucleation of twins was more difficult than their growth and provide additional support that slip may be a pre-requisite for twinning on these planes. Also, the fact that the tendency for twinning in polycrystalline titanium decreases with increase in interstitial solute content and decrease in grain size suggests that slip may be important in the nucleation of twins, since dislocation motion is impeded by both impurities and a decrease in grain size. The decrease in stress with temperature for the $\{10\bar{1}1\}$ twins in Fig. 5.39 is then interpreted to mean that twin nucleation no longer controls the yield stress in this temperature range (Ref. 46).

Based on results obtained on specially oriented single crystals deformed in uniaxial tension led Akhtar (Ref. 143) to conclude that slip is not a prerequisite for $\{10\bar{1}2\}$ twinning even at low temperatures. Further, in contrast to the results of Fujishiro and Edington (Ref. 158) in compression, he found that the yield stress at which $\{10\bar{1}2\}$ twinning occurred decreased with increase in temperature, Fig. 5.40.

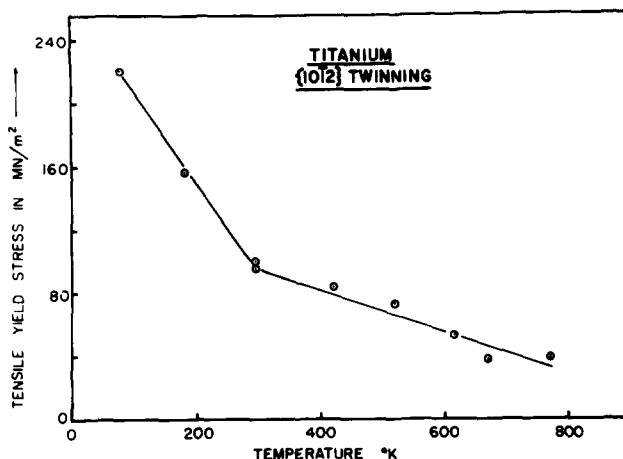


Fig. 5.40 Tensile yield stress versus temperature for titanium crystals which exhibited $\{10\bar{1}2\}$ twinning. From Akhtar (Ref. 143).

Akhtar (Ref. 143) concluded from his results in uniaxial tension that a critical resolved shear stress law did not hold for twinning on the $\{10\bar{1}2\}$ and the $\{11\bar{2}1\}$ planes in titanium. Similarly, Fujishiro and Edington (Ref. 158) concluded that a critical resolved shear stress law did not apply to the $\{10\bar{1}2\}$, $\{11\bar{2}1\}$ and $\{11\bar{2}2\}$ modes in compression. As pointed out by Cahn (Ref. 329), a critical resolved shear stress for twinning is not expected, because the macroscopic twinning stress will depend upon the exact nature of the dislocation arrays which provide the stress concentration leading to the nucleation of twins.

Other considerations pertaining to $<\text{c+a}>$ slip and to twinning in titanium are found in Refs. 30, 41, 56, 332 - 334.

5.1.6 Plastic Deformation of Polycrystals

Active Deformation Modes:

As mentioned above in Section 5.1.2 the deformation kinetics of polycrystalline titanium specimens are in agreement with those for prism glide in single crystals, indicating that the rate controlling process is associated with the motion of prism glide dislocations. Further, agreement between the tensile yield stress and the CRSS for prism glide occurs for a Taylor orientation factor $M = 2.5$, this value being in reasonable accord with that expected from the texture of the polycrystalline specimens.

Direct evidence that the active primary slip system during the plastic deformation of polycrystalline titanium sheet (~0.3 at.% C+N+O) is prism glide has been presented by Scheckman and Brandon (Ref. 42), who investigated the active slip systems in cold rolled and annealed sheet by TEM. The secondary slip systems observed by them were either prismatic or first order pyramidal; basal slip was rarely observed. Although $\langle c+a \rangle$ slip occurred to a limited extent, they concluded that this system did not play a significant role in the plastic deformation of titanium sheet at room temperature. The operative slip modes were in accord with these expected based on the CRSS values and the texture of the sheet. However, gross plastic deformation could only occur in grains containing favorably oriented prism planes by the development of pile-ups at stresses well above the CRSS. In other grains, they proposed that twinning may be responsible for the plastic deformation and provides a plastic shear component perpendicular to the basal plane.

Results and conclusions similar to those of Scheckman and Brandon (Ref. 42) were reported by Conrad, Okazaki, Gadgil and Jon (Ref. 169) and by Williams, Sommer and Tung (Ref. 196). In addition, these investigators found that the prism dislocations became more restricted to their glide plane, i.e. cross slip became more difficult, as the total interstitial content of the specimen was increased. Also, the frequency of twinning decreased with increase in interstitial content.

That twinning in titanium provides for a shear component out of the basal plane had also been recognized by Kocks and Westlake (Ref. 335), who pointed out the importance of twinning in titanium and other CPH metals in meeting the von Mises criterion that five independent deformation modes must be available to insure compatibility between the macroscopic strains in adjacent grains (Ref. 336-340). Experimental evidence that twinning in titanium provides a deformation mode with a shear component normal to the basal plane is provided by the results of Lii, Ramachardron and Reed-Hill (Ref. 182), who found that the cross section of specimens became less elliptical as the deformation temperature was decreased; see Fig. 4.47. Along with the change from elliptical to circular cross section there occurred a significant increase in the volume fraction of twins. In addition to the direct contribution to plastic deformation made by the twinning shear, twinning can play an important role by reorienting grains which are unfavorably oriented for slip into a more favorable position (Ref. 341). As pointed in Section 4.2.2, the twinning modes observed during the tensile deformation of titanium polycrystals of ~20 μm grain size include $\{10\bar{1}2\}$, $\{11\bar{2}2\}$ and $\{11\bar{2}4\}$. In coarse-grained (2-6 mm dia.) specimens the $\{11\bar{2}1\}$ mode was also noted (Ref. 155).

Finally, it should be mentioned that based on an analysis of textures in titanium, Williams and Eppelsheimer (Ref. 164) concluded that $\{0001\}$ slip, $\{10\bar{1}2\}$ and $\{11\bar{2}2\}$ twinning occur at approximately equal critical resolved shear stresses, with slip on $\{10\bar{1}0\}$ and $\{10\bar{1}1\}$ occurring at higher critical stresses. Also, rolling textures in titanium and zirconium could be accounted for if $\{11\bar{2}3\}$ slip was permitted to occur (Ref. 342).

Dislocation Multiplication and Structure:

A detailed study of the multiplication and structure of dislocations in deformed polycrystalline titanium wire specimens was carried out by Conrad and coworkers (Refs. 169, 246, 247) using TEM. In the early work by Jones and Conrad (Ref. 246), the observed increase in dislocation density ρ with strain ϵ for specimens deformed at 300K was construed to consist of two linear regions (see Fig. 5.41), an initial region of high slope ($\sim 15 \times 10^{11} \text{ cm}^{-2}$) which occurred up to a strain of 1-2%, followed by a second region whose slope was about an order of magnitude smaller. The initial region (Stage I) was in general characterized by nonhomogeneous groups or bands of dislocations within the grains (see, for example, Figs. 4.53b and c, 5.42, 5.43a and 5.44a); whereas in Stage II the dislocations were more homogeneously distributed throughout the grains (Figs. 4.53d, 5.43c and d, and 5.44c and d). However, the transition between the two stages was not always sharply defined by clear differences in dislocation structure throughout the entire specimen. An increase in interstitial content led to a higher value of ρ at which Stage II began and produced an increase in the slope of this stage; also the transition from the first to the second stage occurred more abruptly. A decrease in grain size caused effects similar to those for an increase in interstitial content, except that the slope of the second stage was not as markedly affected.

A single linear increase in dislocation density with strain was reported by Biwas, Cohen and Breedis (Ref. 343) for A-50 (~0.5at.% O_{eq}) and A-70 (~1.0at.% O_{eq}) titanium specimens (grain size estimated to be 30 and 25μm respectively) deformed at room temperature. The slopes of the straight lines yielded $1.7 \times 10^{11} \text{ cm}^{-2}$ and $1.9 \times 10^{11} \text{ cm}^{-2}$ respectively for the dislocation multiplication coefficients in the two materials. These values of $d\rho/d\epsilon$ are similar to those for the second stage in Fig. 5.41, suggesting that the results by Biwas, Cohen and Breedis probably refer to this stage of dislocation multiplication in titanium. Worthy of note is that the dislocation multiplication coefficients for Stage II in titanium are similar in value to those reported for the deformation of FCC and BCC polycrystalline metals (Ref. 344-348).

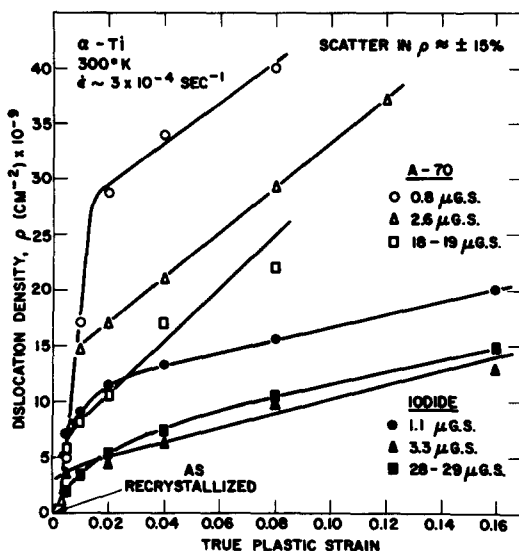


Fig. 5.41 Dislocation density versus strain for A-70 titanium (~lat.% O_{eq}) and iodide titanium (~0.1 at.% O_{eq}) specimens of different grains sizes deformed at room temperature. From Jones and Conrad (Ref. 246).

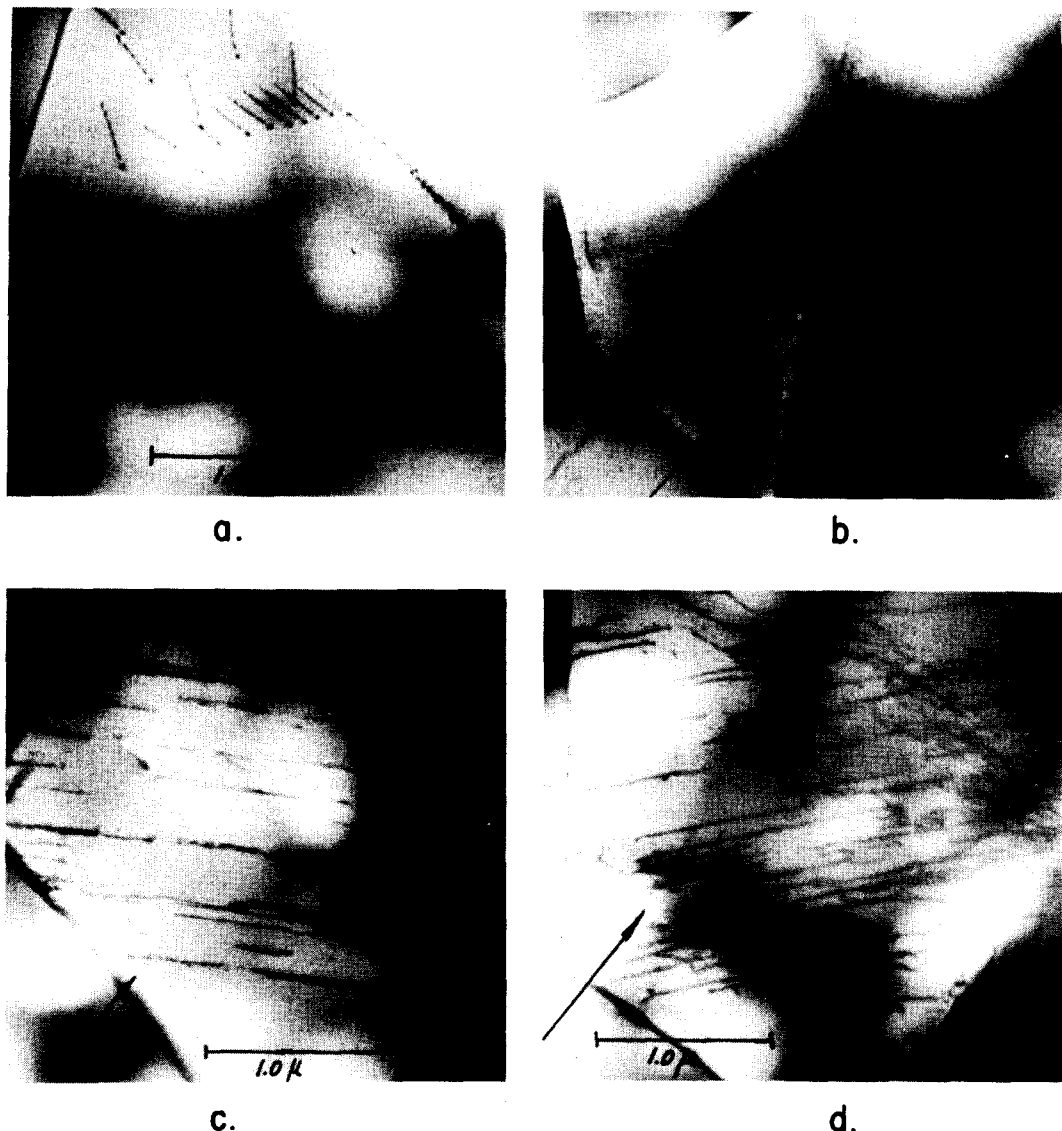


Fig. 5.42 Dislocation structures in A-70 titanium of $2.6\mu\text{m}$ grain size deformed to indicated strains at room temperature: (a) $\epsilon=0.003$, (b) $\epsilon=0.003$, (c) $\epsilon=0.0065$ and (d) $\epsilon=0.0065$. From Jones, Cooke, Conrad and Banerjee (Ref. 261).

In later work, Conrad and coworkers (Refs. 169,247) considered the ρ versus ϵ curves to be parabolic in form, Figs. 5.45 and 5.46. In these plots the dislocation density for a given strain increases with decrease in grain size and with increase in interstitial content over the entire strain range considered. Approximately linear relationships were found to apply to the results of Figs. 5.45 and 5.46 and those of Fig. 5.41 when $\rho^{1/2}$ was plotted separately versus $\epsilon^{1/2}$, $d^{-1/2}$ or $C_i^{1/2}$, while maintaining the other two parameters constant (Refs. 169,246). The combined effect of these three variables could be described by the empirical relation

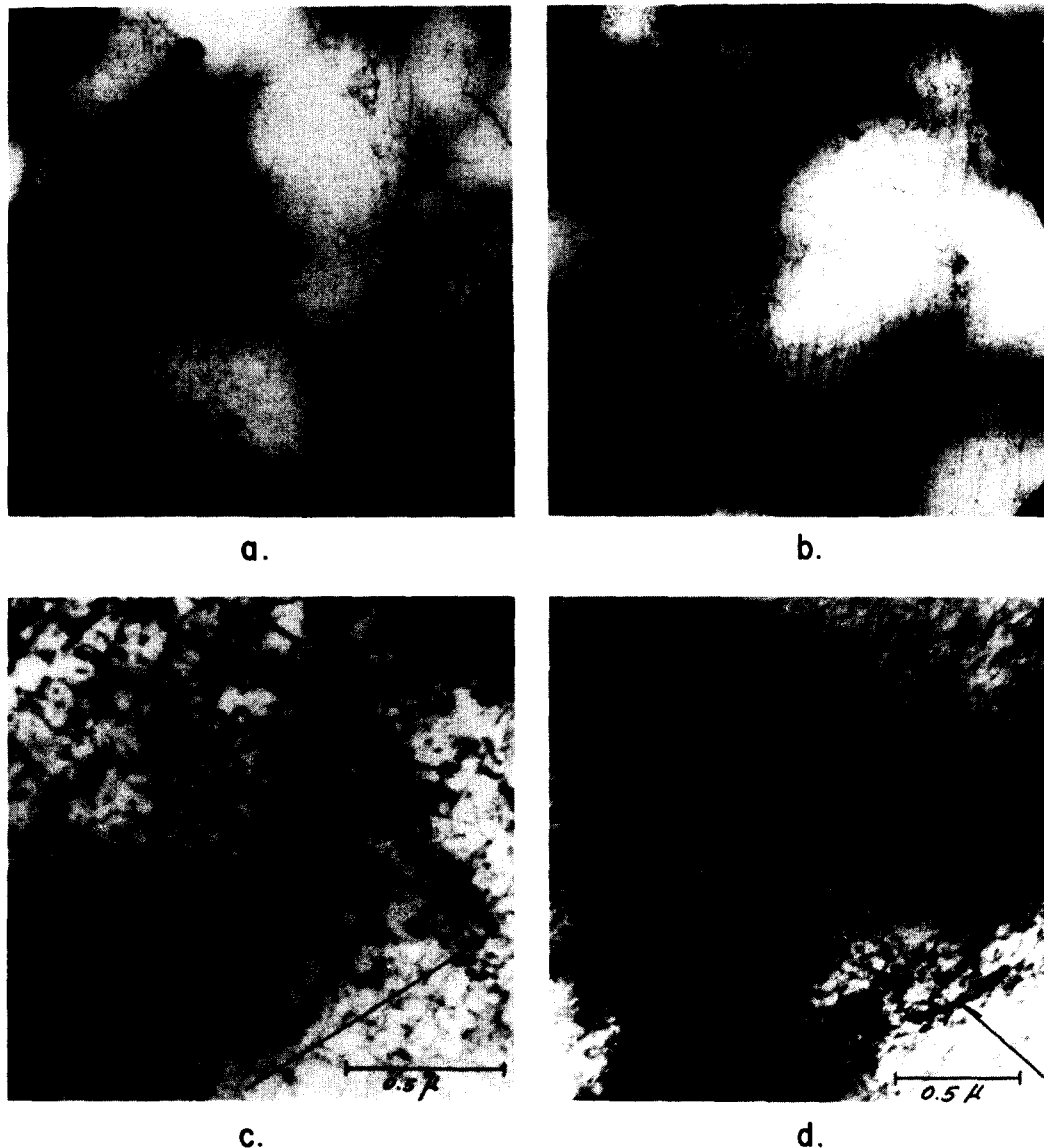


Fig. 5.43 Dislocation structures in A-70 titanium of $2.6\mu\text{m}$ grain size deformed to indicated strains at room temperature: (a) $\epsilon=0.01$, (b) $\epsilon=0.02$, (c) $\epsilon=0.04$ and (d) $\epsilon=0.08$. From Jones, Cooke, Conrad and Banerjie (Ref. 261).

given above in Section 4.2.2, namely (Ref. 246)

$$\rho^{\frac{1}{2}} = A\mu^{\frac{1}{2}}[1+7C_j^{\frac{1}{2}}] [3 \times 10^2 \epsilon^{\frac{1}{2}} + Bd^{-\frac{1}{2}}], \text{cm}^{-1} \quad (4.11)$$

where A and B are constants equal to approximately one and have units of $\text{Kg}^{-\frac{1}{2}}$ and $\text{cm}^{\frac{1}{2}}$ respectively, $\mu (=C_{66})$ is in units of Kg/cm^2 , C_j in atomic fraction and d in cm.



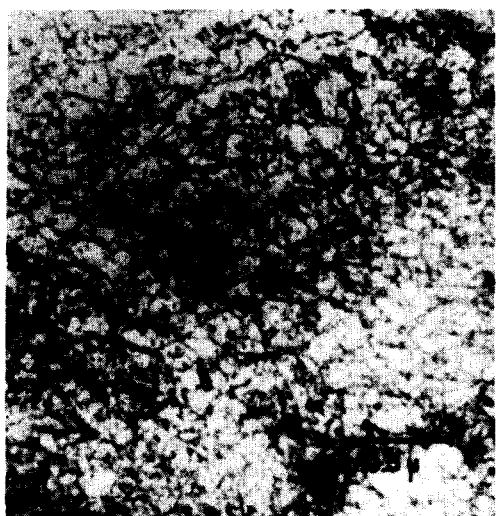
a.



b.



c.



d.

Fig. 5.44 Dislocation structures in A-70 titanium of $18\mu\text{m}$ grain size deformed to indicated strains at room temperature:
(a) $\epsilon=0.005$, (b) $\epsilon=0.01$, (c) $\epsilon=0.02$, (d) $\epsilon=0.04$. From Jones,
Cooke, Conrad and Benerjee (Ref. 261).

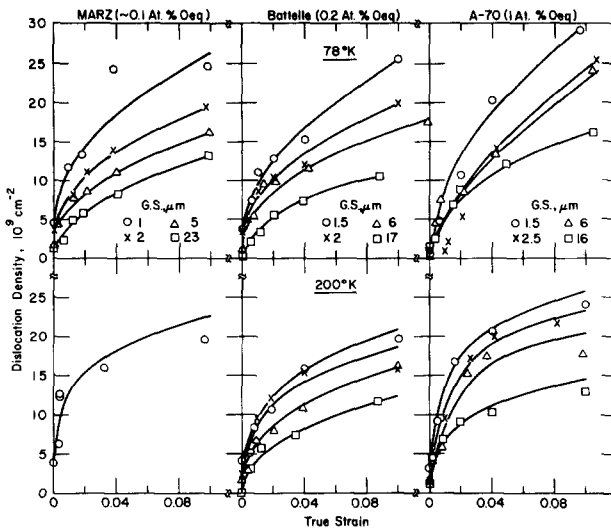


Fig. 5.45 Dislocation density versus strain for MARZ, Battelle and A-70 titanium specimens of various grain sizes deformed at 78 and 200K. From Conrad, Okazaki, Gadgil and Jon (Ref. 169).

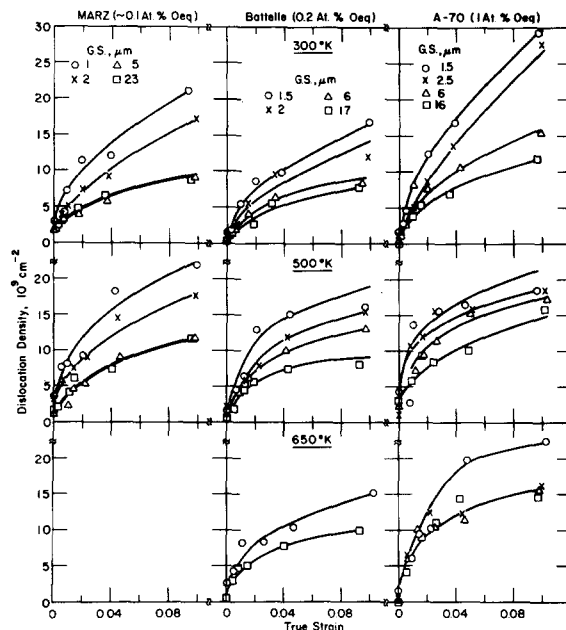


Fig. 5.46 Dislocation density versus strain for MARZ, Battelle and A-70 titanium specimens of various grain sizes deformed at 300, 500 and 650K. From Conrad, Okazaki, Gadgil and Jon (Ref. 169).

Some theoretical models for dislocation multiplication are listed in Table 5.14. One way of comparing the experimental results for titanium with these models is to consider how $d\rho/d\varepsilon$ varies with ρ . Plots of $d\rho/d\varepsilon$ versus ρ for Battelle and A-70 titanium with two extremes in grain size deformed at room temperature (derived from the curves in Fig. 5.46) are presented in Fig. 5.47.

TABLE 5.14 Theoretical Models for Dislocation Multiplication.

Author	Relation	Comment
Gilman [†]	(a). $\rho = Ae^{\frac{1}{2}}$ $A = 2K/b\bar{v}^{\frac{1}{2}}$ $K = d\rho/dt$ \bar{v} = average dislocation velocity.	Fixed concentration of sources.
	(b). $\rho = \rho_0 + M\varepsilon$ $M = m/b$ m = multiplication coefficient	Multiplication by double cross-slip.
Bergstrom ⁺⁺	$\frac{d\rho}{d\varepsilon} = U(\varepsilon) - A - \Omega\rho$ $\rho = \frac{U-A}{\Omega} (1-e^{-\Omega\varepsilon}) + \rho_0 e^{-\Omega\varepsilon}$ U = rate of increase of mobile dislocation density by creation and/or remobilization A = rate of annihilation of mobile dislocations Ω = the probability of remobilization and annihilation through reactions between mobile and immobile dislocations	Total dislocation density with strain due to four processes: (a) creation, (b) immobilization, (e) remobilization and (d) annihilation of dislocations. Mobile dislocation density does not vary with strain
	$\rho = \rho_0 + (U-A)\varepsilon$	For small values of the product $\Omega\varepsilon$

Notes:

[†] John J. Gilman, Micromechanics of Flow in Solids, McGraw-Hill, New York (1969).
⁺⁺ Y. Bergstrom, Mat. Sci. Eng. 5 193 (1969/70).

Considered in this way, the experimental results do not strictly conform to either Gilman's (Ref. 348) double cross-slip model or to Bergstrom's (Ref. 349) model with U and Ω independent of strain. On the other hand, log-log plots of $d\rho/d\varepsilon$ versus ρ (Fig. 5.48) can be considered to yield straight lines of unit negative slope giving

$$d\rho/d\varepsilon \approx A/\rho \quad (5.51)$$

which upon integration yields

$$\rho^2 = \rho_0^2 + 2A\varepsilon \quad (5.52)$$

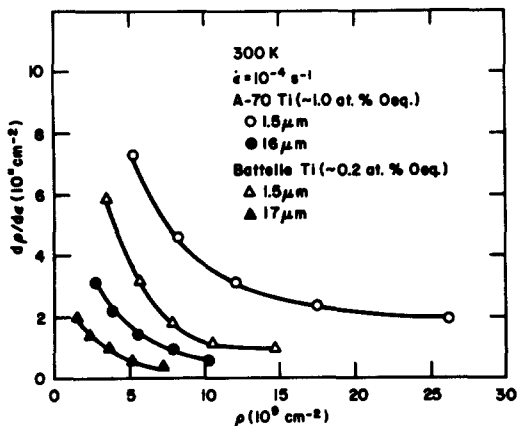


Fig. 5.47 $d\rho/d\epsilon$ versus ρ for Battelle and A-70 titanium with two extremes in grain size deformed at 300K (taken from curves in Fig. 5.46).

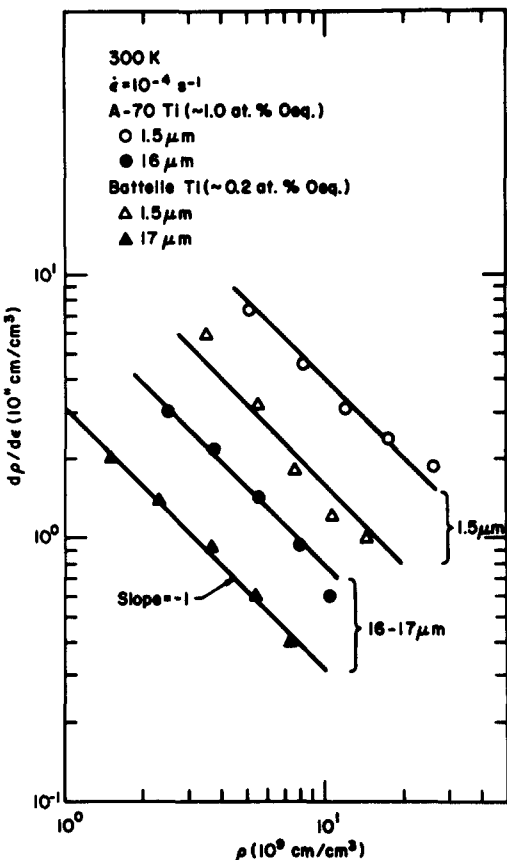


Fig. 5.48 Log-log plots of $d\rho/d\epsilon$ versus ρ for Battelle and A-70 titanium with two extremes in grain size deformed at 300K (taken from the curves in Fig. 5.46).

where ρ_0 is the initial dislocation density and $2A$ represents the multiplication coefficient. For small values of ρ_0 , Eq. 5.52 reduces to Gilman's model (Ref. 348) based on a fixed number of sources (his model (a) in Table 5.14).

In view of the scatter normally associated with dislocation density measurements by TEM, one may well question the specific curves drawn through the ρ versus ϵ data points in Figs. 5.45 and 5.46 and in turn relationships and conclusions based on the slopes desired therefrom. If we consider the ρ versus ϵ curves to consist of two linear regions as in Fig. 5.41, then the second region would yield

$$\rho = \rho_0 + A\epsilon \quad (5.53)$$

in keeping with Bergstrom's model for small values of $\Omega\epsilon$ and the multiplication of dislocations by the double cross-slip mechanism (Refs. 348, 350, 351). This mechanism is generally considered to be operative in FCC and BCC metals and one expects that it might also occur in CPH metals, especially since the dislocation multiplication coefficients have similar values. Further, the "cell-type" dislocation tangle structure observed in titanium (Figs. 4.53, 4.91, 4.92, 5.49), which becomes more pronounced with increase in purity and temperature is indicative of cross-slip activity, supporting the double cross-slip multiplication mechanism.

That Bergstrom's model may describe dislocation multiplication in deformed titanium is suggested by the results of Okazaki, Masuda and Conrad (Ref. 352). These authors assumed that the dislocation density as a function of strain was given by Bergstrom's relation in Table 5.14 and then calculated the parameters therein by matching with the aid of a computer the experimental stress-strain curves with the well known expression for strain hardening

$$\sigma = \sigma_f + \alpha \mu b \rho^{\frac{1}{2}} \quad (5.54)$$

where σ_f is the resistance to dislocation motion by all obstacles other than dislocations, α a constant (of the order of 2 for Ti) and μ the shear modulus. The values of the dislocation multiplication parameters so derived for a Ti-0.25 at.% alloy are presented in Table 5.15. They are in accord with those obtained directly from dislocation measurements on BCC and FCC metals by Bergstrom and co-workers (Refs. 349, 353-355) and yield dislocation densities as a function of strain for titanium which are in reasonable accord with those determined by TEM given in Figs. 5.41, 5.45 and 5.46. Further, the derived values of σ_f are in reasonable accord with those expected for this titanium-interstitial alloy ($O+N+C \approx 0.3$ at. %), assuming $\sigma_f \approx \sigma_i(0.2\%) \approx \sigma^*$; see Figs. 4.75, 4.79 and 4.95. Employing this approach on a number of Ti-C, Ti-N and Ti-O alloys of varying grain size and interstitial content tested at 200-500K, Okazaki, Masuda and Conrad (Ref. 352) found that (U-A) increased approximately linearly with interstitial content and with the reciprocal of the grain size relatively independent of temperature, in reasonable accord with the TEM measurements. The parameter Ω was found to be proportional to the square root of the temperature, the proportionality constant A varying as the square root of the interstitial content in the order $A/\sqrt{C}: A/\sqrt{O}: A/\sqrt{N} = 0.8:1.0:1.4$.

Assuming that dislocation multiplication in titanium occurs by the double cross-slip mechanism, Conrad and Okazaki (Ref. 247) proposed that the increase in dislocation density resulting from an increase in interstitial content was due to the increased tendency for dislocations to be deflected out of their slip planes by the interstitial atom obstacles. They argued that the higher the density of internal stress centers, the greater is the probability that a dislocation will leave its slip plane. Further, they proposed that the probability p that a dislocation will leave its slip plane is inversely proportional to the square of the wave length λ of the long-range internal stress field associated with the interstitial solutes, so that

$$p = A/\lambda^2 \quad (5.55)$$



Fig. 5.49 Cell-type dislocation structure in Battelle titanium (~0.2at.% O_{eq.}) of 16μm grain size deformed to $\epsilon=0.09$ at room temperature.

where A is a constant. If solute atoms from neighboring planes contribute to the long-range stress, $\lambda = bC_i^{1/3}$; whereas if only solute atoms in the slip plane are responsible, then $\lambda=b/C_i^{1/2}$. Inserting these relationships for λ into Eq. 5.54 gives for the effect of interstitial concentration on the dislocation density

$$\rho = BC_i^{2/3} \quad (5.56)$$

or

$$\rho = B'C_i \quad (5.57)$$

where B and B' are constants. The experimentally observed effect of interstitial content on the dislocation density in titanium (e.g. Eq. 4.11) is in reasonable accord with Eq. 5.57. However, to fully account for the effect of interstitial solutes on dislocation density by the double cross slip mechanism, one must also take into consideration the fact that the stacking fault energy decreases with increase in interstitial content (Refs. 343,356), which in turn makes cross slip more difficult. Hence, if the above mechanism for the increase in dislocation density with interstitial content applies, then the deflection of dislocations out of the glide plane by the interstitial solutes must have a greater effect on dislocation multiplication than the increased difficulty of cross slip resulting from a lower stacking fault energy.

TABLE 5.15 Values of the Bergstrom Dislocation Multiplication Parameters for a Ti-0.25 at.% O Alloy . From Okazaki, Masuda and Conrad (Ref. 358).

T (K)	G.S. (μm)	U-A (10^{11}cm^{-2})	Ω	ρ_0 (10^8cm^{-2})	σ_f (MN/m 2)
200	2	1.30	3.1	1.9	262
	4	1.23		2.3	253
	15	0.80		3.0	232
300	2	1.16	3.8	2.8	214
	4	0.86		1.9	198
	15	0.44		2.3	179
400	2	1.30	4.4	1.4	160
	4	0.88		1.8	149
	15	0.51		2.7	123
500	2	1.81	4.9	1.0	97
	4	1.12		1.3	92
	15	0.52		1.5	78

Another way in which interstitial solutes might affect the dislocation density is through the average distance \bar{s} which dislocations move before becoming entangled and immobilized, rather than on an increased tendency for cross slip. Starting with the relation for the strain due to dislocation motion

$$\epsilon = \rho b \bar{s} \quad (5.58)$$

one obtains upon rearranging

$$\rho = \epsilon / b \bar{s} \quad (5.58a)$$

Assuming \bar{s} to be proportional to the square of the wave length of the internal stress centers due to interstitial solutes gives

$$\rho = A \epsilon C_i \quad (5.59)$$

which is also in qualitative accord with experimental results. Further, as pointed out by Conrad (Refs. 357-360) one might expect on geometrical grounds for \bar{s} to be proportional to the grain size as well. The effect of grain size d on the dislocation density would then be given by

$$\rho = B \epsilon / bd \quad (5.60)$$

where B is a constant. Again, Eq. 5.60 is in qualitative accord with the experimentally observed effect of grain size on dislocation density. This model for the effect of grain size on the dislocation density is illustrated in Fig. 5.50. Since the multiplication parameter U in Bergstrom's (Ref. 349) model is inversely proportional to \bar{s} , the above considerations yield U proportional to the interstitial content and to the reciprocal of the grain size, in keeping with the

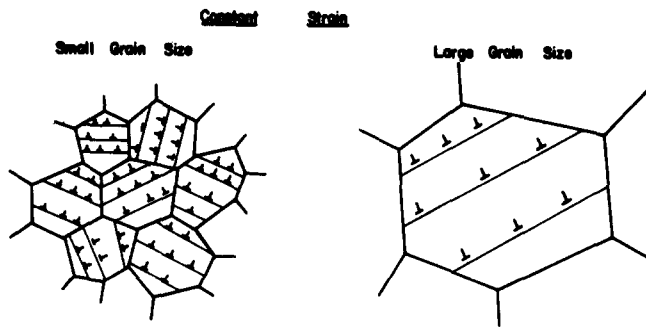


Fig. 5.50 Schematic for the effect of grain size on the dislocation density through the effect on the average slip distance. From Conrad (Ref. 360).

results of Okazaki, Masuda and Conrad (Ref. 352).

In addition to their influence on the free slip distance, grain boundaries in titanium can act as dislocation sources; see, for example, Figs. 4.99 and 5.51. As pointed out by Li (Ref. 361) grain boundary ledges can act as donors of dislocations in the manner illustrated in Fig. 5.52. The dislocation density resulting from such ledges has been calculated by Li to be

$$\rho = 8m/\pi d \quad (5.61)$$

where m is the grain boundary ledge density (number per unit length or length per unit area). The grain size dependence of ρ given by Eq. 5.61 is again in keeping with that observed.

A third way in which the grain size can influence the dislocation density has been pointed out by Ashby (Ref. 362); see Fig. 5.53. Illustrated here is that additional dislocations are needed to correct for the voids or overlaps which would otherwise occur when the individual grains deform according to their respective slip systems. These dislocations provide for compatibility of the deforming grains and are termed geometric dislocations to distinguish them from those which are statistically stored within the grains. Ashby calculated the density of the geometric dislocations to be

$$\rho^g = \epsilon/4bd \quad (5.62)$$

According to Ashby the statistically stored dislocation density ρ^s would be that of an "equivalent single crystal"; i.e. a single crystal so oriented that it deforms on the same slip systems as the grain under consideration. The total dislocation density would then be the sum of ρ^g and ρ^s . Ashby proposed that ρ^g would dominate at small strains leading to a dislocation density which is directly proportional to the strain and inversely proportional to the grain size.

Expanding on Ashby's model, it is here proposed that there may also occur an effect of grain size on ρ^s through its effect on the free slip length as discussed above (Eq. 5.60). The total dislocation density is then given by

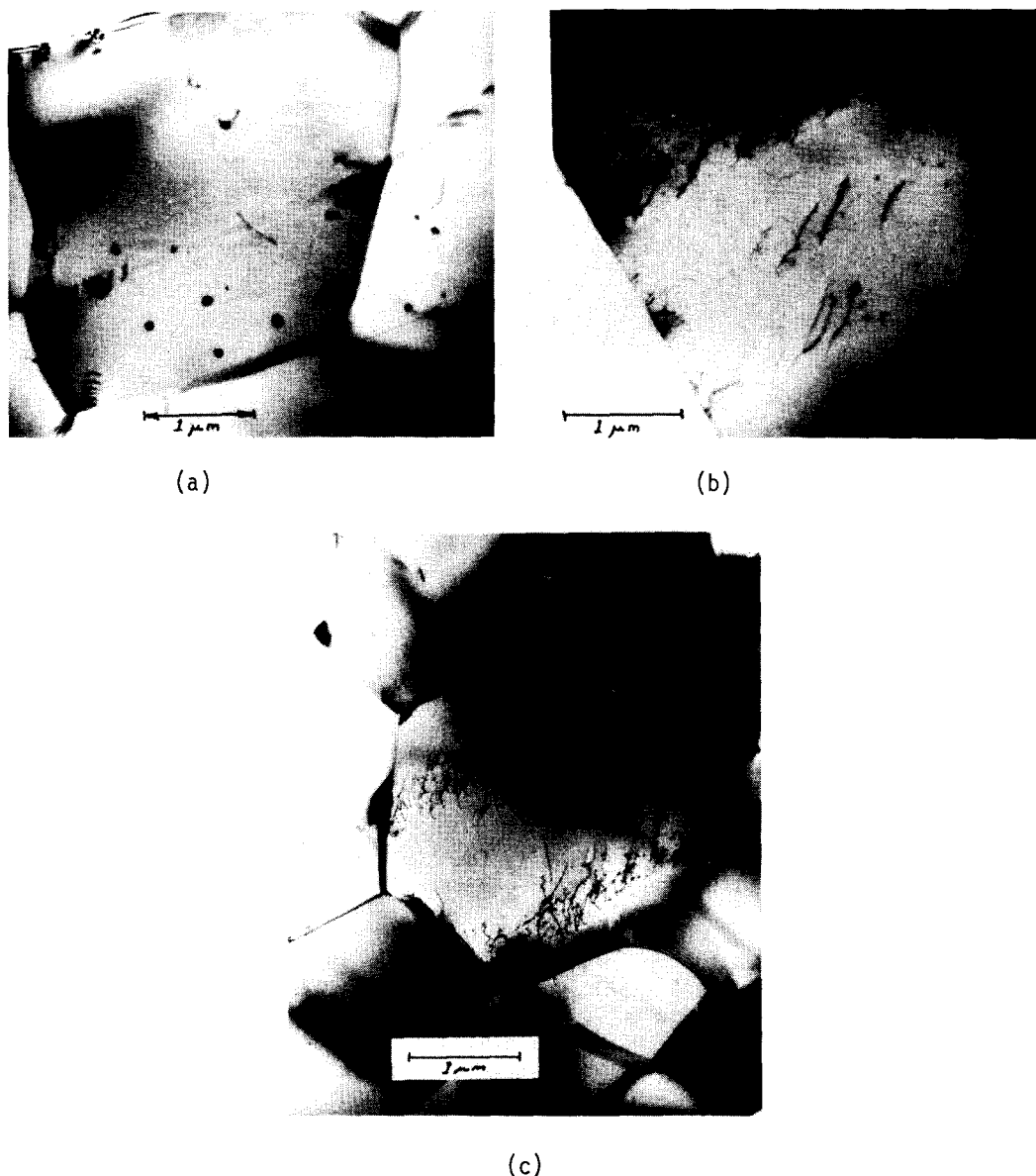


Fig. 5.51 Dislocations emanating from grain boundaries in A-70 Ti deformed to $\epsilon=0.002$: (a) $1.5\mu\text{m}$ grain size deformed at 500K (b) $6\mu\text{m}$ grain size deformed at 78K (c) $2.5\mu\text{m}$ grain size deformed at 200K.

$$\rho = \rho^g + \rho^s = \epsilon/4bd + B\epsilon/bd \quad (5.63)$$

$$= B'\epsilon/bd \quad (5.63a)$$

The inverse grain size effect on dislocation density would then apply to larger strains than expected on the basis of ρ^g alone, in accord with experimental observations.

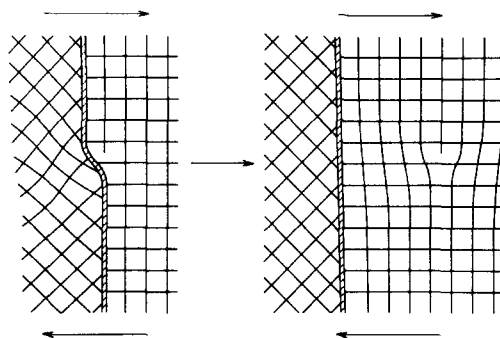


Fig. 5.52 Grain boundary ledge acting as a donor of a dislocation. From Li (Ref. 360).

It is now clear that the multiplication of dislocations in titanium is governed primarily by the strain and grain size, with lesser influence of the total stress or temperature (and presumably the strain rate). However, the mechanisms by which dislocation multiplication occurs in deformed titanium have yet to be positively identified. The double cross-slip mechanism appears to be the most likely mechanism at strains greater than about 1%. Grain boundary ledges could be an important source for dislocations at small strains. The observed increase in dislocation density with decrease in grain size probably arises from all three of the causes considered: (a) an increase in the number of grain boundary ledges, (b) an increase in the number of geometric dislocations required for compatibility of the deformed grains and (c) a decrease in the free slip distance. The first two are probably dominant at small strains ($\epsilon < \sim 1\%$), whereas the third at larger strains. The increase in dislocation density with interstitial content seems to be due to the effect of interstitials on the free slip distance.

Conrad, Okazaki, Gadgil and Jon (Ref. 169) interpreted the effects of strain and grain size on dislocation multiplication in titanium by considering the three terms which result upon squaring Eq. 4.11 to give

$$\rho = \alpha^2 \epsilon + 2\alpha\beta\epsilon^{1/2} d^{-1/2} + \beta^2 d^{-1} \quad (4.11a)$$

where α and β are constants which depend on the interstitial content. They considered the first term on the right side of Eq. 4.11a to refer to the multiplication of dislocations in single crystals, the last term to the multiplication at small strains and the middle term to the combined effect of strain and grain size. Good agreement was obtained between α^2 determined from dislocation density measurements on titanium single crystals by Cass (Ref. 45) and that derived from the measurements on polycrystalline specimens. Assuming that the third term represented the generation of dislocations from grain boundary ledges, they obtained using Eq. 5.61 ledge densities of $\sim 10^5 \text{ cm}^{-1}$, which are reasonable. To obtain agreement between the middle term and the effects of grain size given by Eqs. 5.60 to 5.63a, they had to make the additional arbitrary assumption that the constant B (or B') in these equations was proportional to the dislocation density. They suggested that an effect of dislocation density on B might arise from an increase in the average free slip length resulting from the higher long-range interval stress which occurs with increase in the dislocation density. Another possibility is that the free slip length, or the density of geometric dislocations, is not simply proportional

to grain size, but depend on ϵ and d in a more complicated manner. For example, agreement with the middle term of Eq. 4.11a occurs if the constant B' of Eq. 5.63a is proportional to $(d/\epsilon)^{1/2}$.

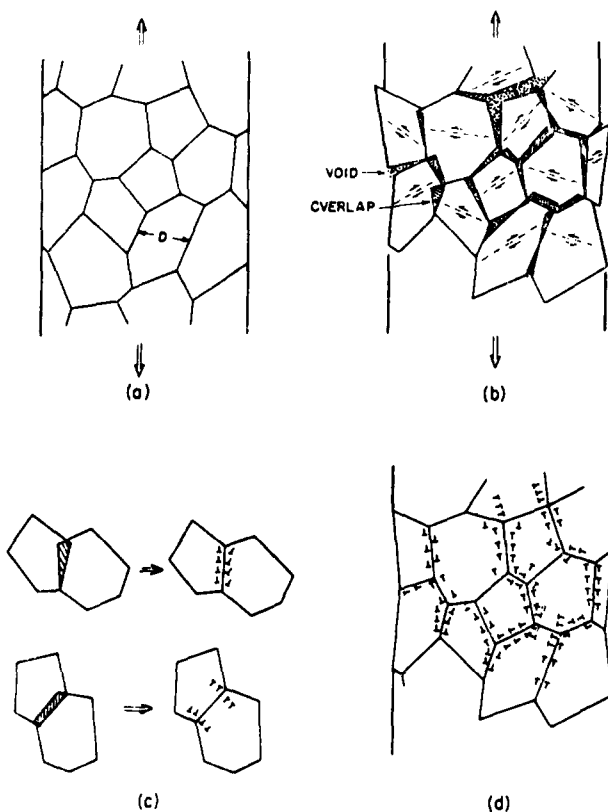


Fig. 5.53 Model illustrating the need for geometric dislocations in the plastic deformation of polycrystals: (a) each grain deforms in a uniform manner, (b) overlap and voids appear, (c) and (d) these are corrected by introducing geometrically-necessary dislocations. From Ashby (Ref. 362).

Considering the dislocation structure, it is now clear that interstitial solutes and temperature have a marked effect on the arrangement of dislocations in deformed titanium. In high purity titanium ($<~0.2$ at.% C), the dislocation structure changes with strain from randomly distributed dislocations or groups of dislocations to tangles and ultimately to a cellular-type network, which is similar to that found in FCC and BCC metals. The cellular network develops at smaller strains and becomes more pronounced as the deformation temperature is increased. With increase in interstitial content the dislocations become more planar, with long, straight, parallel screw dislocations on the prism planes being observed at small strains for interstitial contents $>~0.5$ at.%. With increase in strain the dislocations in these higher interstitial content materials become entangled leading eventually to a fine network of intertwined dislocations, which develops into a cellular-type network at temperatures above 300K. The strain and temperature

at which the cellular network appears increases with increase in interstitial content.

Two explanations have been given for the planar arrangement of dislocations observed for the higher interstitial contents (mainly oxygen). Williams, Sommer and Tung (Ref. 196) suggest that this dislocation structure results because of short range ordering of the interstitial solutes, which precedes the longer range order found in more concentrated Ti-O solid solutions (Ref. 11). On the other hand, Biwas (Ref. 363) and Biwas, Cohen and Breedis (Ref. 343) attribute the long, straight, parallel screw dislocations in the prism planes to: (a) an increasing drag force due to interstitial solutes on the screw dislocations compared to edge dislocations and (b) an increased difficulty for cross-slip between the prism and basal planes because of a lower stacking fault energy and/or a higher friction stress on the basal plane due to the solutes. In high purity titanium, cross slip from the prism planes to the basal planes and back again to the prism planes occurs readily. This leads to the formation of edge dislocation dipoles, which pin the glide dislocations thereby producing tangles and eventually cell walls.

Considering cross slip in titanium, Biwas (Ref. 363) deduced that dislocations can dissociate most readily on basal planes, to a lesser extent on prism planes and not at all on pyramidal planes. He proposed that on the basal planes they dissociate into $1/9[1\bar{1}\bar{2}0]$ and $2/9[\bar{1}1\bar{2}0]$ partials. The partials on the prism plane recombine for cross slip onto the basal plane, where dissociation into Shockley partials is considered to occur immediately. The Shockley partials must then coalesce before the dislocation can return to the prism plane for its continued motion.

Whether the difficulty of cross slip between the prism and basal planes in titanium is in fact mainly due to the dissociation of the dislocations on the basal planes as proposed by Biwas (Ref. 363) or results from their greater dissociation on the prism planes as suggested by the work of Aldinger (Ref. 317) is not clear.

Yield Point:

Although dislocation pile-ups are observed to occur in titanium (see Figs. 4.53b and 5.51a) limited work by the present author suggests that the yield points observed in titanium-interstitial alloys (see Figs. 4.40 and 5.54) are of the Johnson-Gilman (Ref. 364) dislocation multiplication type rather than the unlocking of dislocations from a solute atmosphere proposed by Cottrell (Ref. 365). In the Johnson-Gilman model a yield point results (i.e. a sudden decrease in the flow stress occurs) when there is a rapid multiplication of dislocations so that a lower average velocity of dislocations is required to maintain the constant crosshead speed of the testing machine. Three factors favor the occurrence of such a yield point: (a) initially there should exist only a small number of dislocations which are mobile, (b) the mobile dislocation density should increase very rapidly with strain and (c) the change in stress for a given change in dislocation velocity \dot{v} (i.e. $\partial\sigma/\partial\ln\dot{v}$ or $\partial\sigma/\partial\ln\dot{\epsilon}$) should be relatively large. All three of these conditions exist when a yield point occurs in titanium.

Support for the Johnson-Gilman model for the yield point in titanium is that the yield point is most pronounced (i.e. the difference between the upper and lower yield stresses is the largest) in the temperature range where the strain rate sensitivity parameter $\partial\sigma/\partial\ln\dot{\epsilon}$ is a maximum, which is approximately 400K; see Figs. 5.54, 4.41 and 4.74. Further, the existence of a critical grain size for the occurrence of a yield point (Fig. 4.63) is consistent with the need for a high rate of dislocation multiplication. Moreover, the fact that the magnitude of the yield drop increases with increase in interstitial content at a fixed temperature (Fig. 4.63) is consistent with the larger value of $\partial\sigma/\partial\ln\dot{\epsilon}$ which results as the interstitial content is increased; see, for example, Fig. 4.74.

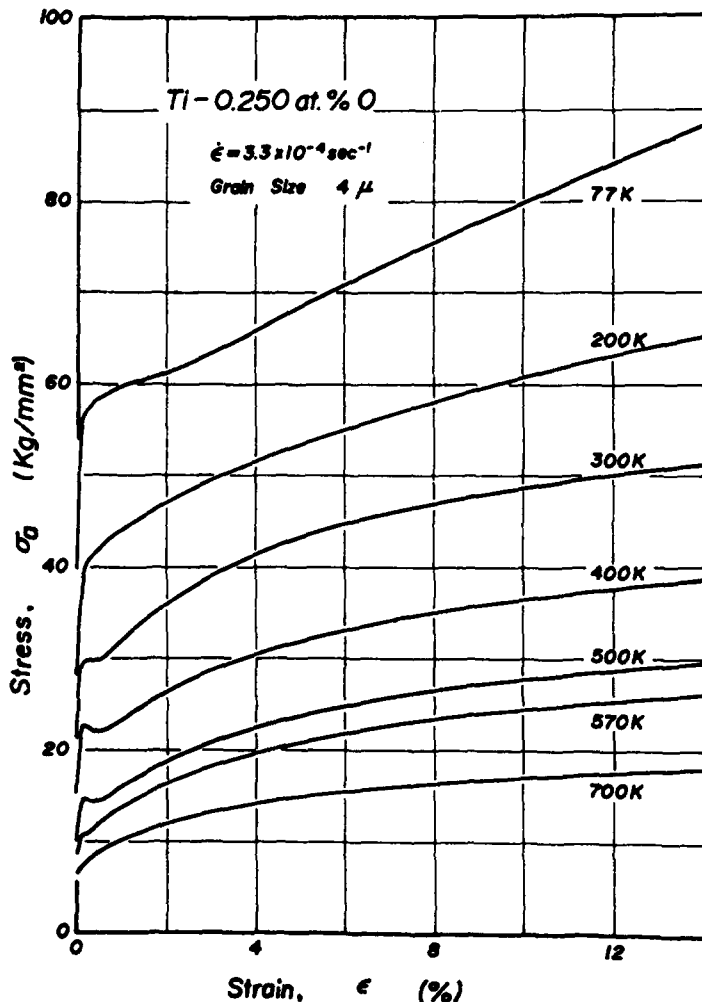


Fig. 5.54 True stress-strain curves for Ti-0.25at.% O alloy at 77-700K.
From Okazaki, Masuda and Conrad (Ref. 352).

Strain Hardening:

The works of Rosi and Perkins (Ref. 183), Wasilewski (Ref. 366) and Reed-Hill and coworkers (Refs. 171, 179, 180, 182, 194, 195, 241, 242, 273) suggest that strain hardening of titanium deformed at 77-700K may be influenced by twinning at the lower temperatures of this range and by dynamic strain aging at the higher temperatures. It has been proposed that both twinning (Refs. 194, 195) and dynamic strain aging (Refs. 171, 179, 273) lead to an increase in strain hardening. Although the influence of dynamic strain aging appears to be clear (Fig. 4.45), the effect of twinning is generally not as well defined, especially when the variations in the amount of twinning are produced by changes in temperature, grain size or interstitial content. This is because these parameters may exert an influence on strain hardening in addition to their influence on twinning, making it difficult to separate out the effects due to twinning.

It has been noted (Refs. 238, 241, 367, 368) that log-log plots of the true stress-true strain curves of polycrystalline titanium (so called Hollomon plots (Ref. 369)) often exhibit two or more linear regions or stages, suggesting that the modes or mechanisms of strain hardening are changing along the stress-strain curve. Similar behavior has been reported for zirconium (Refs. 370-373) and other metals (Refs. 374-378). However, as pointed out by Monteiro and Reed-Hill (Ref. 241), log-log plots of the strain hardening coefficient $d\sigma/d\varepsilon$ versus strain ε (i.e. so-called Crussard-Jaoul plots) should provide more sensitive indicators of any changes in the deformation behavior. As pointed out in Section 4.2.4 such Crussard-Jaoul plots for titanium (Figs. 4.89-4.92) can be considered to consist of three regions or stages. These stages appear to be characterized by specific dislocation structures: Stage I, planar, dislocations; Stage II, dislocation tangles; Stage III, a fine dislocation network or dislocation cells. The changes in the dislocation structure are however not nearly as sharply defined or abrupt as the changes in the slopes of the Crussard-Jaoul plots.

Stage I only occurs in specimens with a high interstitial content and at the lowest temperatures. As discussed above, the planar dislocation structure associated with this stage could reflect either a difficulty for cross slip or the existence of short range ordering of the interstitial solutes, the former being the more likely cause. As mentioned above, whether the difficulty of cross slip arises mainly from the dissociation of dislocations on the basal planes (Refs. 343, 363) or from their dissociation on the prism planes (Ref. 317) is not clear. An alternative, but less tenable, explanation for the planar slip is that the conditions of high interstitial content and low temperature inhibit the operation of dislocation sources within the grains or grain boundaries, thereby limiting the number of active slip planes.

Garde, Aigenthaler and Reed-Hill (Ref. 195) attribute Stage II (their Stage I) to a rapid rate of twin development with strain, i.e. to a larger value of $dV_t/d\varepsilon$, where V_t is the volume fraction of twins. However, Keshavan, Sargent and Conrad (Ref. 198) argue on the basis of an analysis of the strain due to twinning that, although twinning may have some influence on the strain hardening rate in Stage II, it is not the dominant factor. Rather, they conclude that Stage II reflects the development of the tangled dislocation structure which is observed.

Regarding Stage III, Reed-Hill and co-workers (Refs. 240, 241) attributed this stage (their Stage II) to the formation of dislocation cells. TEM observations by Keshavan, Sargent and Conrad (Refs. 238, 239) support this explanation. However, for the higher interstitial contents, the dislocation structure in specimens deformed at 300K and below has more the appearance of a fine network (Figs. 5.43d and 5.44d) than the well-defined cells commonly observed in deformed FCC and BCC metals. The fine network becomes more cellular in appearance as the temperature is increased above 300K (see, for example, Fig. 4.54).

The fact that the strain required for the beginning of Stage III decreases with increase in temperature is in keeping with the development of a dislocation network or cell structure in titanium. However, the fact that the strain also tends to decrease with increase in interstitial content (see Figs. 4.89 and 4.90 and Ref. 240) is not consistent with the decrease in stacking fault energy which occurs as the interstitial content increases (Ref. 356). Arunachalam, Pattanaik, Monteiro and Reed-Hill (Ref. 240) attributed the tendency for Stage III to occur earlier as the interstitial content was increased to: (a) an increase in $\langle c+a \rangle$ slip, (b) a change in dislocation structure from uniform to banded and (c) the suppression of twinning, all due to the increase in interstitial content. They proposed that deformation under such conditions would probably lead to a better defined "cell" structure. Further, Monteiro and Reed-Hill (Ref. 241) proposed that dynamic strain aging also influences the dislocation structure so that only a

single stage (presumably Stage III defined here) occurs for commercial titanium deformed at 400-750K.

Of interest regarding the effect of interstitials on Stage III is the work of Ramani, Mukhopadhyay, Rodrigues and Krishnan (Ref. 372) and Mannan and Rodrigues (Ref. 373) on zirconium, who noted stages similar to Stages II and III shown here for titanium (their Stages I and II); also the dislocation structures were similar. They concluded from their TEM observations that Stage III (present designation) could be attributed to the formation of a dislocation cell structure by cross slip as a dynamic recovery process. In keeping with this explanation they found that Stage III occurred at larger strains with decrease in temperature and with increase in interstitial content. The increase in strain for the beginning of Stage III with increase in interstitial content for zirconium is thus opposite to the behavior noted for titanium.

Theoretical considerations of strain hardening (Refs. 379-381) lead to the well known relation between the resolved shear stress τ and the dislocation density ρ

$$\tau = \tau_f + \alpha \mu b \rho^{\frac{1}{2}} \quad (5.64)$$

where τ_f is the resistance to dislocation motion by all obstacles other than dislocations, α a geometric constant of the order of 0.5, μ the shear modulus, and b the Burger vector. An impressive amount of data in support of Eq. 5.64 has been compiled by a number of investigators (Refs. 245, 358-360, 382-385). That the data on titanium are also in accord with this relation is shown in Figs. 4.93 and 4.94. Considering the results on titanium given in Table 4.6, the values of α' presented there are approximately equal to α of Eq. 5.64 when we take the Taylor orientation factor $M = 2.5$ and the shear modulus μ as either the polycrystalline shear modulus μ or the effective prism plane dislocation modulus $\sqrt{K_e K_s}$. Slightly larger values of α are obtained for $\mu = K_s$ and significantly smaller values for $\mu = K_e$ for the prism plane.

The values of $\alpha (= \alpha')$ from Table 4.6 range between 0.34 and 0.88 with an average of 0.67, being relatively independent of grain size, interstitial content and temperature, and in turn dislocation structure. In a separate study (Fig. 5.55), the values of α for Battelle titanium and a Ti-7.4 at.% Al alloy range between 0.6 and 0.9, again relatively independent of grain size and temperature; further they are not influenced by the aluminum addition. Biwas, Cohen and Breedis (Ref. 343) reported α values of 0.56 and 0.64 for A-50 and A-70 titanium respectively deformed at room temperature. Values of α reported for zirconium (Ref. 372) are 1.68 at 77K, 0.88 at 300K and 0.64 at 442K when M was taken to be 2.5. The large effect of temperature on α for zirconium differs from the results on titanium. Whether or not the effect of temperature on the shear modulus was taken into account in the determination of α for zirconium is not mentioned. If it was not, this could account for a significant portion of the reported temperature variation of α in this metal. The values of α for titanium and zirconium are similar in magnitude to those for FCC and BCC metals in general (Refs. 245, 358-360, 380-385), being however on the high side of those reported for the other two crystal structures.

The specific dislocation mechanism responsible for strain hardening in polycrystalline titanium at low temperatures has yet to be identified. Of significance is that the relationship between the flow stress and dislocation density for strains up to about 10% (the limit of TEM measurements) is not noticeably influenced by the dislocation structure, i.e. whether, the dislocations are planar, in tangles, in a fine network or in cells. Also, no difference is detected for those conditions where twinning or dynamic strain aging are prominent compared to when they

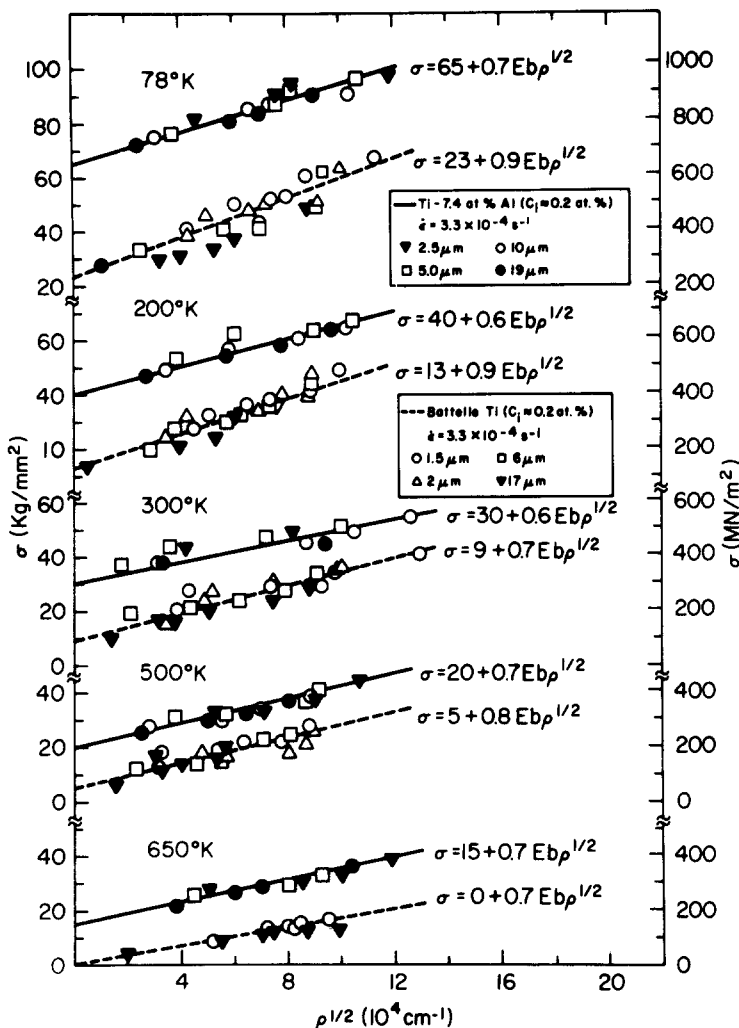


Fig. 5.55. Flow stress versus square root of dislocation density as a function of grain size and temperature for unalloyed Battelle Ti and Ti-7.4 at. % Al. From Conrad and Wang (Ref. 385).

are not. Further, as seen in Fig. 5.55, titanium alloys exhibit approximately the same value of α as unalloyed titanium of the same interstitial content, even though the dislocation structure and twinning frequency differs significantly, i.e. mainly planar dislocations and no twinning for the Ti-Al alloy compared to dislocation tangles and cells with appreciable twinning for the unalloyed Battelle titanium. The effects of temperature, strain rate and solute content (interstitial and substitutional) are thus principally through the τ_f term of Eq. 5.64. Since for the titanium-interstitial alloys $\tau_f \approx \tau^*$ and α is essentially independent of temperature, it is concluded that dislocations in titanium contribute mainly to the long-range internal stress field, i.e. to the athermal component of the flow stress τ_μ . Direct evidence for the increase in the long-range internal stress with increase in dislocation density is provided by the curvature in the dislocations observed by TEM in deformed specimens; see Figs. 4.99 and 4.100.

A comparison of the values of σ_f with the tensile stresses σ_i and σ^* and with $2.5 \tau_{crss}$ for prism glide has been presented as a function of temperature in Fig. 4.95 for two extremes in interstitial content. For the most part reasonable accord exists between these various flow stress parameters. However, the

value of 2.5 τ_{crss} for prism glide tends to be larger than the polycrystalline parameters at temperatures of 77K and below, being especially noticeable for the high purity material. One explanation for this difference is that it is due to twinning, which is known to occur more readily as the purity and grain size are increased and the temperature decreased. On the other hand, the disagreement could reflect an influence of texture on the Taylor orientation factor M ($=\sigma/\tau_{crss}$), a smaller M occurring for the weaker, split texture of the large grain size specimens compared to the fine grain size material; see Fig. 4.39. For example, better accord between the single crystal τ_{crss} and the polycrystalline stress parameters results when M is taken to be 2.0 for the coarse grain size specimens rather than 2.5. Some support that the difference between the single and polycrystalline stress values may be due to the effect of texture on M rather than twinning is provided by the results on the polycrystalline Ti-7.4 at.% Al alloy (wire specimens) shown in Fig. 5.55. This alloy had a wire texture (Ref. 386) very nearly the same as that of high purity titanium but exhibited no twinning at temperatures $\geq 77K$. A better fit between τ_{crss} for prism glide and the polycrystalline stress parameters was obtained for the alloy when M was taken to be 2.0 rather than 2.5. On the other hand, the large value of 1.55 for the ratio $\sigma^*(d = 1\mu m)/\sigma^*(d = \infty)$ for the high purity materials (Fig. 4.78) suggests that an additional factor may contribute to the decrease in σ^* at large grain sizes. Further consideration of the influence of grain size on the flow stress of polycrystalline titanium is given in the section to follow on grain size hardening.

The strain hardening of titanium (iodide Ti, Ti50, A-70Ti and Ti-7.4 at.% Al) at large strains ($\epsilon > 1$) produced by wire drawing at 300K was investigated by Biwas, Cohen and Breedis (Ref. 343). The true stress-true strain curves for these materials exhibited parabolic strain hardening up to a strain of about 1.7, following which they became approximately linear, the transition strain from parabolic to linear strain hardening increasing with increase in interstitial content. The variation of the strain hardening rate $d\sigma/d\epsilon$ with strain for the four titanium materials is presented in Fig. 5.56; included for comparison are typical results for FCC and BCC metals. To be noted is a slight increase in $d\sigma/d\epsilon$ with increase in grain size for the A-70Ti. Comparing the four titanium materials, it is seen that interstitial solutes exert a marked influence on the strain hardening rate, the effect of interstitials being much larger than that of grain size and of the aluminum substitutional solute. Further, the strain hardening of the HCP titanium

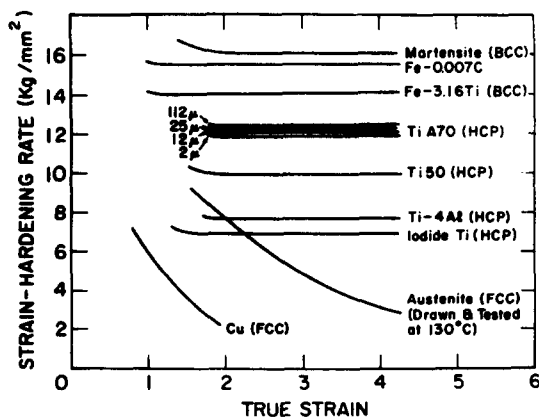


Fig. 5.56 Strain hardening rates of α -titanium and other metals at large strains. From Biwas, Cohen and Breedis (Ref. 343).

materials is greater than that of the FCC copper and austenite, but less than that of the BCC iron alloys and martensite. Worthy of note is that grain size dependence of the flow stress of A-70Ti was found to follow the Hall-Petch relation up to strains of 3.5. The friction stress σ_f increased with strain, whereas the Hall-Petch slope K decreased.

TEM observations by Biwas, Cohen and Breedis (Ref. 343) of the dislocation structure produced by the deformation of the titanium materials to large strains revealed that the dislocations in iodide titanium formed a cellular network, which became clearly recognizable at strains as low as 0.06. With increased deformation the lattice misorientation between adjacent cells increased and they became elongated in the wire drawing direction, decreasing in width in the transverse direction. The flow stress was found to show a better fit when plotted versus the reciprocal of the cell size than versus the reciprocal of the square root of the cell size; see Fig. 5.57. In contrast to the situation in iodide titanium, dislocations in Ti50, A-70Ti and Ti-7.4at.% Al tended to be distributed more uniformly at all levels of strain up to the limit investigated. At small strains, the dislocations were restricted to prism plane slip bands and had a large screw component. At high strains, severe tangling of the dislocations occurred but there was no clear evidence of a cellular structure. The development of a cellular dislocation network in high purity titanium and its lack in the higher interstitial content materials was attributed to an increased tendency for cross slip with increase in stacking fault energy as the interstitial content is reduced.

Based on their results, Biwas, Cohen and Breedis (Ref. 343) proposed the

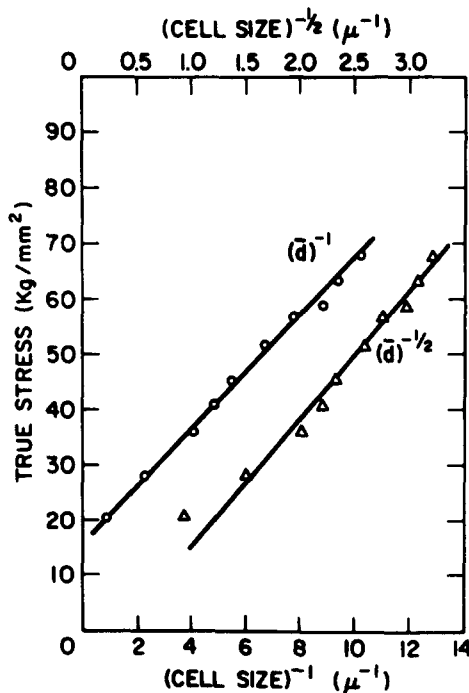


Fig. 5.57 Flow stress of wire-drawn iodide Ti versus $(\text{cell size})^{-1}$ and versus $(\text{cell size})^{-\frac{1}{2}}$. From Biwas, Cohen and Breedis (Ref. 343).

following expression for the flow stress of titanium over a wide strain range

$$\sigma = \sigma_i + \gamma K d^{-\frac{1}{2}} + \alpha_{ub}(\rho_f^W)^{\frac{1}{2}} + \beta_{ub}/l \quad (5.65)$$

where σ_i is the friction stress, K the Hall-Petch coefficient for grain size strengthening, d the grain size, γ a constant which varies from unity to zero with increasing strain because grain boundaries become indistinguishable from cell walls when the latter develop large misorientations, l is the chord length of cell-wall "windows" containing dislocations of a lower density ρ_f^W , which can be cut by the gliding dislocations similar to a forest. Except for the windows, the cell walls are considered to consist of dense impenetrable arrays of dislocations acting essentially as grain boundaries. They assumed the "window" cord length l to vary linearly with the cell size d' , and therefore at large strains the last term of Eq. 5.65 overrides the Hall-Petch term, giving a linear relation between flow stress and cell size. When cells do not form, the last two terms of Eq. 5.65 are replaced by the usual dislocation interaction term $\alpha_{ub}\rho^{\frac{1}{2}}$, where ρ now includes the total dislocation density.

Grain Size Hardening:

The increase in flow stress with decrease in grain size (grain size hardening) observed for titanium (Figs. 4.64 to 4.70) can be interpreted to reflect an effect of grain size on both the thermal and athermal components of the flow stress. The results of Figs. 4.93, 4.94 and 5.55 indicate that the effect on the athermal component τ_u is mainly through the increase in dislocation density with decrease in grain size, which in turn contributes to τ_u through the $\alpha_{ub}\rho^{\frac{1}{2}}$ term in Eq. 5.64. Inserting Eq. 4.11 for $\rho^{\frac{1}{2}}$ into Eq. 5.64 we obtain

$$\tau = (\tau_f + \alpha_{ub}A\varepsilon^{\frac{1}{2}}) + \alpha_{ub}Bd^{-\frac{1}{2}} \quad (5.67)$$

$$\equiv \tau_i(\varepsilon) + K_T d^{-\frac{1}{2}} \quad (5.67a)$$

where $\tau_i(\varepsilon) = (\tau_f + \alpha_{ub}A\varepsilon^{\frac{1}{2}})$ and $K_T = \alpha_{ub}B$. A and B are constants which include effects of interstitial content and temperature. Reasonable agreement has been obtained between the values of σ_i ($=M\tau_i$) and K ($=MK_T$) taken directly from Hall-Petch plots and those derived indirectly through dislocation density measurements and employing Eq. 5.67 (Refs. 169,246); see, for example, Fig. 5.58.

The results of Fig. 4.95 suggest that the effect of grain size on the thermal component of the flow stress τ^* (Fig. 4.77) reflects more a softening (when compared with the τ_{crss} for prism glide) which occurs upon increasing the grain size, rather than a hardening due to a decrease in grain size. As discussed above, the softening could be due to twinning or could result from a decrease in the orientation factor M as the grain size becomes larger. Some support for the latter explanation is provided by the fact that the decrease in temperature dependence of σ^* with increase in grain size is balanced by an increase in the strain rate sensitivity of the flow stress (Fig. 4.73) to yield a relatively constant value of Q^* (Fig. 4.108). The orientation factor M cancels out in the equation relating Q^* to $\partial\sigma^*/\partial T$ and $\partial\ln\dot{\epsilon}/\partial\sigma$, since

$$Q^* = \Delta H_{\tau^*} = -kT^2 \left(\frac{\partial \ln\dot{\epsilon}}{\partial T} \right)_T \left(\frac{\partial \tau^*}{\partial T} \right)_{\dot{\epsilon}} \quad (5.68)$$

$$= -kT^2 \left(M \frac{\partial \ln\dot{\epsilon}}{\partial \sigma} \right)_T \left(\frac{1}{M} \frac{\partial \sigma^*}{\partial T} \right)_{\dot{\epsilon}} \quad (5.68a)$$

That twinning does not seem to play a significant role in the effect of grain size on σ^* is indicated by the fact that the Hall-Petch slope K and its temperature dependence are relatively independent of the interstitial content (Fig. 4.69), whereas interstitials are known to have a significant influence on the amount of

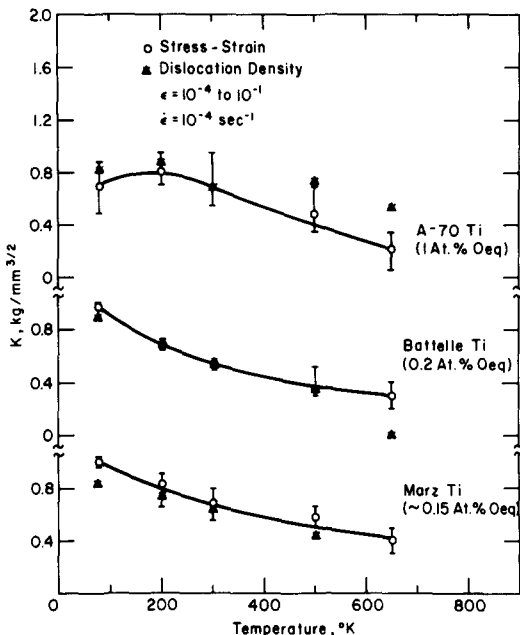


Fig. 5.58 Comparison of the Hall-Petch constant K with that derived from dislocation density measurements ($\alpha' Eb\beta$). From Conrad, Okazaki, Gadgil and Jon (Ref. 169).

twinning. It thus appears that the effect of grain size on the thermal component of the flow stress σ^* in titanium is in large part due to the changes in the orientation factor M which result from changes in texture as the grain size is altered.

If the effect of grain size on the flow stress of titanium is largely through the Taylor orientation factor M , then the effect of temperature on the Hall-Petch slope K must also be due largely to this cause. A contribution to the increase in K with decrease in temperature will also occur from the increase in dislocation density which occurs as the temperature is lowered. This effect of temperature will be included in the constant B of Eq. 5.67.

Finally, worthy of mention are the analyses of the effect of grain size on the flow stress of CPH metals by Armstrong and coworkers (Refs. 387-392). They interpret the Hall-Petch equation in the more classical sense, namely in terms of a stress concentration produced by a pile-up of dislocations against the grain boundaries, which propagates plastic flow across the grain boundary. This gives for the Hall-Petch equation

$$\sigma = M \tau_0 + M K_s d^{-1/2} \quad (5.69)$$

where τ_0 is the single crystal resolved shear stress and K_s the stress concentration required to propagate slip across the grain boundary. They assume that τ_0 in CPH metals is equal to the resolved shear stress for glide on the easiest slip system(s) and K_s refers to the more difficult glide (or twinning) systems required to operate for continuity of strain at the grain boundary. K_s is related to the resolved shear stress τ_c for the more difficult system controlling plastic flow

in the boundary regions through

$$K_S = A[\bar{M}^* \mu b / 2\pi\alpha]^{1/2} \tau_c^{1/2} \quad (5.70)$$

where A is a constant, \bar{M}^* the orientation factor for the more difficult deformation system, α a numerical constant depending on the edge or screw character of the dislocation pile-up and μ and b have their usual meaning. Taking the activation volume $v = \bar{M}kT(\partial \ln \epsilon / \partial \sigma)_T$, they obtain from Eqs. 5.69 and 5.70

$$v^{-1} = v_0^{-1} + (K/2\bar{M}v_c\tau_c)d^{-1/2} \quad (5.71)$$

where v_0 is the activation volume for the easiest glide system and v_c is that for the more difficult system. For titanium the easiest glide system is $\{10\bar{1}0\} <11\bar{2}0>$ and the more difficult systems are expected to be either the $(0002) <11\bar{2}0>$ or the $\{11\bar{2}3\} <11\bar{2}2>$ systems.

Armstrong and coworkers (Refs. 287-392) have obtained reasonably good agreement between experimental results and Eqs. 5.69-5.71 for the CPH metals Cd, Zn and Mg. Considering the results presented here on Ti, qualitative accord exists for the effect of grain size on the activation volume and for the decrease in the Hall-Petch slope K with increase in temperature. However, the fact that $\sigma_j(\epsilon=0.2\%) / \bar{M}$ for Ti is smaller than τ_{crss} for prism glide is not in keeping with the model. Also, one expects that τ_c might increase with interstitial content, leading to an effect of interstitial content on K and its temperature dependence, which is not found to occur (Fig. 4.69).

Internal Stress:

The work of Conrad and coworkers (Refs. 176, 249, 250, 254) indicates that the Seeger back-extrapolation method provides a good measure of the long-range internal stress τ_u opposing the motion of dislocations in titanium. Reasonable agreement is obtained between τ_u determined by this method and (a) the $\alpha \mu b \rho^{1/2}$ term of Eq. 5.64 and (b) the maximum internal stress derived from the curvature of dislocations in unloaded specimens (Fig. 4.100). In contrast, σ_{int} determined by the usual stress relaxation or decremental unloading methods exhibits a temperature dependence greater than that of the most temperature dependent modulus of titanium, suggesting that the internal stress determined by these relaxation methods includes a thermal component in addition to the athermal long-range internal stress. At stresses near τ_u the stress relaxation behavior during decremental unloading has been found to undergo first negative relaxation (an increase in stress with time) followed by positive relaxation (a decrease in stress with time) (Ref. 254). The stress at which the negative relaxation persists for a long time was found to be approximately equal to τ_u determined by the Seeger method.

Okazaki, Aono, Kaneyuki and Conrad (Ref. 254) propose that the change from negative-to-positive relaxation may be due either to some rearrangement of dislocations during relaxation or to the existence of regions within the grains where the long-range internal stress is higher than in others. At a critical stress, the dislocations in the regions of higher long-range internal stress would begin to move backwards, while those in the regions of lower internal stress would still be moving forward, the relaxation curve reflecting the sum of the two processes. As the applied stress is further decreased, it is expected that eventually the dislocations moving backwards will be in the majority and the relaxation curve will exhibit only negative relaxation.

The results obtained to date do not permit a decision regarding whether the rearrangement of dislocations or the existence of a spectrum of long-range internal stresses is responsible for the negative-to-positive relaxation in titanium. Moreover, it is not clear why the negative-to-positive relaxation occurs in Ti and Fe,

which contain a high concentration of short range obstacles, whereas it does not occur in Cu with a lower concentration of such obstacles (Ref. 254).

5.1.7 Fracture of Polycrystals:

The work of Reed-Hill and coworkers (Refs. 171,197,182,194,273) and of Conrad, Keshavan and Sargent (Ref. 260) suggests that the fracture and ductility of titanium may be influenced by twinning at low temperatures and by dynamic strain aging at 500-700K, similar to the effects of temperature on strain-hardening. The increase in ductility at low temperatures with increase in grain size and purity (Figs. 4.116 and 4.117) is in keeping with the concurrent increase in twin activity for these conditions. Also, the effects of temperature, grain size and interstitial content on the work to fracture W (area under the stress-strain curve) at temperatures below 300K (Fig. 4.115) are in keeping with the influence these variables have on twinning. For tests above 300K, the decrease in ductility with increase in grain size (Figs. 4.114, 4.116 and 4.117) and the irregular behavior of the fracture stress (Fig. 4.112) at 500-700K can be attributed to the influence of dynamic strain aging.

As discussed in Section 4.2.4, the fracture surfaces of titanium specimens tested at low temperatures had a dimpled appearance. Fig. 5.59 compares the measured dimple size for the fracture of A-70Ti with the relation by Hahn and Rosenfield (Refs. 393,394), which is based on the model by McClintock (Ref. 395) for the growth of voids during plastic flow which eventually lead to fracture. Hahn and Rosenfield's relation yields

$$\ln\left(\frac{D}{D_0}\right) = \left\{ \frac{\sqrt{3}}{2(1-n)} \sinh \left[\frac{\sqrt{3}}{2} \left(1-n \right) \left(\frac{2\sigma_r}{\sigma_F} + 1 \right) \right] + \frac{3}{4} \right\} \bar{\epsilon}_F \quad (5.72)$$

where D_0 and D are the initial and final void sizes, $n = \partial \ln \sigma / \partial \ln \epsilon$ the strain hardening exponent and σ_r is the radial stress component in the neck of a tensile specimen given by $\sigma_r = \sigma_F \ln(1 + a_F/2R)$ (Ref. 262); a_F is the radius of the neck at fracture and R is its radius of curvature. σ_F and ϵ_F are the effective flow stress and strain at fracture respectively. To be noted in Fig. 5.59 is that there exists reasonable agreement between the measured dimple size and that predicted by Eq. 5.68 to a size of about 15 μm , beyond which the calculated size increases while that

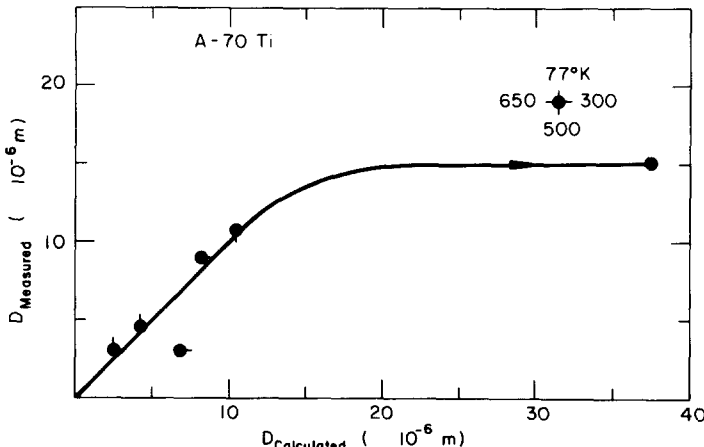


Fig. 5.59 Comparison of the average measured dimple size for the fracture of A-70Ti at 77-650K with that calculated. From Conrad, Keshavan and Sargent (Ref. 260).

measured remains constant at approximately the maximum grain size considered.

Krafft (Ref. 396) showed that the following relation may be used to correlate the plane-strain fracture toughness parameter K_{Ic} with the plastic flow properties of a material

$$K_{IC} = nE\sqrt{2\pi d_T} \quad (5.73)$$

where n is the strain hardening exponent, E Young's modulus and d_T the process zone size. This correlation is based on identifying the onset of fracture with the attainment of tensile instability, i.e. upon reaching a strain equal to n the necking strain in a zone of average size d_T ahead of the main crack. The fracture process is considered to consist of necking and subsequent tensile rupture of small elemental "cells" lying along the crack front. Assuming that the dimple size corresponds to d_T , Conrad, Keshavan and Sargent (Ref. 260) calculated K_{Ic} for MARZ and A-70Ti titaniums using Eq. 5.69. A comparison of the ratio of $(K_{Ic}/\sigma_{ys})^2$, which is a measure of the critical flaw size at the yield stress, versus the yield stress divided by the modulus is given in Fig. 5.60. It is seen that the values of $(K_{Ic}/\sigma_{ys})^2$ for titanium are similar to those obtained for a number of metals by the usual fracture toughness test methods.

Worthy of mention at this point is the study by Hirth and Froes (Ref. 397) on the interrelation between the fracture toughness of titanium alloys and general tensile properties. Considering relations which had been previously proposed (including that of Eq. 5.69) and several new ones derived by them, they found for alloys exhibiting a limited range of microstructures that the simpler correlations gave the best fits, with $K_{IC} \propto (\gamma \cdot s)^{-1}$ being the best one. For alloys with a wide range of microstructures, more complex correlations which included microstructural parameters were found to be superior.

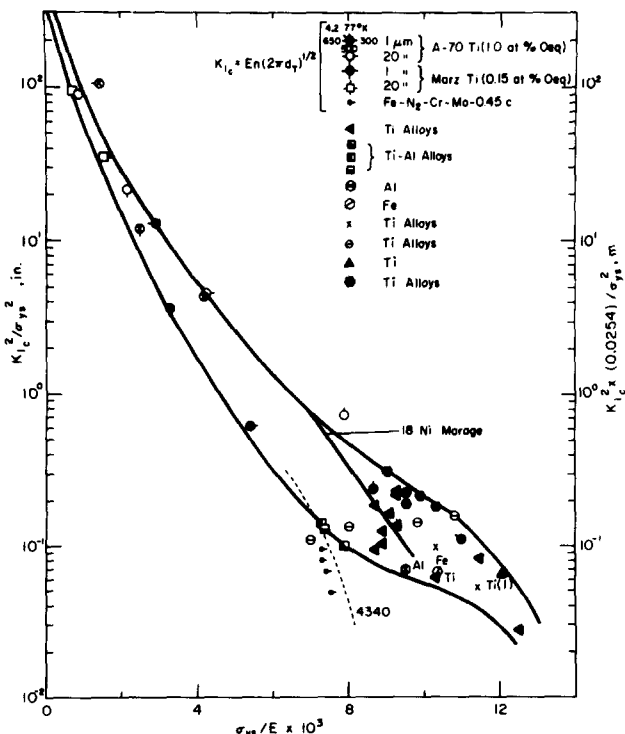


Fig. 5.60. Comparison of the plane-strain crack size parameter of titanium with other engineering materials. From Conrad, Keshavan and Sargent (Ref. 260).

Finally, of interest are the modes of fatigue cracking in titanium. This subject has recently been reviewed by Sugano and Gilmore (Ref. 398) and the reader should refer to their paper for details and references. In pure titanium, fatigue deformation and crack initiation have been found by some investigators to occur at deformation twins. Fresh twins were observed to be continuously introduced during fatigue at high strain amplitudes and cracks initiated preferentially on the twin boundaries. Contrary to these observations, other investigators noted slip band cracking and "slipless cracking", the latter originating and propagating in the general direction of maximum shear. Further, it was shown that the major cyclic deformation mode was by slip and that the surface area fraction of twins was less than 10%, even at a total strain amplitude of 1.0%.

In their own studies of fatigue damage in large grain size (average grain size of 0.0127m) A40 titanium ($O+N+C = 0.77$ at .%) tested in cyclic torsion at low (± 0.003) and high (± 0.008) strain amplitudes, Sugano and Gilmore (Ref. 398) found that the strain amplitude influenced the deformation mode and the nature of the macroscopic crack propagation. At the high strain amplitude the slip processes normally operative in titanium were observed and microcracking occurred on the (0001) and the $\{10\bar{1}0\}$ slip planes. At the low strain amplitude twin plane cracking occurred on the $\{10\bar{1}1\}$, $\{10\bar{1}0\}$ and $\{11\bar{2}3\}$ planes in addition to the normal slip plane cracking. At both low and high strain amplitudes cracking was observed on the $\{11\bar{2}0\}$ plane, which is neither a slip nor a twinning plane in titanium. They proposed that this cracking mode resulted from a dislocation reaction which formed sessile dislocations on the $\{11\bar{2}0\}$ planes. Since they only observed crystallographic cracking in their large grain size specimens, Sugano and Gilmore (Ref. 398) proposed that the non-crystallographic cracking reported by others for fine grained commercial titanium indicates that the mode of cracking is dependent on the grain size.

5.2 Intermediate Temperatures ($0.3 < T/T_m < 0.4$)

5.2.1 Prism and Basal Glide in Single Crystals

Studies on the deformation of single crystals in the intermediate temperature regime have been principally on high purity materials. Consequently, pronounced dynamic strain aging effects such as have been observed for polycrystals have not been identified during either prism or basal glide at these temperatures. The CRSS for prism glide is characterized by an extended plateau in this temperature region (Fig. 4.12); a plateau also occurs for basal glide, but is of more limited extent (Fig. 4.26). In the case of prism glide, the interstitial solute thermal obstacles appear to have become transparent in this temperature range and the plateau stress is probably due to the long-range internal stress associated with the original defect structure plus the additional dislocations produced during the deformation. Thermally activated cross slip associated with prism glide seems to occur with ease in this temperature range. In the case of basal glide, the rate controlling mechanism operative in the low temperature regime (Peierls stress or cross slip) continues almost to the end of the intermediate temperature region before giving way to an athermal mechanism of rather short extent. Again, the athermal region is probably due to the initial defect structure and that introduced by the deformation associated with τ_{crss} .

Worthy of mention is that pronounced serrations were observed for prism glide in zirconium single crystals with 120 ppm oxygen deformed at 723K, which is in the plateau region for this metal (Ref. 399). The absence of twin markings on the specimen indicated that the observed load drops were due to dynamic strain aging.

5.2.2 Plastic Deformation and Fracture of Polycrystals

Static Strain Aging:

In Section 4.2.5 it was shown that static strain aging in a Ti-0.41at.%0 alloy could be considered to consist of four stages (Fig. 4.124). Donoso and Reed-Hill (Ref. 272) attributed the rapid return of a yield point independent of time and temperature observed in Stage I to a Haasen-Kelly (Ref. 400) unloading yield point, which had been previously identified in titanium deformed at 300-423K by Malik and Dickson (Ref. 401). For Stage II aging, Donoso and Reed-Hill (Ref. 272) obtained an activation energy of 50.5 Kcal/mole from Arrhenius plots of the time to achieve given values of the upper and lower yield point stress increases following aging (Fig. 4.134), and a value of 51.8 Kcal/mole from an analysis of strain aging due to Hartley (Ref. 402), which is similar to one employed earlier by Bolling (Ref. 403),

$$\gamma T^{2/3} \propto [D_0 \exp(-Q/kT)]^{2/3} \quad (5.74)$$

where γ is the time coefficient of Eq. 4.30 and D_0 and Q are the pre-exponential and activation energy for the diffusion of the interstitial solute responsible for strain aging. The values of Q for Stage II aging are in good agreement with those reported for the diffusion of oxygen in titanium; see Table 2.6 and Refs. 404 and 405. Based on the observed kinetics, Donoso and Reed-Hill (Ref. 272) concluded that the Stage II static strain aging in the Ti-0.41at.%0 alloy followed the Cottrell model of aging (Refs. 402,403,406,407), whereby the oxygen atoms drift to the dislocations and pin them.

Dolobelle and Oytana (Ref. 408) questioned the conclusion of Donoso and Reed-Hill (Ref. 272) that static strain aging in their Ti-O alloy is a Cottrell long-range diffusion type. Rather, they proposed that Stages II and III aging is better explained as the pinning of dislocations by a short-range Snoek ordering mechanism resulting from the reorientation of oxygen-oxygen and/or oxygen-substitutional solute atom pairs (Refs. 409-417). They showed that the observed kinetics of the yield point return are in agreement with those for the anelastic Snoek relaxation and proposed that the relaxation is probably due to the reorientation of interstitial oxygen atoms about substitutional iron atoms. They proposed that Stage IV aging corresponds to a Cottrell atmosphere formation.

In response to these comments, Donoso, Watson and Reed-Hill (Ref. 418) acknowledged that Snoek ordering of Fe-O pairs could possibly be responsible for the yield point return in Stage II, but hesitated accepting this mechanism for two reasons: (a) the relaxation times calculated for the reordering of Fe-O pairs from the data of Pratt, Bratina and Chalmers (Ref. 411) using the method of Browne (Ref. 416) were about four times smaller than those determined empirically from their aging data and (b) the size of the stress increase in Stage II was about 50% of the total recovered stress, which is about three times larger than is exhibited by a typical BCC metal, where the internal friction strength is almost two orders of magnitude larger.

Finally, worthy of mention regarding static strain aging in titanium are the results of Dickson, Desrosiers and Malik (Ref. 419), who found for tests on commercial titanium Ti-40 (and for zirconium and zircaloy-2) that dislocations which become pinned by aging under a high stress at 363-573K become unpinned upon unloading to and subsequent aging at a low stress. Since significant unpinning did not occur when the second aging stress was equal to or greater than the internal stress for zero relaxation, these authors concluded that the unpinning is associated with the reversal of the direction in which dislocations are gliding or are bowed out during the unloading.

Dynamic Strain Aging:

The activation energy of 50-60 Kcal/mole obtained for various dynamic strain aging phenomena in commercial titanium (Fig. 4.135) is in accord with that for the diffusion of oxygen (Table 2.6 and Refs. 404,405) and is in keeping with theoretical models for dynamic strain aging (Eqs. 3.89,3.90 and Refs. 420, 421). The value of 10 Kcal/mole in Fig. 4.135 can be considered to be in accord with that for the diffusion of hydrogen. However, no clear identification with the diffusion of an interstitial solute can be made for the 30 Kcal/mole observed at 500-600K (Fig. 4.135) nor of the 7 Kcal/mole at 600-800K (Fig. 4.136).

Garde, Aigenthaler, Woodruff and Reed-Hill (Ref. 422) explained the stronger dynamic strain aging effects due to oxygen in titanium compared to zirconium to the fact that oxygen produces a greater change in the c/a ratio in titanium, thereby yielding a larger tetragonal component to the dislocation-interstitial interaction. They found that the hydrostatic component of the interaction given by

$$P = K\Delta V \quad (5.75)$$

where ΔV is the misfit volume or change in atomic volume per impurity atom and K the bulk modulus, did not differ significantly for the two metals.

Sasano and Kimura (Ref. 276) showed that both substitutional and interstitial solutes are involved in dynamic strain aging in titanium. They pointed out that interstitial solutes only interact weakly with screw dislocations in titanium and that a strong locking is needed to produce the pronounced dynamic strain aging effects observed. They proposed that the stronger locking results from the anisotropic distortion produced by substitutional-interstitial solute atom pairs, in keeping with the stronger anelastic relaxation effects noted for such pairs in titanium (Refs. 409 to 417). Further, the magnitude of the anisotropy and hence the strength of the interaction between dislocations and the atom pairs should be larger the greater the size difference between the substitutional solutes and titanium atoms, which was found by them to be the case. Finally, they proposed that the two sides of the parallelogram in Fig. 4.136 which yield the larger activation energy reflect the diffusion of the interstitial solute atom of the pair, whereas the two sides yielding the lower activation energy reflect the diffusion of the substitutional atom.

The reduction in the strength of the work hardening and ductility features of dynamic strain aging in titanium with decrease in grain size (Figs. 4.130 and 4.131) was interpreted by Donoso, Watson and Reed-Hill (Ref. 274) to be due to a lowering of the temperature at which dynamic annealing becomes significant. This lowering was attributed to the increase in work hardening rate (increase in dislocation density) which occurs with decrease in grain size. Further, these authors proposed that the rapid drop-off in stress on the high temperature side of the work hardening peak in the vicinity of 800K ($\dot{\epsilon} \approx 10^{-4} \text{ s}^{-1}$) is due to the onset of dynamic annealing (dislocation climb) and therefore the kinetics (interrelationship between temperature and strain rate) of this peak reflect self-diffusion of titanium atoms rather than interstitial diffusion. The slightly higher activation energy observed for the work hardening peak (57-60 Kcal/mole) as compared to that for the beginning of serrations in the stress-strain curves (41-50 Kcal/mole) was taken to support this conclusion. Optical and TEM microstructural studies supported the occurrence of dynamic annealing on the high temperature side of the work hardening peak.

Fracture:

As discussed above, commercial titanium exhibits a minimum in ductility in the intermediate temperature range (Figs. 4.46,4.129 and 5.61), the effect decreasing with reduction in interstitial content (see Figs. 4.118 and 5.62). However,

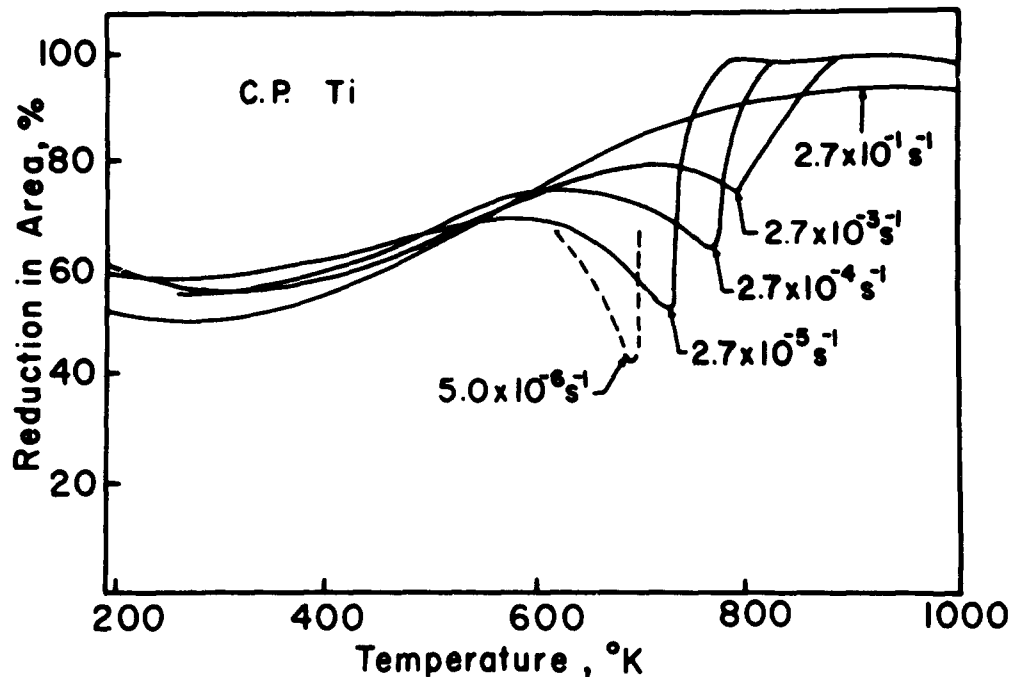


Fig. 5.61 Effect of strain rate on the reduction in area of commercial purity titanium (0.4 at.%) as a function of temperature. From Donoso, Santhanam and Reed-Hill (Ref. 275).

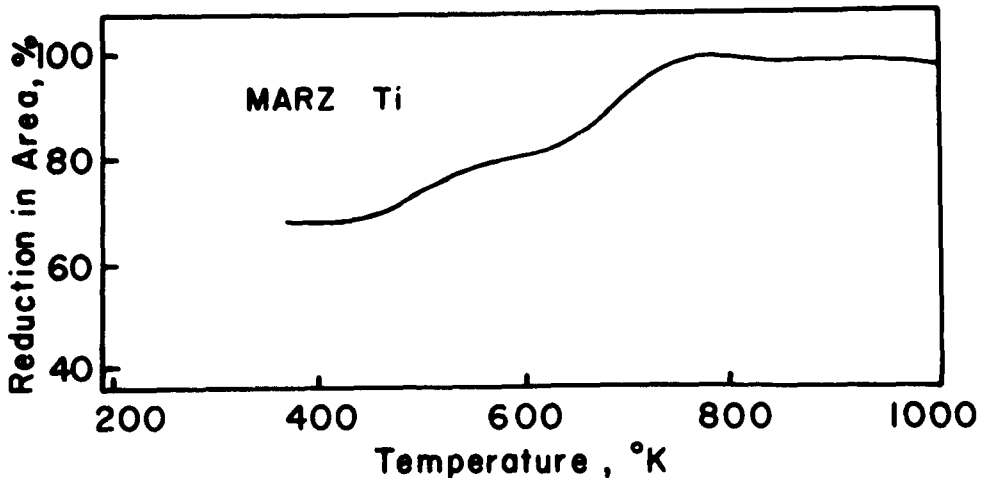


Fig. 5.62. Effect of temperature on the reduction in area of MARZ zone-refined titanium deformed at a strain rate of $5 \times 10^{-4} s^{-1}$. From Donoso, Santhanam and Reed-Hill (Ref. 275).

the mode of fracture in this temperature region is similar to that at lower temperatures, being of the ductile type with dimples, indicating that fracture occurred by void coalescence (Ref. 275, 423). The dimples for fracture between 500 and 970K were, however, deeper and exhibited sizes much larger and edges much smoother and less angular than those observed at lower temperatures (Ref. 423). Rao, Rao and Rao (Ref. 423) termed the fracture mode of commercial purity titanium in this temperature range "intergranular creep fracture", in keeping with the plastic deformation map for titanium (Ref. 424).

Donoso, Santhanam and Reed-Hill (Ref. 275) found no evidence of surface cracks on the exterior surface of specimens deformed to fracture at a temperature and strain rate corresponding to the ductility minimum. However, a large number of pores occurred in the central region of the neck (Fig. 5.63), whose density was greatest at the smallest cross section and decreased to essentially zero outside the neck region. Most pores appeared to lie at triple lines or at the juncture of three grain boundaries. These authors concluded that the pores had apparently nucleated at grain boundaries and the fracture method corresponded to the intergranular microvoid coalescence designation by Schulz and McMahon (425). Whether or not the voids nucleated at precipitates lying along the grain boundaries had not been determined.



Fig. 5.63 Cross section of a commercial purity titanium specimen deformed at $2 \times 10^{-4} \text{ s}^{-1}$ and 743K to just before fracture, showing pores in the region of the neck. From Donoso, Santhanam and Reed-Hill (Ref. 275).

5.3 High Temperatures ($T > 0.4 T_m$)

5.3.1 Prism and Basal Glide in Single Crystals

In the case of prism glide, the intermediate temperature plateau in the critical resolved shear stress versus temperature curve terminates at ~850K (for a strain rate of 10^{-4} s^{-1}), being followed by an increase in the temperature dependence of τ_{CRSS} , which reaches a maximum at ~950K before decreasing again to a small value at ~1100K; see Figs. 4.26 and 4.28. To the author's knowledge, no detailed investigation into the mechanism(s) operative during prism glide at high temper-

atures ($T > 850\text{K}$) have been made up to now. It is however expected that diffusion controlled mechanisms are operative at these temperatures and that the rate controlling mechanism may be dislocation climb (Ref. 399).

In the case of basal glide, the critical resolved shear stress also decreases rapidly above about $\sim 850\text{K}$; see Figs. 4.26 and 4.28. A discontinuity occurs in the values of the apparent activation volume v and the apparent activation energy Q at $\sim 800\text{K}$ (see Figs. 4.28 and 4.29) suggesting that a different mechanism is rate controlling above this temperature compared to below. The work of Akhtar (Ref. 143) indicates that basal glide deformation at $T > 900\text{K}$ is given by

$$\dot{\gamma} = A\tau^n \exp(-Q/kT) \quad (5.48)$$

with $n = 4$ and $Q = 2.5\text{ev}$. As pointed out in Section 5.1.4, these values of n and Q are more nearly those for a diffusion controlled mechanism than a cross slip mechanism. Hence, dislocation climb could also be the rate controlling mechanism for basal glide at high temperatures.

5.3.2 Plastic Deformation and Fracture of Polycrystals

Plastic Deformation:

From an analysis of data in the literature (Ref. 187,277,278) and their own results on commercial Ti-50A, Doner and Conrad (Ref. 163) showed that the plastic deformation of titanium at high temperatures was described by the relation found to apply to the high temperature creep of metals in general (Ref. 136), namely

$$\frac{\dot{\epsilon}_s kT}{D\mu b} = A\left(\frac{\sigma}{\mu}\right)^n \quad (5.76)$$

where $\dot{\epsilon}_s$ is the steady-state tensile strain rate, μ the shear modulus, D the appropriate diffusivity coefficient (i.e., bulk, grain boundary, or dislocation core), b the Burgers vector and σ the applied tensile stress. A and n are constants which depend upon the particular operating mechanism (see Table 3.5). That the plastic flow of titanium at high temperatures follows Eq. 5.76 is shown in Fig. 5.64. The value of the diffusion coefficient D was here taken to be $1.0 \exp(-57.800/RT) \text{ cm}^2\text{s}^{-1}$. The choice of 57.8 Kcal/mole for the self-diffusion coefficient in alpha titanium was based on the activation energy for the high temperature deformation given in Fig. 5.65. The slope at low stresses of the plot of Fig. 5.64 yields $n = 4.55$, which is in accord with the values of $m = 1/n$ given in Fig. 4.137 determined by strain rate cycling tests.

The value of 57.8 Kcal/mole for the activation energy for diffusion employed in Fig. 5.64 is about twice that of the anomalously low values reported for alpha titanium by Dyment and Libanati (Refs. 426, 427). As pointed out by Le Claire (Ref. 428), titanium belongs to a group of metals (Group IVA) for which self- and substitutional solute diffusion are anomalous. The anomalies consist of a curvature in the $\ln D$ versus $1/T$ plots and with Q and D_0 values substantially smaller than those expected on the basis of empirical correlations with the melting point and with Zener's (Ref. 429) theory of D_0 . These anomalies have been explained on the basis of either a continuous variation of the activation energy and entropy with temperature (Refs. 429,430) or bimodal diffusion mechanisms (Refs. 428,431-434). When a bimodal diffusion mechanism is considered, the Q and D_0 values agree quite well with empirical correlations and those given in Table 2.5. The value of 57.8 Kcal/mole derived from the high temperature deformation results therefore seems to be reasonable. The value of $1.0 \text{ cm}^2\text{s}^{-1}$ for D_0 was chosen on the basis of known D_0 values for normal diffusion behavior in metals, which fall between 0.05 and $5 \text{ cm}^2\text{s}^{-1}$ (Ref. 428).

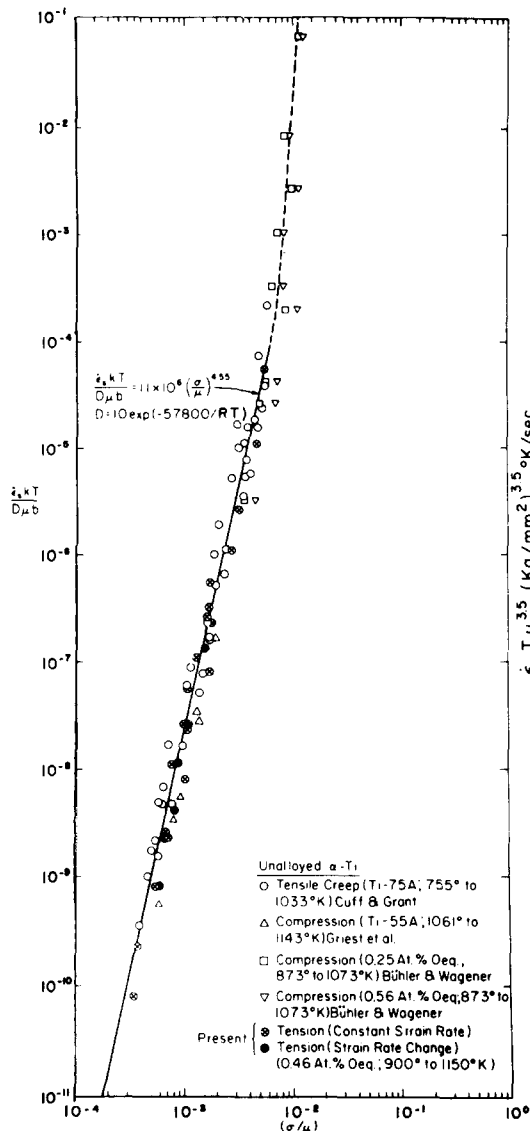


Fig. 5.64 Log-log plot of $\dot{\epsilon}_s kT / D_{\mu b}$ versus σ/μ for the high temperature plastic deformation of α -Ti. From Doner and Conrad (Ref. 163).

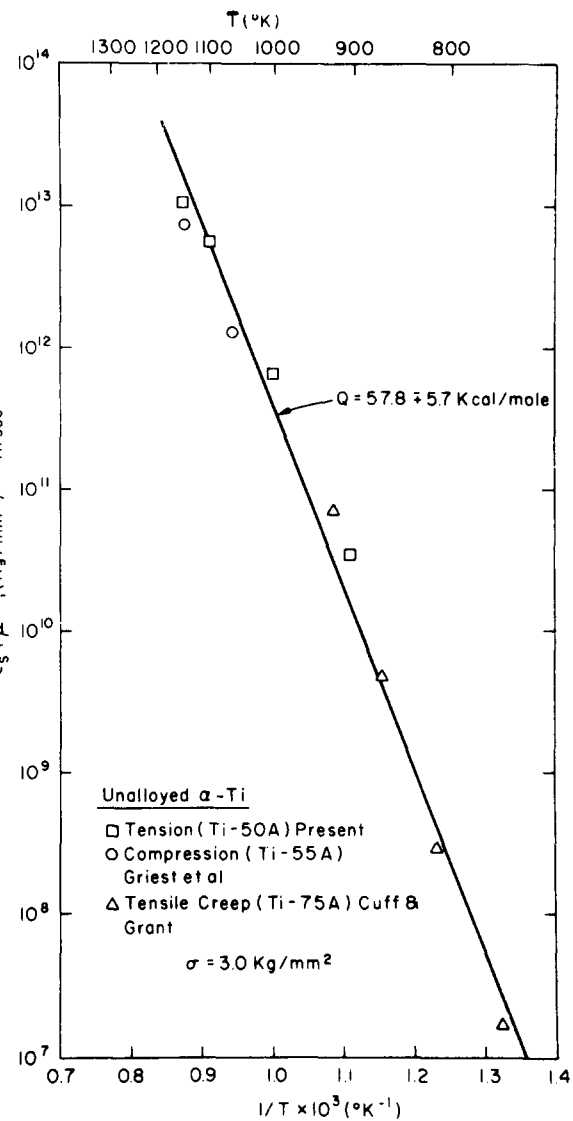


Fig. 5.65 Log $(\dot{\epsilon}_s Th^{3.5})$ versus $1/T$ for the steady state high temperature deformation of α -Ti. From Doner and Conrad (Ref. 163).

The results of Fig. 5.64 thus lead to the conclusion that the high temperature deformation of alpha titanium is diffusion controlled. A comparison of the data for titanium with the predictions of various theoretical climb-controlled creep mechanisms (Ref. 435) is presented in Fig. 5.66. It is here seen that of the various mechanisms considered, only two, namely Weerstman's glide and climb (Ref. 436) and Blum's climb (Ref. 437) mechanisms fit the experimental data well. Of the two, Weerstman's glide and climb mechanism is preferred, since its stress exponent and pre-exponential factor are in better accord with the experimental values. This conclusion is in accord with the findings of Bird, Mukherjee and Dorn

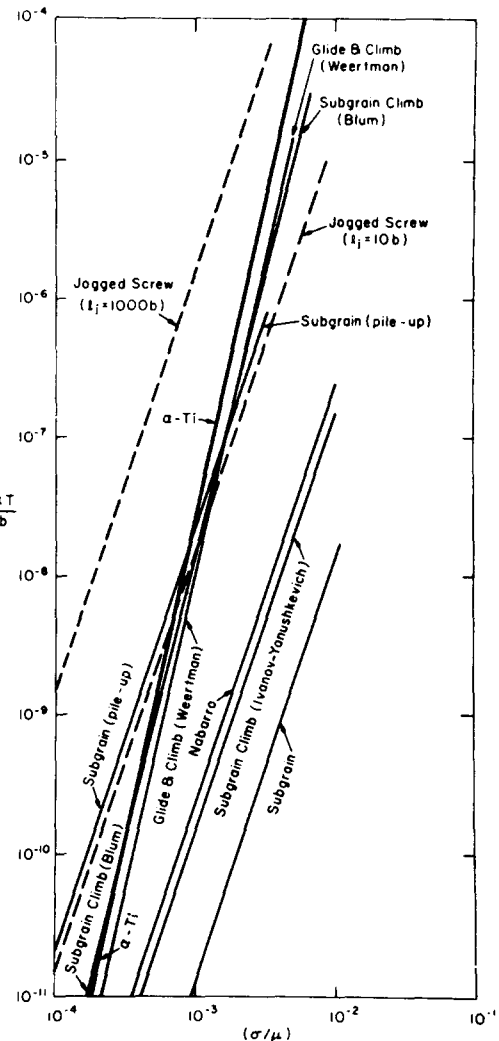


Fig. 5.66 Log-log plot of $\dot{\epsilon}_s kT / \mu D_b$ versus σ/μ for various theoretical creep mechanisms and for the experimental data on α -Ti. From Doner and Conrad (Ref. 163).

(Ref. 136) for other CPH metals. They correlated the available experimental data on a number of nominally pure CPH metals and concluded that they all deformed by climb-controlled creep at high temperatures. Table 5.16 gives the stress exponents and the pre-exponential factors obtained from their correlations along with the experimental values for α -Ti. It is here seen that the values of the constants A and n for α -Ti agree quite well with those for the other CPH metals.

Worthy of note is that the results given in Fig. 5.64 are independent of the interstitial content, indicating that the high temperature deformation of α -Ti is not significantly influenced by the presence of interstitial solutes. Further, the data for the deformation of β -Ti lie along the curve in Fig. 5.64 for α -Ti, providing the appropriate diffusion coefficient is employed, i.e. $D_\beta = 1.0 \exp(-50,000/RT)$ (Ref. 2).

TABLE 5.16 The Stress Exponent n and the Constant A for Climb-controlled Creep of Nominally Pure CPH Metals. From Doner and Conrad (Ref. 163).

Metal	c/a	Temperature Range, T/T _m	n	A
Cd	1.886	0.58 to 0.71	4.3	1x10 ³
Zn	1.856	0.60 to 0.78	4.6	3x10 ⁴
Mg	1.624	0.50 to 0.60 0.59 to 0.76	5.7 5.7	6x10 ⁶ 8x10 ⁷
α -Tl	1.598	0.58 to 0.85	5.0	1x10 ⁸
α -Ti	1.587	0.39 to 0.59	4.6	1x10 ⁶

Creep of titanium at stresses appreciably below those in Fig. 5.64 has been investigated by Malakondaiah and Rao (Ref. 438). Alpha titanium springs with grain sizes ranging from 59 to 787 μm were tested in creep at 823 to 1098K and at stresses of the order of 10^{-6} to 10^{-5}N/mm^2 . For specimens with grain sizes in the range of 254 to 787 μm they observed a Harper-Dorn (Ref. 439) type of creep given by

$$\dot{\varepsilon}_{\text{HD}} = A_{\text{HD}} D_v \sigma b / kT \quad (5.77)$$

where D_v is the lattice diffusion coefficient. The experimentally determined activation energy for this creep was 55.4 Kcal/mole. The deformation of a specimen with a grain size of 149 μm was established by them to be within the Nabarro-Herring (Refs. 440 and 441) creep regime defined by

$$\dot{\varepsilon}_{\text{NH}} = A_{\text{NH}} \Omega D_v \sigma / d^2 kT \quad (5.78)$$

where Ω is the atomic volume and d the grain size. The activation energy for this specimen was 57.6 Kcal/mole. These activation energies for the creep of α -Ti at very low stresses are in accord with those for deformation at higher stresses given above, providing additional support that the activation energy for self-diffusion in titanium is of the order of 55-60 Kcal/mole.

Stress Rupture:

The activation energy of 60-80 Kcal/mole reported for the stress rupture of α -Ti (Ref. 280 and Fig. 4.141) is in accord with that indicated above for self-diffusion. The diffusion controlled mechanism which governs rupture in titanium has not been clearly identified. One possibility is that it is dislocation climb, since high temperature fracture is often controlled by plastic deformation processes (Ref. 442).

5.4 Deformation and Fracture Maps

Based on the considerations in this chapter, the principal rate controlling mechanisms which appear to be operative during the plastic flow of polycrystalline titanium containing a total interstitial content greater than ~0.1 at % at various temperatures ($\dot{\varepsilon} \approx 10^{-4} \text{s}^{-1}$) are presented in Fig. 5.67. Near 0K pronounced serrations occur in the stress-strain curves, which are deduced to be due to adiabatic heating. At temperatures below about $0.3T_m$ thermally activated overcoming of interstitial solute obstacles by dislocations gliding on the first order prism planes is rate controlling; dynamic strain aging occurs from 0.3 to 0.4 T_m and dislocation climb

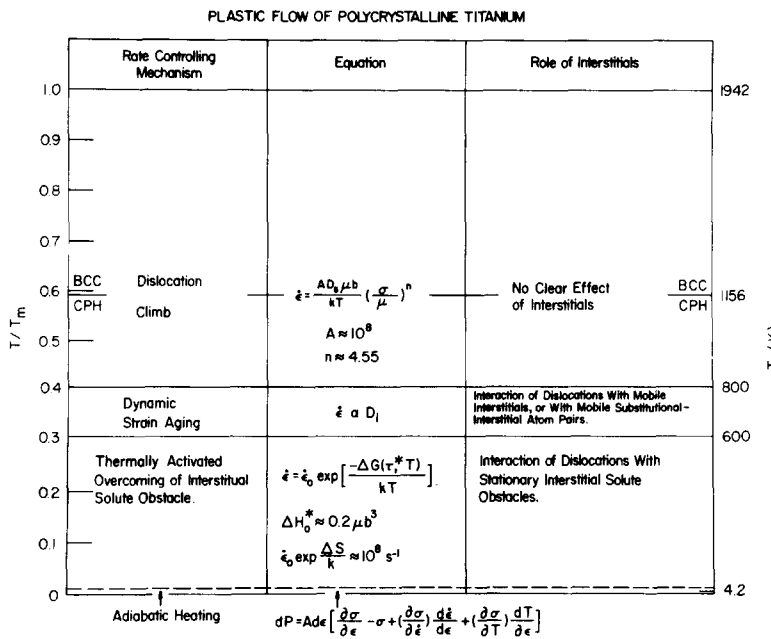


Fig. 5.67 Principal mechanisms operative during the plastic flow of polycrystalline titanium ($C_i > 0.1$ at.%) at various temperatures. Prism glide is the principal deformation mode. $\dot{\epsilon} \approx 10^{-4} s^{-1}$.

above $0.4 T_m$. The temperature limits for each of these mechanisms are only approximate and will depend on strain rate; also they depend on grain size and substitutional solute content. Furthermore, it is expected that at interstitial contents significantly below 0.1 at.% intrinsic mechanisms such as overcoming the Peierls stress, cutting forest dislocations or cross slip may become dominant at low and intermediate temperatures. The exact interstitial content at which this may occur has not yet been determined. The results available to date suggest that this interstitial concentration limit is below 0.05 at.%.

The exact role of twinning in the plastic deformation of polycrystalline titanium is not completely clear. Besides providing an additional deformation mode to maintain continuity of the grains and to promote isotropy of deformation, twinning appears to increase the strain hardening rate. All of these effects of twinning lead to improved ductility in titanium. Our understanding of the mechanisms by which twinning produces the observed effects is still very meager.

Finally, it should be mentioned regarding Fig. 5.67 that at very low stresses, Nabarro-Herring (Eq. 5.78) or Harper-Dorn (Eq. 5.77) creep will replace dislocation climb as the rate controlling process.

Based on information available at the time, Okazaki, Odawara and Conrad (Ref. 424) constructed the Ashby-type (Ref. 443) deformation mechanism maps shown in Figs. 5.68 and 5.69. The theoretical shear strength was taken to be $\mu/20$; and $\sigma = \sqrt{3} \tau$, employing the von Mises criterion. For the dislocation glide region the applied shear stress was taken as

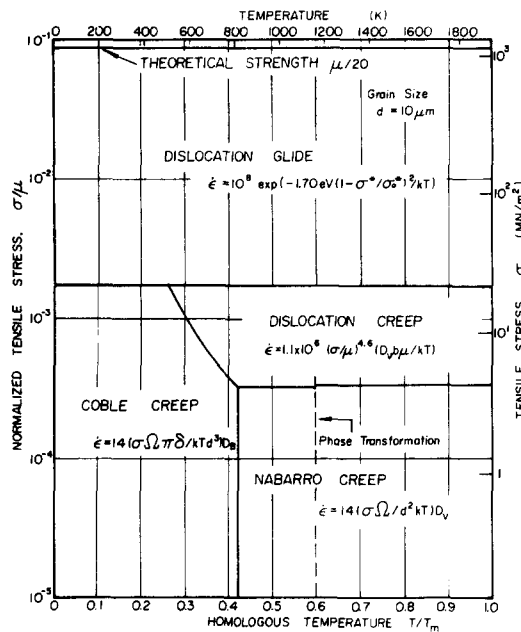


Fig. 5.68 Deformation mechanism map for zone-refined titanium with a grain size of $10\mu\text{m}$. From Okazaki, Odawara and Conrad (Ref. 424).

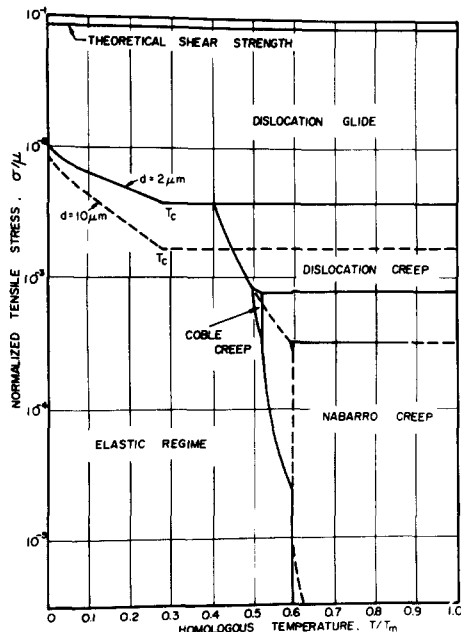


Fig. 5.69 Deformation mechanism map contour for the 0.2% yield stress of zone-refined titanium of 2 and $10\mu\text{m}$ grain size at a strain rate of 10^{-8}s^{-1} . From Okazaki, Odawara and Conrad (Ref. 424).

$$\tau = \tau^*(T, \dot{\gamma}, C_i) + 0.5\mu b[\rho(\gamma, d, C_i)]^{1/2} \quad (5.79)$$

with $\mu = 3E/8$. τ^* was obtained from

$$\dot{\epsilon}_2 = \dot{\epsilon}_0 \exp[-\Delta G_0(1-\tau^*/\tau_0^*)^2/kT] \quad (5.80)$$

with $\dot{\epsilon}_0 = 10^8 s^{-1}$, $\Delta G_0 = 1.7 eV$ and $\tau_0^* = 0.17 \mu$. The effect of grain size was on the dislocation density ρ through Eq. 4.11.

Dislocation creep was taken to be given by

$$\dot{\epsilon}_3 = A(D_v \mu b / kT)(\sigma/\mu)^n \quad (5.76a)$$

with $A = 1.1 \times 10^6$ and $n = 4.6$ for both the alpha and beta phases of titanium. $D_v = 1.0 \exp(-58,000/RT)$ for the alpha phase and $D_v = 1.0 \exp(-50,000/RT)$ for the beta phase.

Nabarro-Herring creep was given by

$$\dot{\epsilon}_4 = 14(D_v \Omega / kT d^2)\sigma \quad (5.78a)$$

where Ω is the atomic volume. When instead grain boundary diffusion controls the deformation, the creep is called Coble creep and is given by

$$\dot{\epsilon}_5 = 14(D_b \Omega \pi \delta / kT d^3)\sigma \quad (5.81)$$

where δ is the effective cross section of a grain boundary for diffusional transport and D_b is the boundary diffusion coefficient. δ was taken to be $2b$, $D_b = 0.8D_v$ and $\Omega = 1.76 \times 10^{-23} \text{ cm}^3$ for the alpha phase and 1.85×10^{-23} for the beta phase.

Fracture mechanism maps (Ref. 444) constructed by Rao, Rao and Roa (Refs. 423 and 445) for iodide titanium and commercial purity titanium (0.5 to 1.0 at.% C_i) are depicted in Fig. 5.70. The observed fracture modes in iodide titanium in order of increasing temperature are: ductile fracture, transgranular creep fracture and rupture. In addition to these modes, commercial titanium exhibits cleavage at low temperatures and intergranular creep fracture at intermediate temperatures. Thus, increasing the interstitial content in titanium leads to embrittlement both at low and intermediate temperatures. Furthermore, the temperature for the occurrence of rupture is increased. These changes in the fracture modes are in keeping with the decrease in ductility which results when the interstitial content is increased; see for example Figs. 4.114 and 4.119.

Alternate plots of the fracture mechanism map for commercial purity titanium are presented in Figs. 5.71 and 5.72. These plots reveal features not clearly evident in Fig. 5.70.

5.5 Tensile Instability

Santhanam and Reed-Hill (Ref. 179) considered the necking characteristics and related ductility of commercial purity titanium rod specimens deformed at temperatures in the vicinity of the ductility minimum, i.e. at temperatures of 600-1000K for strain rates of 10^{-5} to 10^{-3} s^{-1} ; see Figs. 5.73 and 5.74. In the high temperature, high ductility region the specimen exhibited a diffuse neck (Fig. 5.75a) and a large necking strain (Fig. 5.74), whereas in the minimum ductility region the neck was sharply localized (Fig. 5.75b) and the necking strain was small. Further, they noted that the strain hardening rate exhibited a maximum at a temperature very close to that at which the necking strain increases abruptly; compare Fig. 5.76 with

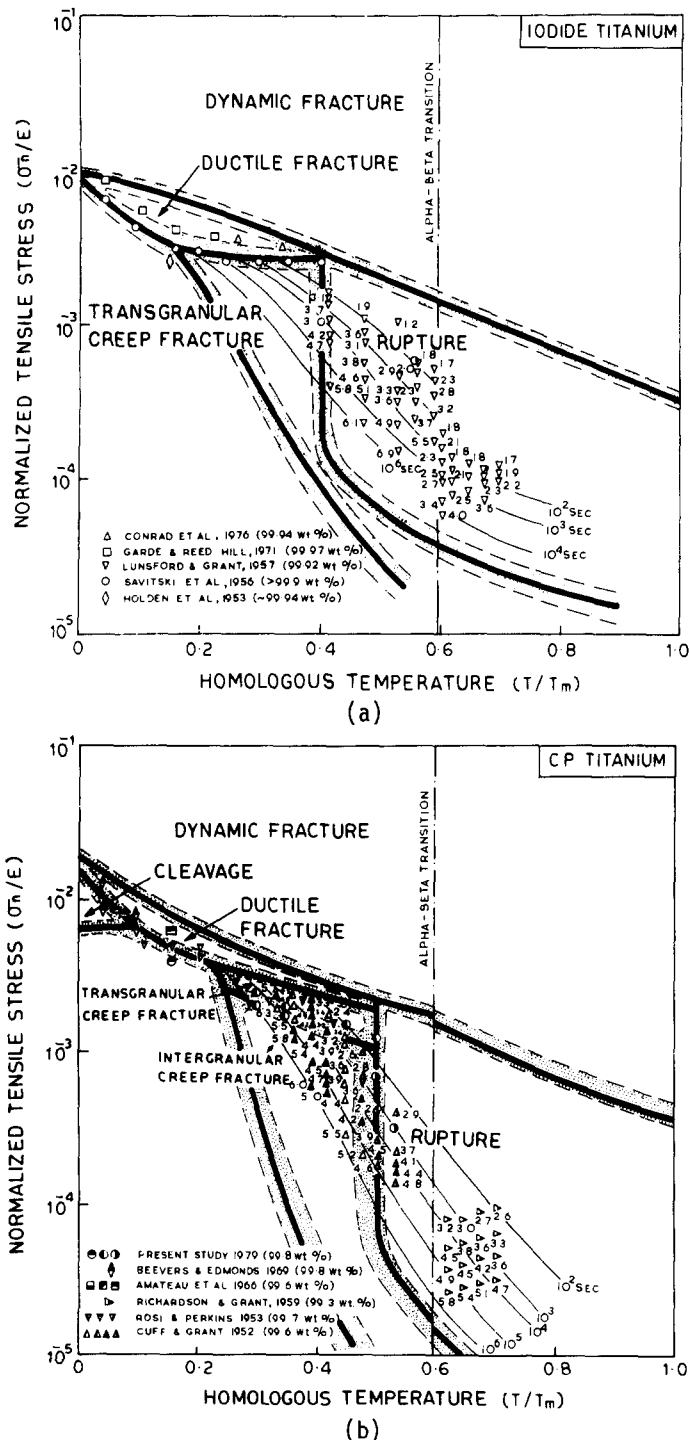


Fig. 5.70 Fracture mechanism maps for (a) iodide titanium and (b) commercial purity (CP) titanium. From Rao, Rao and Rao (Refs. 423 and 445).

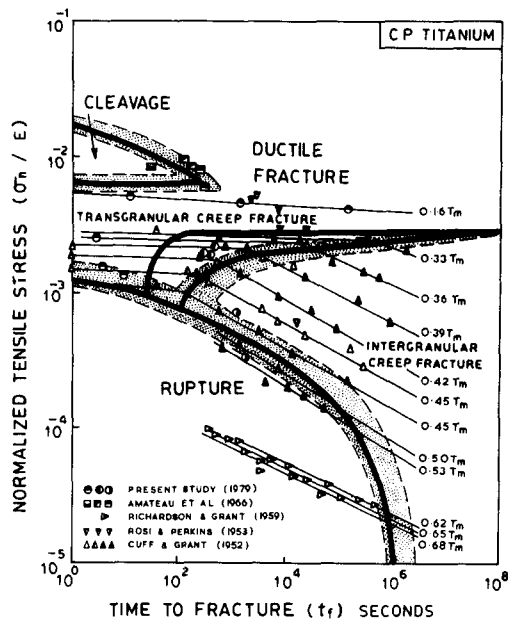


Fig. 5.71 Fracture mechanism map of the second type for CP titanium. Superimposed straight lines are isothermal stress-rupture lines. From Rao, Rao and Rao (Ref. 423).

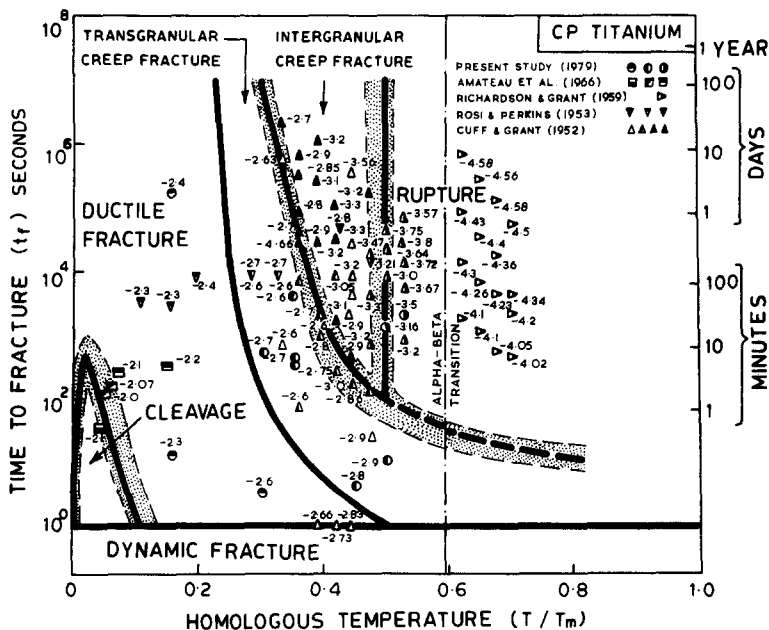


Fig. 5.72 Fracture mechanism map of the third type for CP titanium. Points are marked with the logarithm of the normalized tensile stress. From Rao, Rao and Rao (Ref. 423).

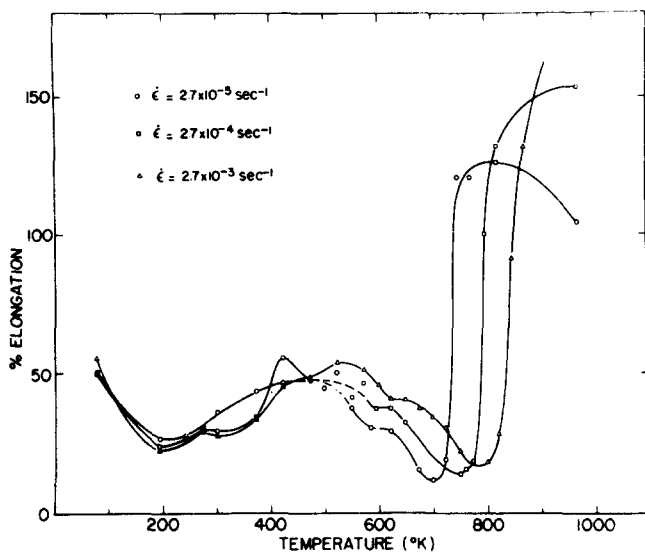


Fig. 5.73 Effect of temperature on the tensile elongation of commercial purity titanium deformed at three strain rates. From Santhanam and Reed-Hill (Ref. 179).

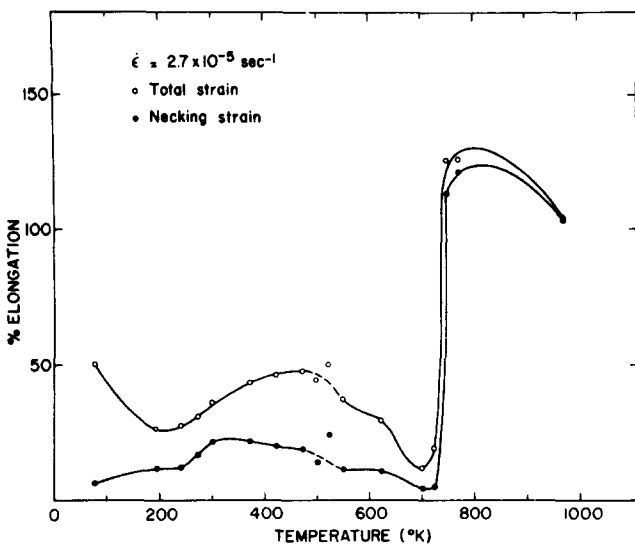


Fig. 5.74 Effect of temperature on the total tensile elongation and on the necking elongation of commercial purity titanium deformed at a strain rate of $2.7 \times 10^{-5} \text{ s}^{-1}$. From Santhanam and Reed-Hill (Ref. 179).

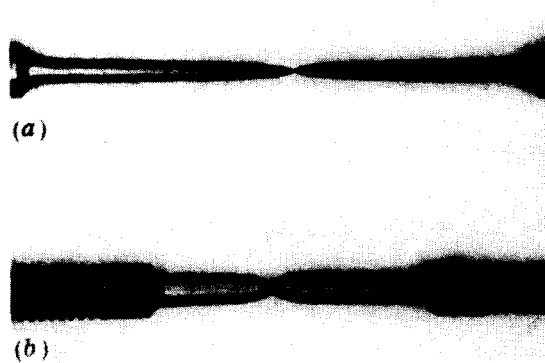


Fig. 5.75 Profiles of fractured cylindrical tensile specimens of commercial purity titanium exhibiting two types of necking behavior: (a) extended or diffuse neck and (b) sharp localized neck. From Santhanam and Reed-Hill (Ref. 179).

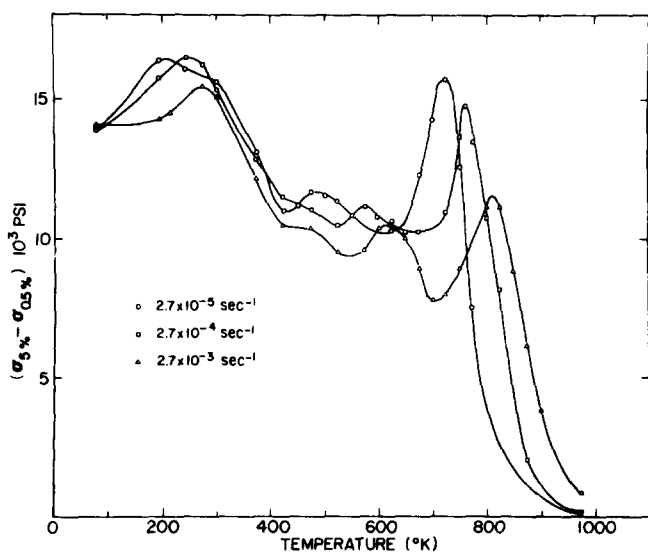


Fig. 5.76 Effect of temperature on the strain hardening parameter $\Delta\sigma$ given by the difference in flow stress at the strains of 5% and 0.5%. From Santhanam and Reed-Hill (Ref. 179).

Fig. 5.74. Moreover, the maximum in the strain hardening rate moved to higher temperatures with increasing strain rate in a manner analogous to the change of the ductility minimum (compare Figs. 5.76 and 5.73).

The growth of the neck in titanium for these conditions was rationalized by Santhanam and Reed-Hill (Ref. 179) in terms of the effect of strain rate on the flow stress, as proposed by Nadai and Manjoine (Ref. 446). However, since the strain rate sensitivity of the flow stress remained quite small throughout the temperature region of both the ductility minimum and the subsequent rapid increase in elongation (Fig. 4.43), they concluded that this effect of strain rate could not be the cause for the observed changes in necking behavior and ductility. Instead, they concluded that the changes were due to the influence of strain rate on strain hardening. As indicated in Fig. 5.76, an increase in strain rate near the strain hardening maximum gives a decrease in strain hardening; this in turn was considered to lead to localization of the neck. At high temperatures, the increase in strain rate produces an increase in strain hardening, leading to a diffuse neck. Strain rate cycling tests in the same temperature regime supported these effects of strain rate on strain hardening. Santhanam and Reed-Hill thus concluded that the large tensile elongation observed immediately above the ductility minimum temperature resulted from the development of a diffuse neck whose growth was governed by the strain rate dependence of the work hardening associated with dynamic strain aging. The sharp neck observed in the minimum ductility temperature region was attributed to the decrease in work hardening rate with increase in strain rate which occurs at these temperatures. The diffuse neck observed at temperatures above about 850K, where the strain hardening and its strain rate dependence become small but the strain rate sensitivity of the flow stress becomes large (Fig. 4.43), was considered to result from the same conditions as those which lead to superplasticity (Refs. 447, 448).

Tensile instability in A-75 titanium sheet specimens deformed at 300-700K and strain rates of 1.33×10^{-4} to $1.33 \times 10^{-2} s^{-1}$ was investigated by Okazaki, Kagawa and Conrad (Ref. 449). Both diffuse and local necking (e.g. Fig. 5.77) were considered. Starting with the relation which describes the fact that the variation of the load along the length of the specimen is zero and assuming that slight

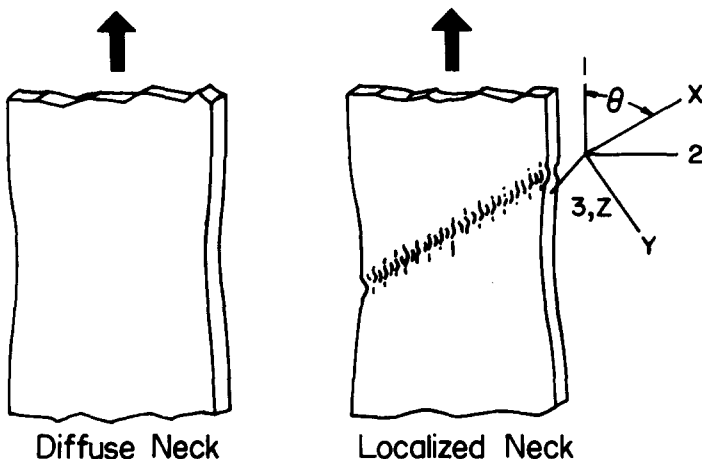


Fig. 5.77 Diffuse and local necking in sheet metal tensile specimens.

variations in the original cross-section area A_0 may exist along the length of the specimen, they derived the following equation for the critical strain at which diffuse necking occurs

$$\varepsilon_d^* = n'_d + \delta \ln A_0 / \delta \ln \varepsilon \quad (5.82)$$

$$= n'_d + \text{Const.} \quad (5.82a)$$

where $n'_d = (\partial \ln \sigma / \partial \ln \varepsilon)$ at $\varepsilon = \varepsilon_d^*$. For tests at constant crosshead speed, one can show (Ref. 450) that for strains up to the beginning of diffuse necking

$$(\partial \ln \sigma / \partial \ln \varepsilon)_\dot{\varepsilon} = d \ln \sigma / d \ln \varepsilon + \dot{\varepsilon} (\partial \ln \sigma / \partial \ln \dot{\varepsilon})_\varepsilon \quad (5.83)$$

or

$$n' = n + m \dot{\varepsilon} \quad (5.83a)$$

where $n = d \ln \sigma / d \ln \varepsilon$ is generally called the strain hardening exponent and $m = \partial \ln \sigma / \partial \ln \dot{\varepsilon}$ the strain rate hardening exponent.

Taking the criterion for local necking to be (Ref. 451)

$$d\sigma/d\varepsilon = \sigma/Z$$

where Z has a value of two for isotropic materials, Conrad (Ref. 452) derived the following equation for the critical strain for local necking in sheet specimens

$$\varepsilon_l^* \approx 2(n_l' + m_l \alpha_l) \quad (5.84)$$

where $\alpha = d \ln \dot{\varepsilon} / d \ln \varepsilon$ gives the strain rate increase which occurs within the diffuse neck as it develops. The subscript l refers to the values at the initiation of the local neck. Assuming that n' and m do not change appreciably following the maximum load and inserting Eq. 5.83a for n' into Eq. 5.84 one obtains for ε_l^*

$$\varepsilon_l^* \approx 2\{n_u + m_u(\alpha_l + \varepsilon_u)\} \quad (5.84a)$$

Eq. 5.84a thus provides an expression for the critical local necking strain in terms of the strain localization parameter α and the material parameters m and n . It can be checked by comparing the measured value of ε_l^* with that predicted by the right hand side (RHS) of Eq. 5.84a.

In the study of tensile instability in A-75 Ti sheet by Okazaki, Kagawa and Conrad (Ref. 449) the strain hardening exponent n was derived as a function of strain from the true stress-strain curves through

$$n = d \ln \sigma / d \ln \varepsilon = (\varepsilon / \sigma) (d\sigma/d\varepsilon) \quad (5.85)$$

The strain rate hardening exponent m was determined by strain rate cycling tests using

$$m = \partial \ln \sigma / \partial \ln \dot{\varepsilon} = \ln(P_2/P_1) / \ln(v_2/v_1) \quad (5.86)$$

where P_1 and P_2 are the loads prior to and following the crosshead speed change from v_1 to v_2 . Typical variations of n and m with strain are illustrated in Figs. 5.78 and 5.79. To be noted in Fig. 5.78 that n is not constant, as is often presumed, but increases with strain, reaching a maximum value near the maximum load, where $n = \varepsilon_u$. In general, the variation of n with strain at the other temperatures investigated (400K, 500K and 700K) was similar. Generally the m values decreased with strain, reaching relatively constant values at strains near the maximum load, as shown in Fig. 5.79. An unusual behavior was however found for the test at 700K

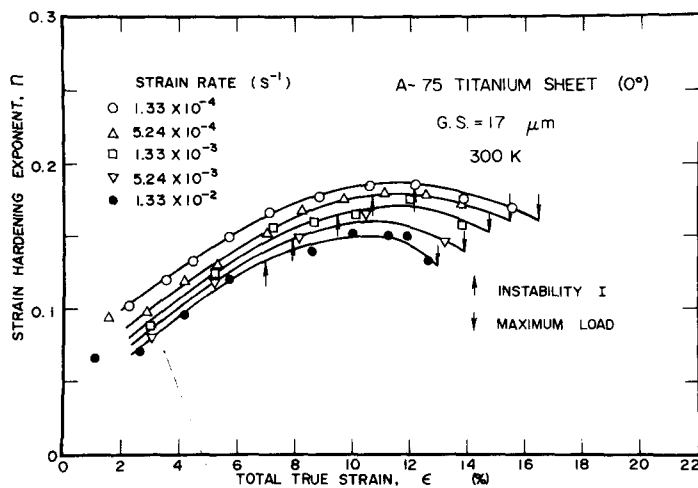


Fig. 5.78 Strain hardening exponent n versus true strain as a function of strain rate for A-75 Ti sheet deformed at 300K. From Okazaki, Kagawa and Conrad (Ref. 449).

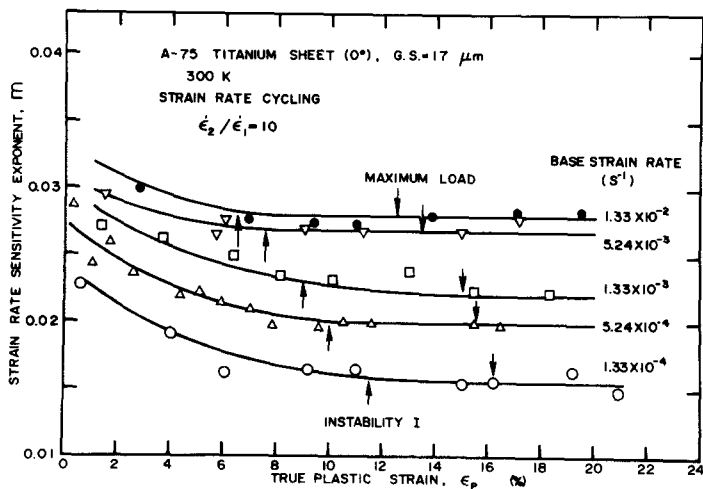


Fig. 5.79 Strain rate hardening exponent m versus true strain as a function of strain for A-75 Ti deformed at 300K. From Okazaki, Kagawa and Conrad (Ref. 449).

(Fig. 5.80), where the m value was initially very small (an order of magnitude smaller than for the other testing conditions). A rather significant drop in m is seen to occur up to the first appearance of a tensile instability following which m increases very rapidly. This results from the fact that once instability begins, the strain rate in the neck region becomes higher than during the prior uniform deformation and m increases accordingly, for m increases markedly with strain rate at 700K (Ref. 449).

The values of α_ℓ were obtained from measurements of the strain localization during diffuse necking employing gridded specimens and step-wise loading. An example of the distribution of the longitudinal and width strains ϵ_1 and ϵ_2 along the length of the specimen noted after each loading step in the series of (1) to (5) is given in Fig. 5.81. Since the test was performed at a constant crosshead speed, each loading step corresponds to a specific time and a curve of ϵ_1 versus time for the element which eventually fractured can be derived; see, for example, Fig. 5.82. $\dot{\epsilon}_1$ is then obtained as a function of ϵ from the slope of the curve given in Fig. 5.82. The slopes of log-log plots of $\dot{\epsilon}_1$ versus ϵ_1 (e.g. Fig. 5.83) at $\epsilon_1 = \epsilon_1^*$ yield the parameter α_ℓ , which ranged between 1.2 and 10.0 for the test conditions investigated.

To be noted in Fig. 5.83 is the sharp change in slope from slightly negative (resulting from the fact that the tests were performed at a constant crosshead speed rather than a constant strain rate) to a rapidly increasing positive value, indicative of the occurrence of a plastic instability. The strain associated with this first evidence of plastic instability is designated as ϵ_I^* and is considered to represent the initiation of diffuse necking, i.e. $\epsilon_I^* = \epsilon_d$. The value of ϵ_I^* is

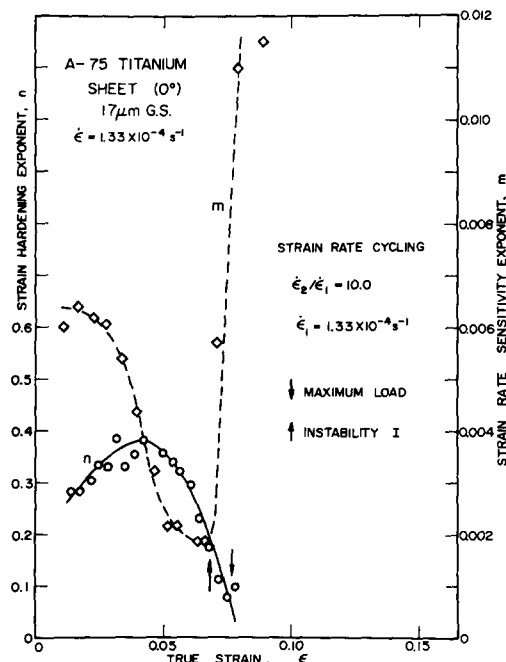


Fig. 5.80 Strain hardening exponent n and strain rate hardening exponent m versus true strain for the deformation of A-75 Ti at 700K and a strain rate of $1.33 \times 10^{-4} \text{ s}^{-1}$. From Okazaki, Kagawa and Conrad (Ref. 449).

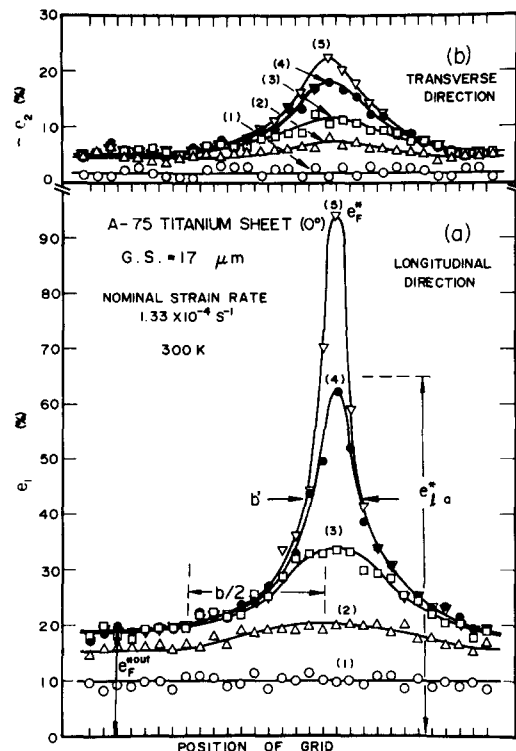


Fig. 5.81 Engineering strain distribution along the length of an A-75 Ti specimen deformed at 300K and a strain rate of $1.33 \times 10^{-4} \text{ s}^{-1}$: (a) longitudinal strain e_1 and (b) width strain e_2 . From Okazaki, Kagawa and Conrad (Ref. 449).

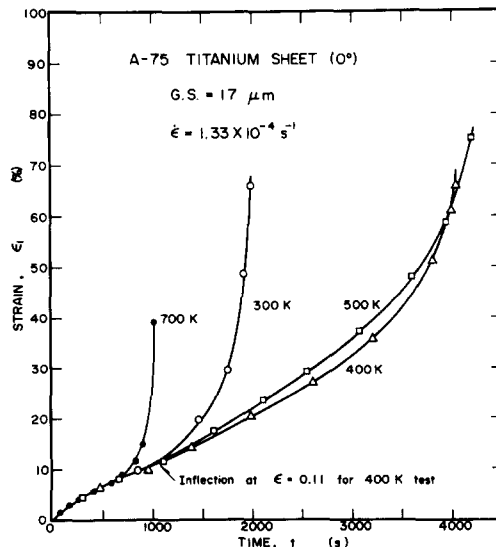


Fig. 5.82 Longitudinal strain ϵ_1 versus time for the grid element which eventually fractured in tests at 300-700K and a strain rate of $1.33 \times 10^{-4} \text{ s}^{-1}$. From Okazaki, Kagawa and Conrad (Ref. 449).

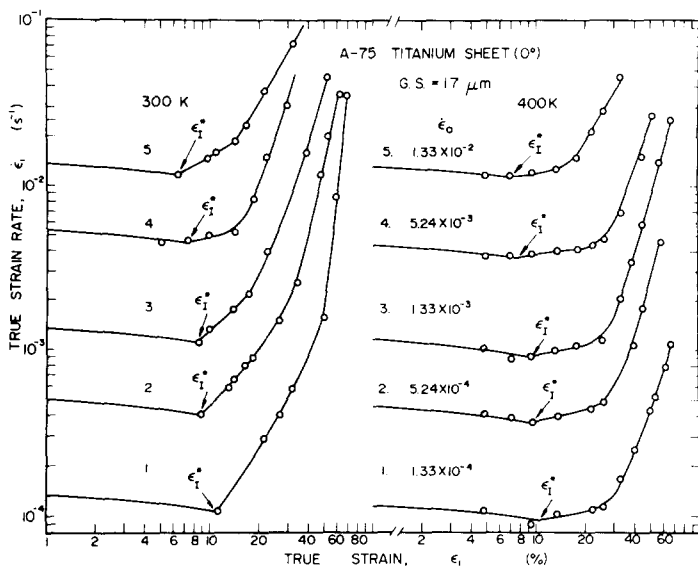


Fig. 5.83 Log-log plots of $\dot{\epsilon}_1$ versus ϵ_1 of the grid elements which eventually fractured for tests at 300 and 400K. From Okazaki, Kagawa and Conrad (Ref.449).

less than ϵ_u , in keeping with the instability criterion defined by Eq. 5.82.

According to Eq. 5.82 one expects ϵ_1^* ($=\epsilon_d^*$) to increase linearly with n_I ($\approx n_d$), since m_e is small). Fig. 5.84 shows that this occurs. The data points at 300 and 400K were obtained for one batch of machined specimens and can be considered to lie on one straight line, whereas another straight line can be drawn through the data points for tests at 500 and 700K, representing a different batch of machined specimens. The two batches had different radii at the shoulder fillets, the 500 and 700K having the sharper radius. Of significance regarding the two straight lines is that they intersect the abscissa. If a specimen did not contain a geometrical

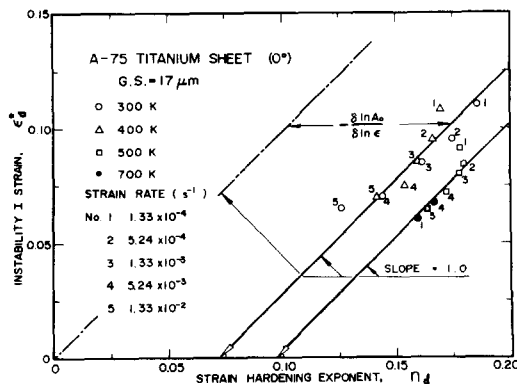


Fig. 5.84 The critical strain for diffuse necking ϵ_d^* versus the strain hardening exponent n_d . From Okazaki, Kagawa and Conrad (Ref. 449).

defect, the straight line relation between ϵ_l^* and n_I should pass through the origin and instability would occur at $\epsilon_u = n_u$, i.e. at the maximum load. The existence of a geometrical defect therefore shifts the straight line from the origin to the right by an amount equal to the factor $-\delta \ln A_0 / \delta \ln \epsilon$. Evident in Fig. 5.84 is that a larger shifting occurs for specimens which have a smaller radius at the fillets.

The critical strain for local necking ϵ_l^* was determined by two methods: (a) the average value of ϵ_l for the grid elements adjacent to the one which fractured (Fig. 5.81) and (b) the value derived from the angle the fracture surface makes with the tensile axis and assuming that local necking represents a condition of plane strain. The critical strains for these two methods are designated $\epsilon_{l_a}^*$ and $\epsilon_{l_b}^*$, respectively in Fig. 5.85, which is a plot of ϵ_l^*/Z versus the combined parameter $\{n_u + m_u(\alpha_l + \epsilon_u)\}$. It is seen from Fig. 5.85 that the measured values of ϵ_l^* conform reasonably well to those given by the RHS of Eq. 5.80.

Finally, from the above considerations it is evident that one must be careful in the choice of the values for strain hardening and strain rate hardening parameters in evaluating necking characteristics, especially if these parameters vary appreciably with strain or strain rate as found in Figs. 5.78 to 5.80. One can be misled if they are taken from the early stages of deformation, where in addition to a smaller strain, the strain rate may be one to two orders of magnitude lower than that existing in a fully developed neck.

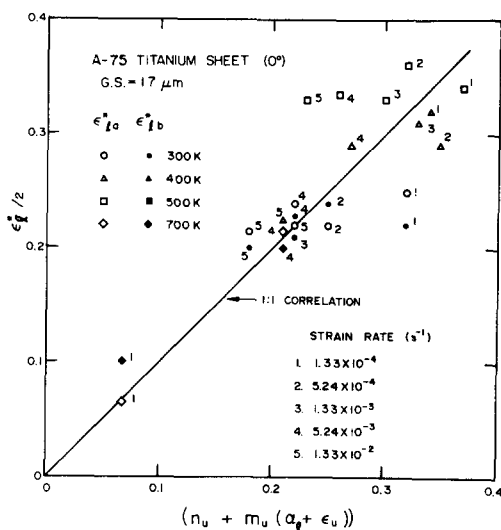


Fig. 5.85 One-half the critical strain for local necking ϵ_l^*/Z versus the parameter $\{n_u + m_u(\alpha_l + \epsilon_u)\}$. From Okazaki, Kagawa and Conrad (Ref. 449).

ACKNOWLEDGEMENTS

The author wishes to acknowledge that initial support for his studies into the mechanical properties of titanium was provided by a grant in 1965 from the Metals Research Foundation, a charitable foundation set up by Dr. William Justin Kroll. Subsequent support was provided by the Air Force Materials Laboratory and by a Themis Grant from the Air Force Office of Aerospace Research. The sustained encouragement of Dr. H. Gegele and Dr. H. Burte of the Air Force Materials Laboratory throughout the author's research efforts has been greatly appreciated.

The author also wishes to express his sincere appreciation to his colleagues and students for their many contributions to both the experimental results and the ideas presented here. Special thanks are due to Dr. K. Okazaki for his sustained contributions.

Finally, the author wishes to thank Mrs. Terri Potter and Mrs. Ruby Land for their efforts in typing the manuscript.

REFERENCES

1. R. I. Jaffee, Prog. Met. Phys. 7, 65 (1968).
2. H. Conrad, M. Doner and B. de Meester, Titanium Science and Technology, Plenum Press, New York, 969 (1973).
3. H. Conrad, B. de Meester, M. Doner and K. Okazaki, Physics of Solid Solution Strengthening, ASM, Cleveland, p1 (1975).
4. W. R. Tyson, Physics of Solid Solution Strengthening, ASM, Cleveland (1975), p.47
5. Metals Handbook, 8th Ed., Vol. 1, ASM, Cleveland (1961).
6. C. Kittell, Introduction to Solid State Physics, Wiley, New York (1968).
7. L. Kaufman, Acta Met. 7, 575 (1959).
8. E. W. Collings and J. C. Ho, The Science Technology and Application of Titanium, Pergamon Press, New York, (1970), p.331.
9. A. D. McQuillan and M. K. McQuillan, Titanium, Academic Press, New York (1956).
10. M. Hansen, Constitution of Binary Alloys, 2nd Ed., McGraw-Hill, New York (1958).
11. S. Weismann and A. Shrier, The Science Technology and Application of Titanium, Pergamon Press, New York, (1970) p. 441.
12. R. I. Jaffee, H. R. Ogden and D. J. Maykuth, Trans. AIME 188, 1261 (1950).
13. G. A. Lenning, G. M. Craighead and R. I. Jaffee, Trans. AIME 200, 367 (1964).
14. F. H. Beck, "Effect of Hydrogen on the Mechanical Properties of Titanium and Its Alloys", NASA Grant No. NGL-36-008-051, Dept. Met. Eng., Ohio State University, Columbus (1975).
15. P. Ehrlich, Z. Anorg. Chem. 247, 53 (1941).
16. E. Bisogni, G. Mah and C. Wert, J. Less Com. Met. 7, 197 (1964).
17. S. Yamaguchi, M. Koiwa and M. Hirabayashi, J. Phys. Soc. Japan 21, 2096 (1966).
18. H. T. Clark, Jr., Trans AIME 185, 588 (1949).
19. W. L. Finlay and J. A. Snyder, Trans AIME 188, 277 (1950).
20. B. Holmberg, Acta Chem. Scand. 16, 1255 (1962).
21. D. Gupta and S. Weinig, Trans AIME 215, 209 (1959).
22. S. Anderson, B. Collen, U. Kuylenstierna and A. Magneli, Acta Chem. Scand. 11, 1641 (1957).
23. I. Cadoff and J. P. Nielsen, Trans AIME 197, 248 (1953).
24. B. Holmberg, B. and T. Dagerhamn, Acta Chem. Scand., 15 919 (1961).
25. M. D. Silver, P. H. Farrar and K. L. Komarek, Trans AIME, 227, 876 (1963).
26. L. Kaufman and H. Nesor, Titanium Science and Technology, Plenum Press, New York, (1973) p. 773.
27. P. E. Armstrong and H. L. Brown, Trans AIME 230, 962 (1964).
28. E. S. Fisher and G. J. Renken, Phys. Rev. 135, No. 2A, A482 (1964).
29. A. J. E. Foreman, Acta Met. 3, 322 (1955).
30. E. S. Fisher and L. C. R. Alfred, Trans. TMS-AIME 242, 1575 (1968).
31. R. Tang, J. Kratochvil and H. Conrad, Scripta Met. 3, 485 (1969).
32. H. Ogden, D. Maykuth, W. Finlay and R. I. Jaffee, Trans AIME 197, 267 (1953).
33. N. Hsu and H. Conrad, Scripta Met. 5, 905 (1971).
34. J. N. Pratt, W. J. Bratina and B. Chalmers, Acta Met. 2, 203 (1954).
35. S. G. Fedofov, Titanium and Its Alloys, Publ. No. 10, I. I. Kornilov Editor, Israel Prog. Sci. Trans., (1966) p. 199.
36. W. H. Graft, D. W. Levinson and W. Rostoker, Trans ASM 49, 263 (1957).
37. B. de Meester, "Deformation Kinetics in Titanium and Titanium Alloys at Low Temperatures", Ph.D. Dissertation, University of Kentucky, 1972.
38. G. Sargent and H. Conrad, Scripta Met. 6, 1099 (1972).
39. R. A. Swalin, Thermodynamics of Solids, 2nd Ed., Wiley, New York(1972).
40. P. G. Partridge, Met. Reviews 118, 169 (1968).
41. M. H. Yoo, Trans TMS-AIME, 245 2052 (1969).
42. D. Shechtman and D. G. Brandon, J. Mat. Sci. 8, 1233 (1973).
43. A. T. Churchman, Proc. Roy. Soc. A226, 216 (1954).
44. J. C. Williams and M. J. Blackburn, Phys. Stat. Sol. 25, K1 (1968).

45. T. R. Cass, The Science, Technology and Application of Titanium, Pergamon Press, New York, (1970) p. 459.
46. N. E. Paton and W. A. Backofen, Met. Trans. 1, 2839 (1970).
47. N. E. Paton, J. C. Williams and G. P. Rauscher, Titanium, Science and Technology, Plenum Press, New York, (1973) p. 1049.
48. N. E. Paton and J. C. Williams, 2nd Int. Conf. Strength of Metals and Alloys, Vol. I, ASM, Cleveland, (1970) p. 108.
49. J. F. Breedis and M. K. Koul, "Relationship of Structure to Strength in Titanium Alloys", Rept. AFML-TR-69-236 (1969).
50. D. A. Koss and J. C. Chesnutt, Titanium Science and Technology, Plenum Press, New York, (1973) p. 1097.
51. W. Tyson, Acta Met. 15, 574 (1967).
52. E. S. Fisher and L. C. R. Alfred, Trans TMS-AIME, 242, 1575 (1968).
53. L. J. Teutonicco, The Science, Technology and Application of Titanium, Pergamon Press, New York, (1970) p. 479.
54. L. J. Teutonicco, Mat. Sci. Eng. 6, 27 (1970).
55. L. J. Teutonicco, Titanium Science and Technology, Plenum Press, New York, (1973) p. 1009.
56. S. Mendelson, J. Appl. Phys. 41, 1893 (1970).
57. T. R. Cass, Trans. TMS-AIME 239, 1864 (1967).
58. M. J. Blackburn, Trans ASM 59, 694 (1966).
59. M. J. Blackburn and J. C. Williams, Trans. TMS-AIME, 239, 287 (1967).
60. L. Rice, C. P. Hinesley and H. Conrad, Metallog. 4, 252 (1971).
61. L. A. Rice and R. J. De Angelis, Metallog. 8, 241 (1975).
62. C. Feng and C. Elbaum, Trans AIME 212, 820 (1958).
63. H. Z. Burrier, M. F. Amateau and E. A. Steigerwald, "The Relationship Between Plastic Deformation and Fracture in Alpha Titanium", Tech. Rept. AFML-TR-65-329 (1965).
64. M. F. Amateau, H. I. Burrier and L. J. Ebert, Trans ASM 59, 920 (1966).
65. D. A. Meyn and G. Sandoz, Trans. TMS-AIME, 245, 1253 (1969).
66. R. J. H. Wanhill, Acta Met. 21, 1253 (1973).
67. A. W. Cochardt, G. Schoeck and H. Wiedersich, Acta Met. 3, 533 (1955).
68. R. L. Fleischer, Acta Met. 10, 835 (1962).
69. W. R. Tyson, Canad. Met. Quart. 6, 301 (1968).
70. W. R. Tyson, The Science, Technology and Application of Titanium, Pergamon Press, New York, (1970) p. 479.
71. F. R. N. Nabarro, Proc. Phys. Soc. 58, 669 (1946).
72. J. D. Eshelby, J. Appl. Phys. 25, 255 (1954).
73. H. Sthele and A. Seeger, Z. Physik 146, 217 (1956).
74. R. L. Fleischer, The Strengthening of Metals, Rheinhold, New York, (1964) p. 93.
75. I. Saxl, Nuclear Res. Inst., Czech. Acad. Sci. Reg. B14, 381 (1964).
76. A. H. Cottrell and B. A. Bilby, Proc. Phys. Soc., London A62, 49 (1949).
77. J. Friedel, Les Dislocations, Gauthier-Villars (1956); Dislocations, Addison-Wesley, Reading Mass. (1967).
78. R. L. Fleischer, Acta Met. 9, 996 (1961).
79. R. L. Fleischer, Acta Met. 11, 203 (1963).
80. G. Kostorz, Z. f. Metallog., 59, 941 (1968).
81. A. W. Cochardt, Acta Met. 3, 533 (1955).
82. A. Akhtar and E. Teghtsoonian, Phil. Mag. 25, 897 (1972).
83. P. Jax, P. Kratochvil and P. Haasen, Acta Met. 18, 237 (1970).
84. J. D. Eshelby, Solid State Physics, Vol. 3, Academic Press, New York (1957) p. 79.
85. W. R. Tyson, Scripta Met. 3, 917 (1969).
86. R. Labusch, Phys. Stat. Sol. 41, 659 (1970).
87. M. Šob, Phys. Stat. Sol. (a) 24K, 133 (1974).
88. M. Šob, J. Kratochvil and F. Kroupa, Czech. J. Phys. B25, 872 (1975).
89. P. Regnier and J. M. Dupouy, Phys. Stat. Sol. 28K, 55 (1968).
90. J. W. Christian, 2nd Int. Conf. Strength of Metals and Alloys, ASM, Cleveland, (1970) p. 29.

91. F. Kroupa and V. Vitek, Canad. J. Phys. 45, 945 (1967).
92. W. Frank and B. Sestak, Scripta Met. 4, 451 (1970).
93. C. Wuthrich and W. Frank, discussion in meeting on Defects in Refractory Metals, Mol, Belgium (1971).
94. V. Vitek, Phys. Stat. Sol. 22, 453 (1967).
95. O. Ruano and G. Elssner, J. Less-Common Met. 40, 121 (1975).
96. H. Susuki, Sci. Rept. Tohoku Univ. Res. Inst. 44, 455 (1952); Dislocations and Mechanical Properties of Crystals, Wiley, New York, (1957) p. 172.
97. A. Akhtar and E. Tehtsoonian, Met. Trans. 6A, 2201 (1975).
98. R. Tyson and H. Conrad, Met. Trans. 4, 2605 (1973).
99. A. H. Cottrell, S. C. Hunter and F. N. R. Nabarro, Phil. Mag. 44, 1064 (1953).
100. R. Labusch, Acta Met. 20, 917 (1972).
101. U. F. Kocks, A. S. Argon and M. F. Ashby, Prog. Mat. Sci. 19, 1 (1975).
102. J. Friedel, Electron Microscopy and Strength of Crystals, Interscience, New York, (1963) p. 634.
103. J. Friedel, Relation Between Structure and Strength in Metals and Alloys, HMSO, London, (1963) p. 410.
104. F. R. N. Nabarro, Proc. Phys. Soc. 58, 669 (1946).
105. N. F. Mott and F. R. N. Nabarro, Report on Strength of Solids, London Phys. Soc., (1948) p. 1.
106. N. F. Mott, Imperfections in Nearly Perfect Crystals, Wiley, New York, (1950) p. 173.
107. A. H. Cottrell, Dislocations and Plastic Flow in Crystals, Oxford University Press, London (1953).
108. R. L. Fleischer and W. R. Hibbard, Relation Between Structure and Strength in Metals and Alloys, HMSO, London (1963) p. 261.
109. U. F. Kocks, Phil. Mag., 13, 541 (1966).
110. U. F. Kocks, Canad. J. Phys. 45, 737 (1967).
111. U. F. Kocks, Proc. Int. Conf. on Strength of Metals and Alloys, Suppl. Trans. JIM 9, 1 (1968).
112. U. F. Kocks, Physics of Strength and Plasticity, MIT Press, Cambridge, (1969) p. 134.
113. A. S. Argon, Phil. Mag. 25, 1053 (1972).
114. A. J. E. Foreman and M. J. Makin, Phil. Mag. 14, 911 (1966).
115. L. M. Brown and R. K. Ham, Strengthening Methods in Crystals, Applied Science Publishers, London, (1971) p. 12.
116. B. R. Riddhagni and R. M. Asimow, J. Appl. Phys. 39, 4144, 5169 (1968).
117. F. R. N. Nabarro, J. Less Common Met. 28, 257 (1972).
118. J. P. Hirth and J. Loethe, Theory of Dislocations, McGraw-Hill (1968).
119. U. F. Kocks, R. Labusch and R. B. Schwarz, 4th Int. Conf. Strength of Metals and Alloys, Lab. Phys. Solid, Nancy, France, (1976) p. 275.
120. U. F. Kocks, Mat. Sci. Eng. 27, 291 (1977).
121. T. J. Koppenael and D. Kuhlmann-Wilsdorf, Appl. Phys. Let. 4, 59 (1964).
122. B. de Meester, C. Yin, M. Doner and H. Conrad, Rate Processes in Plastic Deformation of Materials, ASM, Cleveland, (1975) p. 175.
123. A. V. Granato, K. Lücke, J. Schlipf and L. J. Teutonico, J. Appl. Phys. 35, 2732 (1964).
124. H. Eyring, J. Chem. Phys. 4, 283 (1936).
125. S. Glasstone, K. Laidler and H. Eyring, Theory of Rate Processes, McGraw-Hill, New York (1964).
126. W. Frank and R. Frydman, Phys. Stat. Sol. (b) 64, 539 (1974).
127. U. F. Kocks, Met. Trans. 1, 1121 (1970).
128. G. Schoeck, Phys. Stat. Sol. 8, 499 (1965).
129. T. Surek, L. G. Juon, M. J. Luton and J. J. Jonas, Rate Processes in Plastic Deformation of Materials, ASM, Cleveland, (1975) p. 629.
130. W. Frank, Phys. Stat. Sol. 26, 197 (1968).
131. W. Frank, Fundamental Aspects of Dislocation Theory, Nat. Bur. Stand., (U.S.) Spec. Pub. 317, II, (1970) p. 1065.

132. R. Labusch, G. Grange, J. Ahearn and P. Haasen, Rate Processes in Plastic Deformation of Materials, ASM, Cleveland, (1975) p. 26.
133. J. D. Baird, The Inhomogeneity of Plastic Deformation, ASM, Cleveland, (1973) p. 191.
134. Y. Bergstrom, Mat. Sci. Eng., 5, 193 (1969-70).
135. Y. Bergstrom and W. Roberts, Acta Met., 19, 815 (1971).
136. J. E. Bird, A. K. Mukherjee and J. E. Dorn, Quantitative Relation Between Properties and Microstructure, Israel University Press, Jerusalem, (1969) p. 255.
137. A. Akhtar and E. Teightsoonian, Met. Trans. 6A, 2201 (1975).
138. T. Tanaka and H. Conrad, Acta Met. 20, 1019 (1972).
139. C. Brehm and P. Lehr, Mem. Sci. Rev. Metallurg. 68, 277 (1971).
140. P. Haasen, Phil. Mag. 3, 384 (1958).
141. A. Seeger, R. Berner and H. Wolf, Z. Phys. 155, 247 (1959).
142. T. Sakai and M. E. Fine, Scripta Met. 8, 541 (1974).
143. A. Akhtar, Met. Trans. 6A, 1105 (1975).
144. T. R. Cass and W. R. Spencer, "Deformation and Strengthening Mechanisms for Solid Solution Phases of Titanium", Martin Marietta Corp. TMR No. 3, Contract AF 33(615)-3863, 1 Sept. 1967 to 29 Feb. 1968.
145. G. Elssner, V. Krohn and O. Ruano, Z.f. Metallkde 67, 311 (1976).
146. A. Seeger, Dislocations and Mechanical Properties of Crystals, Wiley, New York, (1957) p. 243.
147. T. Sakai and M. E. Fine, Acta Met. 22, 1359 (1974).
148. E. Levine, Trans AIME 236, 1558 (1964).
149. V. A. Moskalenko and V. A. Puptsova, Fiz. Metal. Metalloved 34, 264 (1972).
150. P. Soo and G. T. Higgins, Acta Met. 16, 177 (1968).
151. H. Conrad, Acta Met. 14, 1631 (1966).
152. T. Tanaka and H. Conrad, Acta Met. 19, 1001 (1971).
153. T. Sakai and M. E. Fine, Scripta Met. 8, 541 (1974).
154. E. Anderson, D. C. Jillson and S. R. Dunbar, Trans AIME 197, 1191 (1953).
155. F. D. Rosi, C. H. Dube and B. H. Alexander, Trans AIME 197, 257 (1953).
156. F. D. Rosi, F. C. Perkins and L. L. Seigle, Trans AIME 206, 115 (1956).
157. T. S. Liu and M. A. Steinberg, J. Met. 4, 1043 (1952).
158. S. Fujishiro and J. W. Edington, "Mechanical Twinning of Titanium Single Crystals", Tech. Rept. AFML-TR-70-176 (1970).
159. T. S. Liu and M. A. Steinberg, Trans. AIME 200, 697 (1954).
160. K. Okazaki, Y. Eguchi and H. Conrad, "Deformation Kinetics in Dilute Ti-Al and Ti-Sn Alloys", Int. Conf. on Titanium, Moscow (May 1976).
161. K. Okazaki and H. Conrad, Met. Trans. 3, 2411 (1972).
162. T. Sakai and M. E. Fine, Scripta Met. 8, 545 (1974).
163. M. Doner and H. Conrad, Met. Trans. 4, 2809 (1973).
164. D. N. Williams and D. S. Eppelsheimer, Trans. AIME 197, 1378 (1953).
165. C. J. McHargue and J. P. Hammond, Trans. AIME 197, 57 (1953).
166. H. Hu and R. S. Cline, TMS-AIME 242, 1013 (1968).
167. C. Yin, M. Doner and H. Conrad, J. Less Common Met. 33, 229 (1973).
168. K. Okazaki and H. Conrad, Trans. JIM 13, 198 (1972).
169. H. Conrad, K. Okazaki, V. Gadgil and M. Jon, Electron Microscopy and Strength of Materials, Univ. Calif. Press, Berkeley (1973) p. 438.
170. C. Yin, "Deformation Kinetics in Commercial Ti-50A at Low Temperatures", Ph.D. thesis, Univ. of Kentucky (1975).
171. A. Garde, A. Santhanam and R. Reed-Hill, Acta Met. 20, 215 (1972).
172. K. Okazaki and H. Conrad, Acta Met. 21, 1117 (1973).
173. E. B. Kula and T. S. DeSisto, ASTM STP 387, (1966) p. 3.
174. N. M. Madhava and R. W. Armstrong, Met. Trans. 5, 1517 (1974).
175. H. Conrad, T. Tanaka and C. Yin, unpublished research, Univ. of Kentucky (1971).
176. C. Yin, M. Doner and H. Conrad, Met. Trans. 6A, 1901 (1975).
177. A. T. Santhanam, Ph.D. thesis, Univ. of Florida (1971).

178. R. E. Reed-Hill, Met. Reviews 2, 218 (1974).
179. A. T. Santhanam and R. E. Reed-Hill, Met. Trans. 2, 2619 (1971).
180. S. N. Monteiro, A. T. Santhanam and R. E. Reed-Hill, The Science, Technology and Application of Titanium, Pergamon Press, New York (1970) p. 503.
181. J. Harding, "The Temperature and Strain Rate Sensitivity of α -Titanium", Report No. 1108/74, Univ. of Oxford (Oct. 1974).
182. Y. Lii, V. Ramachandran and R. Reed-Hill, Met. Trans. 1, 447 (1970).
183. F. D. Rosi and E. C. Perkins, Trans. ASM 45, 972 (1953).
184. R. Zeyfang, R. Martin and H. Conrad, Mater. Sci. Eng. 8, 134 (1971).
185. K. Stetina, Scripta Met. 3, 57 (1969).
186. N. R. Kiessel and M. J. Sinnott, Trans. AIME 197, 331 (1953).
187. F. B. Cuff and H. J. Grant, Iron Age 170, 134 (1952).
188. D. R. Luster, W. W. Went and D. W. Kaufman, Materials and Methods 37, 100 (1953).
189. S. Agrawal, G. Sargent and H. Conrad, Met. Trans. 4, 2613 (1973).
190. S. Agrawal, G. Sargent and H. Conrad, J. Less Common Met. 34, 201 (1974).
191. C. C. Law and D. N. Beshers, Scripta Met. 6, 635 (1972).
192. P. Rodriguez, P. Dasgupta, S. Mannon, S. Vagarali and K. Samuel, Scripta Met. 7, 671 (1973).
193. K. Okazaki and H. Conrad, JIM, 14, 368 (1973).
194. A. H. Garde and R. E. Reed-Hill, Met. Trans. 2, 2885 (1971).
195. A. H. Garde, E. Aigltinger and R. Reed-Hill, Met. Trans. 4, 2461 (1973).
196. J. C. Williams, A. Sommer and P. Tung, Met. Trans. 3, 2979 (1972).
197. H. Conrad, unpublished research, Univ. of Kentucky (1973).
198. J. C. R. Guimaraes and R. J. De Angelis, Met. Trans. 4, 2379 (1973).
199. M. Keshavan, G. Sargent and H. Conrad, Met. Trans. 6A, 1291 (1975).
200. R. Reed-Hill, E. Buchanan and F. Calfwell, Trans. AIME 233, 1716 (1965).
201. J. C. R. Guimaraes and R. J. De Angelis, Mater. Sci. Eng. 13, 109 (1974).
202. J. C. R. Guimaraes and R. J. De Angelis, private communication, Univ. of Kentucky (1976).
203. J. Freidel, Electron Microscopy and Strength of Crystals, Interscience, New York (1963) p. 605.
204. R. Orava, G. Stone and H. Conrad, Trans. ASM 59, 171 (1966).
205. H. Conrad, Canad. J. Phys. 45, 581 (1967).
206. R. L. Jones and H. Conrad, Scripta Met. 2, 239 (1968).
207. H. Conrad and R. Jones, The Science Technology and Application of Titanium, Pergamon Press, New York (1970) p. 480.
208. K. Okazaki and H. Conrad, Trans. JIM 13, 205 (1972).
209. K. Okazaki, K. Morinaka and H. Conrad, Trans. JIM 14, 470 (1973).
210. K. Okazaki, M. Momochi and H. Conrad, Titanium Science and Technology, Vol. 2, Plenum Press, New York (1973) p. 1131.
211. K. Okazaki, K. Kanakogi and H. Conrad, Jap. Met. Soc. 37, 1250 (1973).
212. K. Okazaki, K. Morinaka and H. Conrad, Trans. JIM 15, 11 (1974).
213. K. Okazaki, T. Itoh and H. Conrad, Trans. JIM 15, 159 (1974).
214. K. Okazaki, K. Tanoue and H. Conrad, Jap. Met. Soc. 38, 300 (1974).
215. K. Okazaki and H. Conrad, Proc. 2nd Int. Conf. on Mechanical Behavior of Materials (ICM II) ASM, Cleveland (1976) p. 18.
216. K. Okazaki, Y. Eguchi and H. Conrad, Z. f. Metallkde. 67, 665 (1976).
217. R. Zeyfang and H. Conrad, Acta Met. 18, 985 (1971).
218. R. Zeyfang and H. Conrad, Z. f. Metallkde. 66, 422 (1975).
219. B. de Meester, M. Doner and H. Conrad, Met. Trans. 6A, 65 (1975).
220. S. Raghuraman, Ph.D. thesis, University of Kentucky (1976).
221. H. Conrad, "Research on Mechanical Behavior of Unalloyed Titanium and Some Selected Alloys", Semiannual Report No. 2, U.S. Air Force Contract F33615-68-C-1052 (Jan. 1969).
222. A. T. Santhanam, V. Ramachandran and R. E. Reed-Hill, Met. Trans. 1, 2593 (1970).

223. R. L. Jones, Titanium Science and Technology, Vol. 2, Plenum Press, New York (1973) p. 1033.
224. K. Okazaki, unpublished results, Kyushu Inst. Technology (1973).
225. H. Conrad, Project Themis "Metal Deformation Processing", Tech. Rept., AFML-TR-71-8 (Apr. 1971).
226. R. W. Armstrong and P. C. Jindal, Trans. TMS-AIME 242, 2513 (1968).
227. R. W. Armstrong, Ultra-fine Grain Metals, Syracuse Univ. Press (1970) p. 1.
228. K. Okazaki and H. Conrad, Trans. JIM 14, 364 (1973).
229. D. Tabor, Hardness of Metals, Clarendon Press, Oxford (1951).
230. J. Numes and F. R. Larson, J. Inst. Met. 91, 114 (1962-63).
231. D. J. Abson, The Science of Hardness Testing and Its Research Applications, ASM, Cleveland (1973) p. 13.
232. C. M. Brown, R. L. Folkman and M. Schussler, "Preliminary Report on the Properties of Sodium Reduced Titanium", AIME Regional Reactive Metals Conf., Buffalo, New York (Mar. 1956), reported in Ref. 1.
233. R. A. Wood, "Titanium Metallurgy Course", New York University (Sept. 1965).
234. G. A. Lenning, C. M. Craighead and R. I. Jaffee, AIME J. Met. (1954) p. 367.
235. C. Crussard and B. Jaoul, Rev. Met. 8, 589 (1950).
236. C. Crussard, Rev. Met. 10, 697 (1953).
237. B. Jaoul, J. Mech. Phys. Solids 5, 95 (1957).
238. M. K. Keshavan, G. A. Sargent and H. Conrad, unpublished results, University of Kentucky (1975).
239. G. A. Sargent, M. K. Keshavan and H. Conrad, Proc. 2nd Int. Conf. Strength of Materials (ICM-II), ASM, Cleveland (1976) p. 1682.
240. S. N. Monteiro and R. E. Reed-Hill, Met. Trans. 2, 2947 (1971).
241. V. Arunachalam, S. Pattanaik, S. Monteiro and R. E. Reed-Hill, Met. Trans. 3, 1009 (1972).
242. S. N. Monteiro and R. E. Reed-Hill, Met. Trans. 4, 1011 (1973).
- 242a. R. E. Reed-Hill, W. R. Cribb and S. N. Monteiro, Met. Trans. 4, 2665 (1973).
243. W. B. Morrison, Met. Trans. 2, 331 (1971).
244. G. W. Geil and N. C. Carwile, NBS Circular 500, Mechanical Properties of Metals at Low Temperatures (1952) p. 67.
245. H. Conrad, High Strength Materials, Wiley, New York (1965) p. 436.
246. R. L. Jones and H. Conrad, Trans. TMS-AIME 245, 779 (1969).
247. H. Conrad and K. Okazaki, Scripta Met. 4, 111 (1970).
248. A. Seeger, Z. f. Naturforsch. 9a 758, 810, 856 (1954); Handbuch der Physik VII/1 and VII/2, Springer, Berlin-Göttingen-Heidelberg (1955), (1958).
249. H. Conrad, Mater. Sci. Eng. 6, 265 (1970).
250. K. Okazaki and H. Conrad, Trans. JIM 13, 205 (1972); Trans. JIM 14, 368 (1973).
251. H. Conrad and K. Okazaki, Scripta Met., 4, 259 (1970).
252. K. Okazaki and H. Conrad, Proc. 2nd Int. Conf. on Mech. Behavior of Materials (ICM II) ASM, Cleveland, p. 18 (1976).
253. P. P. Tung and A. W. Sommer, Met. Trans., 1, 947 (1970).
254. K. Okazaki, Y. Aono, T. Kaneyuki and H. Conrad, Mater. Sci. Eng., 33, 253 (1978).
255. R. E. Reed-Hill and J. R. Donoso, Scripta Met., 9, 1305 (1975).
256. U. Essman, Phys. Stat. Solids, 12, 723 (1965).
257. M. Jon and H. Conrad, unpublished results, University of Kentucky (1971).
258. D. H. Sastry and K. I. Vasu, Acta Met., 20, 399 (1972).
259. B. deMeester, M. Doner and H. Conrad, Z.f. Metallkde., 64, 775 (1973).
260. H. Conrad, M. K. Keshavan and H. Conrad, Proc. 2nd Int. Conf. Mech. Behavior of Materials (ICM-II), Special Vol., ASM, Cleveland, p. 538 (1978).
261. R. L. Jones, F. W. Cooke, H. Conrad and B. R. Banerjee, "Investigations to Understand the Deformation and Strengthening Mechanisms of the Solid Solution Phases of Titanium," Franklin Inst., Tech. Rept., AFML-TR-68-28 (Feb. 1968).
262. P. W. Bridgman, Trans. ASM, 32, 553 (1944).

263. E. R. Marshall and M. C. Shaw, Trans. Asm, 44, 705 (1972).
264. R. I. Jaffee and I. E. Campbell, Met. Prog., 55, 356 (1949).
265. N. G. Turner and W. T. Roberts, Trans. TMS-AIME, 242, 1223 (1968).
266. H. A. Lipsitt and D. Y. Wang, Trans. AIME, 221, 918 (1961).
267. N. G. Turner and W. T. Roberts, J. Less-Common Met., 16, 37 (1968).
268. C. J. Beevers and J. L. Robinson, J. Less-Common Met., 17, 345 (1969).
269. D. I. Golland and C. J. Beevers, Met. Sci. Jnl., 5, 174 (1971).
270. D. I. Golland and C. J. Beevers, J. Less-Common Met., 23, 174 (1971).
271. J. L. Robinson and C. J. Beevers, Titanium Science and Technology, Vol. 2, Plenum Press, New York, p. 1245 (1973).
272. J. R. Donoso and R. E. Reed-Hill, Met. Trans., 8A, 945 (1977).
273. A. T. Santhanam and R. E. Reed-Hill, Scripta Met., 4, 529 (1970).
274. J. R. Donoso, P. G. Watson and R. E. Reed-Hill, Met. Trans., 10A, 1165 (1979).
275. J. R. Donoso, A. T. Santhanam and R. E. Reed-Hill, Proc. 2nd Int. Conf. on Mech. Behavior of Materials (ICM-II)- Special Vol. ASM, Cleveland, p. 515 (1978).
276. H. Sasano and H. Kimura, 3rd. Int. Conf. on Titanium, Moscow, Paper V-4, p. 117, (May 18-21, 1976).
277. H. J. Griest, A. M. Sabroff and P. D. Frost, Trans. ASM, 51, 935 (1959).
278. H. Bühler and H. W. Wagener, Bänder Blache Rohre, 6, 677 (1965).
279. M. Kehoe and R. W. Broomfield, Titanium Science and Technology, 4, Plenum Press, New York, p. 2167 (1973).
280. R. L. Orr, O. D. Sherby and J. E. Dorn, Trans. ASM, 46, 113 (1954).
281. V. Ramachandran, D. H. Baldwin and R. E. Reed-Hill, Met. Trans., 1, 3011 (1970).
282. C. Zener and J. H. Hollomon, J. Appl. Phys., 15, 22 (1944).
283. Z. S. Bazanski, Proc. Roy. Soc., 240A, 229 (1957).
284. J. C. Erdmann and J. A. Jahoda, "Calorimetry of Instantaneous Heat Sources Arising from Plastic Tensile Deformation at Low Temperatures," Document DI-82-0311, Boeing Scientific Research Lab. (Oct. 1963).
285. J. C. Erdmann and J. A. Jahoda, "Calorimetry of Transient Phenomena in Metals at Low Temperatures," Document DI-82-0384, Boeing Scientific Lab. (Oct. 1964).
286. G. Y. Chin, W. F. Hosford and W. A. Backofen, Trans. TMS-AIME, 230, 1043 (1964).
287. R. S. Culver, Metallurgical Effects at High Strain Rates, Plenum Press, New York, p. 519 (1973).
288. Y. V. R. K. Prasad, N. M. Madhova and R. W. Armstrong, "The Strengthening of HCP Materials Due to the Presence of Grain Boundaries," ONR Tech. Rept. No. 16, Contract No. N00014-67-A-0239-0011, NR031-79, (Jan. 1975).
289. C. Wang and H. Conrad, unpublished research, University of Kentucky (1976).
290. M. Ruhle, G. Elssner and O. Ruano, 9th Int. Congr. Electron Microscopy, 1, 336 (1978).
291. P. Haasen and R. Labusch, Mat. Sci. Eng., 12, 216 (1973).
292. O. D. Carlson, D. G. Alexander and G. Elssner, Met. Trans., 8A, 99 (1977).
293. R. Labusch and R. B. Schwarz, Nucl. Metall., 20, 650 (1976).
294. Z. S. Basinski, R. A. Foxall and R. Pascual, Scripta Met., 6, 807 (1972).
295. M. Z. Butt and P. Feltham, Acta Met., 26, 167 (1978).
296. H. L. Geigel and T. Duvall, "Thermally Activated Deformation in Alpha Titanium," Tech. Rept. AFML-TR-69-59, Air Force Materials Laboratory, Wright-Patterson Air Force Base, Ohio (April 1969).
297. K. R. Evans, Trans. TMS-AIME, 242, 649 (1968).
298. R. J. Arsenault and T. Cadman, Rate Processes in Plastic Deformation of Materials, ASM, Cleveland, p. 102, (1975).
299. R. L. Jones and H. Conrad, Acta Met., 15, 649 (1967).
300. K. Ono, J. App. Phys., 39, 503 (1957).
301. J. Kratochvil and H. Conrad, Scripta Met., 4, 815 (1970).

302. Z. S. Bazinski, Aust. J. Phys., 13, 284 (1960).
303. H. Conrad, R. Armstrong, H. Wiedersich and G. Schoeck, Phil. Mag., 6, 177 (1961).
304. A. Seeger, S. Mader and H. Kronmuller, Electron Microscopy and Strength of Crystals, Interscience, New York, p. 665, (1963).
305. M. Bocek and B. Kaska, Phys. Stat. Sol., 4, 325 (1964).
306. J. Friedel and G. Saada, Work Hardening, Met. Soc. Confs. Vol. 46, Gordon and Breach, New York, p. 1, (1966).
307. A. Seeger, Work Hardening, Met. Soc. Confs. Vol. 46, Gordon and Breach, New York, p. 27, (1966).
308. P. B. Hirsch and T. E. Mitchell, Work Hardening, Met. Soc. Confs. Vol. 46, Gordon and Breach, New York, p. 65 (1966).
309. H. Conrad, G. London and V. Damiano, Anisotropy in Single-Crystal Refractory Compounds, Vol. 2, Plenum Press, New York, p. 153 (1968).
310. J. V. Sharp, Proc. 6th Int. Conf. Electron Microscopy, Vol. I., Maruzen Co., Tokyo, p. 305 (1966).
311. G. Das and T. E. Mitchell, Met. Trans., 4, 1405 (1973).
312. D. B. Snow and J. F. Breedis, Proc. 2nd Int. Conf. Strength Metals and Alloys, Vol. II, ASM Cleveland, p. 418 (1970).
313. A. Akhtar and E. Teightsoonian, Acta Met., 19, 655 (1971).
314. H. S. Rosenbaum, Deformation Twinning, Gordon and Breach, New York, p. 43 (1964).
315. J. E. Dorn and S. Rajnak, Trans. AIME, 230, 1052 (1964).
316. J. Friedel, Internal Stress and Fatigue in Metals, Elsevier, Amsterdam, p. 238 (1959).
317. F. Aldinger, Beryllium Science and Technology, Plenum, New York, p. 7 (1979).
318. J. E. Dorn and J. B. Mitchell, High Strength Materials, Wiley New York, p. 510 (1965).
319. S. Boffi and G. Caglioti, Energ. Nucl., 20, 622 (1973).
320. P. Regnier and J. M. Dupouy, Phys. Stat. Sol., 39, 79 (1970).
321. T. G. Carnahan and T. E. Scott, Met. Trans., 4, 27 (1973).
322. L. P. Chupyatova, G. E. Chuprikov and D. N. Prokorova, Russian Met., 6, 128 (1974).
323. D. B. Snow and J. F. Breedis, Acta Met., 22, 419 (1974).
324. A. Seeger, Handbuch der Physik Vol III/1, Springer Verlag, Berlin-Heidelberg, p. 638 (1955).
325. G. B. Olson and M. Cohen, Met. Trans., 7A, 1897, 1905 (1976).
326. A. G. Crocker and M. Bevis, The Science, Technology and Application of Titanium, Pergamon Press, New York, p. 453 (1970).
327. M. O. Tucker, The Science, Technology and Application of Titanium, Pergamon Press, New York, p. 433 (1970).
328. R. L. Bell and R. W. Cahn, Proc. Roy. Soc., A239, 494 (1957).
329. R. W. Cahn, Deformation Twinning, Gordon and Breach, New York, p. 1 (1964).
330. D. Hull, Deformation Twinning, Gordon and Breach, New York, p. 121 (1964).
331. T. L. Altshuler and J. W. Christian, Acta Met., 14, 903 (1966).
332. S. Mendelson, The Strength of Metals and Alloys, Suppl. Trans. JIM Vol. 9, p. 812 (1968).
333. S. Mendelson, J. Appl. Phys., 41, 1893 (1970).
334. M. H. Yoo, Scripta Met., 2, 537 (1968).
335. U. F. Kocks and D. G. Westlake, Trans. TMS-AIME, 239, 1107 (1967).
336. R. von Mises, Z. Angew. Math. Mech., 8, 161 (1928).
337. G. I. Taylor, J. Inst. Met., 62, 307 (1938).
338. G. W. Graves and A. Kelley, Phil. Mag., 8, 877 (1963).
339. U. F. Kocks, Acta Met., 6, 85 (1954).
340. U. F. Kocks, Phil. Mag., 10, 187 (1964).
341. R. Clark and G. B. Craig, Progress Metal Physics, 3, 115 (1952).
342. M. L. Picklesimer, Electrochem. Technol., 4, 289 (1966).

343. C. Biwas, M. Cohen and J. F. Breedis, The Microstructure and Design of Alloys, Vol. 1, Proc. 3rd. Int. Conf. on Strength of Metals and Alloys, Cambridge, England, p. 16 (1973).
344. C. N. Reid, A. Gilbert and A. R. Rosenfield, Phil. Mag., 12, 409 (1965).
345. A. Gilbert, B. A. Wilcox and G. T. Hahn, Phil. Mag., 12, 649 (1965).
346. H. Conrad, S. Feuerstein and L. Rice, Mater. Sci. Eng., 2, 157 (1967).
347. H. Conrad, S. Feuerstein and L. Rice, Suppl. Trans. JIM, 9, 481 (1968).
348. J. J. Gilman, Micromechanics of Flow in Solids, McGraw-Hill, New York, p. 190 (1969).
349. Y. Bergström, Mater. Sci. Eng., 5, 193 (1969/70).
350. J. S. Koehler, Phys. Rev., 86, 52 (1952).
351. E. Orowan, Dislocations in Metals, AIME, New York, p. 69 (1954).
352. K. Okazaki, I. Masuda and H. Conrad, 3rd Int. Conf. Titanium, Moscow V-1, p. II-2 (May 18-21, 1976).
353. Y. Bergstrom, Mat. Sci. Eng., 9, 101 (1972).
354. Y. Bergstrom and B. Aronsson, Met. Trans., 3, 1951 (1972).
355. W. Roberts and Y. Bergstrom, Acta Met., 21, 457 (1973).
356. E. A. Metzbower, Met. Trans., 8A, 279 (1977).
357. H. Conrad, Electron Microscopy and Strength of Crystals, Interscience, New York, p. 299 (1961).
358. H. Conrad, Rev. Metal. CENIM, 5, 519 (1969).
359. H. Conrad, Ultrafine-Grain Metals, Syracuse Univ. Press, Syracuse, N.Y., p. 213 (1970).
360. H. Conrad, Reinstoffe in Wissenschaft und Technik, Akademie-Verlag, Berlin, p. 409 (1972).
361. J. C. M. Li, Trans. TMS-AIME, 227, 239 (1963).
362. M. F. Ashby, Phil. Mag., 21, 399 (1970).
363. C. P. Biwas, Ph.D. Dissertation, MIT (Jan. 1973).
364. W. G. Johnson and J. J. Gilman, J. Appl. Phys., 30, 129 (1959).
365. A. H. Cottrell, Trans. AIME, 212, 192 (1958).
366. R. J. Wasilewski, Trans. ASM, 56, 221 (1963).
367. F. R. Larson and J. Numes, Trans. ASM, 54, 481 (1961).
368. H. W. Rosenberg, Met. Trans., 8A, 451 (1977).
369. J. H. Hollomon, Trans. AIME, 162, 268 (1945).
370. C. E. Coleman and D. Hardie, J. Inst. Met., 94, 387 (1966).
371. D. Lee, Met. Trans., 1, 1607 (1970).
372. S. V. Ramani, P. Mukhopadhyay, P. Rodrigues and R. Krishnan, Proc. Int. Symp. Defect Interactions in Solids, Bangalore, India (1972).
373. S. L. Mannan and P. Rodriguez, Trans. Ind. Inst. Met., p. 49 (June 1973).
374. J. H. Hollomon, Trans. AIME, 164, 268 (1945).
375. W. B. Morrison, Trans. ASM, 59, 824 (1966).
376. B. W. Christ and G. V. Smith, Acta Met., 15, 809 (1967).
377. C. T. Liu and J. Gurland, Trans. TMS-AIME, 242, 1535 (1968).
378. C. T. Liu, R. W. Armstrong and J. Gurland, J. Iron and Steel Inst., 209, 142 (1971).
379. H. Wiedersich, J. Met., 16, 425 (1964).
380. F. N. Nabarro, Z. S. Bazinski and D. B. Holt, Adv. Phys., 13, 193 (1964).
381. D. Kuhlman-Wilsdorf, Work Hardening, Gordon and Breach, New York, p. 97 (1968).
382. H. M. Otte and J. J. Hren, Experimental Mechanics (Soc. Exp. Stress Analysis), 6, 177 (1966).
383. M. Doner, H. Chang and H. Conrad, Met. Trans., 5, 1383 (1974).
384. M. Doner, H. Chang and H. Conrad, Met. Trans., 6A, 1017 (1975).
385. H. Conrad and K. Wang, 5th. Int. Conf. Strength of Metals and Alloys (ICSMAS) Vol. 2, Pergamon Press, New York, p. 1067 (1978).
386. P. Ganesan, K. Okazaki and H. Conrad, Met. Trans., 10A, 1021 (1979).
387. R. W. Armstrong, Acta Met., 16, 347 (1968).

388. R. W. Armstrong, Defect Interactions in Solids, Ind. Inst. Science, Bangalore (1972); J. Scien. Ind. Res., 32, 591 (1973).
389. Y. V. R. K. Prasad and R. W. Armstrong, Ind. J. Tech., 11, 513 (1973).
390. R. W. Armstrong, Canad. Met. Quart., 13, 187 (1974).
391. Y. V. R. K. Prasad and R. W. Armstrong, Phil. Mag., 29, 1421 (1974).
392. Y. V. R. K. Prasad, N. M. Madhava and R. W. Armstrong, Proc. 4th Bolton Landing Conf. on Grain Boundaries in Engineering Materials, Lake George, N.Y. (June 9-12, 1974).
393. A. R. Rosenfield and G. T. Hahn, Trans. ASM, 59, 962 (1966).
394. A. R. Rosenfield, Met. Reviews, 13, 29 (1968).
395. F. A. McClintock, Ductility, ASM, Cleveland, Ohio, p. 255 (1968).
396. J. M. Krafft, Appl. Mat. Res., 3, 88 (1963).
397. J. P. Hirth and F. H. Froes, Met. Trans., 8A, 1165 (1977).
398. M. Sugano and C. M. Gilmore, Met. Trans., 11A, 559 (1980).
399. A. Akhtar, Met. Trans., 6A, 1217 (1975).
400. P. Haasen and A. Kelley, Acta Met., 5, 192 (1957).
401. L. M. Malik and J. I. Dickson, Mater. Sci. Eng., 17, 67 (1975).
402. C. S. Hartley, Acta Met., 14, 1237 (1966).
403. G. F. Bolling, Phil. Mag., 4, 527 (1959).
404. J. Stringer, Acta Met., 8, 758 (1960).
405. O. V. Ignatov, M. S. Model, L. F. Sokiriansky and A. Y. Shinyaev, Titanium Science and Technology, Vol. 4, Plenum Press, New York, p. 2535 (1973).
406. A. H. Cottrell and B. A. Bilby, Proc. Phys. Soc. London, 62A, 49 (1949).
407. S. Harper, Phys. Rev., 83, 709 (1951).
408. P. Delobelle and C. Oytana, Met. Trans., 9A, 740 (1978).
409. D. Gupta and S. Weinig, Acta Met., 10, 292 (1963).
410. P. G. Fuller and D. R. Miller, Metal Sci., p. 16 (1977).
411. J. N. Pratt, N. J. Bratina and B. Chalmers, Acta Met., 2, 203 (1954).
412. D. R. Miller, Trans. AIME, 224, 275 (1962).
413. F. Povolo and E. A. Bisogni, Acta Met., 14, 711 (1966).
414. F. Povolo and E. A. Bisogni, Acta Met., 15, 701 (1967).
415. D. R. Miller, The Science, Technology and Application of Titanium, Pergamon Press, New York, p. 401 (1970).
416. K. M. Browne, Acta Met., 20, 507 (1972).
417. S. Mishra and M. K. Asundi, Titanium Science and Technology, Vol. 2, Plenum Press, New York, p. 883 (1973).
418. J. R. Donoso, P. G. Watson and R. E. Reed-Hill, Met. Trans., 9A, 742 (1978).
419. J. I. Dickson, R. Derosiers and L. M. Malik, Scripta Met., 14, 311 (1980).
420. H. Yoshinaga and S. Morozumi, Phil. Mag., 23 (1971).
421. H. Yoshinaga, K. Toma, K. Abe and S. Morozumi, Phil. Mag., 23, 1387 (1971).
422. A. M. Garde, E. Aigenthaler, B. N. Woodruff and R. E. Reed-Hill, Met. Trans., 6A, 1183 (1975).
423. Y. Krishna Mohan Rao, V. Kutumba Rao and P. Rama Rao, Scripta Met., 13, 851 (1979).
424. K. Okazaki, T. Odawara and H. Conrad, Scripta Met., 11, 437 (1977).
425. B. J. Shulz and C. J. McMahon, Met. Trans., 4, 2485 (1973).
426. C. M. Libanati and F. Dyment, Acta Met., 11, 1263 (1967).
427. F. Dyment and C. M. Libanati, J. Mat. Sci., 3, 349 (1968).
428. A. D. Le Claire, Diffusion in Body-Centered Cubic Metals ASM, Cleveland, p. 3 (1965).
429. C. Zener, J. Appl. Phys., 22, 372 (1951).
430. J. I. Federer and T. S. Lundy, Trans. TMS-AIME, 227, 592 (1963).
431. G. V. Kidson, Conad. J. Phys., 4, 1563 (1963).
432. G. M. Newman, Z. Phys. Chem., 5T, 166 (1966).
433. R. F. Peart and J. Askill, Phys. Stat. Sol., 23, 263 (1967).
434. D. Graham, Diffusion in Body-Centered Cubic Metals ASM, Cleveland, p. 27 (1965).

435. J. Weertman, Rate Processes in Plastic Deformation of Materials ASM, Cleveland, p. 315 (1975).
436. J. Weertman, Trans. ASM, 61, 681 (1968).
437. W. Blum, Phys. Stat. Sol. (b), 45, 561 (1971).
438. G. Malakondaiah and P. Rama Rao, Scripta Met., 13, 1187 (1979).
439. J. G. Harper and J. E. Dorn, Acta Met., 5, 654 (1957).
440. F. R. N. Nabarro, Rept. Conf. on Strength of Solids, The Phys. Soc., London, p. 75 (1948).
441. C. Herring, J. Appl. Phys., 21, 437 (1950).
442. H. Conrad, Mechanical Behavior of Materials at Elevated Temperatures, McGraw-Hill, New York, p. 218 (1956).
443. M. F. Ashby, Acta Met., 20, 887 (1972).
444. M. F. Ashby, Fracture 1977 - (ICF4) Vol. 1, Univ. Waterloo Press, Waterloo, Canada, p. 1 (1977).
445. Y. Krishna Mohan Rao, V. Kutumba Rao and P. Rama Rao, to be publ. 4th Int. Conf. on Titanium, Kyoto, Japan (May 1980).
446. A. Nadai and M. J. Manjoine, Trans. ASME, 63, A77 (1941).
447. W. A. Backofen, I. R. Turner and D. H. Avery, Trans. ASM, 57, 980 (1964).
448. D. H. Avery and J. M. Stuart, Surfaces and Interfaces II, Syracuse Univ. Press, Syracuse, N.Y., p. 371 (1968).
449. K. Okazaki, M. Kagama and H. Conrad, Acta Met., 27, 301 (1979).
450. H. Conrad, M. Y. Demeri and D. Bhatt, Formability: Analysis, Modeling and Experimentation, TMS-AIME, p. 208 (1978).
451. W. A. Backofen, Deformation Processing, Addison-Wesley, Reading, Mass. (1972).
452. H. Conrad, J. Mechwork. Tech., 2, 67 (1978).